Violations of K-Conservation in ^{178}Hf

by

Adam B. Hayes

To Carol Elizabeth Hayes, who made this work possible

but did not live to see it completed.

Curriculum Vitae

The author was born in Pennsylvania in 1972 and grew up in rural New Jersey. He entered the Rochester Institute of Technology in 1991. While there he worked on the development of mass spectrometer systems for off-gas analysis and isotope-level identification of trace contaminants as a co-op student for Lockheed Martin (then Martin Marietta), and later, on the characterization of novel magnetic materials under Professor A. Entenberg. He earned a Bachelor of Science degree in physics in 1996 and entered the University of Rochester. He earned a Master of Arts degree in 2000 while working on the PHOBOS detector for the quark-gluon plasma experiments at RHIC under Professor F. Wolfs. From 1999 until the present, he completed the present dissertation research under the guidance of Professor Douglas Cline.

Acknowledgments

This work is the result of the combined efforts of many individuals and groups. I would like to thank everyone who assisted in the experimental work or the refinement of the dissertation or offered advice and encouragement, in particular the following people.

Prof. Douglas Cline offered superb and essential advice and guidance. Dr. Ching-Yen Wu was invaluable in clearing up conceptual questions through many thoughtful conversations. Both Dr. Wu and Prof. Cline made vital contributions to the experimental work. Dr. M. Simon provided much advice, essential technical training and lessons in physics. Mr. R. Teng's technical expertise was indispensable in the design and execution of experiments and the production of several figures in this dissertation. Messrs. K. Adams, T. Melanson, K. Madison and B. Schulz of the Instrument Machine Shop provided expert machine work. The dexterity of Mr. L. Kuntz was instrumental in preparing electronics for the activation experiment. Mr. D. Munson provided essential computer maintenance and assistance. Dr. Hui Hua gave careful assistance in the setup of the activation experiment.

Collaborators around the world participated in experiments, experimental design, took shifts during the experiments and gave advice and assistance for which I am grateful: A. O. Macchiavelli and K. Vetter of LBNL; J. Gerl, Ch. Schlegel and H. J. Wollersheim of GSI; P. Napiorkowski and J. Srebrny of Warsaw University; R. Janssens, C. J. Lister, E. F. Moore, R. Pardo, D. Seweryniak and the operations staff of ANL; J. Ai, H. Amro, C. Beausang, R. Casten, A. A. Hecht, A. Heinz, R. Hughes and D. Meyer of WNSL at Yale; P. Chowdhury of U. Mass., Lowell.

Abstract

Analysis of the electromagnetic population of high-K bands has revealed the breakdown of the K-selection rule with increasing spin in quadrupole-deformed nuclei. The measured electromagnetic matrix elements which couple the $K^{\pi}(t_{1/2}) = 8^-(4\text{s})$, $6^+(77\text{ns})$ and $16^+(31\text{y})$ isomer bands to low-K bands in ^{178}Hf have revealed the population paths and solved the decades-old mystery of the Coulomb excitation of the $K^{\pi} = 8^-$ isomer.

The $K^{\pi} = 2^+, 4^+, 6^+, 8^-$ and 16^+ bands, as well as one previously unknown band in ^{178}Hf were populated by electromagnetic excitation of an 89%-enriched, 0.5 mg/cm^2 target using a 650 MeV ^{136}Xe beam. Gammasphere and Rochester's CHICO particle detector provided event-by-event Doppler-shift corrected γ-ray data in the thin-target experiment, resolving populations of the isomer band states as low as 10^{-4}, normalized to the $8_{\text{GSB}}^- + \rightarrow 6_{\text{GSB}}^+$ transition yield. The Coulomb excitation data extended the γ-, 4^+ and 6^+ bands from the 6^+, 7^+ and 13^+ levels to the 14^+, 16^+ and 14^+ levels, respectively.

In a second experiment, a ^{178}Hf beam was activated by a 5-target stack of natural Ta targets at 72%—88% of the Coulomb barrier. Activation cross sections of the 16^+ isomer of 0.6(2)—11(3) mb were measured for 72%—88% of the Coulomb barrier during offline counting.

The population paths and matrix elements from low-K to high-K bands were deduced from the combined analysis of the two experiments, showing that K-mixing in the low-K bands is the primary cause of the K-forbidden transitions. The observed onset of K-mixing is consistent with rotational alignment effects in the low-K bands and pure wave functions in the high-K bands. The measured transition strengths to each high-K band are sensitive indicators of the distribu-

tion of K values in the low-K bands. Transition strengths to the $K^\pi=4^+, 6^+, 8^-$ and 16^+ bands gauged the onset with increasing spin of the $2 \leq K \leq 6$, $4 \leq K \leq 8$, $5 \leq K \leq 11$ and $14 \leq K \leq 18$ admixtures, respectively, in the GS and γ-bands. Implications regarding Coulomb depopulation and stimulated emission of isomers are discussed.

Contents

List of Tables

List of Figures

Chapter 1

Introduction

The transition from spherical symmetry to axial symmetry in nuclei as N and Z move farther from the magic numbers creates an intrinsic frame with a special axis defined by the shape of the nuclear drop, whereas an intrinsic frame has no meaning in a sphere of indistinguishable particles. The question naturally arises, "What effect does the appearance of a meaningful intrinsic frame or the reduction of rotational symmetry have on the physics of the nucleus?" This has been an important subject of investigation in nuclear physics for about 70 years, partly in terms of the significance of the projection of the nuclear spin on the symmetry axis, the number K. The experimental focus of the present work is on the electromagnetic population mechanisms of the "K-isomers," but the broader subject is the conservation of the quantum number and the veracity and universality of the "K selection rule" in electromagnetic transitions in nuclei.

Here, the importance of the K quantum number in nuclear physics is developed through both the historical and physical background. The motivation for K-isomer research is presented, followed by a summary of related work and the questions that the present work addresses.

1

1.1 History

The chemical term *isomer* defines two molecules as isomers if they are composed of geometrically different arrangements of the same atoms [19]. The sagacious introduction of the term into nuclear physics proved to be in perfect analogy with the chemical term. After explaining isotopic differences in 1913 [20] Soddy differentiated species by "any new property concerned with the nucleus of the atom" (qtd. in [19]) in his 1917 and 1919 papers [21, 22], which eventually came to be understood in terms of changes in the shape or single-particle orbits. While this would naturally differentiate long-lived states, the original meaning was more general. Today the term *isomer* occasionally takes Soddy's general definition, but throughout this work a nucleus will be termed an *isomer* only if it differs from the ground state in its single-particle configuration or collective shape *and* has a lifetime much longer than what would be expected for a "single-particle" transition, typically > 1 ps (Chapter 2).

Frederick Soddy [20]

In 1921, Hahn, known for the discovery of the fission of uranium and thorium, first observed isomerism in a $t_{\frac{1}{2}} = 1.175$ m state of what is now known to be ^{234}Pa [19]. The concept of the K quantum number, the projection of the

nuclear spin on the body-fixed symmetry axis, was introduced by von Weisza-cker in 1936 [23]. Beginning about twenty years later, metastable nuclei were discovered which came to be known as "K-isomers." The K-selection rule forbids transitions where the change in K is greater than the electromagnetic multipole order, and their long lifetimes were found to be the results of large changes in the K quantum number in their decay transitions. In the 1950's the first landmark theoretical work in K-isomerism by Bohr and Mottelson [24] appeared, followed by the discovery of the well-known $K^\pi = 8^-$, $t_{\frac{1}{2}} = 4$ s K-isomer of ^{178}Hf by Fel-ber [25] *et al.* [26, 27]. The frequent occurrence of K-isomers as evidence of the K selection rule, combined with the finite transition probabilities of "forbidden" decays, asserts the importance of continued investigation of K-conservation.

Otto Hahn [28]

1.2 Physics

The electromagnetic excitation of high-K states is greatly hindered by conserva-tion of the K quantum number. Electromagnetic excitation probabilities decrease by many orders of magnitude with increasing multipole order, while for Coulomb excitation the probability of multiple-step excitations decreases approximately ex-

ponentially with the number of steps, making the electromagnetic excitation of high-K states from the ground state so unlikely that the Coulomb excitation of the 8^- isomer has remained a mystery for more than 20 years since it was first reported.

A "good" quantum number can be defined as a constant of motion, or equivalently, as an eigenvalue whose operator commutes with the Hamiltonian. Superposition, or "mixing," of states with different values of a quantum number are incompatible with the idea of that number being "good." The K quantum number commutes with the Hamiltonian if the potential is axially symmetric, and electromagnetic transitions for which the change in K is larger than the electromagnetic multipole order are forbidden, a similar condition to that required by conservation of angular momentum. The frequent occurrence in nuclei of γ-decay transitions which do not obey the K-selection rule clearly indicates that the K-quantum number is only approximately conserved. The study of K-isomerism is then directly related to conservation laws in nuclear physics.

1.3 Motivation

The $K^\pi = 8^-$ ($t_{1/2} = 4$ s) isomer (Figure 4-1) in ^{178}Hf was first populated by Coulomb excitation in 1982 by Hamilton *et al.* [29] and again in 1993 by Xie *et al.* [30], but the population path and the apparent violation of the K-selection rule remained unexplained. The unexpected population of high-K isomers to measurable levels by Coulomb excitation has brought into question the goodness of the K quantum number.

These two investigations of the K-selection violations in the 8^- isomer excitation measured the yield of the isomer state alone, without measuring the accompanying excitation of the rotational band built on the isomer. Thus, they showed the overall strength of the K-selection rule in terms of the total isomer

4

excitation cross sections. In order to find the path through the nuclear states from the GSB to the 8^- isomer band, more detailed study was necessary, and the pair of experiments in the present work will be shown to determine the excitation paths.

Another recent success in the study of K-isomerism is the photo de-excitation of ^{180}Ta, the only naturally occurring K-isomer. The photo-de-excitation has revealed a path that can be exploited to make non-K-conservative transitions, but the important parameters related to the loss of K-conservation and the rate of failure of K-conservation with these parameters is still not known. Interpretation of the ^{180}Ta research has validated several possible explanations of the stellar nucleosynthesis of the isomer, including the p-process, the s-process and the ν-process [31]. Continued work is directed at explaining the natural occurrence of the isomer.

The high energy density of enriched isomer material has created much continuing interest in the possibility of releasing the isomer energy electromagnetically [32, 33]. In pure form, the 16^+ isomer of ^{178}Hf (^{178m2}Hf) has an energy density of about 10^4 MJ/cm^3, only about a factor of 100 smaller than that of fission isotopes. While there have been no repeatable measurements of stimulated emission in ^{178m2}Hf, the success in ^{180}Ta has spurred the quest for stimulated emission in other isomers. Coulomb excitation into isomer states and of isomer targets may also impact the difficult goal of producing enriched isomer targets [34, 35].

The central objective of the present work is to determine the extent to which the K selection rule breaks down by explaining the electromagnetic excitation of three of the high-K ^{178}Hf isomers. Electromagnetic matrix elements will be measured, revealing K-allowed and K-forbidden paths through the nuclear excited states to high-K bands, and the following questions will be addressed.

1. How "good" is the quantum number K?

2. What observables or variables are associated with the onset of K-

5

conservation violations?

3. What are the critical values of those variables?

4. How sudden is the loss of K conservation with respect to these variables?

5. What can the loss of K conservation tell us about nuclear structure (the wave functions)?

6. Can the results be generalized to the many other K-isomers in the $A \approx 180$ region?

7. What are the implications in other areas of physics?

8. Can an understanding of K-selection violation lead to practical realizations?

9. What research should come next?

In the next chapter the relevant theoretical concepts are explained, including the Coulomb excitation theory for heavy ions and the analytical methods used. Chapter 3 presents the first of two Coulomb excitation experiments, excitation of an enriched ^{178}Hf target by a ^{136}Xe beam using the CHICO particle detector and Gammasphere. The analysis of the γ-ray yields, including the prompt yields in the isomer bands is explained in Chapter 4. Chapters 5, 6 and 7 present a ^{178}Hf beam activation experiment using natural tantalum targets, followed by the analysis of the $K^\pi = 16^+$ isomer Coulomb activation. Chapter 8 presents the level scheme extended in the first experiment, along with observed γ-decays. The electromagnetic properties of the ^{178}Hf states, including the measured matrix elements and isomer cross sections are discussed in Chapter 9. The final chapters, 10 through 12 discuss various implications of the results as they relate to the

goodness of K, the possibility of exploiting the breakdown of K-selection, and directions for future work.

Chapter 2

Theory

Single particle states in a deformed nucleus were first examined in the 1950's by Moszkowski [36], Mottelson [37], Nilsson [38], Gottfried [39] and Alaga in his doctoral thesis [40]. A brief history of the early work can be found in Alaga's 1957 paper [41]. In the past ten years or so, quantitative studies of single- or multi-quasiparticle K-isomers have begun in an effort to explain the apparent K-selection rule violations defined below. The principal question has been a debate between Coriolis mixing and tunneling through a collective shape barrier.

This chapter outlines the collective degrees of freedom of deformed (non-magic) nuclei, leading to electromagnetic (EM) selection rules. The phenomenological description of K violations follows, including the well-known empirical rule of Rusinov, which most systematic studies of isomer lifetimes use as a basis of comparison. The quantitative results of the Coriolis mixing and the tunneling theories are discussed. Coulomb excitation theory and the details of numerical calculations used in the present work are presented.

2.1 Collective Properties

The Collective Model essentially relates the Shell Model to the collective (but still quantum mechanical) behavior of the nucleus. The sum of the wave functions of all of the nucleons is almost spherically symmetric for closed-shell nuclei. For nuclei with Z or N far from the magic numbers (2, 8, 20, 28, 50, 82, and 126), the sum of many particle wave functions in open shells gives a collective shape that is no longer spherically symmetric [42], leading to collective phenomena such as rotations, vibrations and fission. Simple quadrupole deformations (prolate ellipsoids) are often described by the parameter

$$\delta \approx \frac{\Delta R}{R}, \tag{2.1}$$

where R is the RMS radius and $\Delta R \equiv R_3 - R_\perp$ [43]. In the case of ^{178}Hf, the deformation is considerable—$\delta \approx 0.26$ [44] (as discussed in [43]).

2.1.1 Nuclear Shapes, Parameterization

The shape of a deformed (non-spherical) nucleus in the intrinsic or body-fixed frame can be described as an expansion of the radius over spherical harmonics with complex coefficients. The spherical harmonics $Y_{lm}(\theta, \phi)$ form a complete set, so any shape where the radius R is single-valued and continuous can be represented by

$$R = R_o \left(1 + \alpha_{00} + \sum_{\lambda=1}^{\infty} \sum_{\mu=-\lambda}^{\lambda} \alpha_{\lambda\mu}^* Y_{\lambda\mu}(\theta, \phi) \right). \tag{2.2}$$

This can be thought of in terms of the Liquid Drop Model, where α_{00} is defined in order to conserve the total volume of the nuclear drop [14]. In the special case of the quadrupole-deformed nucleus, the radius can be parametrized in the Hill and Wheeler coordinates β and γ as

$$R(\theta, \phi) = R_0 \left\{ 1 + \beta \sqrt{\frac{5}{16\pi}} (\cos\gamma(3\cos^2\theta - 1) + \sqrt{3}\sin\gamma\sin^2\theta\cos 2\phi) \right\}, \tag{2.3}$$

9

so that β deformations ($\beta \neq 0$) are axially symmetric (about the polar axis) and γ deformations are triaxial [14]. Symmetry about the polar axis will be seen to be important to the conservation of the angular momentum projection K on the polar axis. The Bohr Hamiltonian describes the effects of β and γ deformations and vibrations as well as collective rotation.

$$H = T_{\rm rot} + \frac{1}{2}B_2(\dot{\beta}^2 + \beta^2\dot{\gamma}^2) + \frac{1}{2}C_{20}(a_{20}(\beta, \gamma) - a_{20}^0)^2 + C_{22}(a_{22}(\beta, \gamma) - a_{22}^0)^2 \quad (2.4)$$

2.1.2 The Quantum Numbers I, J, R, and K

Because the particles in the collective core of a nucleus are identical and indistinguishable, rotation of the nucleus about a symmetry axis has no meaning, and the only *collective* rotations which need to be considered are those about the non-symmetry axes. The angular momentum $\vec{R}$ due to the collective rotation of a deformed (non-spherical) nucleus therefore has no component along a symmetry axis, the 3-axis in Figure 2-1. In the mass 180 region quadrupole deformations prevail, and there is one symmetry axis. The total angular momentum $\vec{I}$ of these nuclei is the sum of $\vec{R}$ and the single-particle contributions $\vec{J}$. Unpaired quasiparticles can of course contribute to the total angular momentum with projections onto all three axes, in general. The projections of the single-particle angular momenta along the symmetry axis are defined as Ω_i, where i designates the particle. The total angular momentum of all of the single particles is called $\vec{J}$ ($\vec{J} = \vec{L} + \vec{S}$), and $K = \Sigma\Omega_i$ is the name given to the projection of $\vec{I}$ on the symmetry axis.

2.1.3 Selection Rules

All Nuclei

For electromagnetic transitions between angular momentum states given by the matrix elements $\langle I_f M_f \mid Q_{\lambda\mu} \mid I_i M_i \rangle$, where $Q_{\lambda\mu}$ is the EM transition operator of order λ and magnetic component μ, the following selection rules apply [43, 14].
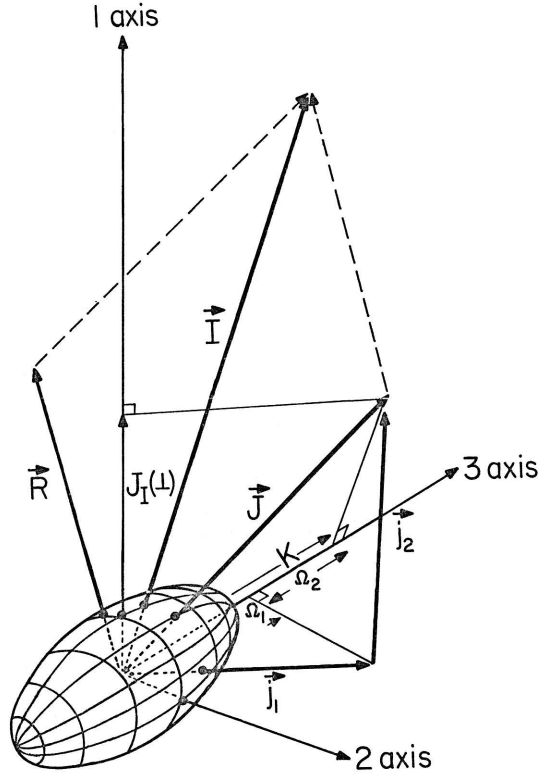
Figure 2-1: A prolate-deformed, axially symmetric nucleus. Angular momenta are shown for collective rotation $\vec{R}$ and each of two single particles $\vec{j_i}$ ($\vec{J} \equiv \Sigma \vec{j_i}$). The total angular momentum $\vec{I} \equiv \vec{J} + \vec{R}$. The components of $\vec{j_i}$ on the symmetry axis (3) are Ω_i, where $K = \Omega_1 + \Omega_2$. Taken from [11].

First, for total spin I,

$$| I_f - I_i | \leq \lambda \leq I_f + I_i, \tag{2.5}$$

which requires that the magnitude of the change in spin, $| \Delta I |$, is not greater than the multipolarity λ of the transition. Second, the magnetic quantum number M is conserved in the nucleus-photon system, so that

$$M_f = M_i + \mu. \tag{2.6}$$

11

Finally, parity is conserved by the EM transition operators.

$$\pi_i \pi_{Q_\lambda} \pi_f = 1, \tag{2.7}$$

where π_{Q_λ} is the parity of the electric or magnetic operator Q. For electric transitions, $\pi_{E\lambda\mu} = (-1)^\lambda$, and for magnetic transitions, $\pi_{M\lambda\mu} = (-1)^{\lambda+1}$, so that odd electric multipole and even magnetic multipole operators always change the sign of the parity eigenvalue.

The above selection rules apply to both spherical and non-spherical nuclei.

Axially Symmetric Nuclei

In a system with no rotation and perfect axial symmetry (and only vibrations in the β dimension), K is a good quantum number. It commutes with the (Bohr) Hamiltonian and must be conserved [14, 43]. Whenever K can be considered a good quantum number, transitions between the states $\mid I_i M_i K_i \rangle$ and $\mid I_f M_f K_f \rangle$ must satisfy the selection rule

$$\mid K_f - K_i \mid \leq \lambda \tag{2.8}$$

in addition to the aforementioned rules [45, 40]. In the Liquid Drop Model, for instance, if symmetry-breaking γ-vibrations can be neglected, then the nucleus is axially symmetric, and I_3 commutes with the Hamiltonian, Equation 2.4. Hence, K is a good quantum number [14] given by $I_3 \mid \psi \rangle = K \mid \psi \rangle$.

2.2 Electromagnetic Matrix Elements

2.2.1 The Wigner-Eckart Theorem

It can be shown that any irreducible tensor operators $\mid IM \rangle$, $Q_{\lambda\mu}$ and $\mid I'M' \rangle$ must satisfy the equation

$$\langle I'M' \mid Q_{\lambda\mu} \mid IM \rangle = (2I'+1)^{-1/2} \langle IM\lambda\mu \mid I'M' \rangle \langle I'\|Q_\lambda\|I\rangle, \tag{2.9}$$

where $\langle IM\lambda\mu \mid I'M' \rangle$ is the Clebsch-Gordan geometric coupling coefficient [43]. The term $\langle I'\|Q_\lambda\|I \rangle$ is referred to as the *reduced matrix element*, and $\langle I'M' \mid Q_{\lambda\mu} \mid IM \rangle$ is the *matrix element*.

In its application to electromagnetic transitions in axially symmetric nuclei (where the number K is important), the Wigner-Eckart theorem relates the matrix element for an electromagnetic transition between two states defined by I and the magnetic quantum number M (and K) to the reduced matrix element for transitions between the two states, defined only by I (and K). The matrix element $\langle I'\|Q_\lambda\|I \rangle$ retains the dependence on K values and commonly denotes the probability amplitude for a transition between states of K_i and K_f, where the initial and final K values may be equal. The $Q_{\lambda\mu}$ operator is identified as $\mathcal{M}(\lambda)$, the electromagnetic transition operator, and the observable reduced matrix element is not a function of μ. The Clebsch-Gordan coefficient then represents the probability amplitude of the appropriate geometric coupling between the initial and final angular momentum states through the photon (real or virtual), and gives the phase information in the Alaga rule and other systematics described in following sections.

The reduced matrix element $\langle I_f\|\mathcal{M}(\lambda)\|I_i \rangle$ is often thought of as the observable, because the transition rates which are usually measured depend on sums and averages over magnetic substates, and μ information is lost. In the following, "matrix element" typically refers to the reduced matrix element, and the intrinsic matrix element is referred to as such. Equations 2.10, 2.11, 2.13, 2.15 *etc.* are instances of the Wigner-Eckart theorem with appropriate normalizations of the basis states and explicit forms of the intrinsic matrix elements.

2.2.2 Matrix Elements for K-Allowed Transitions

Intraband Transitions

The matrix elements for the dominant intraband transitions, namely E2 and M1 transitions, are given by the following equations [43]. For E2 transitions,

$$\langle I_f K \parallel E2 \parallel I_i K \rangle = (2I_i + 1)^{1/2} \langle I_i K 20 \mid I_f K \rangle \sqrt{\frac{5}{16\pi}} e Q_o, \qquad (2.10)$$

where $\sqrt{\frac{5}{16\pi}} e Q_o$ is typically referred to as the electric quadrupole moment of the band, and $\langle I_i K \lambda \mu \mid I_f K \rangle$ is the Clebsch-Gordan coefficient giving the probability amplitude of an appropriate coupling between the initial and final states after emitting a photon carrying angular momentum λ with magnetic component μ. Static moments, where $I_i = I_f$, represent the so-called reorientation, where only the μ substate changes. This can be an important effect in Coulomb excitation, where the probability of reorientation must be considered during interactions between nuclei, but not during the subsequent γ-decay.

For M1 magnetic transitions,

$$\begin{aligned}
\langle K I_2 \| M1 \| K I_1 \rangle &= \left(\frac{3}{4\pi}\right)^{1/2} \frac{e\hbar}{2Mc} (2I_1 + 1)^{1/2} \times \left((g_K - g_R) \left[K \langle I_1 K 10 \mid I_2 K \rangle \right.\right. \\
&\left.\left. \quad - b(-1)^{I_1 + 1/2} 2^{-1/2} \langle I_1 \frac{1}{2} 11 \mid I_2 \frac{1}{2} \rangle \delta(K, \frac{1}{2}) \right] \right. \\
&\left. \quad + g_R \sqrt{I_1(I_1 + 1)} \delta(I_1, I_2) \right),
\end{aligned} \qquad (2.11)$$

where b is the "decoupling parameter" for transitions between $K = \frac{1}{2}$ states, and $g_K - g_R$ is the effective gyromagnetic ratio of the particle(s) and rotor. [43]. This reduces to

$$\langle K I_2 \| M1 \| K I_1 \rangle = \left(\frac{3}{4\pi}\right)^{1/2} \mu_N (2I_1 + 1)^{1/2} (g_K - g_R) K \langle I_1 K 10 \mid I_2 K \rangle \qquad (2.12)$$

for $K \neq \frac{1}{2}$ and $I_1 \neq I_2$. Here, $\mu_N \equiv \frac{e\hbar}{2Mc}$ is the nuclear magneton. M1 excitations are not important in the experiments in this work, because the electric interactions are dominant in Coulomb excitation.

Interband Transitions

The "Alaga rule" for electromagnetic decays between states of differing K values is a direct consequence of the Wigner-Eckart theorem [43, 14]. (Alaga's selection rules [41, 40] actually include more than just electromagnetic transitions.) The Alaga rule is usually written in terms of the Clebsch-Gordan coefficients.

$$\langle K_f I_f \| \mathcal{M}(\lambda) \| K_i I_i \rangle = \tag{2.13}$$
$$\sqrt{2I_i + 1} \Big[\langle I_i K_i \lambda K_f - K_i \mid I_f K_f \rangle \times \langle K_f \mid \mathcal{M}(\lambda, \mu = K_f - K_i) \mid K_i \rangle$$
$$+ (-)^{I_i + K_i} \langle I_i - K_i \lambda K_i + K_f \mid I_f K_f \rangle \times \langle K_f \mid \mathcal{M}(\lambda, \mu = K_i + K_f) \mid \bar{K}_i \rangle \Big]$$

for $K_i \neq 0$ and $K_f \neq 0$, or

$$\langle K_f I_f \| \mathcal{M}(\lambda) \| K_i I_i \rangle = \sqrt{2I_i + 1} \langle I_i 0 \lambda K_f \mid I_f K_f \rangle \tag{2.14}$$
$$\times \langle K_f \mid \mathcal{M}(\lambda, \mu = K_f) \mid K_i = 0 \rangle \begin{cases} \sqrt{2} & K_f \neq 0 \\ 1 & K_f = 0 \end{cases}$$

for $K_i = 0$. The terms $\langle K_f \mid \mathcal{M}(\lambda, \mu) \mid K_i \rangle$ are referred to as the intrinsic matrix elements. $\bar{K}$ represents the opposite orientation of the K projection on the symmetry axis. In Equation 2.13, the matrix elements $\langle K_f \mid \mathcal{M}(\lambda, \mu = K_i + K_f) \mid \bar{K}_i \rangle$ are identically zero for $K_i + K_f > \lambda$. (The notation of Bohr and Mottelson [43] is used throughout this work, with the exception that the magnetic components are called "μ" to avoid confusion with the hindrance defined below.)

Transition Probabilities and Lifetimes

The reduced transition probability $B(E(M))$ is defined as

$$B(E(M)\lambda; I_i K_i \to I_f K_f) \equiv \frac{\mid \langle I_f K_f \| E(M)(\lambda, \mu) \| I_i K_i \rangle \mid^2}{2I_i + 1} \tag{2.15}$$

for electric(magnetic) transitions, where the divisor $2I_i + 1$ represents an average over the unobserved initial magnetic substates [14]. Γ_γ is given by the expres-

sion [14]

$$\Gamma_\gamma = \frac{8\pi(\lambda+1)}{\lambda((2\lambda+1)!!)^2}\left(\frac{E_\gamma}{\hbar c}\right)^{2\lambda+1} B(E(M)\lambda; I_i K_i \to I_f K_f). \qquad (2.16)$$

Enhancement of the total decay width by internal conversion is described by the internal conversion coefficients α, giving

$$\Gamma_i = \Gamma_\gamma^i(1+\alpha_i), \qquad (2.17)$$

for the ith decay branch and the total decay width of the state,

$$\Gamma_{\text{total}} = \sum_i \Gamma_i. \qquad (2.18)$$

The width is related to the lifetime τ by

$$\Gamma_{\text{total}} = \frac{\hbar}{\tau}. \qquad (2.19)$$

Typical Single-Particle and Collective Lifetimes

Weisskopf has estimated the maximum reduced transition probability of the electromagnetic decay of a single-particle state,

$$B(\mathcal{M}\lambda) = \frac{e^2}{4\pi}\left(\frac{3}{\lambda+3}\right)^2 R_o^{2\lambda}, \qquad (2.20)$$

the "Weisskopf estimate" or "Weisskopf unit" [46]. This simple calculation takes into consideration only the nuclear radius and the multipole order of the transition and does not include the spin-dependence. Collective transitions which result from rotation or vibration of the nuclear drop may have considerably higher transition probabilities. For instance, for $E_\gamma \approx 500$ keV transitions in $A \sim 180$ nuclei, the electric transitions may have Weisskopf estimates corresponding to lifetimes of $\sim 10^{-15}$ s for electric dipole (E1) transitions, $\sim 10^{-9}$ s for electric quadrupole (E2) transitions, and so on. Electric quadrupole transitions of the order of hundreds of W.u. are common in the GS bands of quadrupole-deformed nuclei in the region, such as hafnium, giving them typical lifetimes of 10^{-12}–10^{-9} s. Reduced transition

probabilities are often expressed in terms of the Weisskopf unit (W.u.), so that the "collectivity" of the transition is apparent. Selection rules for electromagnetic transitions based on the quantum numbers described below impose restrictions on both single-particle and collective transitions, leading to isomerism in some cases.

2.3 Isomer Phenomenology

Isomers were discovered in hafnium as early as 1957 with the discovery of the ^{178m1}Hf 8^- K-isomer by Felber *et al.* [25]. The concluding sentence of the Felber paper, referring to what is now known as the 8^- isomer, reads

> ...in so far as K is a good quantum number E1 radiation is completely
> forbidden. The very long observed life-time indicates that K is, indeed,
> a rather good quantum number in this region of the periodic table.

The selection rule of Equation 2.8 forbids transitions in axially symmetric nuclei where K is not conserved in the nucleus-photon system. In reality, K-forbidden decays where $\mid \Delta K \mid > \lambda$ are regularly observed and are merely hindered, and some qualifications must be made.

Rusinov [12] proposed a rule to relate the forbiddenness $\nu \equiv \mid \Delta K \mid - \lambda$ to the hindrance $F_\nu \equiv \frac{t_{1/2}^{\mathrm{meas}}}{t_{1/2}^{\mathrm{W}}}$ (or the *reduced hindrance* $f_\nu \equiv F_\nu^{\frac{1}{\nu}}$), where $t_{1/2}^W$ is the Weisskopf single-particle estimate of the half-life. Rusinov's rule,

$$\log F_\nu = 2(\mid \Delta K \mid - \lambda), \tag{2.21}$$

qualitatively describes the slope of $\log F_\nu$ versus ν, but some decays have discrepancies in F_ν of several orders of magnitude, as shown in Figure 2-2. Furthermore, the range of half-lives for a single value of ν, even for transitions of a single multipolarity, make the rule a poor predictor. Löbner compiled a wider variety of lifetime data broken down by multipolarity [47]. Even after Löbner's classification, the Rusinov rule still does not predict lifetimes even within an order of magnitude in

Figure 2-2: τ^{exp} and $\tau^{\text{ind.part.}}$ are the experimental value and the Weisskopf estimate of the lifetime of an isomer state, respectively. $\nu = \mid \Delta K \mid -L$ is the forbiddenness, where $L \equiv \lambda$ is the multipole order. The "empirical rule" $\log F_W = 2\nu$ is shown. From Rusinov [12].

most cases. However, the qualitative description agrees with K being a conserved quantity in the ideal case: there is a strong correlation between hindrance and forbiddenness.

The often cited work of Rusinov (1961) contains the clearest general description of the problem.

> The K selection rule will be obeyed strictly only when K is a "good"
> quantum number, i.e., when the internal and rotational motions are
> completely independent of each other. In actuality there is always
> some coupling between these two forms of motion, and K is only an
> approximate quantum number. [12]

18

If there is some mixing mechanism or asymmetry about the "symmetry" axis induced by rotation, then the mixing should be expected to be small near the band head where $\vec{R}$ and its resulting Coriolis and centrifugal effects are small, and to increase above the isomer band head as the rotational frequency increases. It will be seen in the Coriolis mixing section that this is one reason that the spin-dependent K-mixing model is so appealing; it has small matrix elements at the band head, where K should be a better quantum number. Bohr and Mottelson write,

> In a quantal system, the frequency of even the lowest rotational exci-
> tations may be so large that the Coriolis and centrifugal forces affect
> the structure in a major way. [43]

So, the observation of K-forbidden transitions can be seen from the point of view of coupling of rotational and single-particle motions (similar to the interaction proposed by Mikhailov [48]) forcing a change in K, or as a breaking of axial symmetry that makes the K quantum number less meaningful. In either case, the conjecture of Bohr and Rusinov suggest models such as the ones described in the next section.

2.4 Preeminent Theories of K-Mixing

The two prominent mechanisms proposed to explain the apparent violation of the K selection rule (Equation 2.8) are Coriolis mixing and penetration of the γ barrier [26, 49, 50, 51]. Coriolis mixing is the effect of the quantum mechanical analogue of the Coriolis force acting to reorient the single-particle angular momenta vectors $\vec{j}_i$ toward the collective rotation $\vec{R}$. This can be seen to add *smaller K_a* admixtures to the wave functions than the *nominal K* value. It is often assumed that this will result only in a significant admixture of $K_a = K - 1$, however high order effects can be shown to be considerable [43]. In a case where
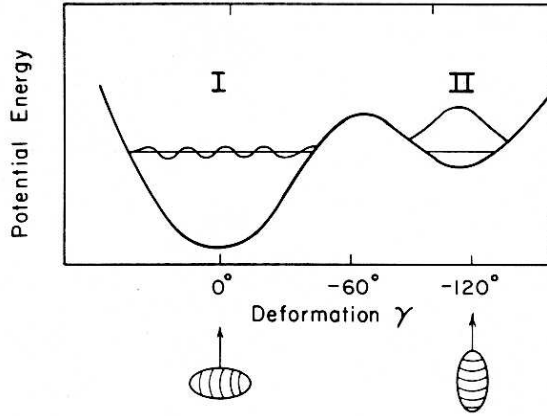
Figure 2-3: A schematic representation of γ-barrier penetration. Region I represents a low-K state where the angular momentum is mostly from rotation $\vec{R}$. Region II represents a single-particle isomer state, where the single-particle angular momentum $\vec{J}$ is aligned with the deformation axis. From [13].

a high-K band has admixtures from Coriolis coupling, it may mix with a low-K band, so that there are admixtures K_a present in the low K band which are greater than its nominal K-value [51, 43]. In addition, a distribution of K admixtures which broadens with increasing density of states at increasing level energy has been postulated(*e.g.* [52]), also leading to the expectation of high-K admixtures in low-K bands. Rotational alignment of single-particle angular momenta and band crossing phenomena are among the empirical evidence for the importance of Coriolis mixing.

Penetration of the γ barrier can be described as a tunneling process between two shapes—two values of the γ shape parameter (Equation 2.3). Tunneling from a rotation-aligned state around $\gamma = 0°$ to a deformation-aligned state near $\gamma = -120°$, illustrated in Figure 2-3, has been used to accurately predict the partial lifetimes of some K-forbidden decay branches of isomers in several γ-soft osmium nuclei [13, 53].
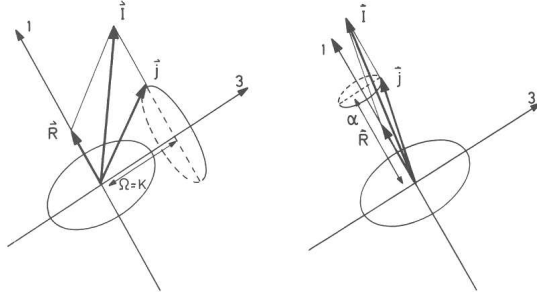
Figure 2-4: The effect of the Coriolis force on single-particle angular momentum. A deformation-aligned state is shown on the left. A rotation-aligned state is shown on the right. From [14].

2.4.1 Coriolis Mixing Model

The quantum mechanical analogues of Coriolis and centrifugal forces give a contribution to the Hamiltonian of a single particle in a rotating deformed nucleus of the form

$$H_c \propto -\vec{R} \cdot \vec{j}, \tag{2.22}$$

which favors alignment of the single-particle angular momentum with the rotation axis, effectively introducing smaller K_a contributions than the nominal K of the band [43]. $H_c \to 0$ at the band head where $\vec{R} = 0$, so the band head remains pure in K. Figure 2-4 shows the Coriolis effect on the angular momentum of a single particle in a prolate spheroid.

The conjectures of Rusinov and Bohr and Mottelson in section 2.3 constitute the justification for models that are based on the forces that arise from collective rotations. The Coriolis mixing models generally do not predict absolute values of F_ν or matrix elements from theory alone—some adjustable parameters remain. (Absolute predictions of the mixing strength can be made for admixtures of $\mid \Delta K \mid = 1$, but these have little relevance in the study of high-ΔK transitions.) Nor do they pertain to predictions about the lifetimes of decays from the band

head where $R = 0$. This is actually an advantage in cases where the isomers have very long lifetimes. If a large matrix element is predicted for an isomer decay, it may be in conflict with the measured lifetime. In cases where the lifetime of the band head is extremely long, but the Coulomb excitation cross section is large for the rotational band built on the isomer, the Coriolis mixing models are appealing.

However, a shortcoming of some spin-dependent mixing (SDM) calculations is that they are based on a perturbation which admittedly breaks down at high spin. Bohr and Mottelson point out that these perturbation calculations do not converge quickly and can be sensitive to high-order terms [43]. So, if a measured set of matrix elements indicates that the band head must be very pure, and that the mixing increases quickly with R, then the experiment can be said to be in agreement with the Coriolis mixing model, even if the exact spin dependence of the matrix elements is not reproduced by the theory.

Treating Single K-Admixtures

Assuming that there is only one significant K-admixture that two bands have in common, transitions between the two bands can be treated with the Alaga rule of Equations 2.13 and 2.15. Since the geometric coupling term in the Alaga rule goes to zero for all K-forbidden transitions, calculation of the matrix elements is limited to admixtures where $K_i = K_f - \lambda, K_f - \lambda + 1, \ldots, K_f + \lambda - 1, K_f + \lambda$. This approach was used by Xie et $al.$ to derive an intrinsic E3 matrix element connecting the GSB to the 8^- isomer band [30] in ^{178}Hf from Coulomb excitation cross sections. A term linear with ΔI^2 (after Mikhailov [48]) can be included in the intrinsic matrix element,

$$\langle K_f \mid \mathcal{M}(\lambda, \mu = K_f) \mid K_i = 0 \rangle = a + b(I_f(I_f + 1) - I_i(I_i + 1)) \qquad (2.23)$$

giving a slow increase in K-mixing with spin [43]. Since the geometric coupling terms (Clebsch-Gordan coefficients) vary over orders of magnitude from level to

level, large experimental γ-ray yield data sets or precise branching ratio data can in principle be used to discriminate between several suspected K admixtures.

Treating Multiple Admixtures

Bohr and Mottelson [43] have produced a spin-dependent K-mixing formula (Equation 2.24 below) for the matrix elements of K-forbidden transitions. Shimizu and Nakatsukasa [49] give a derivation of the formula, based on a variation of the Cranking Model.

The Cranking Model was developed by Inglis [54, 55] to calculate physical observables by moment of inertia considerations. The model assumes some postulated wave function for the nucleus, and calculates the moment of inertia for different configurations by rotating the nucleus. The variation on the Cranking Model of Inglis used to obtain Equation 2.24 differs from the standard Cranking Model. Whereas the standard Cranking Model is more applicable at high spin, the present variation uses the limiting values of the perturbation as $R \to 0$. Hence, it works at low spin, but becomes unrealistic at high spin [49].

The matrix elements obtained are given by

$$\langle K_f \parallel M(\lambda) \parallel K_i I_i \rangle = N\sqrt{2I_i + 1}\langle I_i K_f - \lambda\lambda\lambda \mid I_f K_f \rangle\sqrt{\frac{(I_i - K_i)!(I_i + K_i + \nu)!}{(I_i - K_i - \nu)!(I_i + K_i)!}}$$
$$\times \langle K_f \mid m_{\Delta K = \lambda + \nu, \mu = \lambda} \mid K_i \rangle, \qquad (2.24)$$

where the normalization, N, is $\sqrt{2}$ for $K_i = 0$ and 1 for $K_i \neq 0$. ($K \neq 0$ states are degenerate, since the projection of $\vec{I}$ on the symmetry axis can take either direction [43].) Mathematically, Equation 2.24 is a perturbation expansion of the matrix elements over $I_\pm$.

To see how the perturbation breaks down for high spin, it is useful to define $H(I_i, K_i, \nu) \equiv \sqrt{\frac{(I_i - K_i)!(I_i + K_i + \nu)!}{(I_i - K_i - \nu)!(I_i + K_i)!}}$. H is implicitly a function of I_f and K_f because of the selection rules for $I_f - I_i$ and the definition of ν, respectively and can be written as $H(I_i, K_i \to I_f, K_f)$. The plot of $\log H/H_{\min}$ in Figure 2-5 shows that the

23

predicted reduced transition strengths of the SDM model explode more quickly for higher values K_f as the nucleus is collectively rotated (increasing $\vec{R}$). The normalization to $H_{\min}$ shows how the factor blows up from the lowest transition between the two bands, where the matrix element can always be set to a reasonable physical value by adjusting the intrinsic matrix element $\langle K_f \mid m_{\Delta K=\lambda+\nu,\mu=\lambda} \mid K_i \rangle$. Assuming that the matrix elements for the band head of the K_f band are set to reasonable physical values, the range of I_f where the transition strengths remain physical is smaller for higher-K_f bands. This is the first failing of the SDM model. In order to keep the reduced matrix elements below realistic upper bounds, the data of the present experiment forced departures from the exact form of Equation 2.24.

2.4.2 γ-Barrier Penetration Model

One of the distinguishing features of this model is that it postulates an impure K state for the isomer band head, or even a triaxial state [56], whereas the Coriolis mixing model does not inherently require mixing at the band head. The hindrance of a γ-decay from a high-K state is calculated by assuming that there may be tunneling through the (β, γ) landscape from a high-K prolate shape to a low-K rotating state, also prolate in shape (Figure 2-3). The β deformation finds the same equilibrium in the initial and final states, as evidenced by the similarity of Q_o values in the isomer bands and the GSB of ^{178}Hf, for example [57, 58]. Narimatsu et al. [59] give a derivation of the following results.

$$T = \frac{1}{1 + e^{2W/\hbar}} \tag{2.25}$$

is the transmission coefficient for tunneling through the barrier, calculated for tunneling through a barrier in the deformation coordinates (ϵ_2, γ), ϵ_2 typically used in the Nilsson Model and γ of Equation 2.3. W is the least action for traversing the two-dimensional barrier. A mixing strength parameter S is calculated assuming
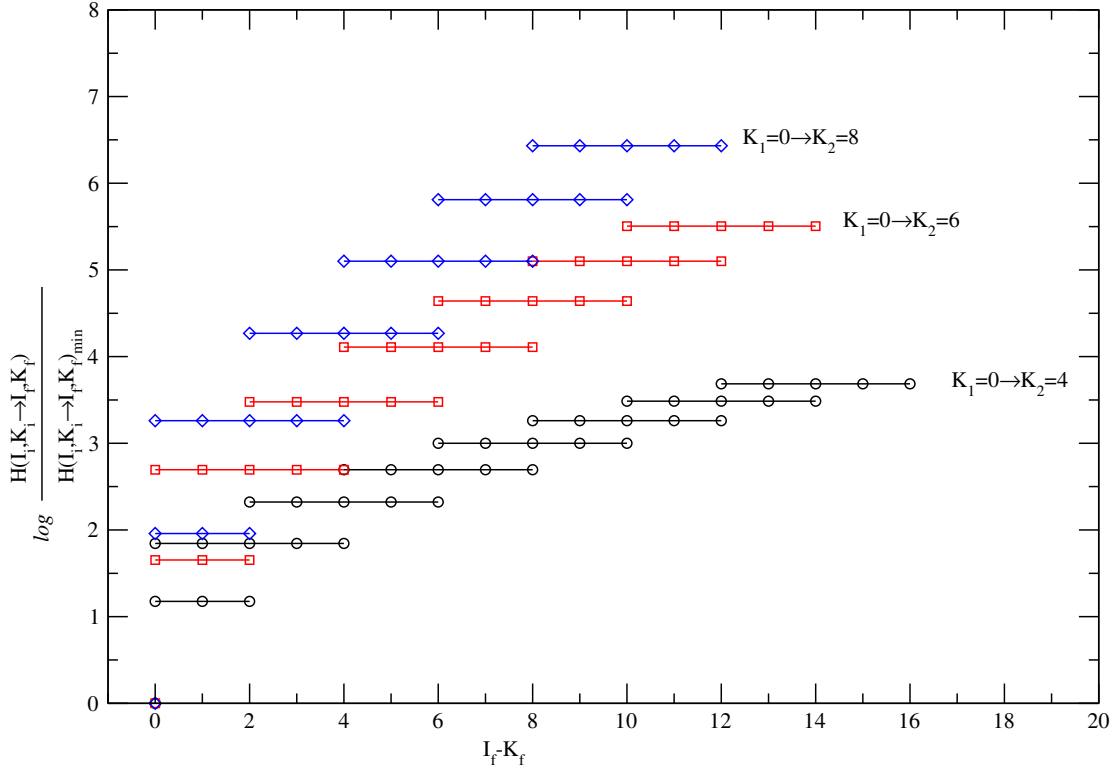
Figure 2-5: Normalized values of the spin-dependent term $H(I_i, K_i \to I_f, K_f)$ of the SDM model (defined in the text) calculated for three values of K_f for the high-K band. The behavior of the spin-dependent term with increasing spin above the band head is shown.

a simple two-state mixing perturbation [60], and the hindrance F_ν can then be calculated according to the model as

$$F_\nu = \frac{1}{TS},\tag{2.26}$$

with no adjustable parameters.

While the appeal of this model is that it makes predictions for the absolute values of the transition probabilities from the band head, its primary shortcoming in explaining the electromagnetic excitation of isomers is that it has not produced quantitative predictions for transitions involving high-spin levels above the band heads.

25

2.5   Semi-Classical Coulomb Excitation Theory

The analysis of experimental data from heavy-ion scattering is greatly simplified if the bombarding energy is far enough below the Coulomb barrier that the nuclear interaction strength is negligible. Even so, the coupled problems of calculating the scattering trajectory and integrating the electromagnetic excitation amplitudes over the trajectory are not exactly soluble. The accurate solution of the quantum mechanical scattering problem requires the inclusion of many partial waves, making some otherwise tractable calculations prohibitively time-consuming. An efficient solution is to employ the semi-classical approximation to the Coulomb excitation problem, where the scattering trajectories are treated classically and the excitations of nuclear states are treated quantum mechanically [61, 62].

For approximately classical electric scattering, the kinematic cross sections are given by the familiar Rutherford cross section:

$$\left(\frac{d\sigma}{d\Omega}\right)_{\text{Ruth}} = \frac{1}{4}\left(\frac{Z_{\text{p}}Z_{\text{t}}e^2}{m_o v^2}\right)^2 \sin^{-4}\frac{\theta}{2} \tag{2.27}$$

in the center-of-mass system, where Z_{p} and Z_{t} are the proton numbers of the target and projectile nuclei, respectively, m_o is the reduced mass, v is the initial projectile speed, and θ is the scattering angle in the zero-momentum frame. Following Alder and Winther [63] and Satchler [64], the formalism for expressing the excitation probabilities of nuclear states can be expressed as follows. The cross section $\left(\frac{d\sigma}{d\Omega}\right)_n$ for Coulomb exciting a nucleus to the final state $\mid n\rangle$ is

$$\left(\frac{d\sigma}{d\Omega}\right)_n = \left(\frac{d\sigma}{d\Omega}\right)_{\text{Ruth}} P_n, \tag{2.28}$$

where P_n is the probability of exciting the state $\mid n\rangle$. The "semi-classical" treatment of the problem consists of approximating the trajectory using classical kinematics, while treating the excitation quantum mechanically. The validity of the semi-classical approximation requires the following limitations on the experimen-

tal parameters [65, 66]. The Sommerfeld parameter $\eta = $ can be defined as

$$\eta = \frac{b}{2\lambda}, \tag{2.29}$$

where $b = b(\theta)$ is the classical distance of closest approach, and λ is the wavelength $\frac{\hbar}{p}$ of the projectile [64]. Large values of $\eta >> 1$ permit the semi-classical approximation. If the wavelength of the projectile is of the order of the scale of the scattering system ($\lambda \sim b$), then the scattering must be treated quantum mechanically. Conversely, systems where $\lambda << b$ ($\eta >> 1$) closely approximate classical scattering systems. For the first (chapter 3) and second (chapter 5) experiments, $\eta = 280$ and 380, respectively, ensuring that the semi-classical approximation is accurate.

It can be shown that the cross section for Coulomb excitation of a particular state $\mid n \rangle$ is small if the collision time τ_{coll} is much greater than the characteristic time τ_n for excitation of the state, sometimes referred to as the "nuclear period" [67]. The collision time is given by

$$\tau_{\text{coll}} \approx \frac{b(\theta)}{2v}. \tag{2.30}$$

Defining $\xi \equiv \frac{\Delta E_{0 \to n}}{\hbar} \tau_{\text{coll}}$ and noting that $\frac{\hbar}{\Delta E_{0 \to n}}$ is of the order of the excitation time τ_n [63], the obvious ideal condition for Coulomb excitation of the state $\mid n \rangle$ is

$$\xi << 1. \tag{2.31}$$

Alder [63] has shown that

$$\frac{\Delta E_{0 \to n}}{E} = \frac{2\xi_{0 \to n}}{\eta}, \tag{2.32}$$

where E is the zero-momentum projectile energy. For few-step excitations, $\xi \lesssim 1$, and $\eta \gtrsim 100$ for typical Coulomb excitation experiments.

The condition $\xi(\theta) >> 1$ is referred to as the "adiabatic limit" [63]. Near this limit, the excitation probabilities behave according to

$$P_n \sim e^{-\xi(\theta)}. \tag{2.33}$$

In the lower limit, $\xi(\theta) << 1$, the interaction can be evaluated using the "sudden approximation," [66] where the numerical integration is carried out only for a short interval of the trajectory around the point of closest approach. The behavior of P_n for large and small adiabaticity suggests a limitation on the maximum energy (or spin) to which a nucleus may be excited, regardless of the projectile energy [67].

The upper limit on the number of excitation steps can be estimated from the probability P_m of an m-step excitation

$$P_m \approx \left(\frac{\chi(\theta)^m}{m!} \right)^2 \qquad (2.34)$$

in the sudden approximation $\xi << 1$ [63]. For a transition from an initial state $\mid 0 \rangle$ to a final state $\mid n \rangle$, the "strength parameter" χ_n is given by

$$\chi_n(\theta) = \frac{\langle n \mid V(b(\theta)) \mid 0 \rangle b(\theta)}{2 \hbar v}. \qquad (2.35)$$

Excitations over multiple steps can have no larger probability than the product of $P_{0 \rightarrow 1} P_{1 \rightarrow 2} \cdots$, neglecting other excitation paths, higher order processes involving reorientation, etc. For approximately equal matrix elements, this gives a fall-off with spin which is approximately exponential in the number of steps n [68] (or, equivalently, the final spin I) which is seen in the present experiments, where ≈ 10 steps of excitation can be observed in all of the species excited.

The dependence of the excitation cross sections on the beam energy and particle masses is elucidated by Bass [67] and Alder [63]. To first order and for small adiabaticity,

$$\sigma_\lambda \sim m_{\mathrm{red}}^{2\lambda-2} E_{\mathrm{beam}}^{2\lambda-3}, \qquad (2.36)$$

where m_{red} is the reduced mass of the system. Coulomb excitation is dominated by electric quadrupole (E2) excitations [68], in which case

$$\sigma_\lambda \sim m_{\mathrm{red}}^2 E_{\mathrm{beam}}. \qquad (2.37)$$

In order to maximize the number of high spin states excited, a high beam energy is desired, while limiting the adiabaticity.

28

Complementary to the requirement $\eta >> 1$ for a classical treatment of the scattering trajectories, there is an empirical criterion for "safe" Coulomb excitation with respect to the measurements of electromagnetic matrix elements. With the upper limit on the bombarding energy,

$$E_{\max}[\mathrm{MeV}] = 1.44 \frac{A_{\mathrm{proj}} + A_{\mathrm{targ}}}{A_{\mathrm{targ}}} \cdot \frac{Z_{\mathrm{proj}} Z_{\mathrm{targ}}}{1.25(A_{\mathrm{proj}}^{1/3} + A_{\mathrm{targ}}^{1/3}) + 5} \cdot \frac{1}{2} \left\{ 1 + \frac{1}{\sin \frac{\theta}{2}} \right\} \quad (2.38)$$

for scattering at the center-of-mass angle θ [69], there is negligible deviation (for heavy ions) from trajectories predicted by classical EM scattering [70, 69]. This is equivalent to the requirement that the classical separation distance between the nuclear surfaces is greater than 5 fm, or that the beam energy is $\leq 80\%$ of the Coulomb barrier for $\theta = 180°$.

More importantly, this safe-energy criterion ensures that the nuclei interact only electromagnetically. With the constraint of Equation 2.38, the nuclear interference is less than 10^{-3} of the electric quadrupole contribution [68, 62]. This greatly simplifies the analysis, removing the nuclear force from the calculations. Figure 2-6 is a contour plot of the safe energy for *backscattering* ($\theta_{\mathrm{proj}} = 180°$) for a range of beam nuclei on a range of target nuclei. Higher beam energies can be used for safe Coulomb excitation if the analysis is limited to safe scattering angles where the classical separation is ≥ 5 fm, as in the experiments described in chapters 3 and 5.

2.5.1 Electromagnetic Interactions

Numerical fits (Chapters 4 and 7) of the electromagnetic matrix elements were carried out using the Rochester semi-classical Coulomb excitation and χ^2 minimization code GOSIA [71]. This code carries out the semi-classical coupled channel calculations described below. Several works give clear, exhaustive descriptions of Coulomb excitation theory, for example [63, 67]. Clear summaries of the problem are found in [72, 66, 68]. The development below follows mainly Czosnyka [72]
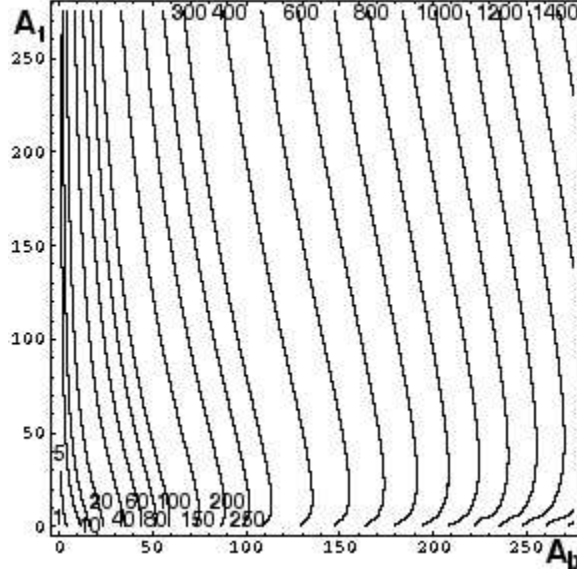
Figure 2-6: Laboratory beam energy (MeV) curves for safe Coulomb excitation (over all angles $0° \leq \theta_{\text{scat}}^{\text{c.m.}} \leq 180°$) for beam (projectile) and target masses A_{b} and A_{t}, respectively.

with some clarifications found in Bass [67] and Alder [63].

The time derivative $\frac{da_k}{d\omega}$ of each amplitude for excitation a_k is *coupled* to all other channels $n \to k$ open to electromagnetic excitation. This is expressed as

$$\frac{da_k(t)}{dt} = \frac{-i}{\hbar} \sum_n a_n(t) \langle \psi_k \mid V(t) \mid \psi_n \rangle e^{\frac{it}{\hbar}(E_k - E_n)}, \tag{2.39}$$

following the notation of [72]. The interaction potential acting on the projectile (target) is given by

$$V_{\text{p(t)}}(t) = \sum_{\lambda=1}^{\infty} \sum_{\mu=-\lambda}^{\lambda} \frac{4\pi Z_{\text{t(p)}} e}{2\lambda + 1} (-)^{\mu} S_{\lambda\mu}(t) \mathcal{M}_{\text{p(t)}}(\lambda, -\mu). \tag{2.40}$$

The subscripts p and t refer to the projectile and the target, Z is the proton number, and $S_{\lambda\mu}$ is given by

$$S_{\lambda\mu}(t) = \begin{cases} \frac{Y_{\lambda\mu}(\theta(t),\phi(t))}{r^{\lambda+1}(t)} & \text{electric interaction} \\ \frac{1}{c\lambda} \frac{\frac{d\vec{r}}{dt} \cdot (\vec{r} \times \vec{\nabla})}{r^{\lambda+1}(t)} Y_{\lambda\mu}(\theta(t),\phi(t)) & \text{magnetic interaction} \end{cases} \tag{2.41}$$

30

The familiar electromagnetic multipole moments are given by

$$\mathcal{M}(E\lambda, \mu) = \int \rho(\vec{r}) r^\lambda Y_{\lambda\mu}(\theta, \phi) d^3\vec{r} \tag{2.42}$$

and

$$\mathcal{M}(M\lambda, \mu) = \frac{1}{c(\lambda + 1)} \int r^\lambda \vec{j}(\vec{r})(\vec{r} \times \vec{\nabla}) Y_{\lambda\mu}(\theta, \phi) d^3\vec{r} \tag{2.43}$$

for electric and magnetic moments, respectively. (The combined $\frac{1}{c^2}$ factor makes the magnetic interaction insignificant in most experiments.) Equation 2.39 can be rewritten as

$$\frac{da_k(t)}{dt} = -i\frac{4\pi Z_{\mathrm{p(t)}}e}{\hbar} \sum_n a_n(t) e^{\frac{it}{\hbar}(E_k - E_n)} \sum_{\lambda\mu} (-)^\mu S_{\lambda\mu}(t)\langle \psi_k \mid \mathcal{M}(\lambda, -\mu) \mid \psi_n \rangle. \tag{2.44}$$

The form of 2.44 can be parametrized in $\epsilon = \frac{1}{sin(\frac{\theta}{2})}$ and $t = \frac{b}{v}(\epsilon \sinh \omega + \omega)$, where θ is the zero-momentum scattering angle, v is the relative speed, and b is the distance of closest approach for $\theta_{\mathrm{lab}} = 180°$. The S interaction functions can then be replaced by "collision functions" of ϵ and ω:

$$Q_{\lambda\mu}^E(\epsilon, \omega) = b^\lambda \frac{(2\lambda - 1)!!}{(\lambda - 1)!} \left(\frac{\pi}{2\lambda + 1}\right)^{\frac{1}{2}} r(\omega) S_{\lambda\mu}^E(t(\omega)) \tag{2.45}$$

and

$$Q_{\lambda\mu}^M(\epsilon\omega) = \frac{c}{v} b^\lambda \frac{(2\lambda - 1)!!}{(\lambda - 1)!} \left(\frac{\pi}{2\lambda + 1}\right)^{\frac{1}{2}} r(\omega) S_{\lambda\mu}^M(t(\omega)). \tag{2.46}$$

Since the electromagnetic excitation makes the collision inelastic, the excitation energy must be taken into consideration in the kinematics. Discrete averages of the initial and final values of b, v and other parameters, "symmetrized" values, have been used [67], in cases where ΔE is small. The most transparent form of the coupled-channel equations from an experimental view is given by [72]

$$\frac{da_k}{d\omega} = -i \sum_{\lambda\mu n} Q_{\lambda\mu}(\epsilon, \omega)\zeta_{kn}^{(\lambda\mu)}\langle I_k \| \mathcal{M}(\lambda) \| I_n \rangle e^{i\xi_{kn}(\epsilon \sinh \omega + \omega)} a_n(\omega), \tag{2.47}$$

giving the excitation amplitudes in terms of the reduced matrix elements $\langle I_k \| \mathcal{M}(\lambda) \| I_n \rangle$, the parameters ζ and ξ and the collision functions. The result is

a system of coupled equations involving the measured quantities $\langle I_k \| \mathcal{M}(\lambda) \| I_n \rangle$, whose behavior is shaped by the adiabaticity ξ, given by

$$\xi_{kn} = \frac{Z_1 Z_2 \sqrt{A_1}}{6.34977} \left\{ \frac{1}{\sqrt{E_p - [1 + \frac{A_1}{A_2}] E_k}} - \frac{1}{\sqrt{E_p - [1 + \frac{A_1}{A_2}] E_n}} \right\} \tag{2.48}$$

and the geometric coupling quantities ζ, the "zeta parameters" which are functions of the $3 - j$ symbols [63].

The direct effect of a large adiabaticity is obvious from Equation 2.47. It is essentially a frequency parameter in $\dot{a}_k$. For large values, the excitation amplitude a_k oscillates rapidly during the collision, and the time average $\langle a_k(t) \rangle \to 0$, so that there is a small probability of excitation. Conversely, small values of ξ will allow a larger value of $\int a_k(t) dt$, and a high probability of excitation in the channel $n \to k$. To first order, $\zeta \sim Z_p$, reiterating that heavier nuclei with higher proton numbers provide better excitation [72].

2.5.2 Experimental and Analytical Considerations

Polarization Effects

Polarization of the nucleus occurs during scattering as a consequence of the conservation of angular momentum, and the γ-ray intensity has an angular dependence in the laboratory frame. The angular dependence in the nuclear frame of reference (Kavka [62] is given by the differential cross section,

$$\begin{aligned}
\frac{d^2\sigma}{d\Omega_{\mathrm{p}} d\Omega_\gamma} &= \frac{1}{\gamma(I)\sqrt{4\pi}} \frac{d\sigma_{\mathrm{Ruth}}(\theta_{\mathrm{p}})}{d\Omega_{\mathrm{p}}} \\
&\times \sum_{k=0,2,4\ldots}^{\infty} \sum_{\mu=-k}^{k} \left\{ \left[\sum_{\lambda=1}^{\infty} \sum_{\lambda'=1}^{\infty} \delta_\lambda \delta *_{\lambda'} F_k(\lambda, \lambda', I_f, I) \right] \right. \\
&\times \left. Q_k G_k(I,t) \rho *_{k\mu}(I) Y_{k\mu}(\theta_\gamma, \phi_\gamma) \right\},
\end{aligned} \tag{2.49}$$

after Alder [63]). The probability tensors or "statistical tensors" $\rho_{k\mu}(I)$ give the excitation probability of the states as functions of the excitation amplitudes of

Equation 2.39, as $t \to \infty$, and $\gamma(I)$ are the probabilities of the emission of the observed γ-rays in the decays of the states I. The quantities δ_λ are the square roots of the γ-decay widths Γ with the phase factors i^λ and $i^{\lambda+1}$ for $E\lambda$ and $M\lambda$ decays, respectively. The angular correlation coefficients F_k are given explicitly in Chapter 6, along with the factors Q_k describing the averaging effect of the solid angle of γ-ray detectors.

The time-dependent electromagnetic fields of the atoms which are excited and ionized while traversing the target "deorient" the polarized nucleus over time. This effect is described by the $G_k(t)$ attenuation factors [62]. Although nuclear polarization effects are completely washed out in the 4π particle and γ-ray collection of the online experiment (Chapters 3 and 4), angular correlation effects must be considered in the offline γ-counting experiment (Chapters 5 and 6) with the activated ^{178m2}Hf samples. In the offline experiment time-dependent deorientation effects are negligible because the half-lives of the states in the cascades are much shorter than the deorientation time.

Treatment of Multiple Excitations

In light ion Coulomb excitation, only the lowest few states are populated, as explained below. Perturbation methods work well, since there are only a few steps during the interaction [63]. But light ion Coulomb excitation is ineffective in exciting high spin states necessary to populate isomer states.

In heavy ion collisions, however, there may be multistep excitations during the interaction [73]. In typical situations, there are too many matrix elements in the problem whose effects are not independent, so the problem needs to be "overdetermined" by using multiple data sets [68], which may consist of multiple combinations of species, data for multiple scattering angles and energies, etc.

Perturbation theory is not efficient in solving Equations 2.47, since many high order terms must be taken into consideration for acceptable accuracy. Instead,

accurate Coulomb excitation codes such as GOSIA must exploit fast computers using numerical solutions. The principal approximation used in the Coulomb excitation calculations in the present work is in the integration over a short range of ω around the point of closest approach, where the values of a_k peak sharply. The excitation functions are integrated over intervals of the the energy loss in the target (typically $< 10\%$ of E_{beam} for thin targets), scattering solid angle and γ-ray detector solid angle.

The χ^2 Minimization Procedure

The least-squares method of fitting matrix elements involves three principal parts, iterated to find the minimum: calculation of the excitation probabilities during the collision, calculation of the subsequent γ-decay yields, and calculation of the inverse figure of merit, χ^2. The Coulomb excitation probabilities of the nuclear states is described above.

The value of χ^2 is normalized to the number of data points (γ-ray yields) N by

$$\chi^2 = \frac{1}{N}\left(\chi_{\text{y}}^2 + \chi_{\text{l}}^2 + \chi_{\text{r}}^2\right), \tag{2.50}$$

where χ^2 is defined in terms of the experimental yields Y_i and their respective errors σ_i according to

$$\chi^2 \equiv \frac{\sum_i (Y_i^{\text{calc}} - Y_i^{\text{exp}})^2}{\sigma_i^2}. \tag{2.51}$$

The terms χ_{y}^2, χ_{l}^2 and χ_{r}^2 represent the contributions from the measured γ-decay yields, the experimental upper limits on the detection of individual γ-rays and the measured branching ratios, respectively. On some χ^2 hypersurfaces, a gradient-derivative search is useful for steering the minimization along narrow valleys, however relatively shallow valleys were encountered in the following experiments. Convergence was achieved typically in ≈ 5 steps using a standard "steepest descent" method, where the search is always steered in the direction $-\vec{\nabla}\chi^2$.

2.6 Summary

The γ-ray yields following Coulomb excitation can be used to fit a set of EM matrix elements, provided that the collision energy is kept below a safe ($\approx 80\%$ of the Coulomb barrier) limit. For higher beam energies, the range of scattering angles can be restricted to eliminate the effects of nuclear forces in the data. The form of the measured matrix elements can then be compared to predictions by various models and used to evaluate the conjecture of particular K admixtures in various bands that are found to be populated by Coulomb excitation. The application of the analytical and numerical methods described above is described in the following analysis chapters.

Chapter 3

Experiment I: ^{178}Hf(^{136}Xe,^{136}Xe)^{178}Hf
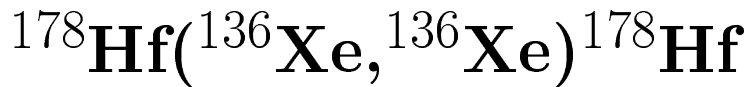
High accuracy and model sensitivity in the measurements of matrix elements for electromagnetic transitions in nuclei using Coulomb excitation is achieved by measuring γ-ray yields $Y(\theta)$ as a function of the particle scattering angle. This provides greater model sensitivity than measurements of the total cross sections of states alone, since two models may predict similar total cross sections but different behavior of $Y(\theta)$. For this reason, an effective instrument for detailed studies of EM matrix elements includes a 4π particle detector with high angular resolution, capable of identifying the scattered beam and recoiling target particles, Rochester's CHICO detector in this case.

In addition, the γ-ray energies must be measured to an accuracy of the order of 1%, in order to resolve γ-rays in complex decay schemes. The detector system must support event-by-event correction of the γ-ray energies for the Doppler broadening seen in decays of short-lived states, less than ≈ 10 ns in the present case. This may be accomplished, as in the present experiment, by utilizing a γ-ray detector array with high angular resolution, Gammasphere, in conjunction with the particle detector described above. The accelerator facilities and detector sys-
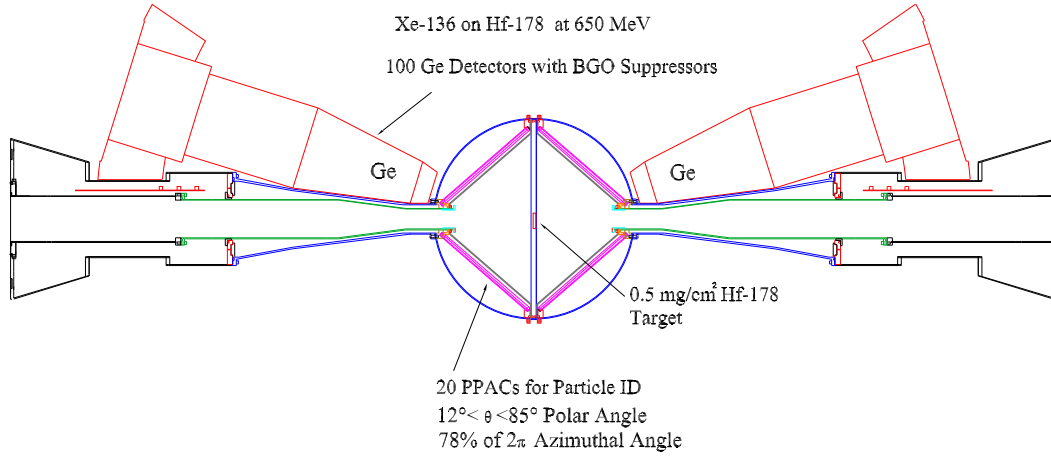
Figure 3-1: The arrangement of CHICO in Gammasphere. The beam traverses the central horizontal pipe through the target foil at the center of CHICO. Two of the 100 operational (110 total) Ge detectors are shown.

tems are described, followed by descriptions of the detector calibration and data reduction and a brief example of the sensitivity of the Gammasphere + CHICO combination in extracting new results from a small quantity of data.

3.1   Facilities and Detectors

The ATLAS superconducting linac at Argonne National Laboratory provided a 650 MeV ^{136}Xe beam on the 0.51 mg/cm^2, 89% enriched ^{178}Hf target for a total of $\approx$ 76 hours. A 1 μs sweeper interrupted the beam, allowing the detection of delayed γ-rays from isomer decays with 10 ns $\lesssim t_{\frac{1}{2}} \lesssim$ 1 μs.

3.1.1   Gammasphere

Gammasphere is a 110-element, BGO-suppressed (bismuth germanate) germanium array. Each germanium crystal subtends an angle of $\approx$ 15° with respect to the collision point with a total coverage of $\approx$ 50% of 4π sr. Seventy of the detectors are further subdivided electronically, increasing the angular resolution. The high angular resolution permits a precise Doppler-shift correction of the γ-ray spectra if the recoil velocity is known, giving an energy resolution of $\approx$ 0.5%. The

Figure 3-2: Diagram of the principal Gammasphere components [15]. The hevimet shields were not installed.

total detection efficiency for a γ-ray in the array is 9.9% at 1.3 MeV, so that γ-ray triples can be collected with good statistics. During the experiment, data were collected from 100 functioning detectors of the 110 detector array.

The γ trigger was generated in BGO suppression mode, using the high-efficiency BGOs to veto Compton scattered γ-rays and γ-rays that were not captured in the Ge crystal (Figure 3-2), improving the peak-to-total ratio (from 0.25 for without suppression to 0.6 with suppression [15]), which reduced the count-rate and background level. The timing window on acceptance of γ-rays was approximately 1 μs.

The γ-ray detection efficiency ϵ was measured as a function of E_γ using data from the γ-ray cascades of four isotopes: ^{238}U, ^{152}Eu, ^{170}Er and ^{178}Hf. The ^{238}U

and ^{170}Er efficiency data were obtained from a 1358 MeV ^{238}U on ^{170}Er experiment which ran just after the present Hf experiment, and the ^{152}Eu data were obtained from a source calibration run. Figure 3-3 shows a six parameter fit to the efficiency data. Using the U, Er and Hf targets, the relative yields of the lower GSB states (where the E2 matrix elements are well known) were combined with ^{152}Eu source data for the high energy tail. The relative intensities of the four sets were normalized while fitting the entire data set to the standard Ge efficiency function [74],

$$\ln \epsilon = \alpha + \{(A + Bx + Cx^2)^{-G} + (D + Ey + Fy^2)^{-G}\}^{-1/G}, \qquad (3.1)$$

where

$$x = \ln(E_\gamma/100 \, \mathrm{keV}), \qquad (3.2)$$

$$y = \ln(E_\gamma/1000 \, \mathrm{keV}) \qquad (3.3)$$

and α is a normalization constant. Figure 3-3 shows the resulting efficiency curve with $A = 5.058, B = 1.702, C = 0(\text{fixed}), D = 5.385, E = -0.6047, F = -0.08950$ and $G = 30.0$ compared to the ^{178}Hf GSB yields.

The γ-ray energy calibration and alignment were done online using the ^{152}Eu source data for all 100 detectors. Following the Doppler-shift correction, the γ-ray energy resolution was $\approx 0.5\%$.

3.1.2 CHICO

Rochester's Compact Heavy Ion COunter consists of 20 isobutane-filled parallel plate avalanche counters (PPACs), which are capable of detecting light and heavy ions including α particles and identifying the scattered particles by kinematics. The PPAC anodes (Figure 3-5) are stretched polypropylene with an evaporated aluminum surface. The cathode boards are printed circuit boards with tinned conducting strips of constant polar angle θ.
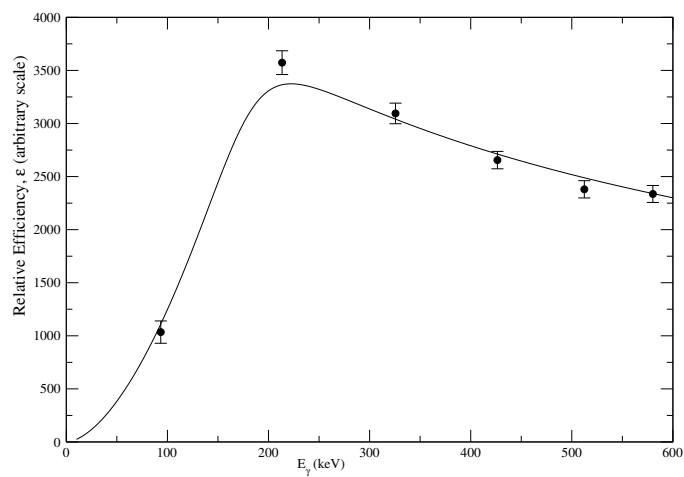
Figure 3-3: Relative efficiency of the Ge array measured from source data from several experiments. Relative efficiency measurements from the present ^{178}Hf experiment are shown.
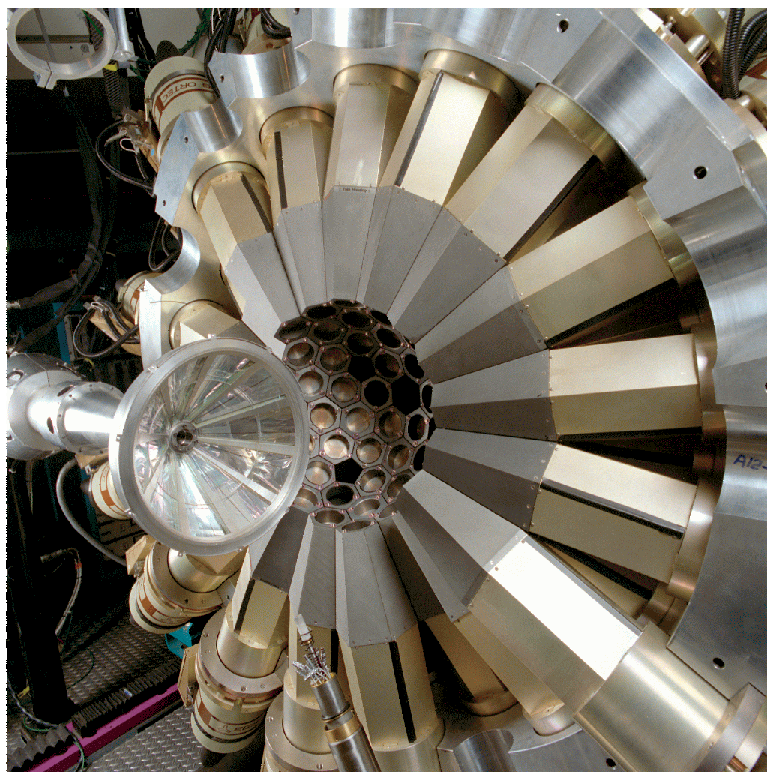
Figure 3-4: One hemisphere of CHICO in one hemisphere of Gammasphere.
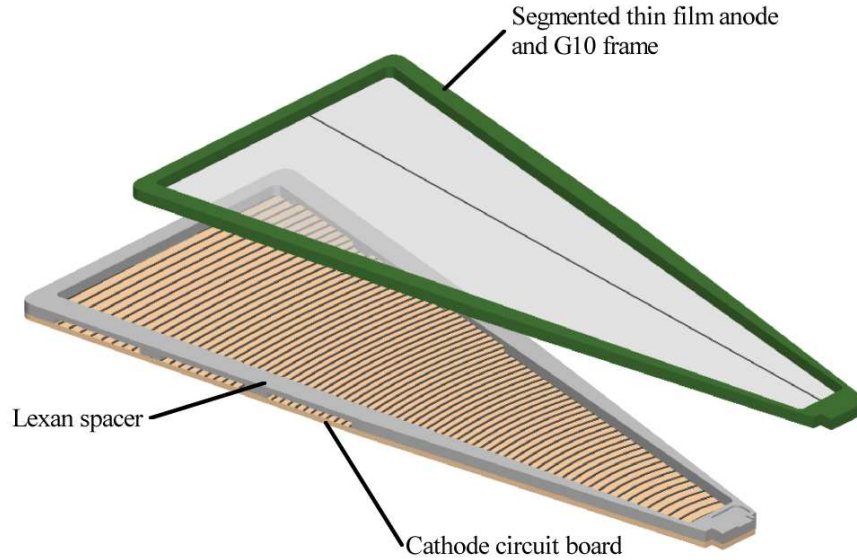
Figure 3-5: An exploded view of one of the 20 PPACs of CHICO [16].

The time-of-flight difference resolution of 500 ps enables separation of the target-like and beam-like particles with a typical mass resolution of 5%. The PPACs lie 13 cm from the center of CHICO, measured along a normal to the PPAC with the normal lying at an angle of 41° from the beam axis. Angular coverage of the scattered ions is $12° < \theta < 85°$ and $95° < \theta < 168°$ in the polar angle with an acceptance of 2.8π sr or 69% of the sphere.

The cathodes are essentially printed circuit boards, with 1° wide tracks of constant polar angle θ on the side facing the target, as shown in Figure 3-5, and a 1 ns per degree delay line on the reverse side. The delay line allows the θ position to be measured by the difference in the signal arrival time between the two ends of the cathode.

The anodes are divided in the azimuthal (ϕ) direction into two unequal $\Delta\phi$ segments of $\frac{2}{3}$ and $\frac{1}{3}$ of the total azimuthal coverage. This uneven division uses only 2 signals per PPAC to give a $\frac{1}{3}$ ($\Delta\phi = \pm 4.7°$) resolution in the azimuthal angle

41

Anode 1

Large segment | Small seg.

3   2   1

1   2   3
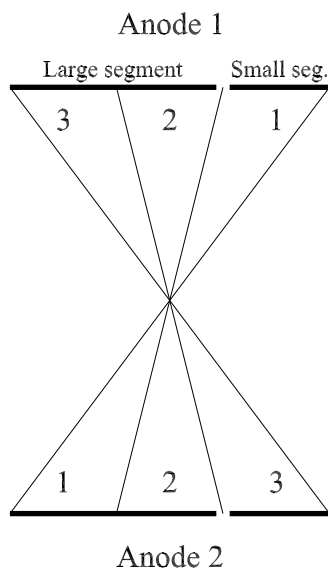
Anode 2

Figure 3-6: Schematic diagram of a pair of opposing anodes [17].

in the following way. Opposing PPACs in the detector (diametrically or in the same half) are arranged as mirror images (Figure 3-6). Because binary collisions result in the final trajectories coplanar with the beam direction ($\phi_1 - \phi_2 = \pi$), the three possible combinations of anodes that are struck uniquely determine the reaction plane and the angles ϕ_1 and ϕ_2. For example, a collision resulting in hits on the small segment of anode 1 and the large segment of anode 2 indicate that the reaction plane is in region 1.

3.1.3 Acquisition Electronics

The CHICO trigger and data acquisition eletronics (Figure 3-7) use a programmable logic unit (PLU) to make trigger decisions on the PPAC anode signals and an AND gate to include a second trigger input from Gammasphere. In the present experiment, the trigger was based on valid two-particle coincidences in CHICO and γ-ray singles ($n \geq 1$) in Gammasphere. The events were two-body interactions, so the initial beam velocity and the scattering and recoil velocities

were coplanar, and the valid scattering events consisted of simultaneous hits on the left and right hemispheres of CHICO. For particle hits $P_L(P_R)$ in the left(right) hemisphere of CHICO and at least one clean (no BGO triggered) γ-ray event P_γ in Gammasphere, the trigger condition was

$$(P_L \cap P_R \cap P_\gamma) \cup \tfrac{1}{N}(P_L \cap P_R), \tag{3.4}$$

where $\tfrac{1}{N}(P_L \cap P_R)$ represents valid two-particle events scaled down by some factor N (i.e. every N^{th} event is passed to the AND gate through the Gammasphere external trigger). The scaled down singles were not utilized in this experiment, necessitating the normalization of all γ-ray yields to a GSB transition. Because the normalization was not absolute in terms of the cross section, in later chapters these are referred to as relative yields.

Constant fraction discriminators (CFDs) generated digital signals from the anode and cathode pulses, while introducing less timing jitter than standard discriminators. A second set of discriminators was used to condition the signals after they traversed the 130 ns delay cables, which convey the timing information to the time to digital converters (TDCs or Ferets). The TDCs were operated in common-stop mode, so that higher TDC channels represented earlier times. Cable delays were used to retard the anode and cathode signals by 130 ns, giving the electronics time to generate the triggers and distribute gates to the fast-encoding readout ADCs (FERAs) for the anode and cathode timing data.
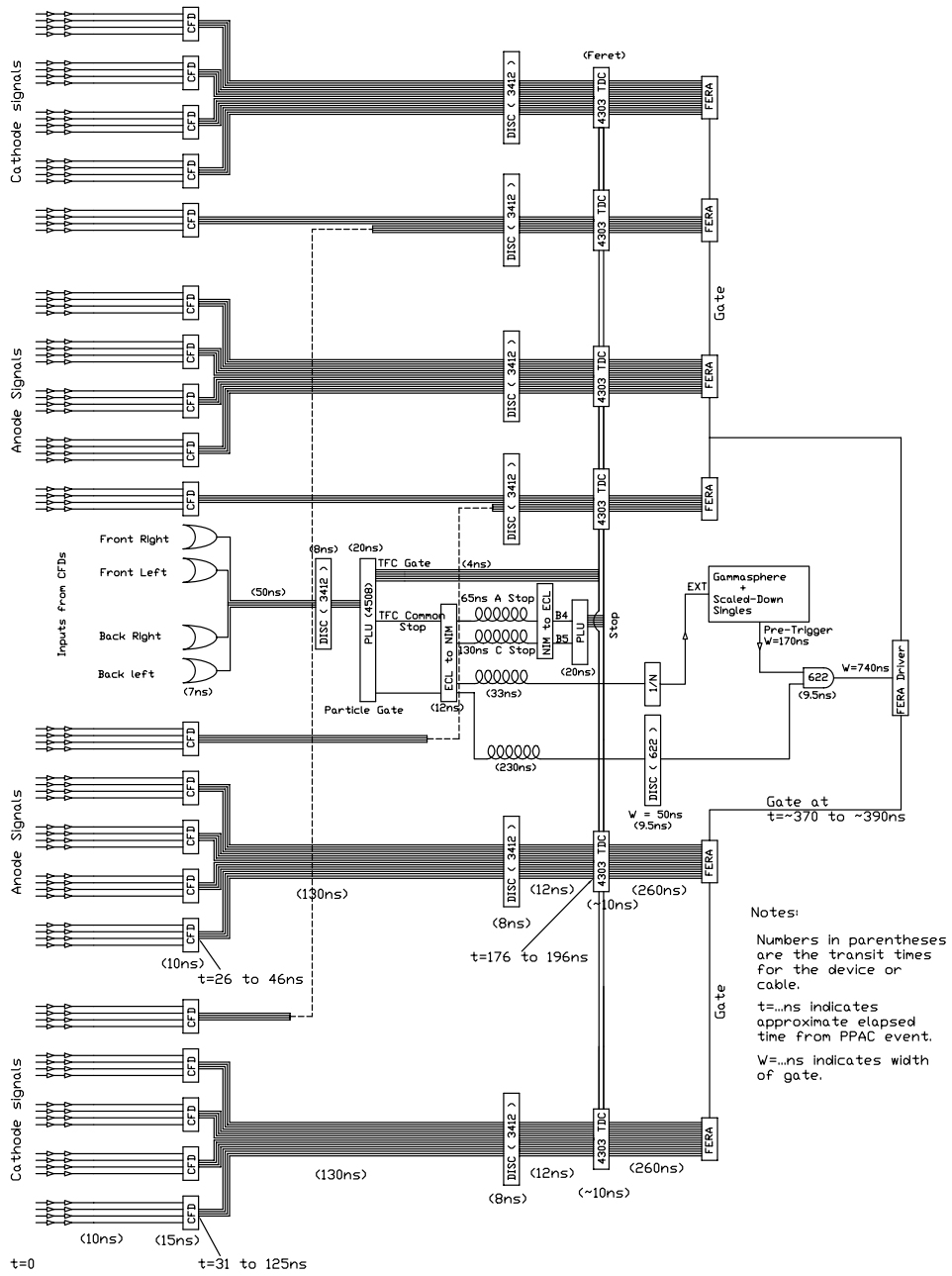
Figure 3-7: Schematic of the CHICO electronics. Adapted from [16].

3.1.4 Target

The 89% enriched ^{178}Hf target was evaporated 0.51 mg/cm^2 thick onto a 0.035 mg/cm^2 carbon foil. The isotopic fractions of the contaminant isotopes are given in Table 3.1. The high sensitivity of the CHICO+Gammasphere combination permitted observation of many states in all but the least abundant isotope.

Isotopic Fractions (%)	
^{174}Hf	< 0.05
^{176}Hf	0.52(5)
^{177}Hf	4.36(5)
^{178}Hf	89.14(10)
^{179}Hf	2.90(5)
^{180}Hf	3.07(5)

Table 3.1: Isotopic analysis of the hafnium target in *atomic* %.

3.2 Run and Data Reduction

3.2.1 Gammasphere

Gammasphere was fitted with 0.002" thick Ta and 0.010" Cu absorbers over the germanium faces to attenuate low energy ($\lesssim$ 100 keV) photons and prevent the flooding of the detector with atomic x-rays. A ≈ 5 μ Ci ^{152}Eu source was used to generate γ-ray energy and efficiency calibration data totalling 80,000 events. The efficiency and energy calibrations are described above. The trigger rate was 4 kHz, which left negligible dead time and 6% pile-up, measured online during the run by comparing signals from both electrodes of the segmented detectors. Data

were collected with the 650 MeV ^{136}Xe beam on target for $\approx$ 76 hours, resulting in $\approx 5 \times 10^8$ usable γ^3 events.

3.2.2   PPAC Calibration

Three fundamental quantities were measured directly in the PPACs. The polar scattering angles θ for the projectile-like and target-like particles were measured from the cathodes. The left-right time-of-flight difference Δt between the two particles detected was measured from the absolute time of each of two anode signals. The azimuthal angle of the scattering plane was obtained from the pair of opposing anode segments on which particles were incident, as described in section 3.1.2.

Gates on Raw Detector Signals In each event, four raw time signals were collected from each PPAC: one from each anode segment (for ϕ measurement) and one from each end of the cathode delay line (for θ measurement). In order to eliminate false events and reduce crosstalk signals between anode segments, a timing gate was set on each anode segment, as shown in the histogram of Figure 3-8. The gate on the cathode time was very broad, so that the only significant cuts on cathode time histogram were the result of the timing gates on the anode signals. The effects of the anode time gates on the cathode time histogram are shown in Figure 3-9. The sharp valleys near channel 800 are the "shadow" of an aluminum support ring at $\theta = 60°$. This shadow was used as a calibration point for the scattering angle θ.

Timing and Crosstalk Resolution When negative charge is induced on an anode segment during the avalanche, a positive charge (cross talk) is induced on the other segment of the same anode, followed by a negative pulse. If the negative cross talk pulse has sufficient amplitude it will trigger its CFD, and either the

46
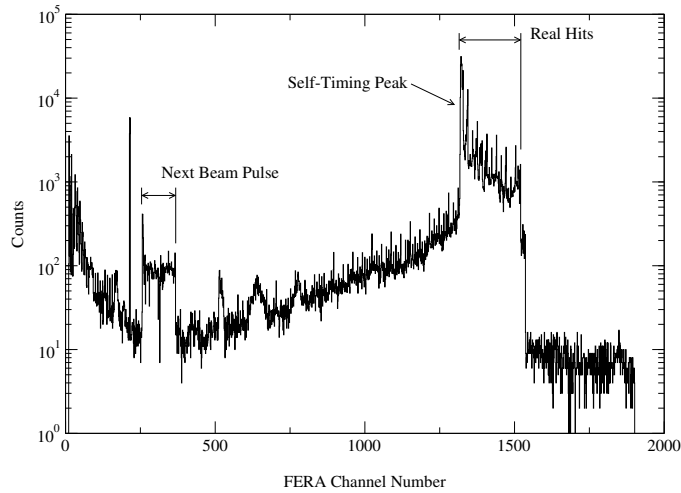
Figure 3-8: A raw anode segment time histogram. Time increases as the channel number decreases, because the TFC's were operated in common stop mode. Approximately 500k events in this anode were scanned before the timing cuts.

cross talk must be resolved, or the event must be discarded. Because the cross talk pulse turns negative later than the pulse from correct segment, timing gates can be used to eliminate cross talk. Figure 3-10 is a two-dimensional histogram of the relative time, by FERA channel number, of the signals from the two segments of an anode. Good anode events must come in a time window located approximately between channels 1250 and 1500 (for this particular anode), as in Figure 3-8. The region bounded approximately by region 'f' is within the time gates of both anode segments, so there were three separate bands of data to evaluate. Region 'a' events had a later time for the horizontal axis and were assigned to the segment represented by the vertical axis. Conversely, the events in region 'c' were assigned to the segment represented by the horizontal axis. (Each event was assigned to the segment registering the earlier hit.) Region 'b' contains events which could not be resolved, because the particle was incident in or near the gap between the segments. These events were eliminated. There is no correlation between the trigger times of the two segments in regions 'd' and 'e', so these events are likely caused by some random event in one segment and can be resolved without

47
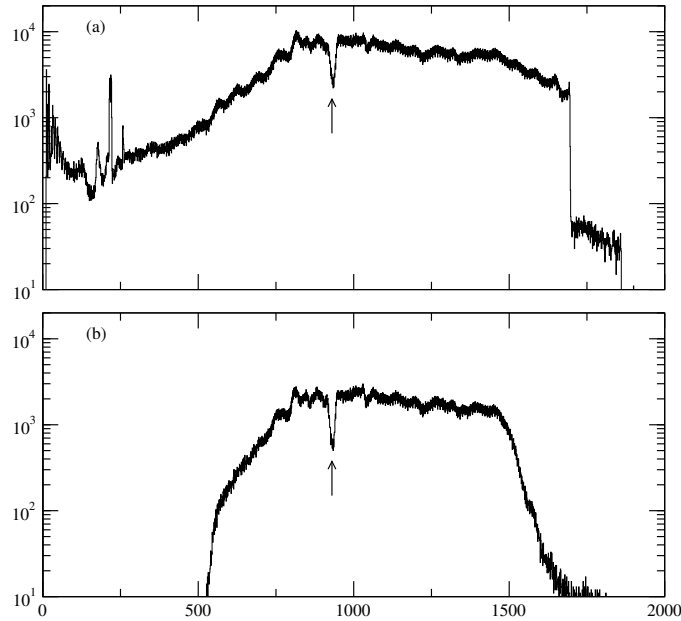
Figure 3-9: Difference spectrum between the signals from each end of a cathode, proportional to the polar angle θ, showing the "shadow" of the 60° aluminum support ring near channel 800. Spurious events in the raw spectrum (a) are removed (b) by gating on the valid timing windows of the anodes.

difficulty.

Cross talk events total less than 10% of the total events. Events where only one anode displayed cross talk between its segments were recovered, while events that displayed cross talk in both anodes were eliminated. These accounted for $\approx 1\%$ of the data.

Angular The azimuthal angle measurement does not need any additional calibration, aside from the cross talk resolution and the obvious cuts of events for which $\phi_1 - \phi_2 \neq \pi$. The polar angle θ was calibrated using a quadratic fit to the known Rutherford scattering kinematics for the two-valued relation $\theta_2(\theta_1)$ (Figure 3-11). The polar angles were calculated from the (nearly linear) function

$$\theta = a + b\Delta x + c(\Delta x)^2, \tag{3.5}$$

48
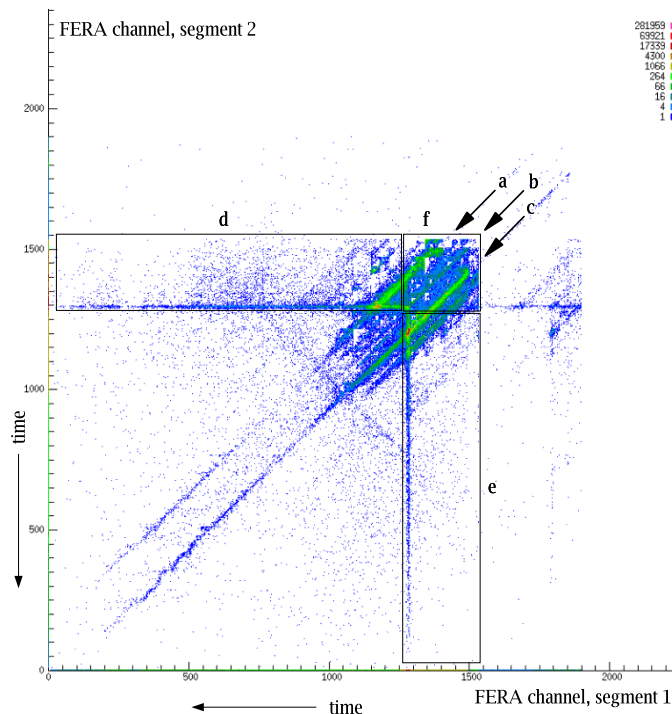
Figure 3-10: A two-dimensional histogram of the cross talk events for the two segments of an anode. The horizontal and vertical axes represent the arrival times of the signals in segments 1 and 2. Note the direction of increasing time.

where x is the time difference in FERA channels between the signals from each end of a cathode. Figure 3-11 is an example of a θ_l vs. θ_r plot for a pair of opposing anodes on the front detector. Good agreement between the theoretical curves calculated from Rutherford scattering theory and the data was achieved in every case, by adjusting only the offset parameter a from the previous calibration. With typical deviations of $\approx 1°$ in the polar angle of the trajectory of the γ-ray emitting particles, an energy resolution of $\approx 0.5\%$ was achieved in the Doppler-shift corrected γ-ray spectra.
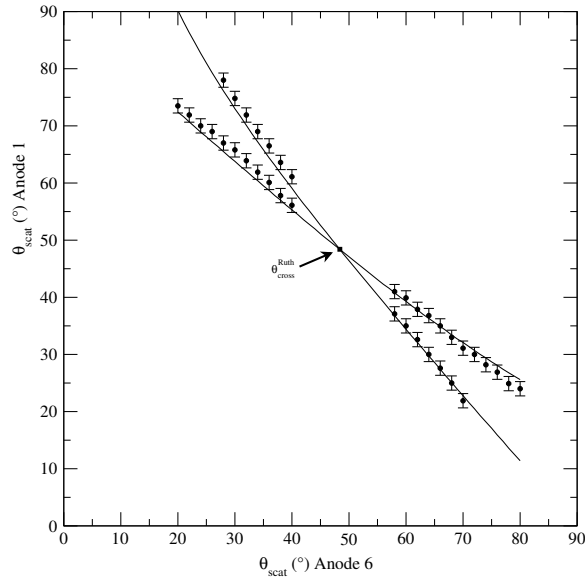
Figure 3-11: An example of calibration of the polar angle θ using Rutherford scattering kinematics.

Alignment of ϕ Subdivisions   The difference in timing alignment of the anode and cathode signals between different PPACs necessitated a careful timing alignment between the anode segments and cathodes for each pair of opposed PPACs. A less precise calibration was sufficient for the timing alignment between different pairs of PPACs, within a few a.m.u. in terms of the particle masses calculated below.

3.2.3   Particle Identification

The 650 MeV ^{136}Xe beam particles could be treated non-relativistically ($\beta =$ 0.1) with regard to the precision needed to resolve the 23% mass difference. Conservation of the classical momentum can be used to differentiate the beam-like and target-like particles without ambiguity by selecting the appropriate regions (Figure 3-12) in the direct measurements of Δt and θ, described in section 3.2.2.
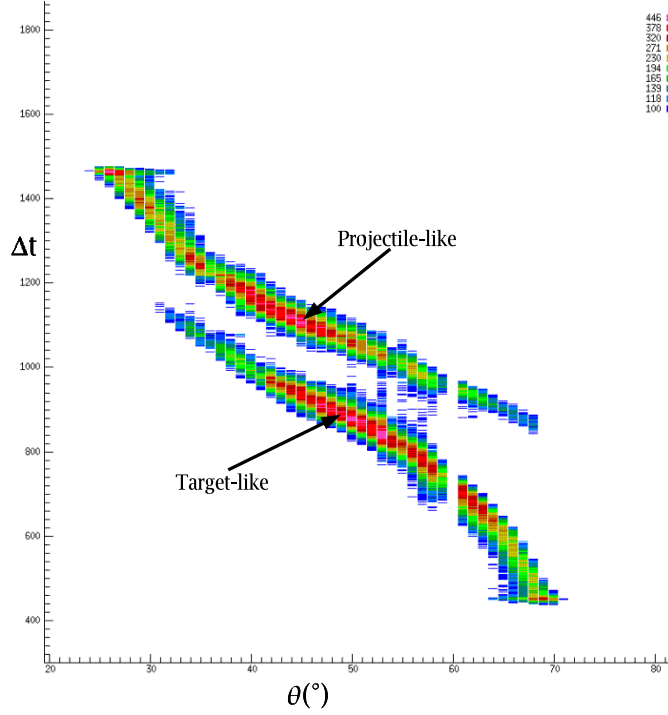
Figure 3-12: The left-right time-of-flight difference histogram, Δt vs. θ with a lower limit at 100 counts for clarity. The gap at $\theta = 60°$ is due to an aluminum support rib.

However, the Δt vs. θ data was transformed into mass m vs. θ:

$$m_1 = \frac{\Delta t + \frac{d_2}{p_2}(m_1 + m_2)}{\frac{d_1}{p_1} + \frac{d_2}{p_2}}, \qquad (3.6)$$

where p_i are the particle momenta and d_i are the flight distances to the PPAC planes. The flight distances are given by

$$d(\theta, \phi) = \frac{d_\perp}{\cos\theta \sin\alpha + \sin\theta \cos\alpha \sin(\phi_{center})} \qquad (3.7)$$

where α is the polar angle of a normal to the PPAC extending through the target center, and ϕ_{center} is the azimuthal angle between the particle trajectory and
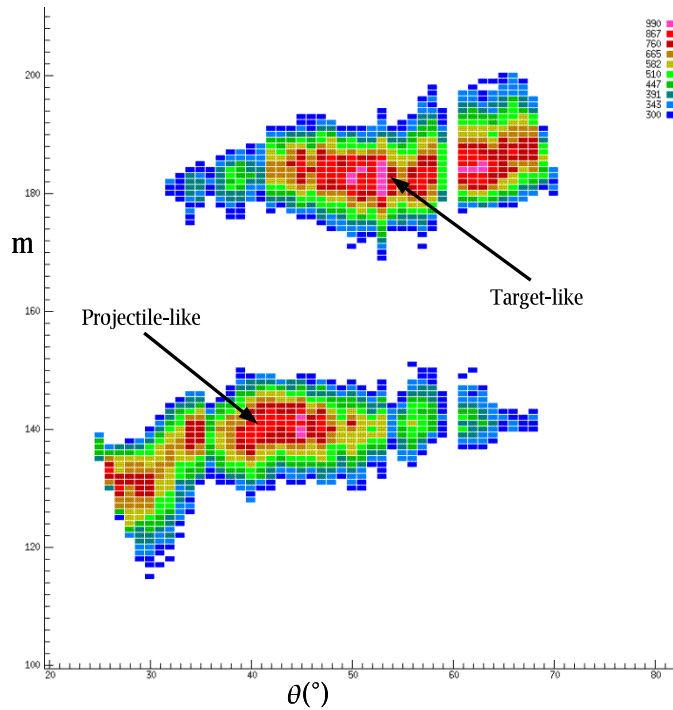
Figure 3-13: A mass m versus θ histogram with a lower limit at 300 counts for clarity.

the center of the PPAC. The mass transformation (Figure 3-13) revealed systematic errors and simplified the construction of gates for particle identification. An additional gate on the θ_1 vs. θ_2 histograms (Figure 3-14) was used to ensure the selection of the proper kinematics in cases where PPAC amplifier oscillations produced satellite peaks in the mass spectra.
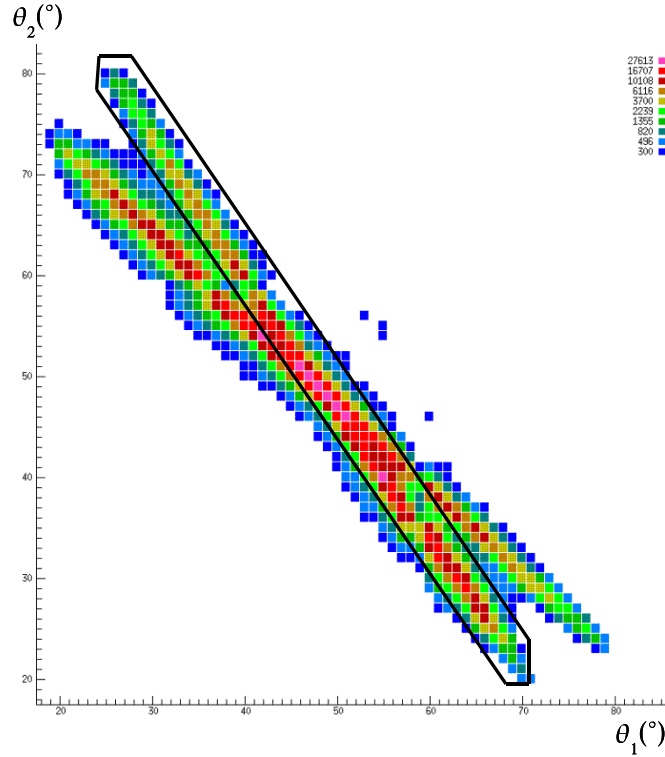
Figure 3-14: A θ_2 vs. θ_2 histogram with a lower limit at 300 counts for clarity. A gate for one solution to the kinematics is shown.

3.2.4 Doppler Correction

The identification of the correct kinematics described in the previous section allows for event-by-event Doppler correction for the γ-ray energy:

$$E_\gamma = E'_\gamma \frac{1 - \beta \cos \theta'_{\text{open}}}{\sqrt{1 - \beta^2}}, \tag{3.8}$$

where E_γ is the natural γ-ray energy in the moving frame and θ'_{open} is the opening angle between the particle and γ-ray trajectories. The identity of the particle emitting each γ-ray can not be determined using the available kinematic data, so the identity was resolved by applying the Doppler correction for the species to be studied uniformly to all of the γ-ray energies. The uncorrected spectra with

53
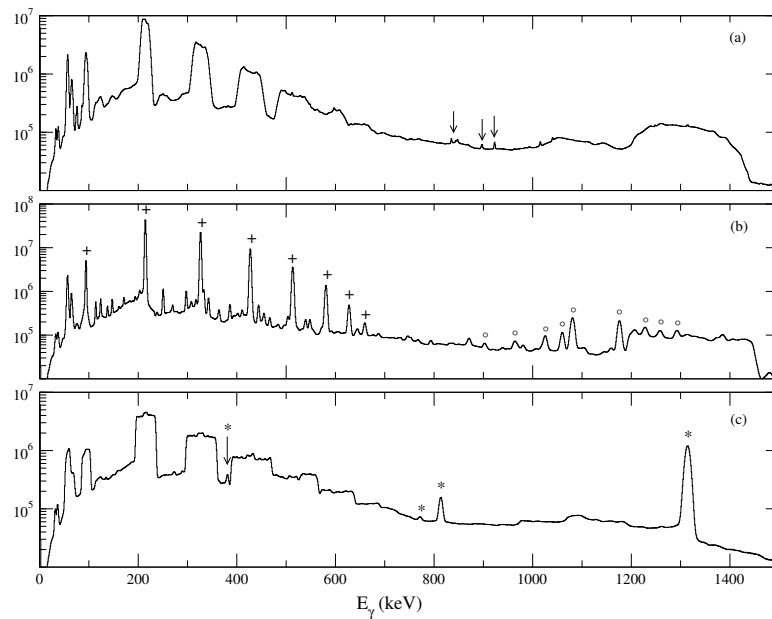
Figure 3-15: The γ-ray spectrum uncorrected for the Doppler shift (a), corrected for the Hf-like nuclei (b) and corrected for the Xe-like nuclei (c). Frame (a) shows candidates for isomer decays, the sharp (unshifted) peaks indicated by the arrows. Frame (b) shows ^{178}Hf GSB transitions (+), γ-band transitions ($\circ$) and other smaller peaks from the GS bands of other Hf isotopes. The ^{136}Xe peaks from beam excitation are marked (*) in frame (c).

Doppler broadened peaks (Figure 3-15a) becomes a set of sharp Hf peaks (Figure 3-15b)when the correction is applied assuming that every γ-ray was emitted by a Hf nucleus. The Doppler-broadened Xe peaks are further broadened by the application of the inappropriate correction, reducing the background under the Hf peaks. Applying a correction assuming that the γ-rays were emitted by the projectile-like particle results in a sharpening of the Xe lines (Figure 3-15c) and a broadening of the Hf peaks.

3.2.5 n-Fold Data Sets

The Doppler correction achieved the 0.5% ΔE_γ resolution and sufficient resolving power to measure γ-ray yields to the 10^{-4} level, relative to the GSB $8^+ \to 6^+$ yield, even with multiple isotopes present in the target. (The normalized yields quoted for the present experiment are expressed as a fraction of the GSB $8^+ \to 6^+$ yield of ^{178}Hf.) The γ-ray singles spectra were effective in measuring the yields of strongly populated states in the GSB and the lower levels of the γ-band, where the yield is above the 1% level.

Prompt-prompt (PP) and promp-delayed (PD) matrices were constructed from the data in $9°$ intervals in the projectile (Xe) scattering angle θ_{scat}. The PP matrices were effective in measuring the γ-band decays to the GSB. The PD matrices were extremely powerful in measuring the yields of the $K = 6^+$ isomer band, where the $t_{\frac{1}{2}} = 77$ ns half life permitted correlations between the prompt intraband transitions and the isomer decays, during the 1 μs sweeper period.

Symmetric cubes of $\geq$ 3-fold γ-ray events were constructed to measure the yields of bands populated at or below the 10^{-3} level, including the isomer bands. The γ-ray energies were compressed from the original linear relation to the ADC channel, greatly reducing the space required to store and manipulate the cube. A discrete stepped compression table was applied using a fit of the peak FWHM as a function of energy to the function

$$\mathrm{FWHM} = (a^2 + b^2 x + c^2 x^2)^{1/2} \tag{3.9}$$

resulting in a FWHM in the expanded cube projections of $\approx$ 2 channels for all energies. The software RADWARE was used to graphically manipulate the cube, applying gates and automatic background subtraction [74]. Asymmetric cubes combining Xe and Hf data were constructed to search for transfer reactions near the Coulomb barrier.

The power of the combination of Gammasphere and CHICO is evident not

only in the ability to measure yields to the 10^{-4} level in the ^{178}Hf target, but also in the data gleaned from isotopic impurities at the $0.5\% - 4\%$ level, using γ triples data. Figure 8-8 shows the GSB spectra of five of the Hf isotopes present in the target. The GSB of ^{180}Hf was extended from spin 12^+ to spin 18^+, using the data of the 3% ^{180}Hf impurity. Ngijoi-Yogo [18] simultaneously placed the 18^+ level in an inelastic scattering experiment which used a 750 MeV ^{136}Xe beam on a ^{180}Hf target.

Chapter 4

Experiment I Analysis

The ^{178}Hf(^{136}Xe,^{136}Xe)^{178}Hf Coulomb excitation experiment provided Doppler-corrected γ-ray information in sufficient quantity ($\sim 10^9$ usable events) to construct γ^2 matrices and γ^3 cubes with statistics that would allow measurement of the γ-ray yields of states populated as low as the 10^{-4} level, relative to the GSB $8^+ \rightarrow 6^+$ transition. Data from γ-ray singles and gated doubles and triples were used to extend several previously known rotational bands as shown in Figure 4-1.

In most cases, the coupled-channel semi-classical Coulomb excitation code GOSIA was used to adjust matrix elements for the relevant transitions and reproduce the experimental data. The γ-ray yields were measured as a function of scattering angle θ_{scat}, making the fits more sensitive to the matrix elements. In some cases, individual reduced matrix elements can be measured, but this usually requires a large amount of data from widely varied experiments [68]. More often, a single model-dependent parameter (intrinsic matrix element) was obtained as the measure of the coupling strength between two bands. The correlated error in the parameter was measured with respect to all other adjustable parameters. The analysis of the $K = 6^+$ isomer band was treated differently, because the partial decay widths of all known decay branches were measured in this work, showing one branch to be more significant than previously thought, and allowing an absolute

measurement of the strengths of the transition probabilities to the 6^+ band.

Using the methods described above, the effectiveness of a particular excitation path between two bands was deduced, either eliminating it as a possibility, or confirming it and measuring the intrinsic matrix element connecting the two bands. An excitation path was eliminated or judged to be insignificant if it could not reproduce the measured data using reasonable reduced transition probabilities for the particular multipolarity and change in single-particle structure. In cases where multiple excitation paths were discovered, the relative importance of each was gauged by removing it from the system and calculating the resulting change in the calculated yields.

Intrinsic matrix elements were extracted from the ^{178}Hf(^{136}Xe,^{136}Xe)^{178}Hf data, connecting the $K = 0^+$ GS, γ-, 4^+, 6^+ and 8^- bands. Upper limits on the reduced transition probabilities between the GSB and the 16^+_{isom} bands were found, in one parameter based on the SDM description. The Alaga rule was found to reproduce K-allowed transitions well, whereas population by K-forbidden transitions was described well by the spin-dependent mixing (SDM) model in several cases.

This chapter gives the methods and details of the fit calculations and the qualitative results which are important in later chapters. Chapter 9 gives the detailed numerical results in tabular form.

4.1 Level Scheme

A level scheme (Figure 4-1) was built on the known levels of the GSB, γ-, 4^+ and isomer bands. Gated γ-ray triples data were used to extend the known bands, using several gate combinations to confirm each new level. Appropriate coincidences and anti-coincidences between γ-rays indicated the appropriate arrangement of new levels. At the highest spin states with measurable populations, the decrease in γ-ray yield with increasing spin (evaluated separately for the even

and odd signatures in $K \neq 0$ bands) ensured that the correct order of levels was inferred.

The GSB The GSB levels were measured to the 20^+ level using gated γ-ray triples data. The 20^+ level found by Mullins [58] was confirmed, but no candidates for the 22^+ state were found.

The γ-band In-band $\Delta I = 1$ transitions in the $K = 2^+$ γ-band are weak, making it difficult to extend the odd-spin unnatural (odd-spin) parity states, although gated triples and doubles were effective in extending the even-spin levels to a tentative spin 16^+. Two candidate bands, "A" and "B" in Figure 4-2, both with γ-ray yields consistent with continuation of the odd spin signature. Band "B" provides a smoother continuation of the energy vs. spin pattern, but a more discriminating test is the continuity of the moment of inertia as a function of rotational frequency (Figure 4-3). The striking similarity between the moments of inertia of the odd and even spin states gives substantial evidence that band "B" is the odd spin signature of the γ-band.

The $K^\pi = 4^+$ Band Using γ-ray triples and a similar analysis technique, the $K = 4^+$ band at 1513.8 keV, thought to be a two-phonon γ-vibrational band [2], was extended from the previously known 7^+ level to a tentative 18^+ level (Figure 4-1). Interband γ-decay branches were observed, connecting the 4^+ band to the 2^+ band by K-allowed transitions. Transitions to the GSB must have a significant E2 component, since the $\Delta I = -2$ branch of the 4^+ band head is comparable in strength to the $\Delta I = 0$ branch. (This is consistent with a previous measurement [2] of an 18(10)% M1 component for the $\Delta I = 0$ branch.) This indicates that K-forbidden E2 and M1 decays are responsible for γ-decay to the GSB and that direct excitation from the GSB via K-forbidden E2 excitations cannot be neglected in the population.

Figure 4-1: A partial ^{178}Hf level scheme. Levels shown were observed in the present experiment. New levels and isomer levels are shown as bold lines. Half-lives are given for the three isomers.
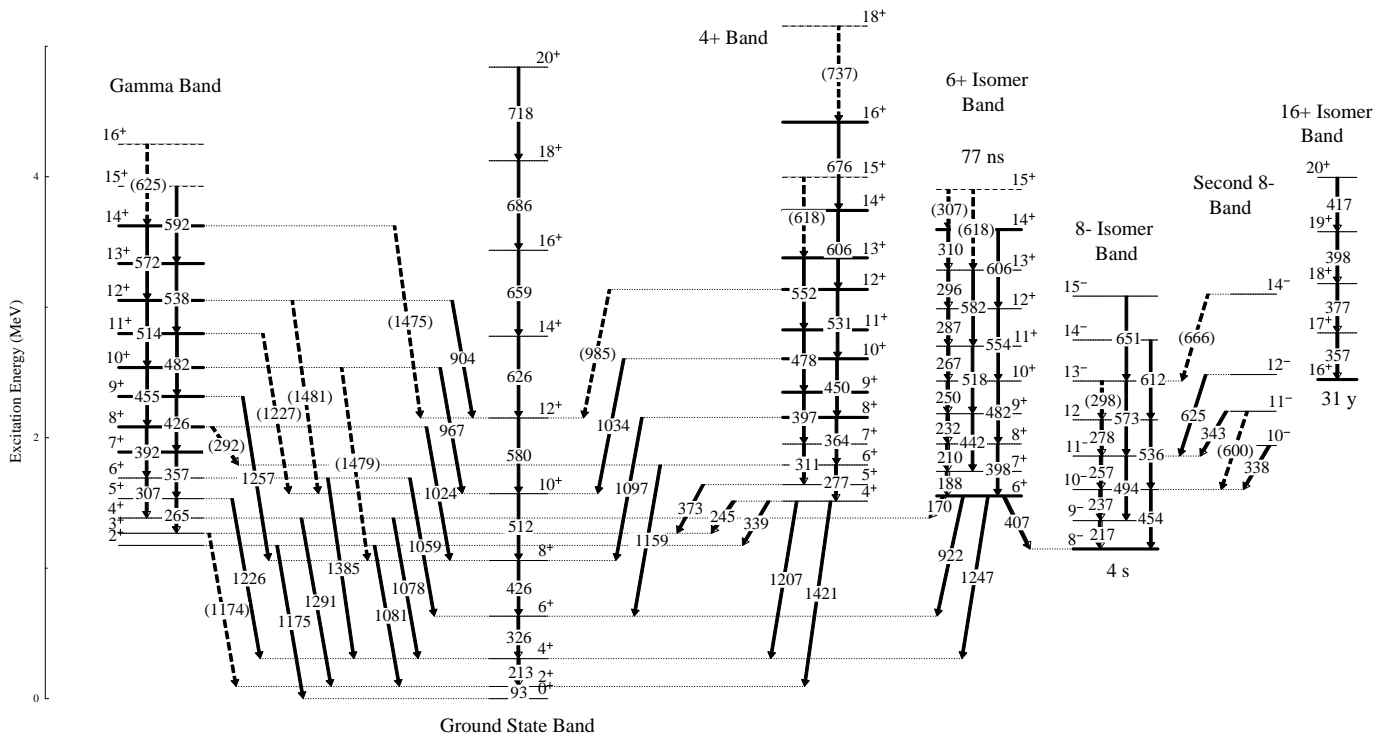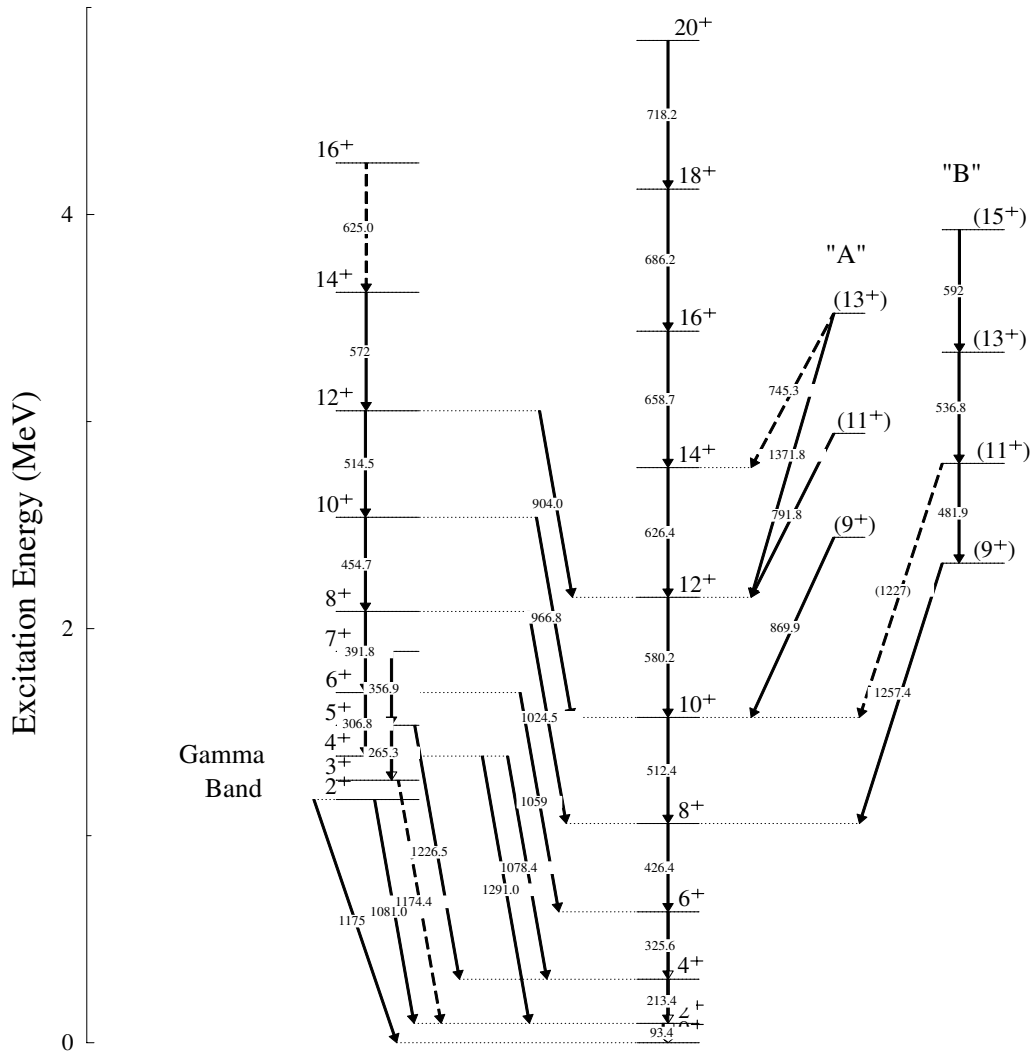
Figure 4-2: Bands "A" and "B", candidates for the odd-spin levels in the γ-band.

The 6⁺ Isomer Band Gated triples were successful in building the known level scheme [58] up to spin 13⁺. A 310 keV transition to the 13⁺ state can be observed in gated triples. A tentative 618 keV transition was placed above the 13⁺ state, based on gated triples and a low-intensity peak in the prompt-delayed data. The tentative 15⁺ level could not be confirmed by a 15⁺ → 14⁺ transition, because
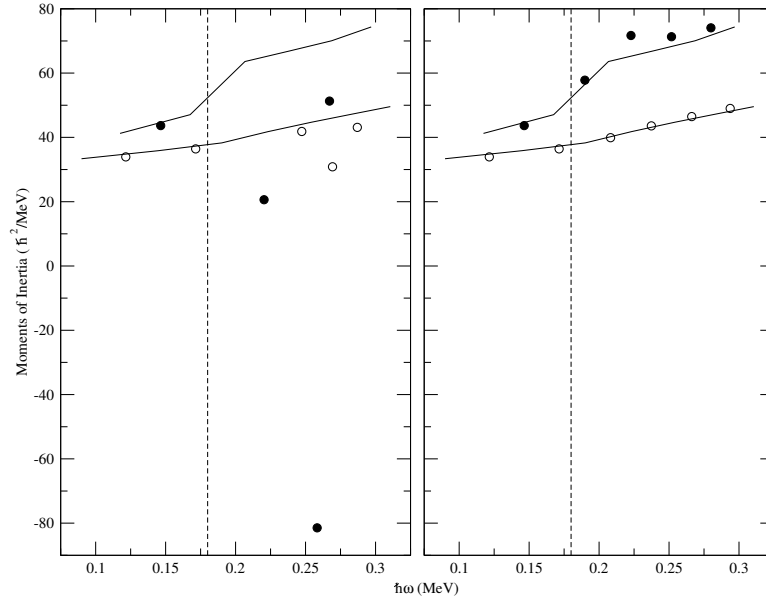
Figure 4-3: Moments of inertia of the two candidate bands "A" (left) and "B" (right) for continuation of the odd signature of the γ-band. The kinematical moment $\mathcal{F}_1$ (open circles) and the dynamical moment $\mathcal{F}_2$ (filled circles) are shown for each level.

the expected 308 keV energy could not be resolved from the 310 keV $14^+ \rightarrow 13^+$ transition energy (Figure 4-1).

The $K \geq 8$ Bands   The 8_1^- isomer band, the 8_2^- band at 1479 keV, and the 16^+ isomer band were observed in prompt triples data, but the bands could not be extended to higher spin. The 14^- isomer band was not unambiguously observed, but the upper limit of its population was measured using prompt $\gamma - \gamma$ data.

4.2 Yield Measurements

4.2.1 Uncorrected Yields

Uncorrected γ-ray yields were extracted as described in this section. The calculation of normalized yields, where corrections are applied for gating, internal con-

version and other efficiency factors, is described in the next section. Raw counts were obtained from Gaussian fits to the spectra with the standard symmetric and asymmetric components for Ge detectors [75] and parabolic fits to the residual background. The purely fit-based errors, typically $\approx \sqrt{n}$, were increased by a factor of $\sqrt{2}$ to account for the background counts, since the peak-to-background ratio was ≈ 1. Figure 4-4 shows the effectiveness of a coincident gate, a logical AND between two γ-rays, in extracting yields of the order of 10^{-4} relative to the GSB. Single gates in double-γ matrices were nearly as effective in some cases, but estimating the background was more difficult, which often obscured the data in a rich background, and false coincidences were a problem.

GSB   Two methods were used to extract the GSB yields. In γ-singles, peaks up to the 14^+ level were measurable for a range of particle scattering angles in $2°$ intervals where they were observable between $20°$ and $80°$. Yields were extracted from triples data in $9°$ intervals up to $\theta_{\mathrm{scat}} = 78°$ above the 6+ to 4+ transition, by gating on two consecutive GSB transitions directly below the measured transition. Generally, the triples data were used in the Coulomb excitation calculations.

The γ-band   Yields for the γ-band decays to the GSB were measured over a range of θ_{scat} by gating in the GSB directly below the level being fed by the γ-band, using both triples and doubles. The relative intensities of the intraband and interband lines from the lower γ-band levels were measured by gating above a level in the γ-band, in a 2-D matrix of all forward-scattering data. From the interband yields from these three levels and the measured branching ratios, the intraband yields were calculated for lower levels. The upper levels of the γ-band have stronger intraband branches, compared to the lower levels.

The $K = 6^+$ Isomer Band   The highest precision yields for the 6^+ band were obtained from the 2-D prompt-delayed (p-d) spectrum (Figure 4-5), which was

63
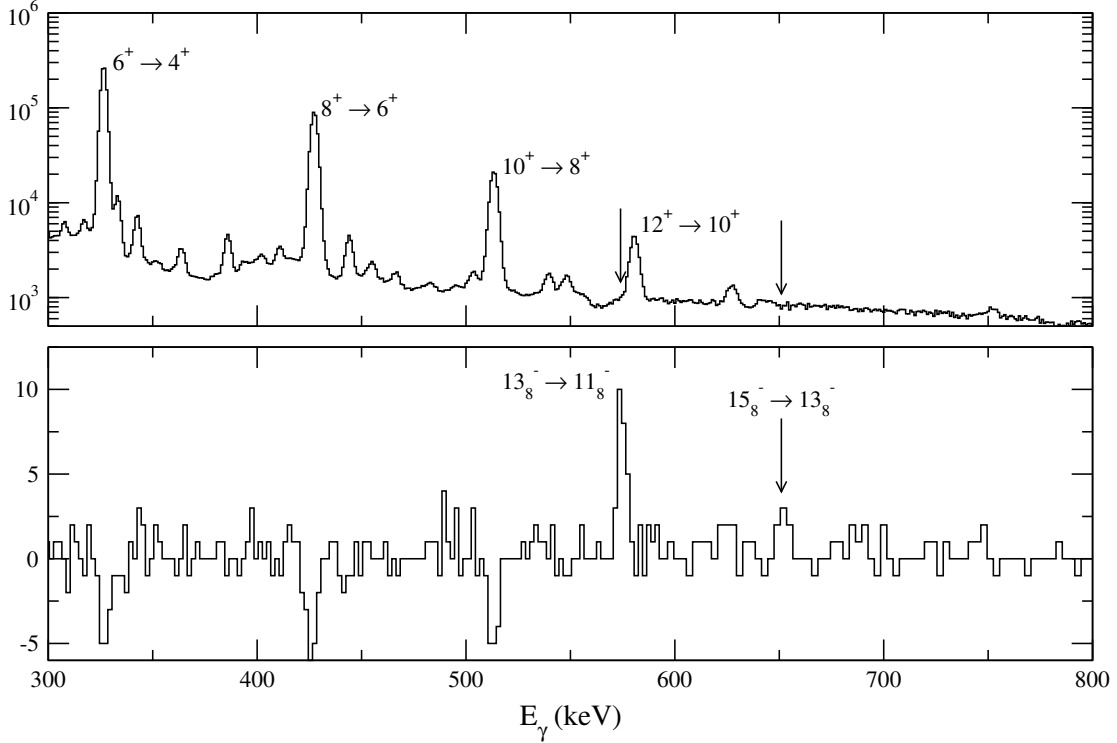
Figure 4-4: Typical γ-ray energy spectra for a scattering angle range $52° < \theta_{scat} < 61°$. The upper histogram shows a γ-singles spectrum with the ^{178}Hf GSB transitions labeled. Most of the smaller peaks are GSB transitions from other isotopes. The lower histogram is the resultant background-subtracted spectrum from a gate on the $9^- \rightarrow 8^-$ and $11^- \rightarrow 9^-$ transitions in the 8^- isomer band. Small oversubtraction of the background due to coincidences between strong peaks and the background results in the "negative peaks.".

divided into $9°$ intervals of θ_{scat}. The delayed γ window of 50ns $< t <$ 500ns provided a very clean gate, owing to the short lifetimes of typical collective transitions. The p-d data had very low noise after background subtraction and enabled very precise and complete measurements of the yields for most transitions in the band. However, the yields obtained from the p-d data required an extra correction to normalize them to the relative yields from prompt γ-ray data. The $9_6^+ \rightarrow 8_6^+$ transition, which had the best precision, was used to calculate a normalization
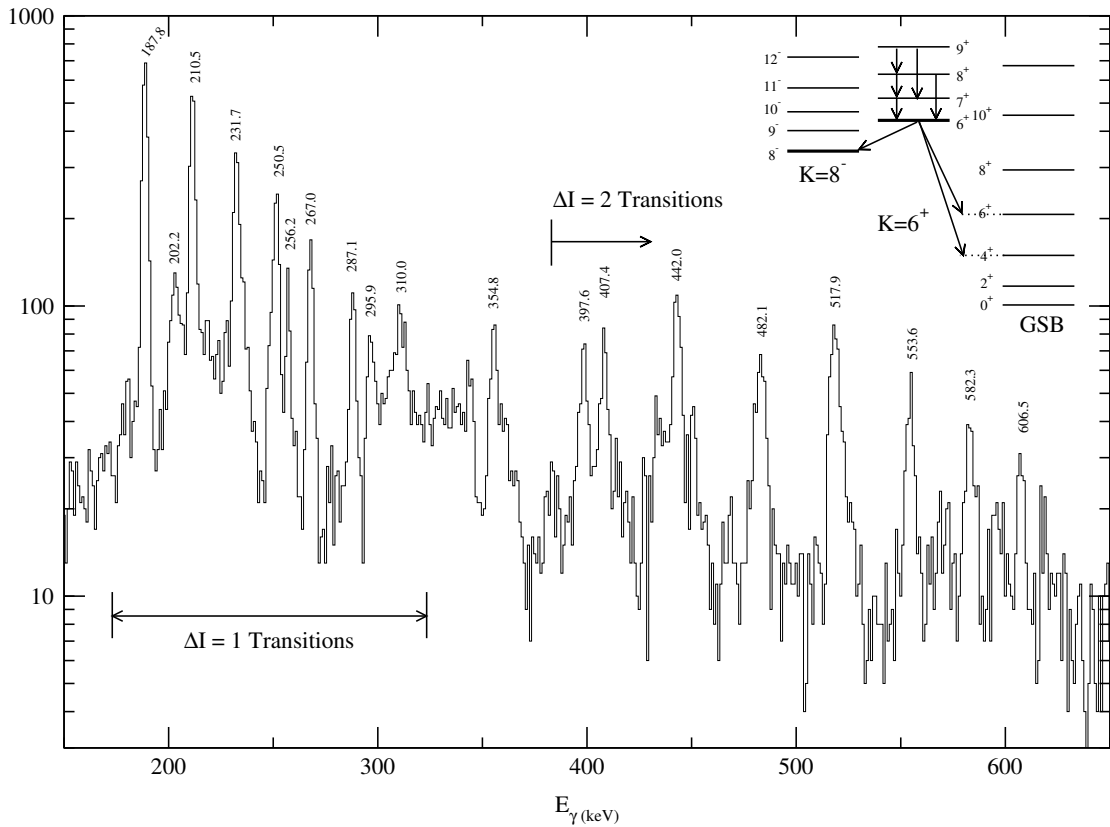
Figure 4-5: A background-subtracted prompt γ-ray resultant spectrum from a gate on the delayed $6^+_{\text{isom}} \to 6^+_{\text{GSB}}$ transition. The $\Delta I = 1$ and $\Delta I = 2$ intraband transitions are labeled by their energies in keV. Several unidentified peaks, such as the 202 and 296 keV peaks appear to be the result of random coincidences between strong GSB yields and delayed 6^+_{isom} decays from different events to which the Doppler-shift correction was inappropriately applied. (The broadened 213 and 325 keV GSB transitions can be seen.)

factor for each angular range, limiting the precision to that of the best triples data for the 6^+ band. Nevertheless, the normalized p-d data are much more precise than the gated triples data would have been for the highest levels, and the yields for transitions below spin 8^+ could not be measured using triples.

Because the p-d matrix gave such clean data, the ratios of the $\Delta I = 1$ branch intensities to the $\Delta I = 2$ branch intensities were measured very precisely and used

65

to calculate the $g_K - g_R$ value for the 6^+ band (chapter 9). The p-d data also provided a precise measurement of the branching ratios of the 6^+ isomer decays. The decay branch to the $K = 4^+$ band head, a highly converted 40 keV branch previously observed [76] but not measured, was measured indirectly in this work by the intensities of the secondary decays of the 4^+ band head (Table 4.4). The strength of this branch, which was previously unmeasured, accounts for 19(1)% of the decay width, including conversion, and is essential in correctly determining the Coulomb excitation paths to the 6^+ isomer band.

The $K^\pi = 8^-$ Bands Some 8^- isomer band yields were obtained from prompt triples, although only three clean gates were available. (The 4 s half-life of the 8^- isomer was too long to allow any selection by delayed γ-ray gating.) Most of the 8^- band transitions lie at the same energies as transitions in the odd-A isotopes in the target. The clean transitions, $12^- \to 11^-$, $11^- \to 10^-$, and $11^- \to 9^-$, were used to extract unambiguous yields, while other in-band gates were used wherever the resultant spectrum was clean enough. Yields could be extracted down to approximately the 10^{-4} level, but only as upper limits in some cases. In a typical background, a minimum of about 10 counts was required to obtain a measurable yield, rather than an upper limit.

Five interband feeding transitions from the upper 8_2^- band were observed, just above the lower limit of observation ($\approx 10^{-4}$), by gating in the 8_1^- isomer band. Yields and upper limits for these transitions were measured where possible. The intraband branches in the upper 8_2^- band were not observed.

The $K^\pi = 16^+$ Band The 16^+ isomer band, unexpectedly populated by Coulomb excitation at the 10^{-4} level at safe angles was observed up to spin 20^+, though it is known up to a tentative spin 23^+ [58]. The 10^{-4} level population and 31 y half life required prompt triples gating, so the only measurable yields were observed for the $19^+ \to 18^+$ transition. More information was derived from the ^{178}Hf

activation experiment than from the $19^+ \rightarrow 18^+$ yield measured here.

The $K = 14^-$ Isomer Band An estimate of the population of the $K = 14^-$ is important to the analysis of the 16^+ activation experiment (Chapter 7) because there is a known feeding branch from the 14^- isomer into the 16^+ isomer. The 68 μs half-life was too long to employ prompt-delayed or delayed-delayed γ-coincidence, and the band is known only up to the 16^- level, making prompt triples useless. (No new levels were found using prompt doubles or triples data.) Prompt doubles gave a relative population upper limit of $\sim 10^{-4}$ for the 14^- band, but the peaks in the gated doubles spectrum are ambiguous and can not be assigned with certainty to the 14^- band without a second available gate. Chapter 7 clarifies the implications of the possible 14^- band population.

4.2.2 Calculation of the Corrected γ-ray Yields

The γ-ray yields were normalized to the $8^+ \rightarrow 6^+$ transition in the GSB, which is the lowest-spin transition having high counts in the gated triples data. (Because of its low 93 keV γ-ray energy, the $2_0^+ \rightarrow 0_0^+$ transition has a poor detection efficiency and is difficult to measure using Gammasphere.)

The corrections made on the gated triples yields are illustrated for a series of $\Delta I = 1$ transitions (Figure 4-6) in equation 4.1. Similar corrections are made for gated doubles, removing one set of factors from equation 4.1 for the unused gate. The relative γ efficiency discussed above is used to correct for the loss of the majority of the γ-rays due to scattering losses, pair production, dead time, etc. by dividing the raw (uncorrected) γ-ray yield Y_{raw} by the product of the relative efficiencies ϵ_i. The terms in brackets are correction factors for internal conversion and the neglected branch from each of the gate levels. The unobservable internal conversion events in the gated branches (1 and 2) diminish the count of the measured γ-ray (3), so a correction factor of $(1 + \alpha_i)$ is applied. If there is a
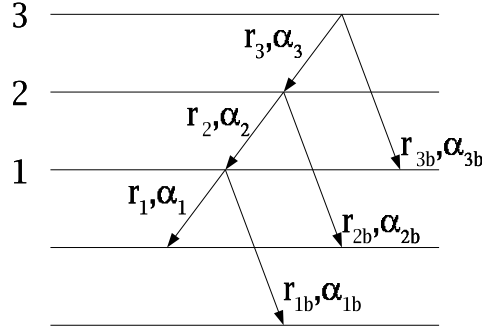
Figure 4-6: Illustration of gates on $\Delta I = 1$ transitions from levels 1 and 2, each with uncounted branches (b), used to measure the yield of a third $\Delta I = 1$ transition from level 3. The relative γ-ray intensities and internal conversion coefficients are given by r and α, respectively.

non-negligible "b" branch at one or both of the gate levels, a correction in the amount of the ratio of the total width of the "b" branch to the γ-decay width of the gated branch, $\frac{r_{1b}(1+\alpha_{1b})}{r_1}$, is included. The result of the correction for each gate is given in brackets in equation 4.1.

For level three, the corrected yield Y is then given by

$$Y = \frac{Y_{\text{raw}}}{\epsilon_1\epsilon_2\epsilon_3}\left[1 + \alpha_1 + \frac{r_{1b}(1+\alpha_{1b})}{r_1}\right]\left[1 + \alpha_2 + \frac{r_{2b}(1+\alpha_{2b})}{r_2}\right]. \tag{4.1}$$

In the case of $\Delta I = 1$ gates of mixed E2/M1 character, the internal conversion coefficients are weighted averages of the E2 and M1 coefficients,

$$\alpha_i = \frac{\delta_i^2\alpha_i^{E2} + \alpha_i^{M1}}{1 + \delta_i^2}, \tag{4.2}$$

where the mixing ratios are given by δ_i.

The most significant source of error is in the measurement of the raw yields in the case of isomer bands, which were populated to about the 10^{-4} level relative to the normalizing $8^+_{\text{GSB}} \rightarrow 6^+_{\text{GSB}}$ transition. In the strongly populated levels of the γ-band and the GSB, the detection efficiency factors introduced the majority of the error, generally $\approx 5\%$ error for each γ-ray gated or measured. The corrections

68

for internal conversion were typically about 5% or less, and the errors introduced were $< 1\%$, even in cases where there were large uncertainties in the mixing ratios.

4.3   Minimization of χ^2:
The $K^\pi = 0^+, 2^+, 4^+, 8^-$ and 16^+ Bands

Iterative Method   For the strongly coupled $K^\pi = 0^+, 2^+$ and 4^+ bands, an iterative fit process was employed to measure the intrinsic and reduced matrix elements. The matrix elements for the most strongly populated band (the GSB) were adjusted first. After finding the matrix elements which gave the minimum value of χ^2, the band with the next highest population (the γ-band) was added to the calculations along with its measured γ-ray yields. This procedure was repeated, fitting all of the adjustable parameters described below at each step. The GSB, the γ-band and the 4^+ band were strongly coupled, so that their matrix elements could not be fit independently without the iterative technique. The isomer bands are populated only to about the 10^{-4} level, as are other high-K bands, so the iterative procedure was not necessary for the relatively small fraction of population diverted to these bands. All of the $K > 4$ bands were treated as small perturbations without any loss of accuracy in the reproduced yields.

Correlated Errors   Final adjustments of each measured matrix element were made by measuring the correlated errors using the following criterion. An increase of 1 in the total χ^2 represents a change of $\pm\sigma$ in the measured quantity x [77].

$$\chi^2(\bar{x} \pm \sigma) = \chi^2(\bar{x}) + 1, \tag{4.3}$$

where $\bar{x}$ is the best value at $\chi^2_{\min}$. Generally, the χ^2 function could be fit using a quadratic in the vicinity of the minimum (Figure 4-7) and the minimum of the quadratic was taken as the best value.
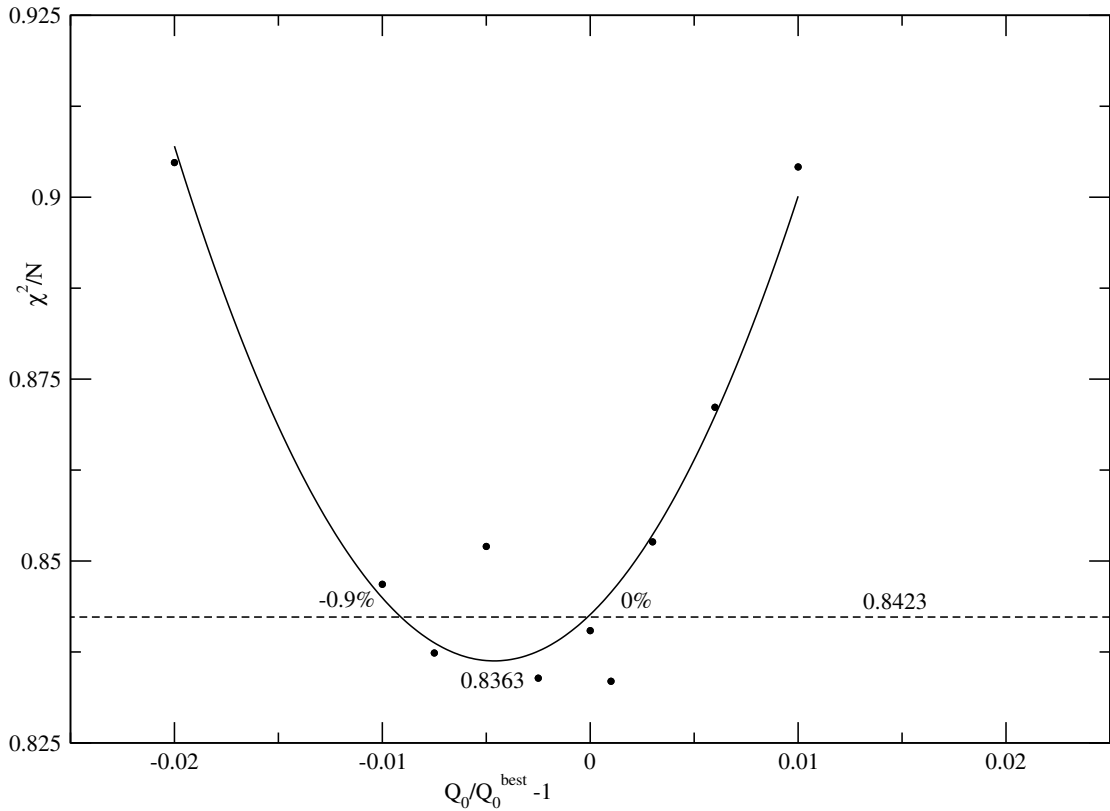
Figure 4-7: A correlated error plot for the GSB quadrupole moment showing the points x_i (text). The abscissa represents the fractional change in the moment. A quadratic fit gives the minimum and best values indicated. $\bar{Q}_0 = 2.164(10)$ eb.

The χ^2 data for the correlated error measurement were calculated by fixing the value of the measured parameter x at each of a set of points $\{x_i\}$ around the vicinity of $\chi^2_{\min}$ (from the GOSIA fits) and fitting all of the other parameters to find a local minimum in χ^2 for each x_i. This produced the best estimate of the error in each matrix element by permitting all of the other parameters to compensate for the change in x, varying within reasonable physical limits.

4.3.1 The $K^\pi = 0^+$ GS Band

Initial Values of the Matrix Elements   Using the rigid rotor model, initial values of the intraband E2 matrix elements were calculated from the value of
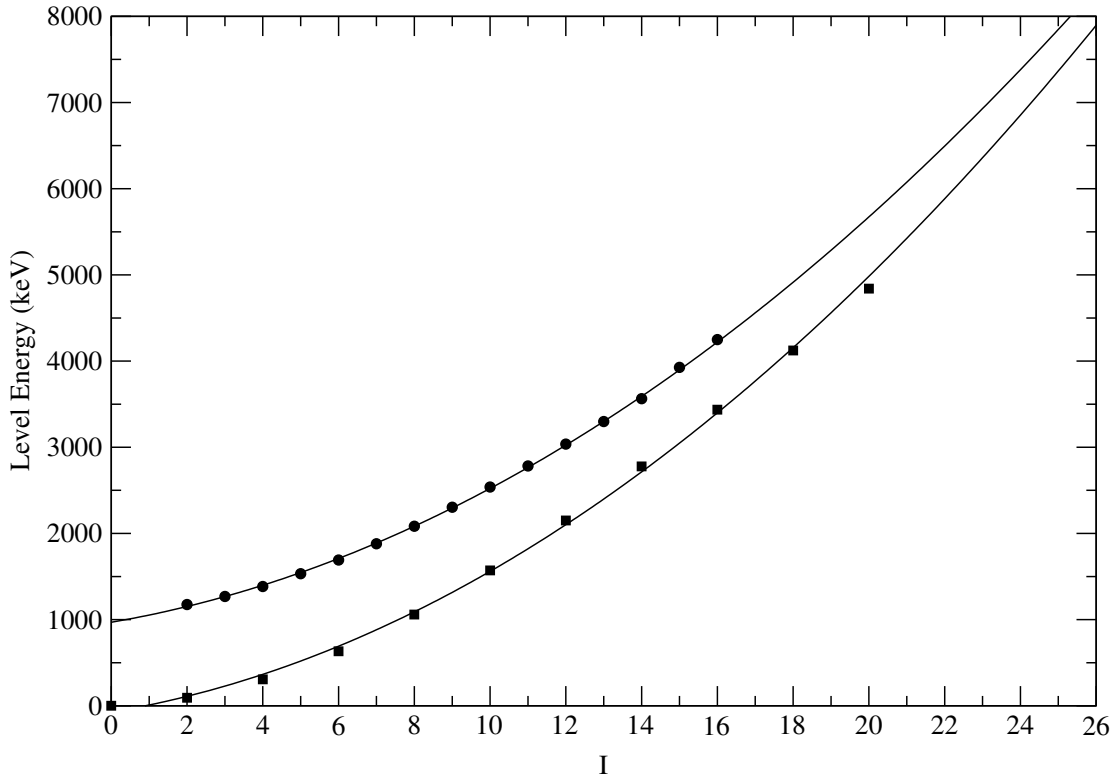
Figure 4-8: The level energies of the GSB and the γ-band. Quadratic fits were used to extrapolate the energies of several unknown levels.

$B(E2; 2_0^+ \rightarrow 0_0^+) = 159$ W.u. [1], giving a value of $\sqrt{\frac{5}{16\pi}} e Q_0 = 2.17$ eb. The intraband E2 reduced matrix elements given by Equation 2.10 were calculated for $K = 0$ for levels up to spin 24^+. Levels up to spin 20^+ were seen in the triples data, while levels 22^+ and 24^+ (as yet unknown) were extrapolated using a quadratic fit to $E(I)$ (Fig. 4-8). Extrapolation of two or more unobserved states is necessary for the accurate calculation of the Coulomb excitation of the highest observed states.

Data Set Both singles and triples data were included in the fit. Singles data were included in bins of $2°$ width in *recoil* angle. In terms of the *scattering* angle, the central angles of these 11 bins range from $\theta_{\text{scat}} = 35.6°$ to $60.4°$. For unsafe scattering beyond $\theta_{\text{scat}} = 52°$ the weight of the data was reduced to $\frac{1}{2}$ ($\frac{1}{4}$, in

terms of χ^2) relative to the data from the safe region, so that nuclear interference effects in the data would not greatly influence the purely electromagnetic analysis. Triples data were included in 3 sets of 9° width in *scattering* angle, of central angles $\theta_{\mathrm{scat}} = 38.5\,°, 47.5\,°$ and $56.5\,°$. As in the singles case, the weight of the data was reduced to $\frac{1}{2}$ for $\theta_{\mathrm{scat}} > 56.5\,°$.

Results   The population of the ground band is insensitive to the magnitudes of the lowest matrix elements, so only E2 matrix elements connecting levels 6^+ through 18^+ were measured individually. Allowing the E2 matrix element connecting each pair of GSB levels, coupled to the static moment of the upper level, to vary independently resulted in a 7 parameter fit of the intrinsic quadrupole moments for the 6^+ through 18^+ levels. The greatest change in the quadrupole moment was an increase of 1.5% from the initial (rotor) value in $\langle 12^+||E2||10^+\rangle$, indicating a single quadrupole moment for the GSB. The correlated error measurements gave $\sqrt{\frac{5}{16\pi}}eQ_o = 2.164(10)$ eb.

The calculated GSB yields reproduced by the fit are shown in Figure 4-9. Up to $I \approx 16^+$, the agreement between the measured and calculated yields is good, but the calculated yields are higher than the measured yields for higher spin. The deviation from the measured yields occurs at the highest levels populated, where the only observable yields are at unsafe scattering angles and nuclear interference could be a significant factor. The results of Figure 4-9 are a small subset of the GSB, γ-band and 4^+ band yields used in the fit, justifying the the systematic deviation in the GSB yields at the χ^2 minimum.

It is also possible that the strong K-mixing of the GSB seen in the analysis of higher-K bands is causing some considerable feeding out of the top of the GSB. For instance, the calculations for the $K = 16^+$ band (Chapter 7) show that at the highest levels populated in the GSB feeding to the 16^+ band at large scattering angles may result in a non-negligible loss in the GSB population, though feeding
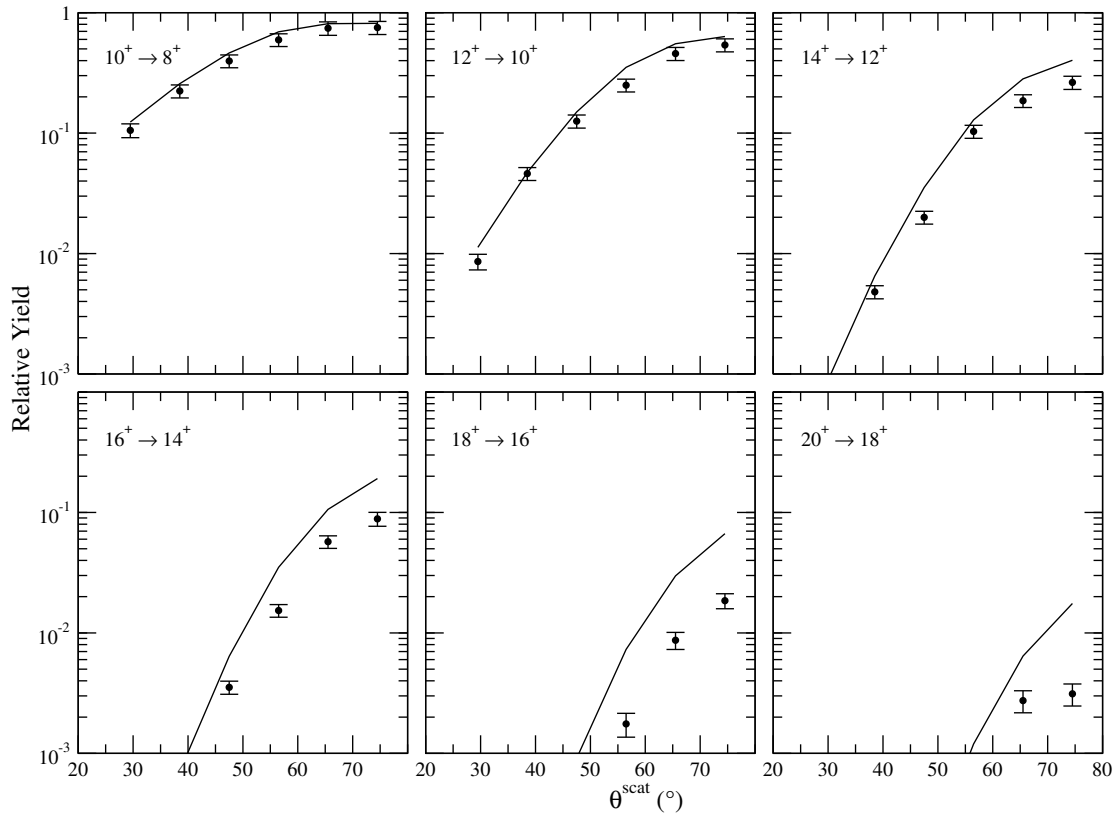
Figure 4-9: The calculated (lines) GSB yields from the best values obtained by the correlated error analysis after the third iteration fit of the GSB matrix elements (during the 4^+ band fit).

is too weak to be measured directly in this experiment. Considerable K-mixing at the top of the GSB could provide other potential feeding or excitation paths to other bands. The χ^2 search did not permit deviations $> 1.5\%$ from the rotor values, even though the calculated yields were low at the highest levels. Regardless of the cause, the small deviations at the top of the GSB are not detrimental to the rest of the analysis.

4.3.2 The $K^\pi = 2^+$ γ-band

The γ-band was populated nearly to the 10% level, relative to the $8^+ \rightarrow 6^+$ GSB yield, for some of the lowest γ-band to GSB transitions. Levels up to spin 20^+ were included in the calculations, the energies of levels 17^+ to 20^+ having been extrapolated (Fig. 4-8).

Initial Values of the Matrix Elements Interband E2 matrix elements connecting the GSB and the γ-band were extracted from a Mikhailov plot (Fig. 4-10) that used branching-ratio data from this experiment as well as other sources. The Mikhailov plot gives the first-order expansion of the intrinsic matrix element in ΔI^2,

$$\langle K_2 \mid m_{\Delta K = \lambda + n, \nu = \lambda} \mid K_1 \rangle = M_1 + M_2(I_2(I_2 + 1) - I_1(I_1 + 1)), \qquad (4.4)$$

and for the coupling of the γ-band to the GSB initial values of $M_1 = 0.202$ eb and $M_2 = -2.64 \times 10^{-3}$. M1 matrix elements were not included, since lower-level interband transitions are entirely E2 [78], and upper-level transitions are predominantly E2 [79, 2]. The non-negligible first-order term in ΔI^2 (the Mikhailov term) seen here for the γ-band implies a strong coupling between the rotational and vibrational degrees of freedom [48] and is the first indication of the influence that rotational motion will be seen to have on the goodness of the K quantum number in the analyses of the higher-K bands.

Intraband E2 matrix elements were assuming the same starting value of the quadrupole moment as for the GSB. (It will be shown that even for high-K bands in ^{178}Hf, the quadrupole moment is within a few percent of the GSB value.) The M1 intraband branches of the γ-band are known to be insignificant, and $\Delta I = 1$ intraband transitions have only been observed for the 6_2^+ state [2, 79, 80], so M1 intraband matrix elements were not included.
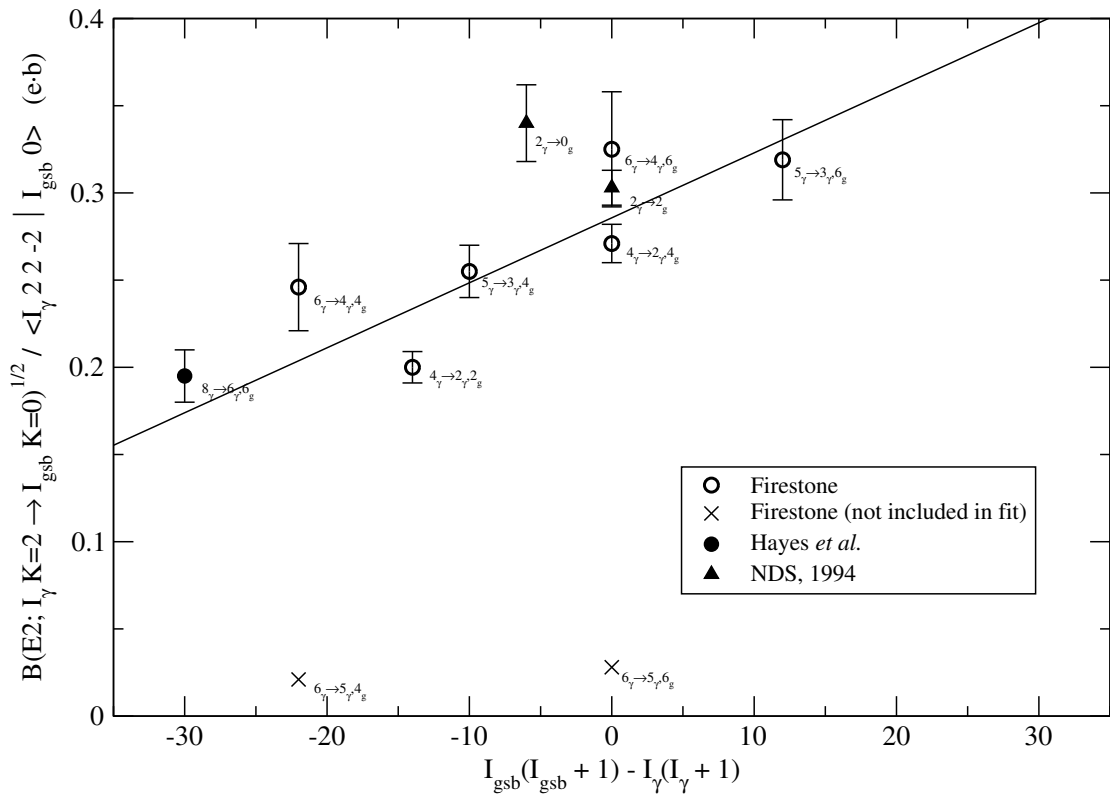
Figure 4-10: A Mikhailov plot for the γ-band. Data are from Firestone [10] and the NNDC [4], as well as the present work.

Fit Parameters All of the intraband E2 matrix elements in the γ-band were varied as one parameter, as were the interband E2 matrix elements connecting to the GSB. These two parameters were varied independently in the minimization.

Data Set In addition to the GSB data, the matrix elements were fit to data taken from singles, doubles and triples. Interband γ- to GS band transition yields from the $6^+, 8^+, 9^+, 10^+$ and 12^+ levels and two of the three measured intraband yields were taken from triples. A third intraband yield was calculated from a branching ratio measured in this experiment. Interband transition yields from the 4^+ and 6^+ levels and of three unresolved doublets were taken from singles.

75

The data were included with the same weights for unsafe scattering angles as in the GSB data.

Results   The final value of the GSB$\rightarrow$ γ-band intrinsic matrix element is $\langle \gamma \mid E2 \mid \text{GSB} \rangle = 0.266(12)\text{eb} - 3.47(15) \times 10^{-3}\text{eb}\{I_\gamma(I_\gamma + 1) - I_0(I_0 + 1)\}$ eb. The individual reduced matrix elements and other results are tabulated in Chapter 9. The agreement between the measured and calculated yields for the γ-band are shown in Figures 4-11 and 4-12. The overall agreement between the measured and calculated yields for a wide range of spin, multipolarity and scattering angles is excellent, especially considering that the γ-band data were fit with only one parameter to describe the connection between the GS and γ-bands. The behavior of the yield versus scattering angle is different for the low- and high-spin states, but the Coulomb excitation calculations reproduce all of the changes of slope and concavity for all of the observed transitions. The only considerable disagreements (by factors of $\approx$2–5) are in the weak intraband transition yields. A more rapid increase in the γ–GSB coupling (a larger Mikhailov term) would also improve the agreement with both interband and intraband γ-ray yields, but the Mikhailov term was extrapolated from the data for $I \leq 8$, which appear to be inaccurate in several cases noted above. Errors in the branching ratios and the difficulty in measuring branching ratios for higher spin may have led to an inaccurate extrapolation of the Mikhailov term.   The overall agreement for the entire set of γ-band data indicates that the Alaga rule and the first order Mikhailov correction describe the rotational-vibrational interaction correctly.   This Mikhailov coupling term will be employed successfully throughout the rest of the analysis for vibrational and single-particle bands.
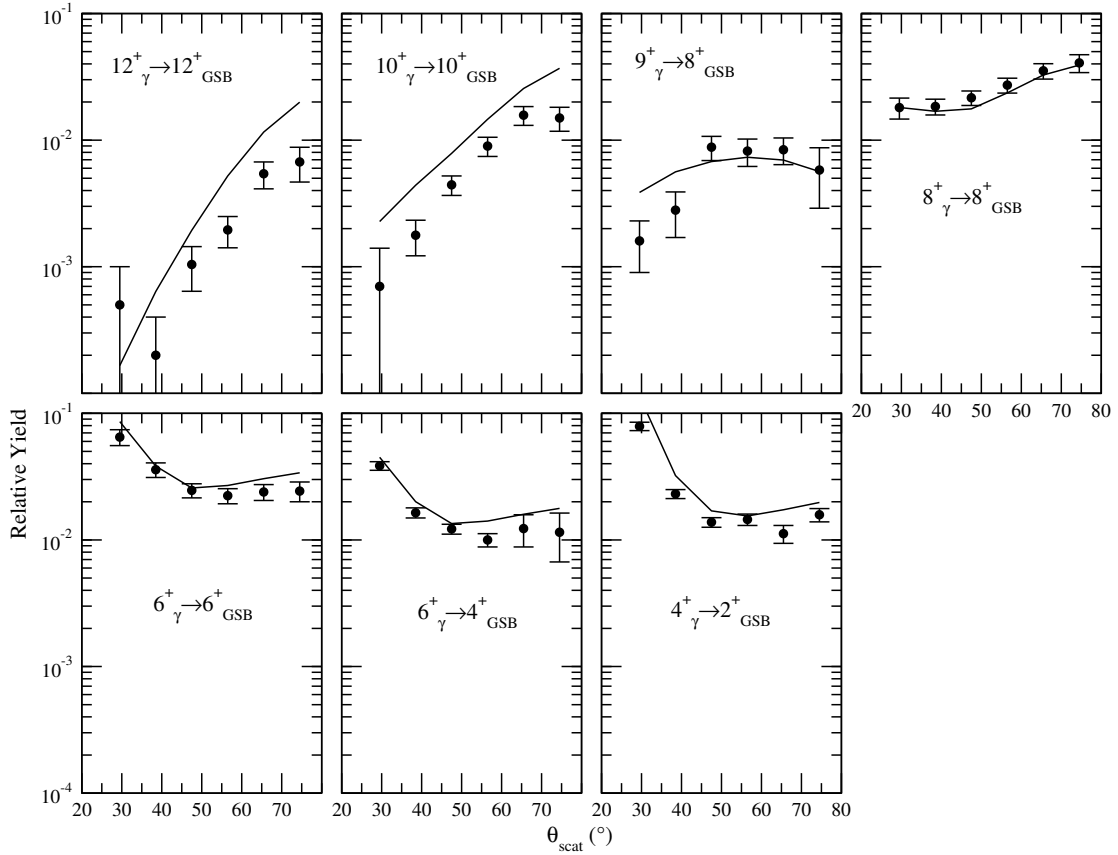
Figure 4-11: Results of the correlated error analysis following the second iteration fit of the γ-band matrix elements (during the 4^+ band fit).

4.3.3   The $K = 4^+$ Band

Initial Values of the Matrix Elements   The E2 and M1 transitions between the GSB ($K = 0^+$) and the $K = 4^+$ band are K-forbidden. The spin-dependent mixing (SDM) model of Bohr an Mottelson was used to couple the reduced matrix elements (Equation 2.24) with an additional Mikhailov term (Equation 4.4). There was sufficient available data for four pairs of intraband and interband ($4^+ \rightarrow$ GSB) decays to make a Mikhailov plot of the $\langle K = 4^+ \mid E2 \mid \text{GSB} \rangle$ matrix element (Figure 4-13). One data point was based on branching ratios from this work, while the others came from branching ratios and mixing ratios previous

77
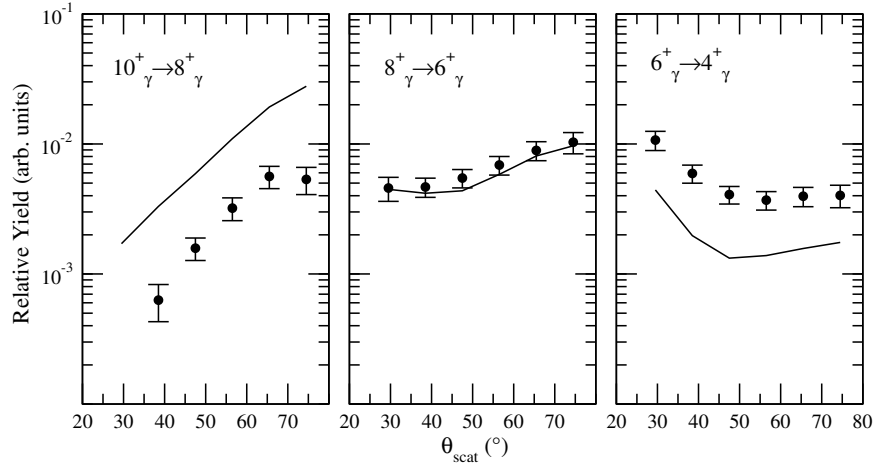
Figure 4-12: Measured and calculated yields after of the second iteration fit of the γ-band matrix elements during the 4^+ band fit, followed by the correlated error analysis.

work [10]. The relations between the reduced transition probabilities $B(E2)$ and the partial γ-decay widths Γ_γ^{E2} and equation 2.10 were used to calculate the values of $B(E2 \downarrow)$.

$$B(E2; K = 4^+ \to K = K_f) = (\frac{5}{16\pi} eQ_o)^2 \langle I_i K 20 \mid I_f^{\text{in-band}} K \rangle^2 (\frac{E_{\text{in}}}{E_{\text{out}}})^5 \frac{\Gamma_{E2}^{\text{out}}}{\Gamma_{E2}^{\text{in}}} \quad (4.5)$$

The widths were calculated using

$$\Gamma_{E2} = \Gamma_{\text{Total}} \frac{\delta^2}{1 + \delta^2} \quad (4.6)$$

and

$$\frac{\Gamma_{E2}^{\text{out}}}{\Gamma_{E2}^{\text{in}}} = \frac{\Gamma_{\text{Total}}^{\text{out}}}{\Gamma_{\text{Total}}^{\text{in}}} \frac{1 + \delta_{\text{in}}^2}{1 + \delta_{\text{out}}^2} \frac{\delta_{\text{out}}^2}{\delta_{\text{in}}^2}. \quad (4.7)$$

The E2 rotational-vibrational coupling in the K-forbidden GSB $\overset{E2}{\to} 4^+$ transitions was calculated from known transition rates [10], giving a very linear ($r = 0.99$) behavior (Figure 4-13) in ΔI^2. With this measured rotational-vibrational coupling, the GSB $\overset{E2}{\to} 4^+$ matrix elements were fit as a single parameter.
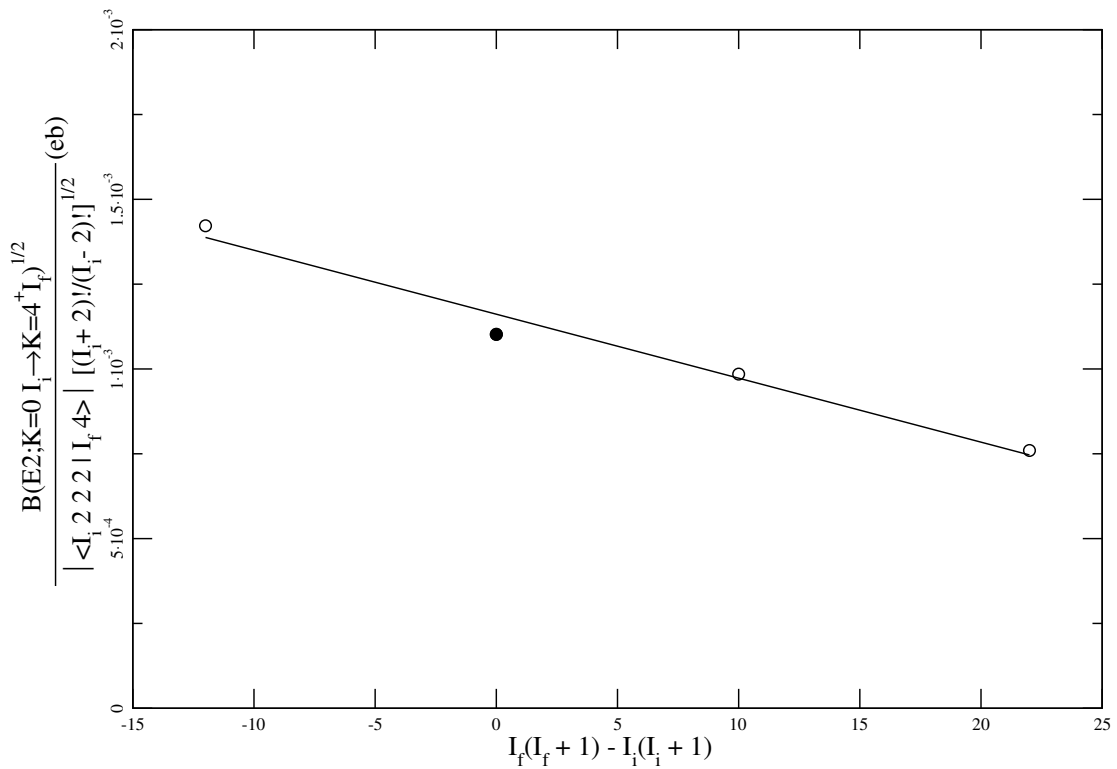
Figure 4-13: A Mikhailov-type plot for the GSB$\rightarrow$ 4^+ transitions. The open circles are from previous work [10] closed circle–this work. The errors are $\approx$ 10%.

In the lower levels of the 4^+ band, the interband decays are known to be predominantly E2 in nature [2, 79]. Starting at about the 7+ level (the uppermost level previously known), the M1 strength in the interband decays begins to compete, but the intraband decays take over at the same time. Interband M1 matrix elements were included, because preliminary fits gave a surprisingly large E2 strength between the γ-band and the 4^+ band, approaching the limit for pure one- and two-phonon γ-vibrational bands [81]. The calculation of the M1 intrinsic matrix element for forbidden transitions between the 4^+ band and the GSB is shown in Figure 4-14. The branching and mixing ratios were taken entirely from other work [10].
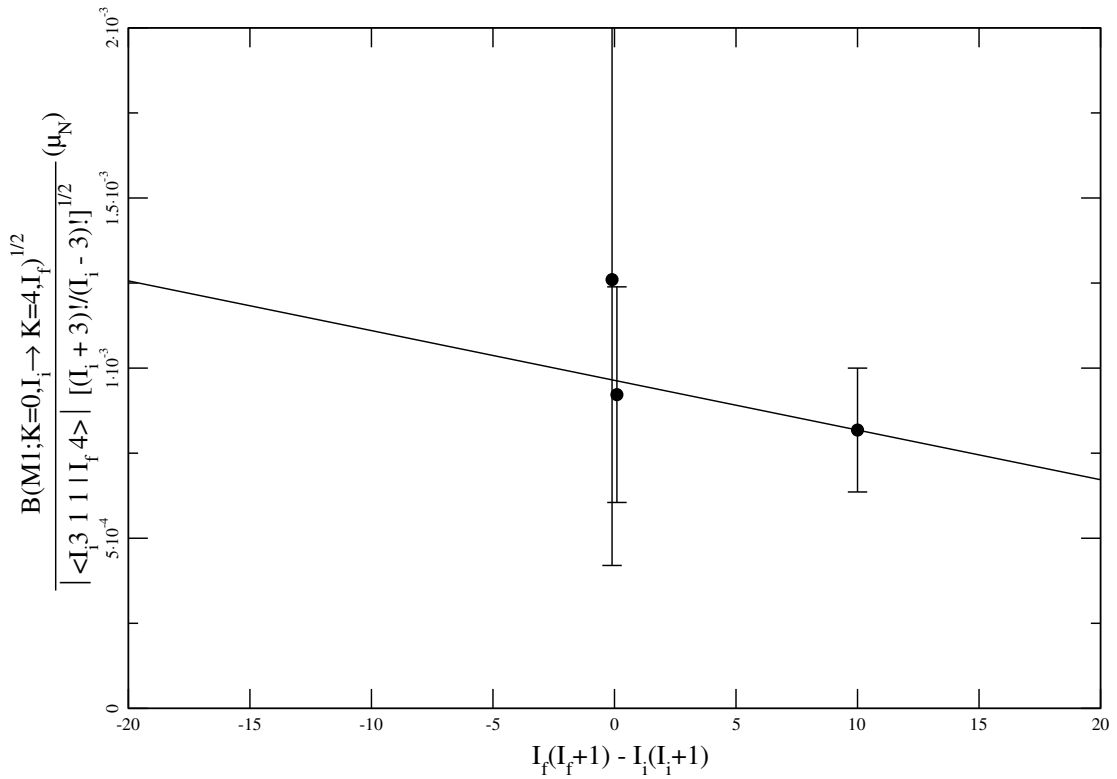
Figure 4-14: A Mikhailov-type plot for the M1 transitions from the GSB to the 4^+ band [10].

Matrix elements connecting the γ-band and the 4^+ band were obtained by similar calculations to those used for the GSB to $K = 4^+$ transitions, however, only three pairs of intraband and interband decays are known [2, 79]. The E2 matrix elements calculated using equation 4.5 were much greater for the two $|\Delta I| < 2$ transitions than for the $|\Delta I| = 2$ transition, indicating that there may be an M1 component. However, the decay branches could not be observed in this experiment, indicating a much smaller M1 component. M1 matrix elements connecting the γ-band and the 4^+ band were not included in the calculations.

The intraband M1 branches in the 4^+ band are more significant than in the γ-band. To calculate the M1 matrix elements, an estimate of $g_K - g_R$ was calculated

from one of the in-band mixing ratios [43]. The mixing ratio can be defined by $\delta^2 \equiv \frac{I_{E2}}{I_{M1}}$ [10], where $I_{M\lambda}$ are the γ-ray intensities of each multipolarity in the decay. Since $\frac{I_{E2}}{I_{M1}} = \frac{\Gamma_{E2}}{\Gamma_{M1}}$, where the $\Gamma_{M\lambda}$ are the partial γ-widths of each multipolarity, the mixing ratio can be written as

$$\delta^2 = \frac{\Gamma_{E2}}{\Gamma_{M1}} = \frac{8.0654 \times 10^{-7} E_{\gamma,MeV}^5 B(E2)_{e^2 fm^4}}{11.575 \times 10^{-3} E_{\gamma,MeV}^3 B(M1)_{\mu_N^2}}. \tag{4.8}$$

Substituting for $B(M\lambda)$ with equations 2.10 and 2.11, and solving for $g_K - g_R$ gives

$$|g_K - g_R| = \frac{0.42711[\sqrt{\frac{5}{16\pi}} eQ_o]_{eb}}{|\delta|} \frac{\langle IK20 \mid I - 1K \rangle}{\langle IK10 \mid I - 1K \rangle} E_{\text{MeV}}. \tag{4.9}$$

The 0.1266 MeV 5^+ to 4^+ transition in the 4^+ band has a known mixing ratio of 0.65(8), giving $|g_K - g_R| = 0.26(3)$ [82]. The M1 matrix elements are given by Equation 2.11.

Intraband E2 matrix elements were calculated assuming the same quadrupole moment as for the GSB, $\sqrt{\frac{5}{16\pi}} eQ_o = 2.174$ eb. In summary, the starting values of the matrix elements are given by the following. Intraband M1 matrix elements were calculated from $g_K - g_R = 0.26(3)$. The γ-band to 4^+ band E2 matrix elements were calculated from an intrinsic matrix element $\langle I_2 K = 4 \mid E2 \mid I_1 K = 2 \rangle = 0.0652$ eb derived from a single known branching ratio. The K-forbidden GSB to 4^+ band E2 matrix elements were calculated according to Equation 2.24 and included the Mikhailov terms (Figure 4-13) $M_1 = 8.2 \times 10^{-4} eb$ and $M_2 = -1.3 \times 10^{-5} eb$ in the intrinsic matrix element. Similarly, the $\nu = 3$ K-forbidden GSB to 4^+ M1 matrix elements were calculated using $M_1 = 9.64 \times 10^{-5} \mu_N$ and $M_2 = -1.46 \times 10^{-6} \mu_N$ (Figure 4-14).

Fit Parameters The three parameters, $\langle K = 4^+ \mid E2 \mid K = 2^+ \rangle$, $\langle K = 4^+ \mid E2 + M1 \mid K = 0^+ \rangle$ (M1 coupled to E2) and $\langle K = 2^+ \mid E2 \mid K = 0^+ \rangle$ were varied in the χ^2 search. Intraband matrix elements were not varied, because a lack of sensitivity to the intraband matrix elements would prevent the fit from converging.

81

Data Set The γ-ray triples data were included for 8 intraband lines and 3 interband decays to the GSB in the $9°$ bins mentioned above, using the same weight for each angular bin as in the previous data sets. All of the data used are shown in the plots of the fit results.

Results The value of χ^2 was minimized for two separate cases: for *destructive* interference between the $\langle K = 4^+ \mid E2 \mid K = 2^+ \rangle$ path and the $\langle K = 4^+ \mid E2 + M1 \mid K = 0^+ \rangle$ path, giving $\chi^2 = 0.83$, and for *constructive* interference between these two paths, giving $\chi^2 = 1.09$ (Figures 4-15 and 4-16). The relative phases of the $\langle K = 4^+ \mid E2 \mid K = 2^+ \rangle$ and $\langle K = 4^+ \mid E2 + M1 \mid K = 0^+ \rangle$ intrinsic matrix elements can not be determined solely from the small difference in the χ^2 values. The best choice of phase is explained in Chapter 9. The matrix elements determined by the fit are summarized in Tables 9.5 through 9.13.

4.3.4 Conclusions from the $K \leq 4$ Bands

The following general conclusions from the successful reproduction of the experimental yields for the $K = 0, 2$ and 4 bands were used as a guide to fitting the higher-K bands.

1. The ^{178}Hf nucleus behaves like a rigid rotor, in terms of the quadrupole moment. The value of eQ_0 is nearly constant in the GSB at 2.164(10) eb, with deviations of $\leq 1.5\%$ between the ground state and the 18^+ state.

2. Measurements of the matrix elements for K-allowed transitions between the GSB, the γ-band and the 4^+ band reproduce the data well. This verifies that the Alaga rule and the Mikhailov coupling terms are sufficient for describing the K-allowed matrix elements in the analysis of high-K bands, i.e. the 6^+ band.
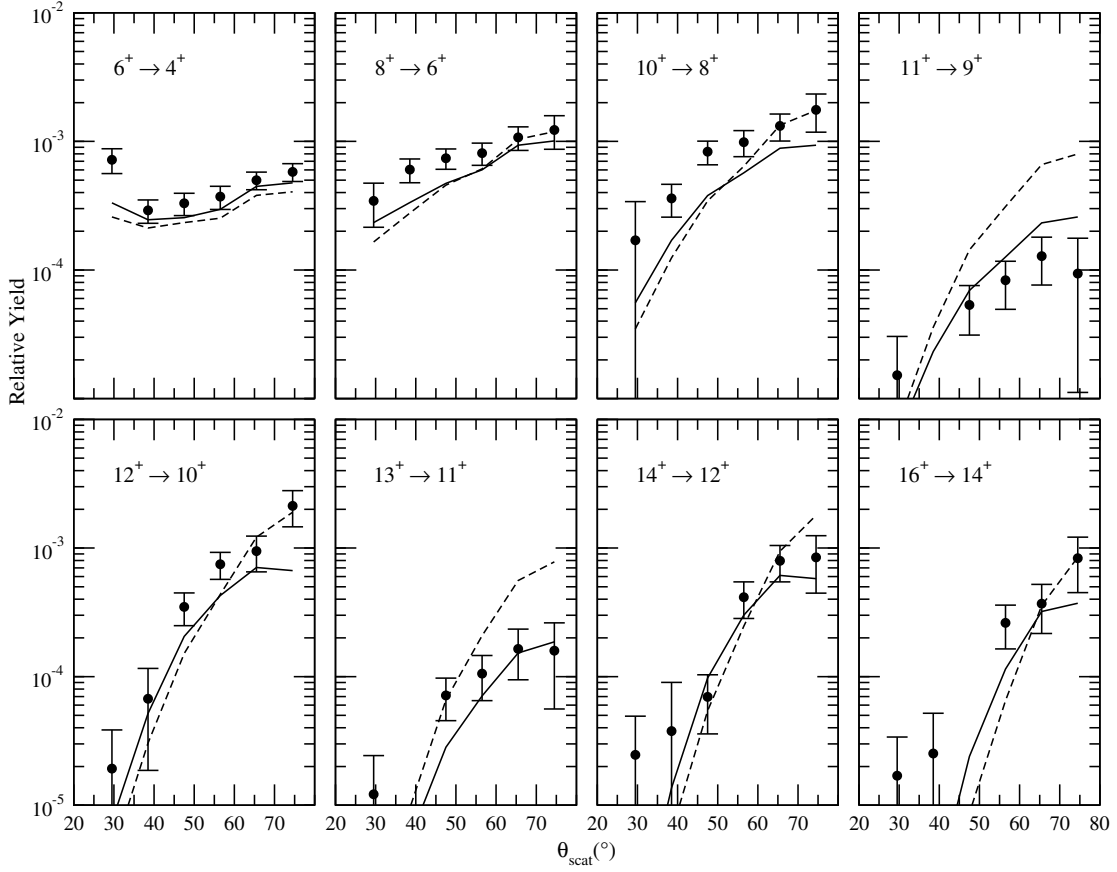
Figure 4-15: Measured and calculated $K^{\pi} = 4^+$ intraband yields showing interference effects. The two possible phases of the $K = 2^+ \rightarrow K = 4^+$ and $K = 0^+ \rightarrow K = 4^+$ intrinsic matrix elements are shown by the solid and dashed lines.

3. The SDM matrix elements were successful in the Coulomb excitation calculations for the population of the 4^+ band from the GSB, showing that the model is useful for low-K and low spin. Obviously, the $\sqrt{\frac{(I_1 - K_1)!(I_1 + K_1 + n)!}{(I_1 - K_1 - n)!(I_1 + K_1)!}}$ term in equation 2.24 will behave pathologically for high spin where the perturbation breaks down. As long as the calculations are restricted to levels having spin I not large compared to K, the SDM description will predict physically reasonable matrix elements. This will be seen to be the case for the 6^+ isomer band.
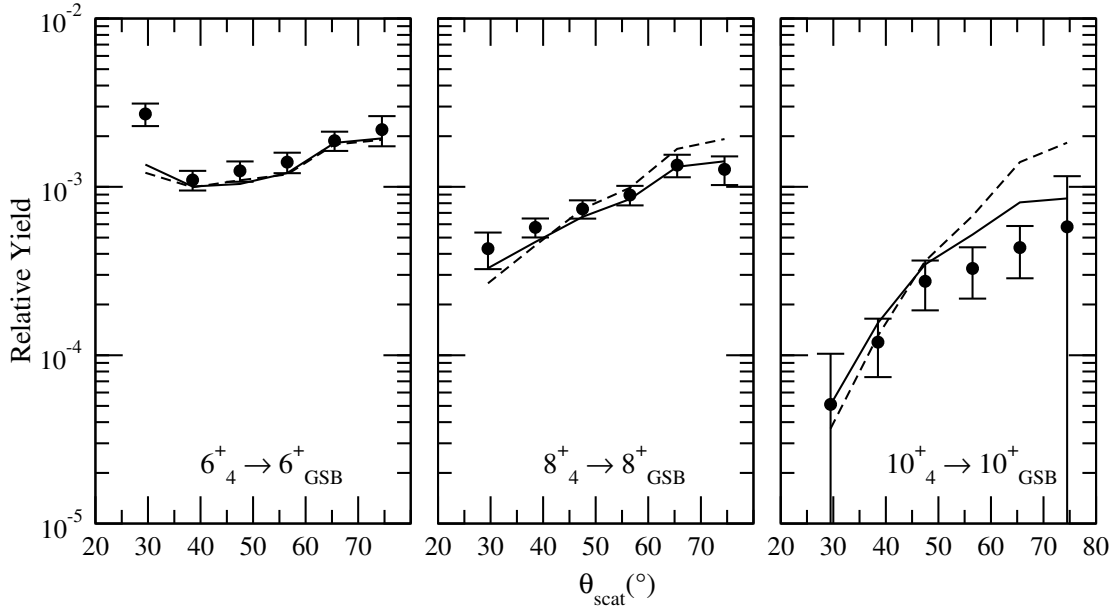
Figure 4-16: Measured and calculated interband yields for the 4^+ band. The two possible phases of the $K = 2^+ \to K = 4^+$ and $K = 0^+ \to K = 4^+$ intrinsic matrix elements are shown by the solid and dashed lines.

4. Coulomb excitation calculations verified that the addition of bands with populations of the order of 10^{-4} does not have a large effect on the measurements of the matrix elements. Consequently, the calculations for the $K > 4$ bands can be treated as small perturbations, and the iterative fitting procedure is not necessary for the isomer bands.

4.3.5   The $K^\pi = 8_1^-, 8_2^-$ Bands

Many coupling schemes were evaluated in fitting matrix elements to reproduce the prompt online yield data of the 8^- bands. The experimental data were reproduced most accurately and with the lowest $B(E3)$ values by two-step excitations to both 8^- bands through the γ-band in conjunction with single-step excitations from the GSB, both using Alaga rule coupling systematics. (The strong mixing between the two 8^- bands (Chapter 9) indicates the need to include both 8^- bands
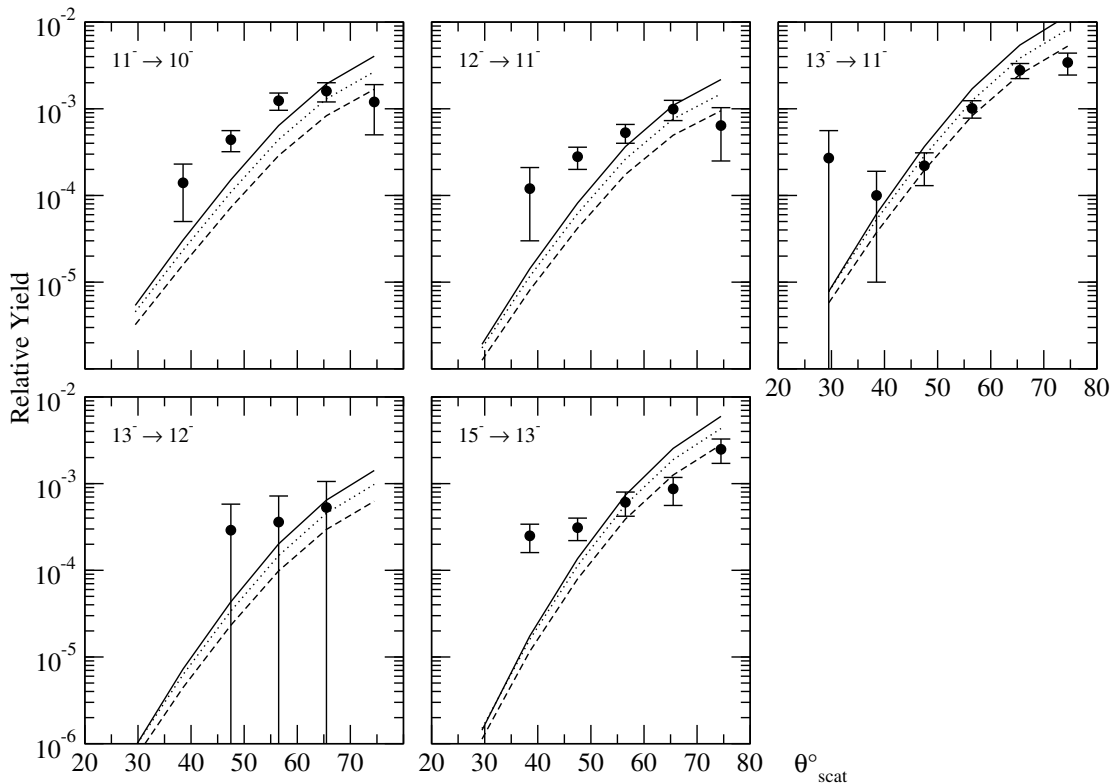
Figure 4-17: Intraband yields of the 8^- isomer band. Calculated yields from the best fit, showing the total calculation (solid line), calculation for the γ-band$\rightarrow 8^-$ path only (dotted line) and the calculation for the GSB$\rightarrow 8^-$ path only (dashed line).

in the Coulomb excitation calculations.) The yields reproduced from the best fit and the experimental data are shown for the 8^- isomer band (Figure 4-17) and for the interband feeding from the upper 8^- band at 1479 keV, the "8_2^-" band, to the 8^- isomer band (Figure 4-18).

Models and Fits

Coupling Systematics   In evaluating the models and coupling schemes available, among the physical grounds for eliminating some were large discontinuities in the matrix element as a function of spin, and large $B(E3)$ values. The principal
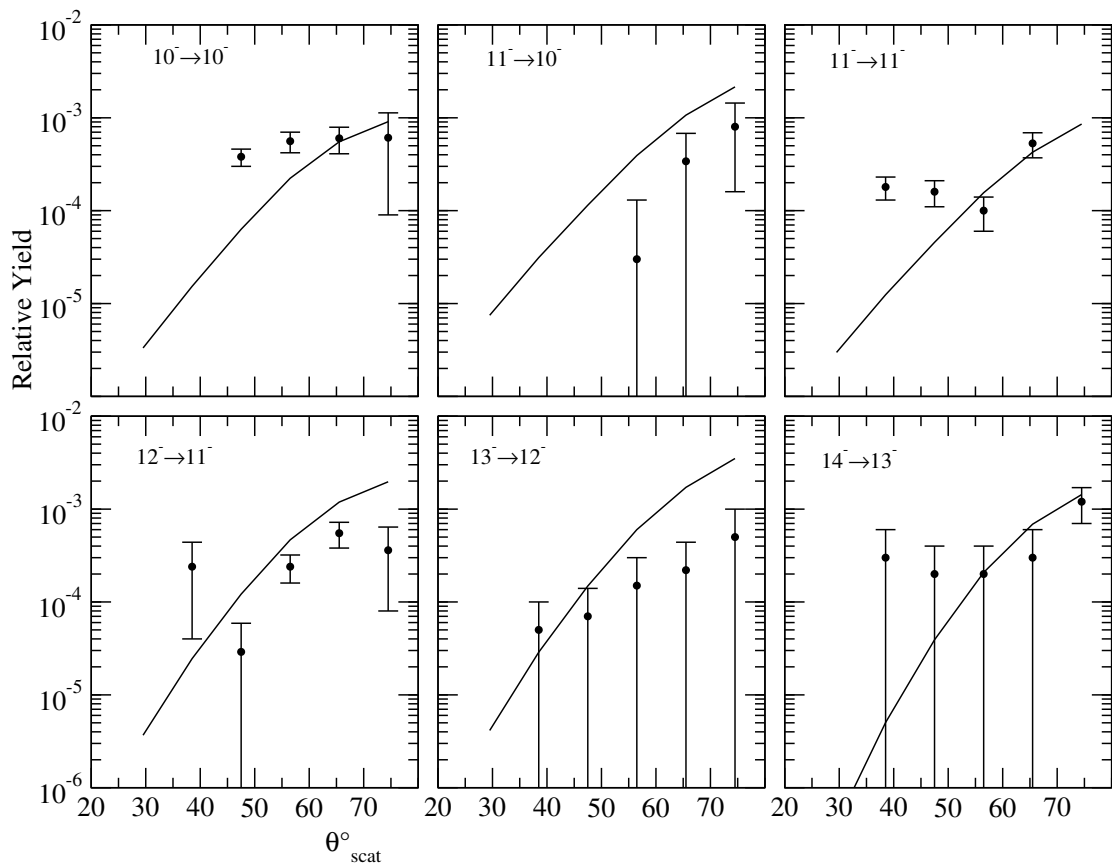
Figure 4-18: Interband yields for γ-decays from the upper 8^- band at 1479 keV to the 8^- isomer band. The calculated yields from the best fit are shown (solid line).

systematics which were evaluated are described below, beginning with those that were eliminated and ending with the model which gave the best result, a $K = 5$ admixture coupling the GSB and the γ-band to both 8^- bands.

Only strongly populated bands with yields of the order of 10^{-2} or greater (i.e. the GSB and the γ-band) are good candidates for populating the 8^- bands. Excitation through bands populated to the $\sim 10^{-4}$ level (e.g. the (upper) 4^+ band and the 6^+ band would require very large transition probabilities to the 8^- bands. This would also lead to a depletion of the population strength of the intermediate

bands. For instance, calculations showed that population of the 8^- isomer band through the 6^+ isomer band with transition probabilities of ~ 1 W.u. reproduced only $\sim 10^{-6}$ of the measured yield.

Since, for a non-zero E1 or E3 moment the isomer can decay to the 8^+_{GSB} level, and for a non-zero E3 moment to the 6^+_{GSB} level, its long lifetime ($t_{1/2} = 4s$) puts a very small upper limit on the E1 and E3 matrix elements that can populate the 8^- state from the GSB. Consequently, if it is not possible to populate the 8^- bands to the measured level without a strong GSB contribution the band head must be quite pure in K, and K-mixing must occur either above the band head in the 8^- band, or in lower-K bands. Two things suggest the latter: Features in the alignment of the GSB and the γ-band suggest that the low-K bands will become strongly mixed at moderate spin, $I \approx 10$ in the case of the GSB and $I \approx 8$ in the case of the γ-band (Figure 8-5). If mixing in the high-K bands is important, then it must enter into the problem very abruptly above the band head, because the long lifetime of the 8^- isomer indicates that it is quite pure. The nearly constant moment of inertia of the 8^- bands does not indicate a sudden onset of mixing.

The SDM description used successfully in explaining the population of the 6^+ isomer band must be expected to fail for some large value of K where the perturbation will break down and predict unreasonably large transition probabilities. The SDM model has the advantage that it predicts less population staggering between the odd- and even-spin levels than other models, in agreement with the experimental data. The SDM model predicts a significantly greater slope $\frac{dY}{d\theta}$ of the yield as a function of scattering angle.

Several models can be conceived which represent a sum of many K-admixtures, each using the Alaga rule systematics. This leads to a set of matrix elements very similar in strength for all transitions. The matrix elements must be forced to fall off for low spin in the case of the GSB$\rightarrow 8^-$ band excitations to preserve the lifetime. When the matrix elements from many admixtures are summed,

the variation between the magnitudes of the reduced matrix elements is reduced. As the $B(E3)$ values converge toward a constant value for all transitions, the isomer cross section increases dramatically. This includes the "RMS" systematic, where the reduced matrix elements are set to a constant value for all transitions, mathematically equivalent to a root-mean-square sum of all possible K admixtures in the low-K band.

A single admixture model was also considered, using a single set of Alaga-coupled matrix elements. In the simplest conceivable scenario, one band contains a single important admixture K', so that $\lambda \geq \mid K' - K \mid$, where λ is the multipolarity of transitions populating the isomer band and K refers to the pure band. If the identity of the impure band is not suspected to be the GSB, one mixing scenario stands out as an interesting candidate, a $K = 0^-$ admixture in the 8^- band [30]. In this case the coupling is from $K = 0^+$ to $K = 0^-$, and only the natural parity states ($I^\pi = 9^-, 11^-$, etc.) are coupled to the low-K band with non-zero matrix elements, eliminating the need to impose an upper limit on matrix elements connecting to the 8^- state to preserve the lifetime. However, the $K = 0^-$ hypothesis, which requires 4 times larger $B(E3)$ values than other admixtures, and all other admixtures in the 8^- bands, were given less credence than admixtures in the low-K bands, as discussed below.

Other single admixtures were evaluated. Since the mixing appears to be in the GSB primarily–though not necessarily exclusively–from the alignment of the low-K bands, the $K = 5$ admixture is likely to be the lowest-K admixture to become important in populating the isomer band by E3 transitions.

Alignment of the γ-band occurs at low spin—γ-vibrations are by definition a breaking of axial symmetry, leading to K-mixing—suggesting that higher-K admixtures may even be found in the γ-band with greater amplitude than in the GSB (Figure 8-5), as evidenced by the population paths determined for the 6^+ isomer band. Coulomb excitation calculations showed that the particular K-

admixture $(5^+, 6^+, \ldots)$ in the low-K band was of secondary importance, compared to the beam and target parameters, the average $B(E3)$ strength, etc.

No theory exists to suggest a suitable attenuation at low-spin to represent the onset of mixing in the low-K band, keeping the cross section from growing unreasonably large compared to the 6^+ and 16^+ isomers, and preserving the lifetime. (Any significant population of the 8^- state from the GSB would affect the lifetime by orders of magnitude.) So, an attenuation function with decreasing spin in the low-K band, approximately an order of magnitude per unit $\hbar$, was applied to the usual Alaga rule. The long lifetime of the isomer indicates that higher K $(5 \leq K \leq 11)$ admixtures are found at higher spin in the GSB (and presumably in the γ-band, judging from the alignment). Lower values of K are expected to enter the GSB wave functions first (Chapter 10), so the $K = 5^+$ admixture was preferred, but all admixtures produce very similar calculated yields and $B(E3)$ strengths.

Multipole Order   Coulomb excitation calculations showed that population by E1 transitions, even where feeding transitions into the 8^- band have $E_\gamma \approx 300\,\mathrm{keV}$, is dominated ($\geq 90\%$) by γ-decay feeding. E1 transitions with reduced transition strengths of the order of 10^{-3} W.u. (compared to known values in the region, *e.g.* $\approx 10^{-3}$ W.u. in ^{178}Hf [83, 84], $\approx 10^{-5}$ W.u. in ^{178}W [83] and ^{179}W [85]) could populate the 8^- bands to the measured levels from the GSB. Population via E1 transitions from the γ-band is similar. Table 4.1 gives the measured upper limits of feeding into the 8^- band, while no γ-ray peaks can be found for any GSB$\rightarrow 8^-$ transitions. The small upper limits rule out any significant E1 contribution to population of the 8^- bands.

A set of extremely large E5 matrix elements, 1 W.u. for the $9_8^- \rightarrow 4_{\mathrm{GSB}}^+$ transition predicted 8^- band yields that were more than 3 orders of magnitude too small, ruling out the possibility of any significant E5 contribution. E3 transitions

Feeding Transition	In-Band Transition	E1 Feeding Upper Limit (%)
$14^{+}_{\mathrm{GSB}} \to 13^{-}_{K=8}$	$15^{-} \to 13^{-}$	2.4
$12^{+}_{\mathrm{GSB}} \to 11^{-}_{K=8}$	$13^{-} \to 11^{-}$	3.9
$14^{+}_{\gamma} \to 13^{-}_{K=8}$	$15^{-} \to 13^{-}$	6.2
$13^{+}_{\gamma} \to 12^{-}_{K=8}$	$13^{-} \to 12^{-}$	45*
$12^{+}_{\gamma} \to 11^{-}_{K=8}$	$13^{-} \to 11^{-}$	3.1
$11^{+}_{\gamma} \to 10^{-}_{K=8}$	$11^{-} \to 10^{-}$	11

Table 4.1: Experimental upper limits on feeding strength into the 8^{-} isomer band taken over the angular range $25° \leq \theta \leq 80°$. *The $13^{-} \to 12^{-}$ $\Delta I = 1$ in-band transition has $< 20\%$ of the strength of the $13^{-} \to 11^{-}$ branch at $\theta_{\mathrm{scat}} = 65.5°$, and only the upper limit of its yield can be measured.

appear to be the only viable solution for populating the 8^{-} bands from low-K bands. A small E1 contribution of $\sim 5\%$ can not be discounted.

Fit Parameters

Fixed Parameters   Several parameters with measured values which were more precise than usually can be measured by χ^{2} fitting in the present data set were fixed at the start of the fit procedure. This reduced the number of adjustable parameters and usually allowed for a fit in two parameters of primary interest.

Intraband M1 moments and interband E2 and M1 intrinsic matrix elements connecting the two 8^{-} bands were derived from the data of Smith [5] and Mullins [58, 9]. These values were preferred over older published values [6, 86], because of the high precision of the branching ratios in the Smith and Mullins data. Intraband M1 matrix elements were calculated from the gyromagnetic ratio $g_{K} - g_{R} = 0.51(5)$ derived from the ratio of intraband $\Delta I = 1$ and $\Delta I = 2$ γ-intensities. The quadrupole moment was assumed to be the same as that of the

GSB. A value of $g_K - g_R = 0.32(4)$ was calculated for the second 8^- band from branching ratios of Mullins [9].

An interband intrinsic matrix element of $\langle K = 8_2^- \mid E2 \mid K = 8_1^- \rangle = 0.17(3)$ eb was calculated from the only known ratio of intraband/interband E2 γ-intensities for the 8^- bands [5]. This allowed an accurate calculation of $\langle K = 8_2^- \mid M1 \mid K = 8_1^- \rangle = 1.10(6)\mu_N$ using branching data of the levels in the 8_2^- band.

Adjustable Parameters The limited data on the second 8^- band necessitated locking some pairs of intrinsic matrix elements as a single parameter, namely $\langle 8_1^- \mid E3 \mid \text{GSB} \rangle$, $\langle 8_2^- \mid E3 \mid \text{GSB} \rangle$ as one parameter and $\langle 8_1^- \mid E3 \mid \gamma \rangle$, $\langle 8_2^- \mid E3 \mid \gamma \rangle$ as a second parameter. Both 8^- bands were populated to approximately equal levels, so within the precision of the measured yields of the 8^- band, this is a good approximation. Intraband and interband E2 and M1 matrix elements were held constant in the fit, at the values derived above.

Results and Discussion

The criterial characteristics of the three systematics described above are summarized in Table 4.2. The single-admixture model gave the best agreement in terms of intraband γ-ray yields, isomer cross section and reasonable $B(E3)$ strengths. The $K = 5$ admixture is the focus of the discussion because it is likely the strongest admixture to be found at low spin (compared to $K = 6, 7, \ldots, 11$), but similar results were found for other single admixtures.

Fitting the measured intraband yields with the SDM model more accurately reproduced the absence of population staggering between odd and even spin levels in the isomer band data, whereas fits of an intrinsic matrix element in the Alaga rule produced more staggering, regardless of the particular admixture used. However, the SDM model fails in the case of the 8^- band, because the high degree of
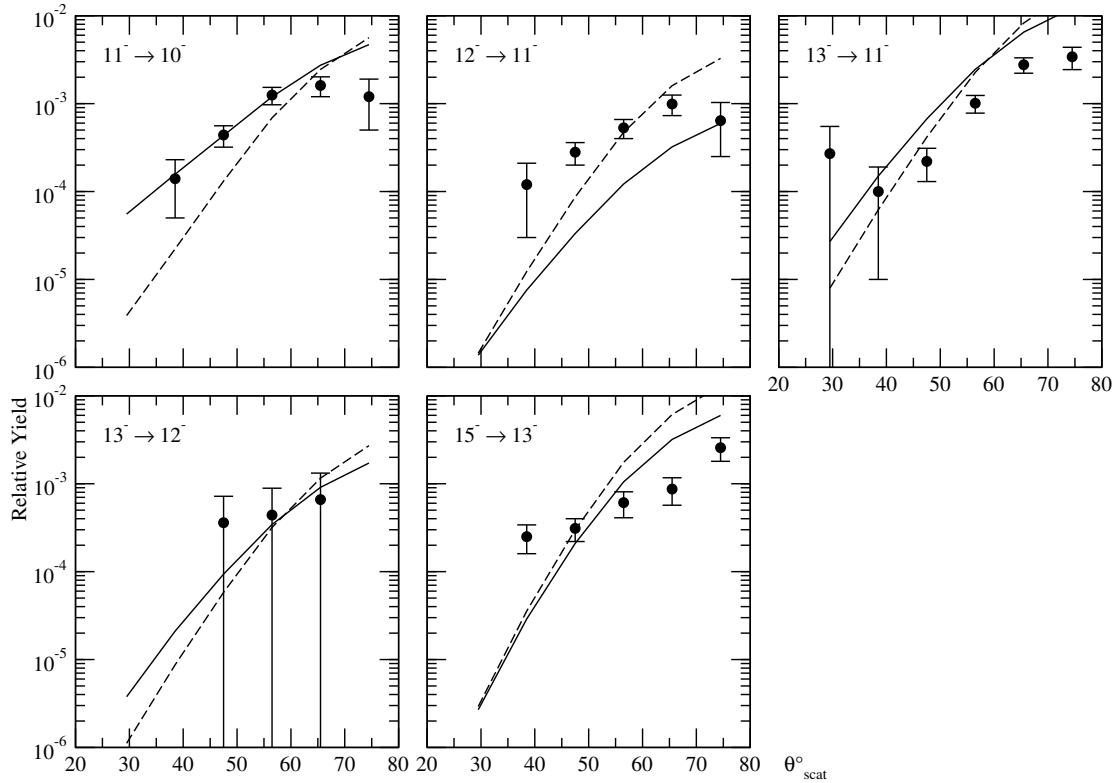
Figure 4-19: In-band yields of the 8^- isomer band. Calculated yields for a $K = 5$ admixture in the GSB (solid line) and for the SDM model (dashed line), both including only one of the two 8^- bands.

forbiddenness causes some matrix elements to explode at high spin, taking values of ~ 100 W.u. to reproduce the measured yields. The slope of yield versus scattering angle is predicted to be too high by the SDM model, about three times higher than with the Alaga rule calculations (Figure 4-19).

The multiple admixture models using Alaga systematics for each admixture produced similar results to the single admixtures, but an unrealistically high cross section. This includes the RMS systematic, which gave a cross section $\sigma_{8^-} = 41$ mb ($25° \leq \theta_{scat} \leq 80°$) in the present experiment, compared to those calculated from the results of the analyses of the 6^+ and 16^+ isomers, 6.4 mb and 4.4 mb, respectively.

92

	Benefits	Problems
Alaga Rule	Matrix elements well-behaved.	Requires attenuation of $B(E3)$ at low spin.
	Yield vs. θ slope is correct.	
RMS Sum of Alaga Terms	Yield vs. θ slope is correct.	Predicts very high isomer cross section.
	Matrix elements well-behaved.	Requires attenuation of $B(E3)$ at low spin.
SDM Model	Naturally small matrix elements at band head.	Still requires attenuation of $B(E3)$ at low spin.
	Less population staggering.	Yield vs. θ $3\times$ too steep.
		Matrix elements explode for $K = 8$.

Table 4.2: Notable features of the coupling models evaluated for the 8^- band.

The single admixture fits produced very similar $B(E3)$ values and fit results to the multiple admixture model and a more reasonable calculated cross section for the isomer, $\sigma_{8^-} = 18$ mb in the present experiment. Fits for $K = 5$ admixtures in the GSB and the γ-band seem to be the most appealing physically, while the yields and cross sections do not vary dramatically for other admixtures. Results for the $K = 0^-$ and $K = 5^+$ admixtures are described below.

For a $K = 0^-$ admixture in the 8^- band, the best agreement with the yield data resulted from an intrinsic matrix element of $\langle K = 0^- \mid E3 \mid K = 0^+ \rangle = 0.33(4)$ eb$^{3/2}$ and reasonable reduced transition probabilities of $1.4 \leq B(E3) \leq 3.1$ W.u. As described above, the idea of a $K = 0^-$ admixture in the 8^- bands

seems unlikely, because it implies a very sudden onset of mixing with increasing rotational frequency in the 8^- band, whereas the alignment of the 8^- band does not seem to occur below the 14^- level.

When the second 8^- band at 1479 keV was included in the calculations, γ-decay feeding from the second 8^- band to the 8^- isomer band reduced the staggering, so that the Alaga rule fits, including those for the $K = 5^+$ admixtures in the low-K bands, gave good results. Allowing population from both the GSB and the γ-band reduced the $B(E3)$ strength required from each band.

In the χ^2 fits, two parameters, one representing the γ-band contribution and one representing the GSB contribution, were adjusted in a χ^2 fit, giving $\langle 8^- \mid E3 \mid \gamma \rangle = 0.36^{+0.00}_{-0.06}$ eb$^{3/2}$ and $\langle 8^-_1 \mid E3 \mid \text{GSB} \rangle = 0.37^{+0.07}_{-0.01}$ eb$^{3/2}$. From these parameters and the forced attenuation at low spin, the Alaga rule gives matrix elements which range from 10^{-4} to 4 W.u. for the GSB connections, except for the very small $\langle I_{8^-} \| E3 \| 6^+_0 \rangle$ and $\langle I_{8^-} \| E3 \| 8^+_0 \rangle$ matrix elements, effectively zero (Figure 4-20). $B(E3)$ values for the γ-band$\rightarrow 8^-$ band transitions ranged from 7×10^{-4} to 4 W.u. (Figure 4-21) with the attenuation at low spin.

Nuclei with $N \approx 100$ have typical octupole strengths closer to 1 W.u. for the $3^-_1 \rightarrow 0^+_1$ transitions, and octupole moments are believed to be more collective than single particle in nature [87], so that there should be some similarity with the neighbors. However, the average strength is about 1 W.u. for the γ-band connections and the GSB connections, in line with values for neighboring nuclei. In ^{208}Pb $B(E3 \downarrow)$ values of about 46 W.u. have also been measured [88], and the strength of the $3^-_2 \rightarrow 0^+_\text{GSB}$ transition in ^{178}Hf has been measured at 4 W.u. [89], so the maximum values here of $\lesssim 4$ W.u. are not unreasonably large. Since the calculated yields are not extremely sensitive to reduction of the few matrix elements with $B(E3) \approx 4$ W.u., additional data might in fact show that the largest matrix elements (by the Alaga rule with $K = 5$) are actually smaller.

Figures 4-17 and 4-18 show the agreement between the measured and calcu-
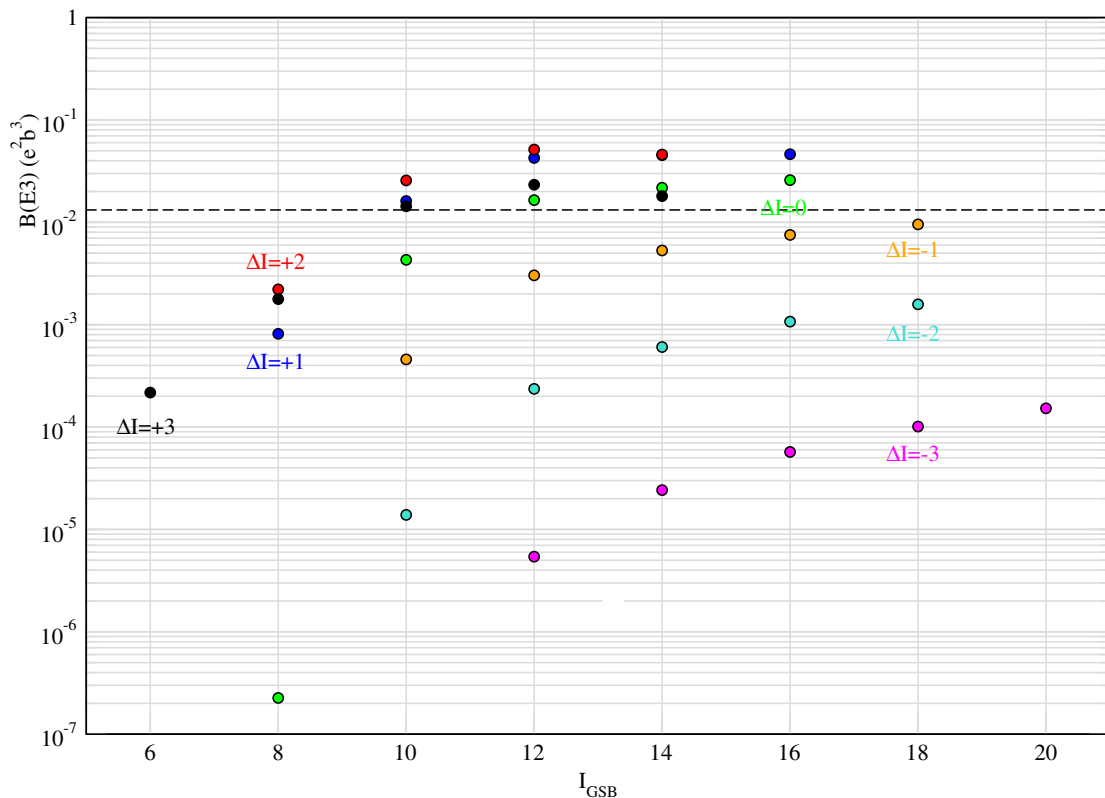
Figure 4-20: $B(E3)$ values of the transitions populating the 8^- bands from the GSB in the best fit described in the text. $\Delta I \equiv I_{8^-} - I_{\text{GSB}}$. The dashed line represents the Weisskopf unit in the *upward* direction, $B(E3; 0^+ \to 3^-)_W = 0.0132$ e^2b^2.

lated 8^- bands yields. The calculated yields for the $K = 5$ admixture put an upper limit on population of the 8^- bands by γ-decay feeding from the low-K bands of $\lesssim 10^{-5}$ of the 8^- band yields.

Conclusions from the 8^- Band Analysis

Calculations using the Alaga rule with $K = 5$ admixtures in the GSB and γ-band and including both 8^- bands connected to both the γ- and GS bands gave the best reproduction of the yields of the two 8^- bands. A $K = 5$ admixture was postulated, rather than $K = 6, 7, \ldots$, because the lower-K admixtures are
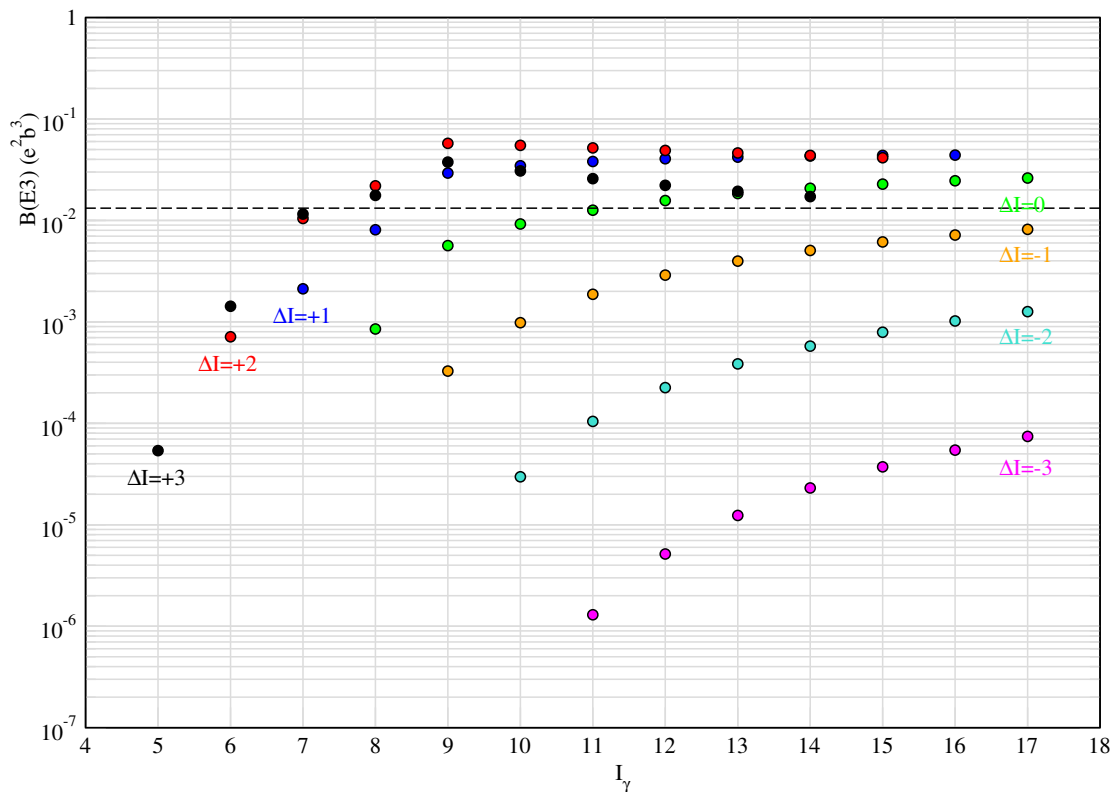
Figure 4-21: $B(E3)$ values of the transitions populating the 8^- bands from the γ-band in the best fit described in the text. $\Delta I \equiv I_{8^-} - I_\gamma$. The dashed line represents the Weisskopf unit in the *upward* direction, $B(E3; 0^+ \to 3^-)_W = 0.0132$ e^2b^2.

expected to be found with greater amplitude and at lower spin than higher-K admixtures. Other K admixtures give very similar results, so that the same general conclusions would be drawn from any postulated admixture. The small population staggering between the natural and unnatural parity states is reproduced, whereas Alaga rule calculations which do not include both 8^- bands greatly overpredict the population staggering. The Coulomb excitations calculations indicate that γ-decay feeding from the upper 8^- band to the 8^- isomer band has a strong effect in reducing the calculated odd-even spin population staggering to better agree with the data (Figure 4-17).

From the χ^2 fit, the population was calculated to be $\approx 50\%$–60% from the γ-band, depending on the scattering angular range. Figure 4-22 shows the principal population paths from the GSB, indicating that with the particular attenuation chosen for the fit (Figures 4-20 and 4-21), the GSB 10^+ level is responsible for the largest fraction of the population. (This is actually quite independent of the particular model chosen and is mostly determined by the experimental parameters, beam energy etc.) The $10^+_{\mathrm{GSB}} \rightarrow 12^-_{K=8}$ and $10^+_{\mathrm{GSB}} \rightarrow 13^-_{K=8}$ excitations are the most effective, with excitation of the unnatural parity 12^- state competing because of the 4 times greater $B(E3)$ value of the Alaga rule systematics for $K = 5$ to $K = 8$ coupling.

Hamilton [29] and Xie [30] have measured the probability of exciting the 8^- isomer from the ground state by various Coulomb excitation experiments. Xie *et al.* measured a lower cross section than Hamilton *et al.*, and calculations of the cross sections for these two experiments based on the matrix elements from the present work lie between the measurements of Hamilton and Xie, as shown below.

The Hamilton Experiment Hamilton *et al.* achieved the first Coulomb excitation of the $K = 8^-$ isomer in a 35 mg/cm^2 ^{178}Hf target with 594 MeV ^{136}Xe ions. By comparing the beam-off γ-ray yield of the GSB $8^+ \rightarrow 6^+$ transition to the beam-on yield, the isomer population was measured relative to the 8^+_{GSB} yield at "$\approx 0.9\%$" (Table 4.3). The best fit to the present data set was used to simulate the Hamilton experiment, integrating over 4π sr scattering and from the incident beam energy of 594 MeV to 0 MeV. This integration with the best fit matrix elements gives a relative isomer decay feed of 0.5%.

The Xie Experiment Bombarding a 0.5 mg/cm^2 ^{178}Hf target with ^{130}Te beams at 560 MeV, 590 MeV and 620 MeV, Xie *et al.* confirmed the Hamilton group's Coulomb excitation of the 8^- isomer, but measured smaller excitation probabilities than in the Hamilton experiment. Delayed GSB γ-ray yields were counted, and
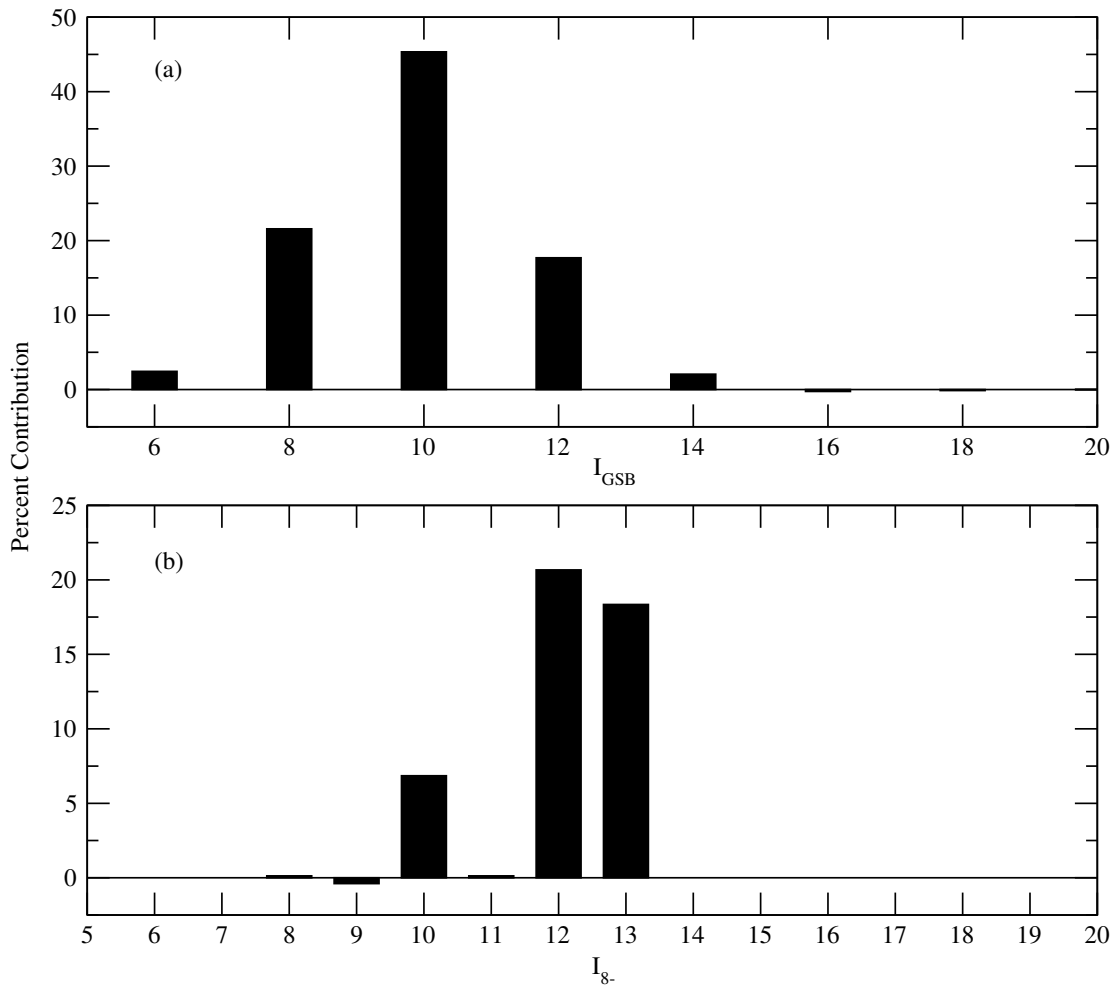
Figure 4-22: The percent contribution of each GSB level (a) and each matrix element $\langle I_{8^-} \| E3 \| I_{\mathrm{GSB}} = 10^+ \rangle$ (b) to the total 8^- isomer population. Calculated from the best fit using the $K = 5$ admixture and the Alaga rule for $\theta_{\mathrm{scat}} = 47.5°$.

the absolute isomer cross sections were measured (Table 4.3). A simulation of the Xie experiment based on the matrix elements obtained in the present experiment gives a cross section σ_{8^-} 5–6 times larger than the Xie measurement.

The present set of model-dependent matrix elements give a good reproduction of the experimental yields with $\chi^2 \approx 1.6$. Comparison with the previous Coulomb excitation results for the isomer shows that the current result lies between those

	Xie *et al.* Cross sections (mb)			Hamilton *et al.* Intensity ratio $\frac{\left(8^+_{\mathrm{GSB}}\to 6^+_{\mathrm{GSB}}\right)_{\mathrm{delayed}}}{\left(8^+_{\mathrm{GSB}}\to 6^+_{\mathrm{GSB}}\right)_{\mathrm{total}}}$
Expt.	^{178}Hf(^{130}Te,^{130}Te)^{178}Hf thin target			^{178}Hf(^{136}Xe,^{136}Xe)^{178}Hf
	560 MeV	590 MeV	620 MeV	Thick target, 594 MeV
Meas.	$2.7\,^{+1.9}_{-1.4}$	$4.3\,^{+3.4}_{-2.0}$	$7.5\,^{+6.1}_{-3.2}$	$\approx 0.9\%$
Calc.	15.7	25.3	37.6	0.5%
$\frac{\mathrm{Calc.}}{\mathrm{Meas.}}$	5.8	5.9	5.0	0.6

Table 4.3: Comparison of predicted 8^- isomer population with the measurements of Xie *et al.* and Hamilton *et al.* The experiments are explained in the text.

of the Xie and Hamilton experiments, while better agreement is found with the Hamilton result.

4.3.6 The $K^\pi = 16^+$ Isomer Band

The first analysis of the 16^+ isomer band was based on a single set of triples yields for the $19^+_{16} \to 18^+_{16}$ transition, in three angular bins (Figure 4-23). The analysis of the 8^- bands showed that there is insufficient population of most of the side bands (*e.g.* the 4^+, 6^+ bands, populated at the 10^{-3} to 10^{-4} level) to populate the high-K isomer bands by multi-step Coulomb excitations.

Two K-mixing descriptions were tested, one using the Alaga rule with a single $K = 2$ admixture in the 16^+ band, and one using the SDM systematics, both in one-parameter fits. The matrix elements following the Alaga rule for the GSB$\to$ 16^+ E2 path could not populate the 16^+ band sufficiently (Fig. 4-23) without exceeding measured upper limits on GSB$\to 16^+$ γ-ray feeding.

The SDM systematics were able to simultaneously reproduce the observed yields (Figure 4-23) with realistic $B(E2)$ values and satisfy the upper limits on γ-decay feeding from the GSB, which were measured at $\sim 10^{-4}$ for safe scattering
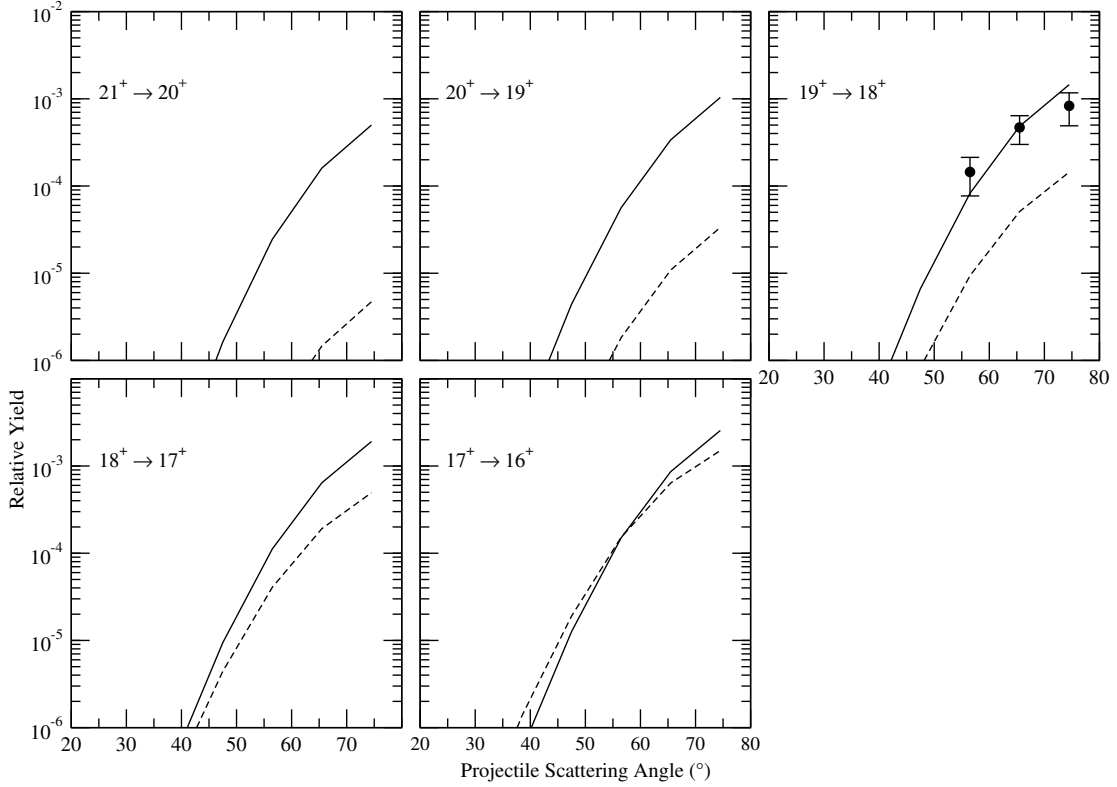
Figure 4-23: Fits to the 16^+ band data. The SDM fit (solid line) with a $B(E2 \uparrow) \approx$ 1 W.u. limit on the matrix elements and the Alaga fit (dashed line) constrained to the measured upper limits on GSB$\rightarrow 16^+$ feeding.

angles. The fit following SDM systematics gave values of $10^{-5} \leq B(E2) \leq 6$ W.u. Although the SDM matrix elements spanned 6 orders of magnitude, the maximum $B(E2)$ strengths required to reproduce the $19^+ \rightarrow 18^+$ yield data were reasonable. There was an insignificant drop in the calculated yields after reducing the highest three values to 0.7 W.u. (no longer obeying the SDM systematics). The calculated yields show that γ-decay feeding from the GSB would dominate the population of the yrast 16^+ band, while direct excitation would contribute only $\sim 10^{-4}$ (low spin) to 10^{-2} (high spin) of the total population.

The GSB$\rightarrow 16^+$ branches which would dominate the feeding have energies of

1.3 to 1.7 MeV and either lie in the background of the Doppler-broadened 1.3 MeV ^{136}Xe peak or have low efficiency in the germanium detectors. A few of the GSB$\rightarrow 16^+$ branches populate the $I \geq 18^+$ levels, where triple-γ gates could be used, but these transitions are predicted by the SDM model to be below the measurable limits in the present experiment.

4.4 The $K^\pi = 6^+$ Isomer Band

Rather than using a χ^2 fit to measure the 6^+ band matrix elements as in the analysis of the data from the other rotational bands, $B(E2)$ values of the 6^+ isomer decays (Figure 4-24) measured using the known 77.5(7) ns half-life were used to extrapolate the matrix elements. Coulomb excitation calculations with these matrix elements reproduced the measured in-band yields of the 6^+ band. The measurement of strong $B(E2)$ values connecting the isomer band with the 0^+, 2^+ and 4^+ bands is a clear indication that each of the bands contributes to the population of the 6^+ isomer band. The only model-dependence is introduced into the calculations by the spin dependence of the K-forbidden matrix elements. It seems that the matrix element $\langle 6^+ \mid E2 \mid 4^+ \rangle = 0.094(3)$ eb has been determined, since the K-allowed transitions between the 4^+ and 6^+ bands should be well-described by the Alaga rule, and the measured $B(E2)$ value determines the intrinsic matrix element. Measurements of the branching ratios of the 6^+ isomer decays in previous work did not include the decay to the 4^+ band head. In the present work, this $6_6^+ \rightarrow 4_4^+$ branch has been measured as 19(1)% of the total decay width (Table 4.4) and proved to be important in correctly measuring the $B(\mathcal{M}\lambda)$ values of all of the branches. A comparison between the previously measured values and the present work shows reasonable agreement in most cases, if the previous measurements are corrected for the strength of the 4^+ branch.

Decay Branch	E_γ (keV)	α_{IC}	Reduced Transition Probability (W.u.)		
			This work	Hague	Hague, adj.
$6_6^+ \xrightarrow{E2} 6_{GSB}^+$	922	0.00498	$8.6(6) \times 10^{-5}$	$1.10(7) \times 10^{-4}$	8.94×10^{-5}
$6_6^+ \xrightarrow{E2} 4_{GSB}^+$	1247	0.00268	$1.16(9) \times 10^{-5}$	$1.25(6) \times 10^{-5}$	1.02×10^{-5}
$6_6^+ \xrightarrow{M2} 8_{K=8}^-$	407	0.291	0.020(3)	0.0269(15)	0.0219
$6_6^+ \xrightarrow{E2} 4_{K=4}^+$	40	216.	1.03(7)	—	—
$6_6^+ \xrightarrow{E2} 4_{K=2}^+$	169	0.516	0.018(3)	0.0375(21)	0.0305

Table 4.4: The measured reduced transition strengths $B(\mathcal{M}\lambda; 6_6^+ \to I_f^\pi, K)$ for the decay branches of the 6^+ isomer, compared with values tabulated in [1] from the data of Hague *et al.* [2]. The Weisskopf unit is taken in the downward direction. The adjusted values are explained in the text.

The measured $B(E2)$ values for the decays from the 6^+ isomer to the GS, γ- and 4^+ bands were used to calculate intrinsic matrix elements using Alaga, Mikhailov and SDM systematics as described previously for the γ- and 4^+ bands. In the case of the K-forbidden decays to the GSB, the Mikhailov term was measured using the two observed branches and the SDM model (Equation 2.24) giving the intrinsic matrix element to first order in ΔI^2 (Figure 4-25).

Similarly, one decay to the $K = 4^+$ band head and one decay to the γ-band each yielded an E2 intrinsic matrix element. The SDM systematic was used to extrapolate the set of γ-band$\to 6^+$ band K-forbidden matrix elements. The K-allowed matrix elements coupling the isomer band to the 4^+ band were extrapolated using the Alaga rule. The γ- and 4^+ band connections were calculated without the Mikhailov term, since there was only one transition to each band.

As in all of the previous cases, the intrinsic E2 matrix element for intraband transitions was assumed to be the same as in the GSB, and rotor values were used. The M1 matrix elements were calculated in the same manner as for the 4^+ band, except that the value of $g_K - g_R$ was measured in this experiment for the
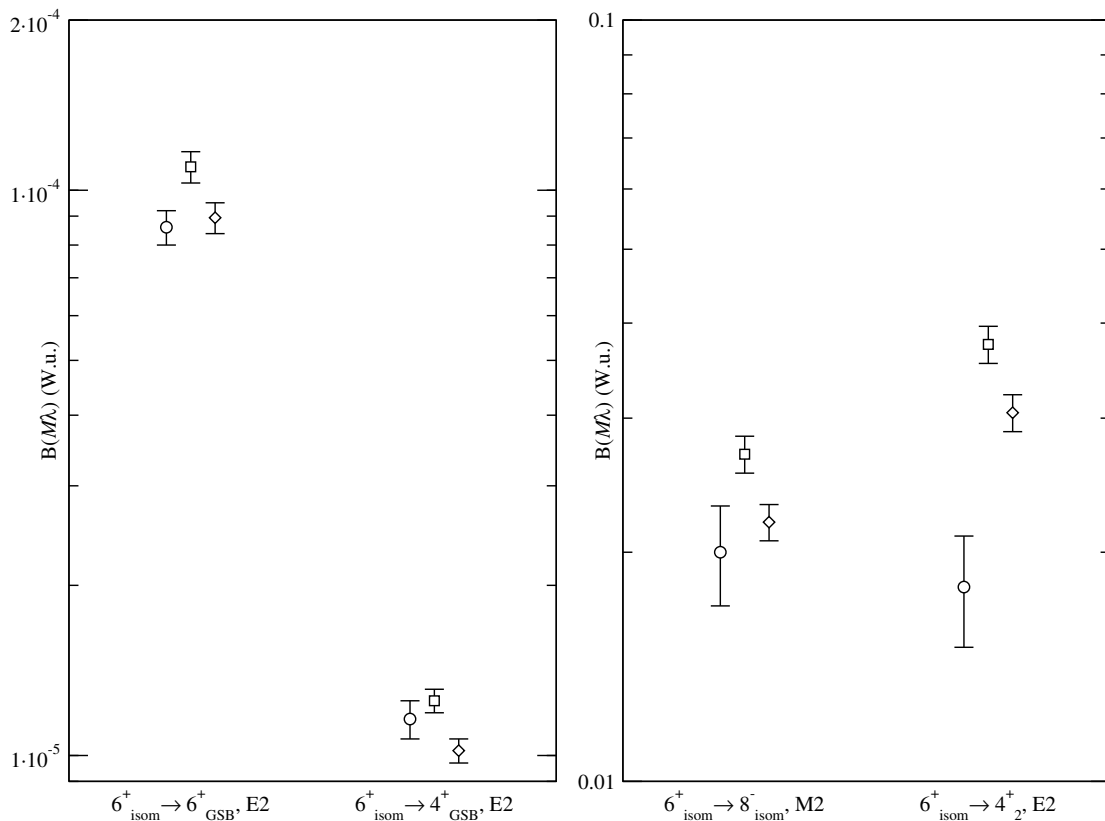
Figure 4-24: The reduced transition strengths $B(\mathcal{M}\lambda \downarrow)$ measured in this work (circles) compared to the previous results of Hague (squares). Hague's measurements corrected (diamonds) for the present measurement of the strength of the $6_6^+ \xrightarrow{E2} 4_{K=4}^+$ branch. The Weisskopf units are $B(E2 \downarrow) = 0.00595$ e^{2}b^2 and $B(M2 \downarrow) = 0.522$ μ_N^2b

6^+ isomer band (Chapter 9).

Summary of the 6^+ Band Matrix Elements The complete set of model-dependent intrinsic matrix elements and reduced matrix elements used in the 6^+ band Coulomb excitation calculations is as follows. In-band M1 matrix elements were calculated using $|g_K - g_R| = 0.56(2)$. Intraband E2 matrix elements were calculated assuming the same quadrupole moment as for the GSB, $\sqrt{\frac{5}{16\pi}}eQ_o = 2.164(10)$ eb. The K-allowed $K = 4^+$ to $K = 6^+$ E2 matrix elements were
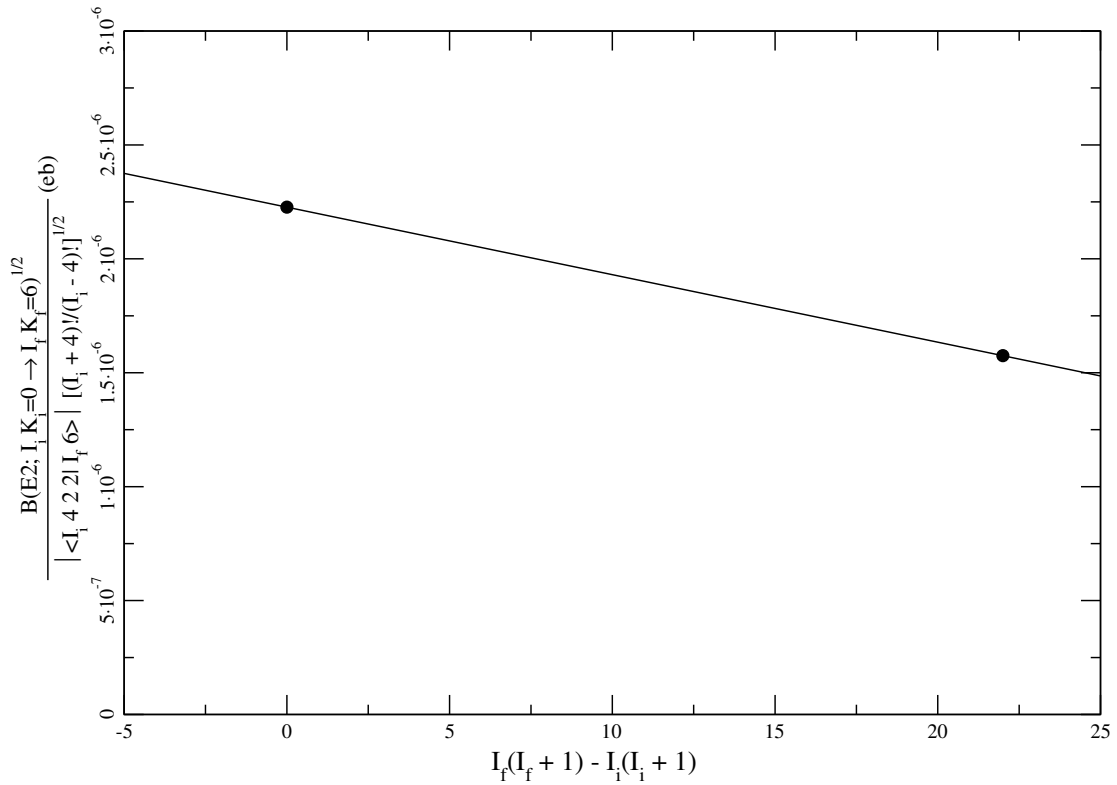
Figure 4-25: Mikhailov-type plot for 6^+ band to GSB transitions. The relative errors are $\approx 4\%$.

calculated from one decay width measurement, giving $\langle K = 6^+ \mid E2 \mid K = 4^+\rangle = 0.094(3)$ eb. One measurement of the $K = 6^+$ to $K = 2^+$ decay width gave the matrix element $\langle K = 6^+ \mid E2 \mid K = 2^+\rangle = 0.00116(10)$ eb, employing equation 2.24 for SDM. The GSB to 6^+ band matrix elements were calculated from a first-order fit (Figure 4-25) of the intrinsic matrix element to ΔI^2 using the SDM description, giving $\langle K = 6^+ \mid E2 \mid K = 0^+\rangle = 1.57(6) \times 10^{-6} - 2.09(7) \times 10^{-8}\{I_6(I_6 + 1) - I_0(I_0 + 1)\}$ (eb).

Error Estimates   The measured errors in the reduced transition probabilities for the 6^+ isomer decay branches were used to directly calculate the errors in the intrinsic matrix elements. The Alaga rule and the SDM model were used

104

to extract the intrinsic matrix elements, so the matrix and their errors are both model-dependent. Each quoted error represents the sum of several contributions, primarily from the measured γ-ray yields ($\lesssim 10\%$), the relative γ-ray efficiency ($\approx 5\%$) and a negligible contribution from the 1% error in the known half-life.

4.4.1 Results

The calculated yields are in agreement with the measured γ-ray triples yields for the 6^+ band for safe scattering angles forward of $60\,^\circ$, as shown in Figures 4-26 and 4-27. The correct phase of the $\langle 6^+ \mid E2 \mid \text{GSB} \rangle$ intrinsic matrix element, relative to the other two population paths cannot be determined. Reversing the sign of $\langle 6^+ \mid E2 \mid \text{GSB} \rangle$ has a $< 1\%$ effect in χ^2 (from 1.41 to 1.42), with the $\frac{1}{2}$ weight of the angular intervals for unsafe scattering angles. The fact that the phase of this matrix element is unimportant ensures that the relative phases of the $\langle 6^+ \mid E2 \mid 2^+ \rangle$ and $\langle 6^+ \mid E2 \mid 4^+ \rangle$ can be determined without ambiguity.

The observation of strong branches of the 6^+ isomer decay to the GS, γ- and 4^+ bands indicates that multiple Coulomb excitation paths are significant. The SDM systematic was again found to give reasonable results for the K-forbidden excitations, reproducing the measured yields using only one or two $B(\mathcal{M}\lambda)$ values to extrapolate each set of K-forbidden matrix elements.

The apparent significance of connections with the GSB and the γ-band depend on the model used, since the Alaga rule does not describe these K-forbidden transitions. The contributions of the GSB and the γ-band have been determined, in so far as the SDM systematic [43] (Equation 2.24) correctly describes the K-forbidden transitions, along with the relative phases of the intrinsic matrix elements $\langle K^\pi = 6^+ \mid E2 \mid K^\pi = 2^+ \rangle$ and $\langle K^\pi = 6^+ \mid E2 \mid K^\pi = 4^+ \rangle$, indicating that constructive interference is required. Figure 4-28 shows the result of removing each of the three principle paths to the 6^+ band. The $> 50\%$ drop in yield with the removal of the γ- and 4^+ band connections shows that they are responsible for
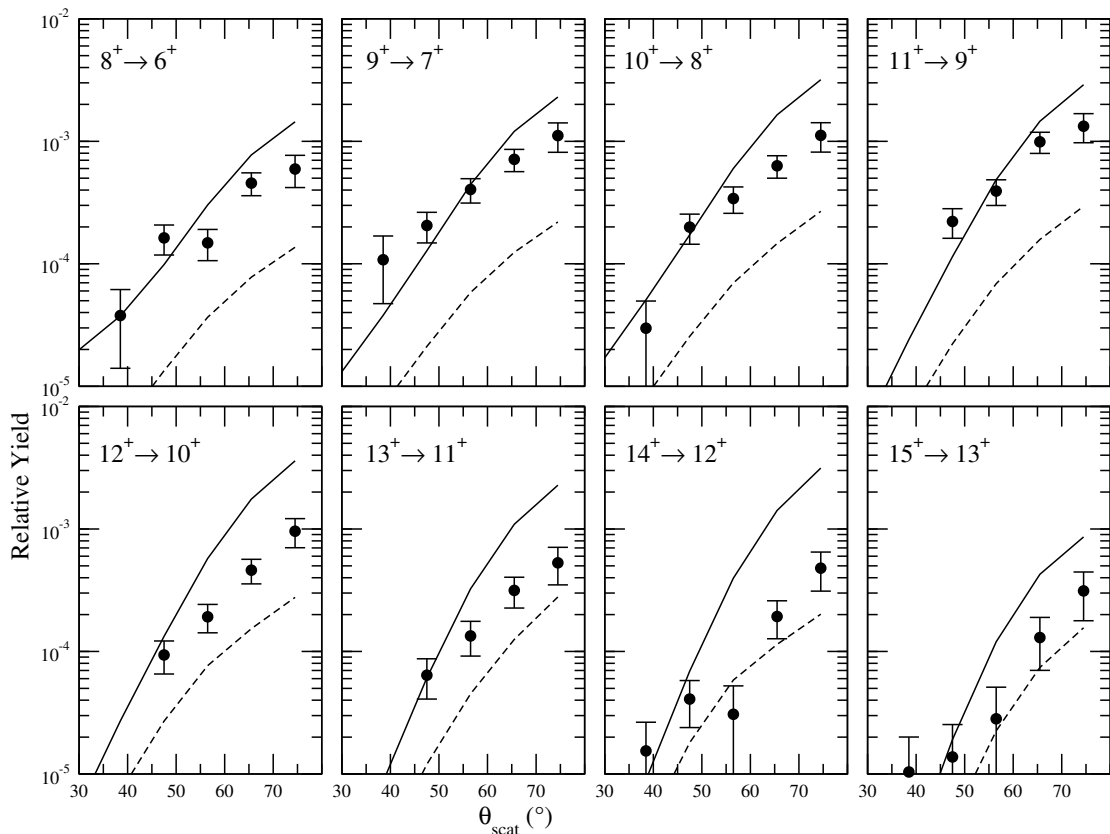
Figure 4-26: Intraband yields of the 6^+ band for even spin. The solid and dashed lines represent Coulomb excitation calculations from measured $B(E2)$ values for opposite relative phases of the intrinsic matrix elements (text).

nearly all of the 6^+ band population at safe scattering angles $\theta_{\mathrm{scat}} < 52°$. The GSB contributes $\leq 25\%$ at forward angles, but may be responsible for the majority of the 6^+ band excitation at unsafe scattering angles.

4.5   The Question of Transfer Reactions

It can be argued that the isomer bands in question could be populated either through Coulomb excitation, which would permit the present explanation of strong K-mixing, or through transfer reactions involving the ^{177,179}Hf contam-
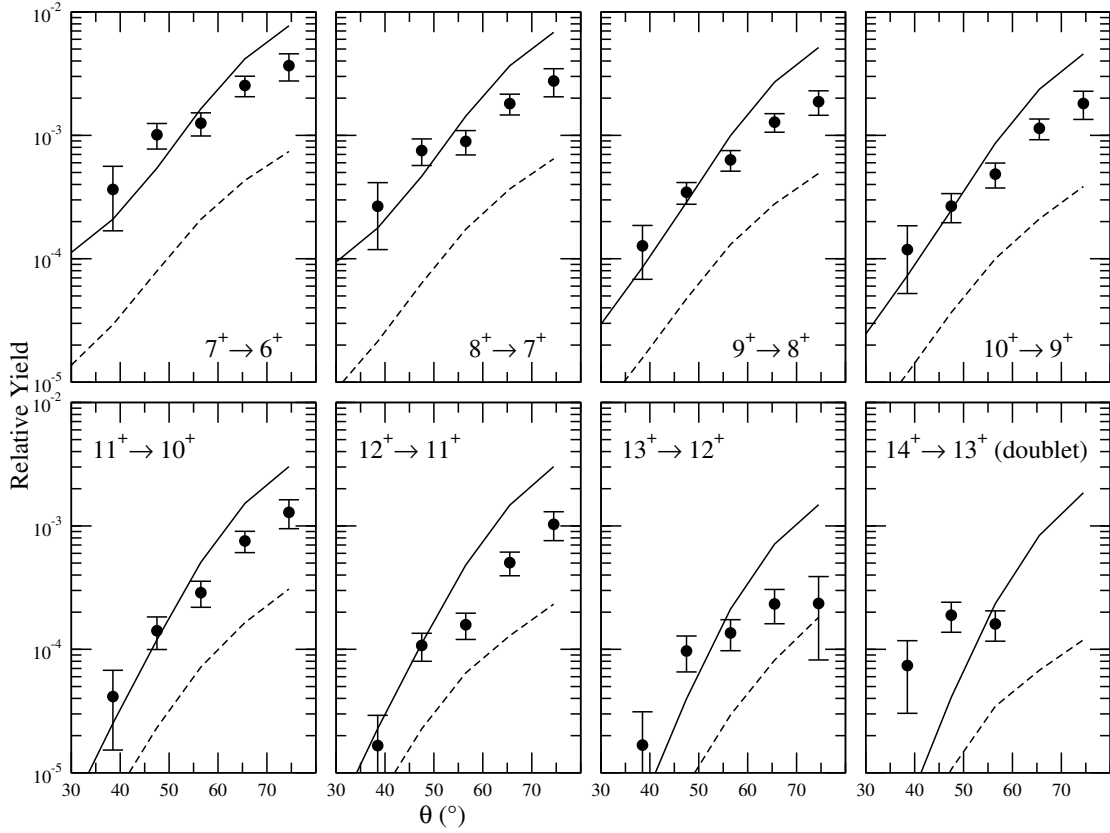
Figure 4-27: Intraband yields of the 6^+ band for odd spin.

inants in the target. The following measurements show that transfer is not a significant concern.

To measure the fraction of the excitations that could have been caused by transfer reactions, the most straightforward approach might be to select events containing transitions in ^{178}Hf and compare the relative amounts of Xe isotopes in coincidence. This is not possible because the background of Doppler-broadened lines of hafnium in the resulting Xe spectra is large and does not allow the observation of small amounts of ^{135}Xe and ^{137}Xe that would result from rare transfer reactions. Figures 4-29, 4-30(b) and 4-31(b) illustrate the difficulty in measuring the ^{177}Hf(^{136}Xe,^{135}Xe)^{178}Hf reaction. The upper limits on transfer reactions were
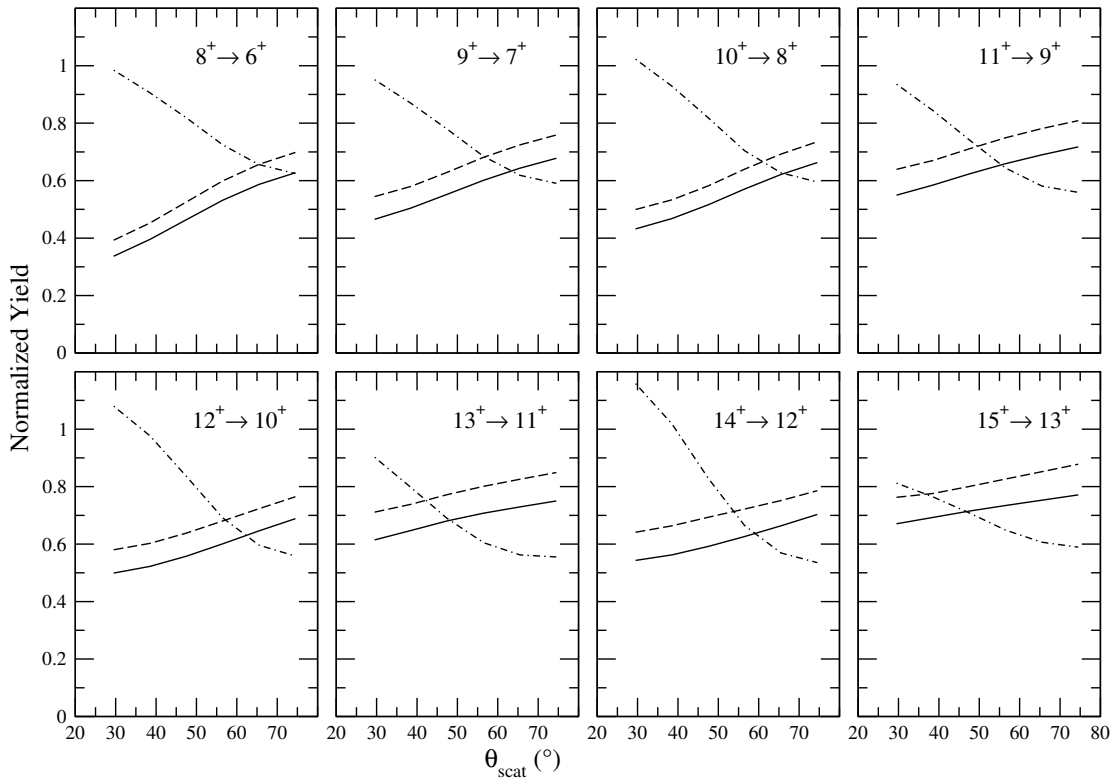
Figure 4-28: Calculated 6^+ intraband yields normalized to the total Coulomb excitation calculations, calculated after removing each of three population paths: $\langle 6^+ \mid E2 \mid \gamma \rangle$ (solid), $\langle 6^+ \mid E2 \mid 4^+ \rangle$ (dashed), $\langle 6^+ \mid E2 \mid \text{GSB} \rangle$ (dashed-dotted).

measured by gating on ^{177}Hf or ^{179}Hf lines in an asymmetric cube where two γ-ray energies were Doppler corrected for Hf and one was corrected for Xe. The relative yields from ^{135,136,137}Xe lines were measured in coincidence.

Figures 4-30(a) and 4-31(a) are the result of a double gate on two arbitrarily selected γ-ray energies that do not occur in coincidence in the isotopes present in the target. After background subtraction, the two resulting spectra did not contain any ^{136}Xe lines, indicating that random coincidences were rare and would not interfere with the measurement. The spectra in Figures 4-30 and 4-31 were used to set an upper limit on the amount of transfer taking place. The 288 keV line could be from a known transition in ^{135}Xe, giving an upper limit on the trans-
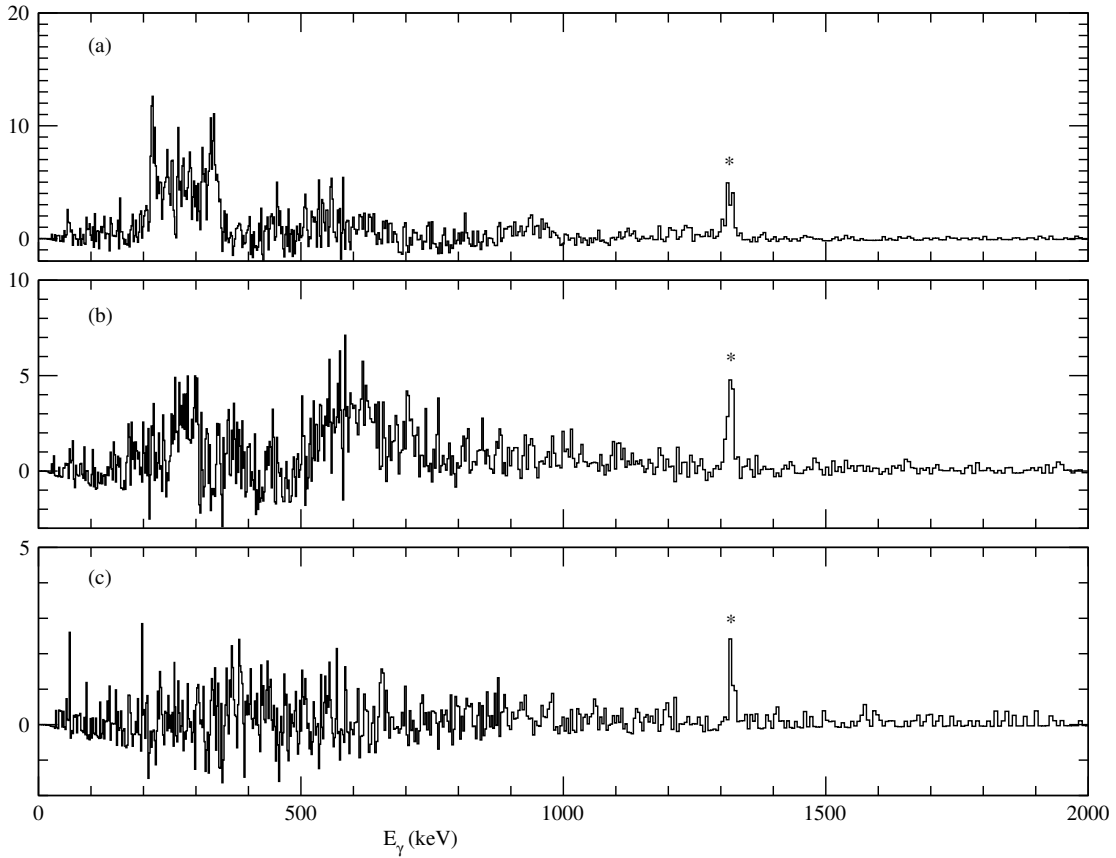
Figure 4-29: Resultant background-subtracted spectra from gates on ^{178}Hf transition energies in an asymmetric Xe-Hf-Hf cube. Data are from the unsafe Coulomb excitation region, $52° \leq \theta_{\text{scat}} \leq 78°$. (a) Gated on 6^+ isomer band. (b) Gated on the 8^- isomer band. (c) Gated on the 16^+ isomer band. (*) The $2^+ \rightarrow 0^+$ transition in ^{136}Xe.

fer reaction ^{178}Hf(^{136}Xe,^{135}Xe)^{179}Hf. No evidence of the ^{178}Hf(^{136}Xe,^{137}Xe)^{177}Hf reaction was seen in the spectra gated for ^{177}Hf.

The data from the safe region, 25° to 52°, shows no indication of transfer; the spectra of Figure 4-30 contain Xe transitions in the 136 isotope only. In the unsafe region, 52° to 78°, the strength of the 288 keV peak in Figure 4-31(c) indicates that approximately 9.9% of the excitation of the ground state band of ^{179}Hf could be due to one-neutron transfer. The target contains 2.9% ^{179}Hf and 89.14% ^{178}Hf, so transfer is occurring at about $(2.9/89.14) \times 9.9\% = 0.32\%$, compared to Coulomb excitation of the ^{178}Hf GSB. It is reasonable to assume that the cross section for

the reaction ^{177}Hf(^{136}Xe,^{135}Xe)^{178}Hf ($Q = -0.4$ MeV) is comparable to that of the ^{178}Hf(^{136}Xe,^{135}Xe)^{179}Hf ($Q = -1.9$ MeV) reaction, since the peak neutron transfer cross section occurs for $Q = 0$, and the Q-values differ by only 1.5 MeV [90]. The target contains 4.36% ^{177}Hf, compared with 89.14% ^{178}Hf, so transfer is occurring at a rate of about $(4.36/89.14) \times 0.32\% \sim 10^{-4}$ compared to Coulomb excitation of the ^{178}Hf GSB in the unsafe region.
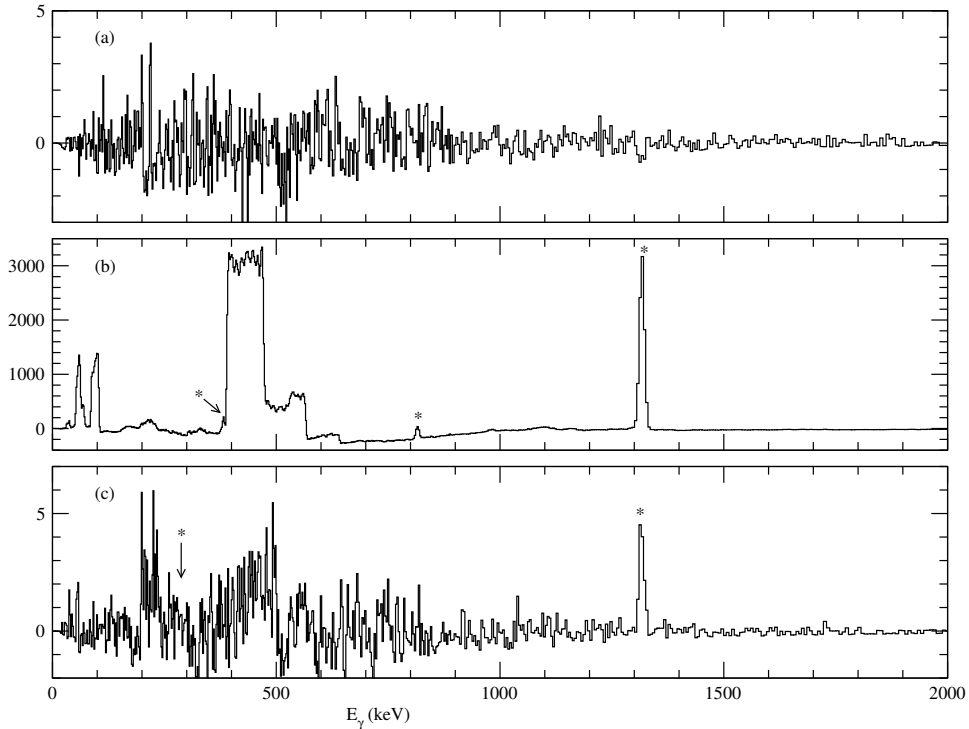
Figure 4-30: Resultant background-subtracted spectra from gates in an asymmetric Xe-Hf-Hf cube in the safe region,$25° \leq \theta_{\mathrm{scat}} \leq 52°$. (a) Gated on "random coincidences" (text). (b) Gated on the GSB of ^{178}Hf. (c) Gated on the GSB of ^{179}Hf. (*) ^{136}Xe transition energies.

The yield due to transfer in the safe region is not observable, having an upper limit of the order of 10^{-5}, and the transfer in the unsafe region is approximately 10^{-4}, compared to the GSB. These transfer reactions are presumably populating many different bands, so their contribution to the yield of any one isomer band is even smaller. Transfer to a 4 quasiparticle state (*e.g.* a state in the 16^+ isomer

110
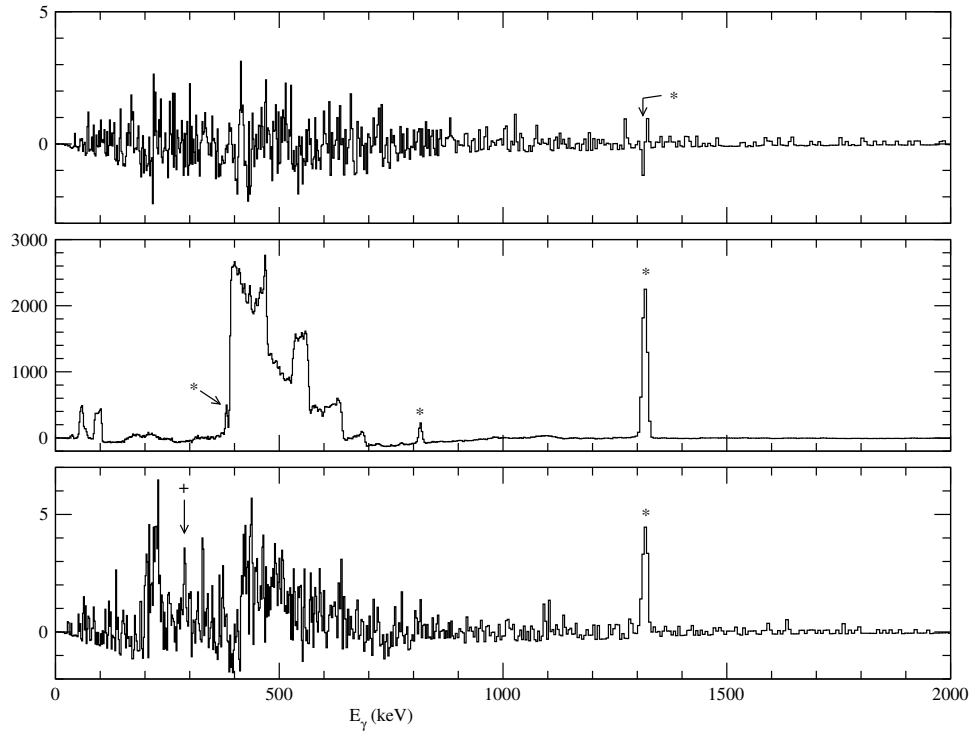
Figure 4-31: Resultant background-subtracted spectra from gates in an asymmetric Xe-Hf-Hf cube in the unsafe region, $52° \leq \theta_{scat} \leq 78°$. (a) Gated on "random coincidences" (text). (b) Gated on the GSB of ^{178}Hf. (c) Gated on the GSB of ^{179}Hf. (+) possible ^{135}Xe transition at 288 keV.

band) is very unlikely, since breaking a second pair of nucleons is a higher-order effect in transfer reactions. In addition, the transfer seen in the unsafe region should be greatest at larger θ_{scat} angles. Since no transfer is seen in the safe region, there should not be a significant amount of transfer near $52°$, even in the unsafe region, where strong isomer populations are already seen. Furthermore, the most compelling argument against the significance of transfer is in the results of the ^{178}Hf beam activation experiment, where the 16^+ isomer was activated with significant cross sections well below the Coulomb barrier.

4.6 Conclusion

Three distinctly different paths have been determined to populate the $K^\pi = 6^+, 8^-$ and 16^+ isomer bands. Multiple-step excitations populate the 6^+ band via the γ- and 4^+ bands primarily, using both K-allowed and K-forbidden transitions. The 8^- bands are excited directly from the γ-band and the GSB by highly K-forbidden E3 transitions. The Hf(Xe,Xe)Hf data are consistent with direct γ-decay feeding into the 16^+ band. However, it will be shown that the additional data provided by the Ta(Hf,Hf)Ta activation experiment leads to a departure from the SDM systematic and that direct excitation is not insignificant in the population of all of the 16^+ isomer band states. These three results, as well as those for the γ- and 4^+ bands have shown that the SDM model is a useful approximation for reasonably low spin and low forbiddenness, ν. The numerical results are compiled and analyzed in Chapters 9 and 10.

Chapter 5

Experiment II: ^{178}Hf Beam Activation

The unexpectedly intense prompt γ-ray yields of the 16^+ isomer band measured in the Hf(Xe,Xe)Hf experiment provided an upper limit of the $\langle 16^+ \mid E2 \mid GSB \rangle$ matrix element of 8×10^{-19} eb based on the SDM model [43]. In an effort to extract a full set set of model-independent matrix elements, a second experiment was devised to measure the excitation of the 16^+ isomer as a function of collision energy. The matrix element $\langle 16^+ \mid E2 \mid GSB \rangle$ was used to predict an excitation function (Figure 5-1) for a stack of five Ta targets, 1 mg/cm^2 thick, irradiated by a ^{178}Hf beam at a beam energy chosen so that the third, fourth and fifth targets would have $E_{\mathrm{beam}} \leq 80\%$ and nuclear effects would be small or insignificant in all five targets. Offline counting of the isomer decays by the cascade shown in Figure 5-2 would then provide the measurement of the cross section. Ideally, the activity could be measured by counting either the 8^- band cascades or the GSB cascades, provided that the branching ratios in the 8^- band are known accurately.

Since the first experiment showed that the excitation function of the GSB levels can be described accurately by the rigid rotor model, the 16^+ band's excitation function can, in principle, be used to extract a large subset of the $\langle I_{16^+} \| E2 \| I_{\mathrm{GSB}} \rangle$
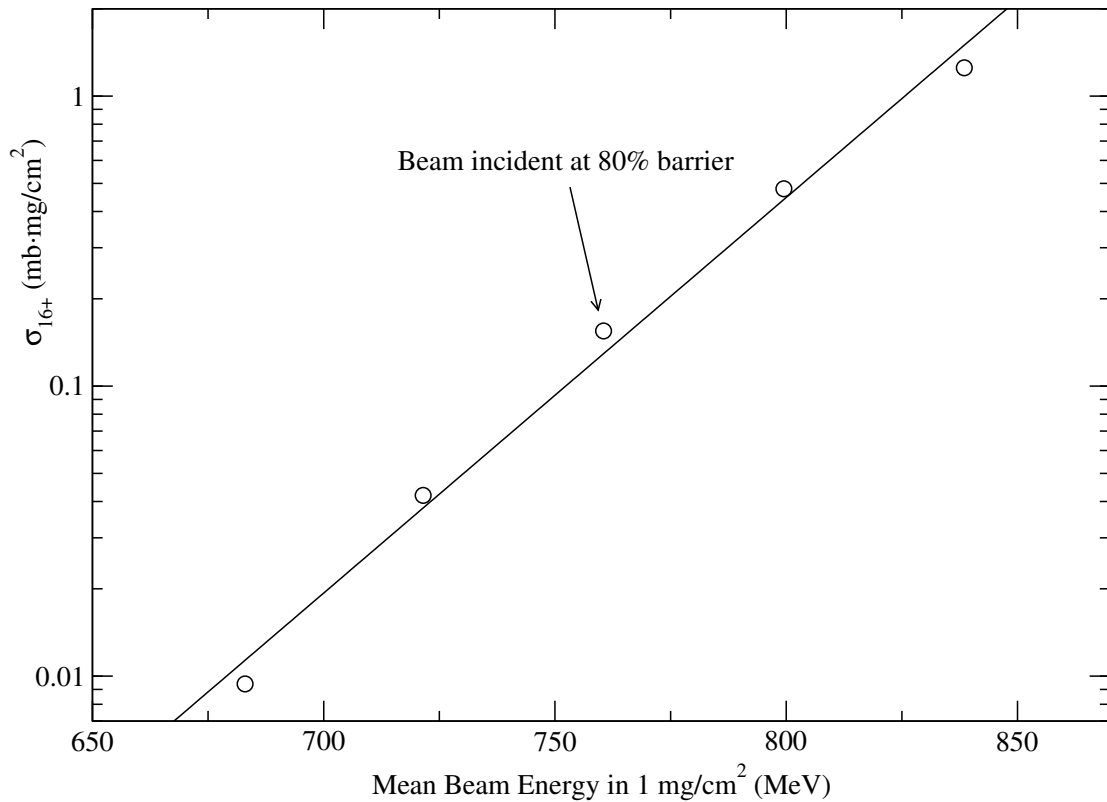
Figure 5-1: The total calculated cross section for populating the $K^\pi = 16^+$ isomer as a function of mean beam energy. For a ^{178}Hf beam of 858 MeV initial energy, the energy difference between each pair of points corresponds to the energy loss in a 1 mg/cm^2 Ta target. The arrow shows the mean energy in the target irradiated at the maximum safe energy.

matrix elements. As the beam energy in the target is increased, higher GSB levels become populated with sufficient strength to contribute to the 16^+ isomer activation, and matrix elements for higher-spin levels become important. Ideally, one matrix element for each GSB level would be far more effective than the others, either because of the change ΔI in spin, or because of the E^5 factor in the γ-decay width in cases where feeding dominates.
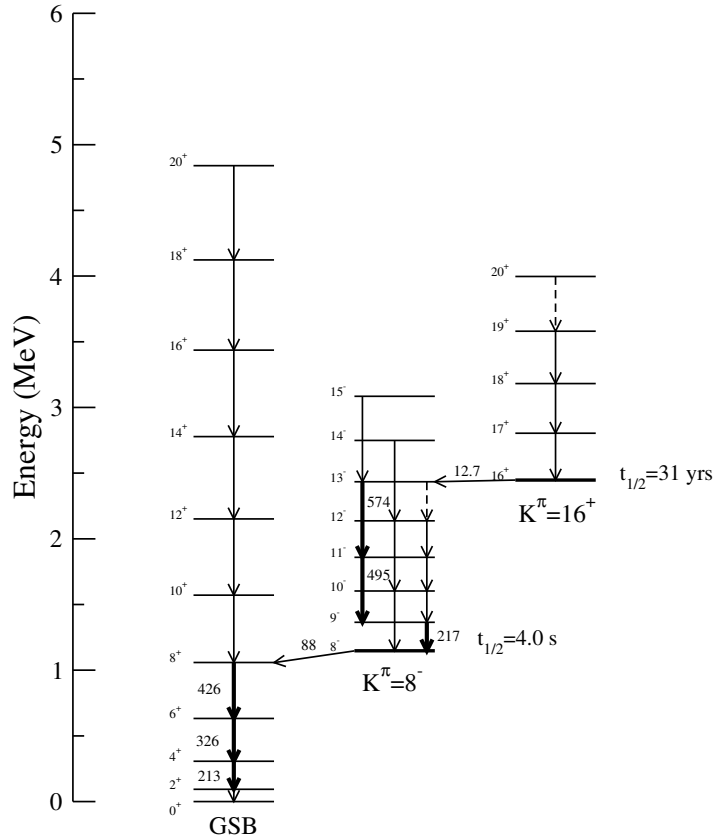
Figure 5-2: A partial level diagram for ^{178}Hf. The γ-decays observed online in the Hf(Xe,Xe)Hf experiment are shown, along with the two isomer decays. The strongest decay cascade (bold arrows) is known from branching ratios. The $\Delta I = 1$ branch from the 13^- level accounts for only $\sim 10\%$ of the total decay width.

5.1   Facilities, Apparatus, Detectors

5.1.1   Beam and Targets

The five 1 mg/cm^2 tantalum targets were arranged parallel in a stack, separated by 0.59 cm long, 1.0 cm diameter hollow cylindrical 42 mg/cm^2 tantalum "catchers" to collect forward-scattered Hf ions, the length chosen to cover $40° \leq \theta_{\text{scat}} \leq 90°$, so that only an insignificant fraction ($\ll 1\%$) of nuclei in the 16^+ state were lost or embedded in downstream targets. The tantalum foils were secured on their mounts using conductive epoxy to prevent charging of the foils.

Offline counting of activated nuclei would use both the targets and the catchers. Attenuation of the γ-rays emitted in the thick catchers would be considerable for $E_\gamma \lesssim 100$ keV, but is $< 3\%$ [91, 4, 92] for the γ-rays ($E_\gamma > 150$ keV) that were counted. Figure 5-3 shows the anticipated cross section as a function of scattering angle for each target, based on the upper limit of $\langle 16^+ \mid E2 \mid GSB \rangle = 8 \times 10^{-19}$ eb from the Hf(Xe,Xe)Hf experiment. Each 1 mg/cm^2 target slowed the 858 MeV ^{178}Hf beam, provided by ATLAS, by about 40 MeV, enabling the collection of data for the entire excitation function using a single beam energy. The sixth target foil, called the "scattering foil," was used to scatter beam and target particles into a silicon detector as a monitor of the beam intensity, as described below.

The scattered beam particles were collected over an angular range of $40° < \theta_{\text{scat}} < 180°$, so large deviations of the beam position on target and high "small-angle scattering" probabilities would introduce significant error into the activation rate measurement. Small-angle scattering calculations were done using SM-SCAT [93], based on the tables of Sigmund and Winterbon [94]. The fraction of particles scattered by multiple electron collisions are shown as a function of θ_{scat} up to 2° in Figure 5-4. To first order, the lateral displacement of the $\sim 10\%$ of Hf ions electronically scattered in the first target by $> 0.5°$ is only ≈ 0.2 mm at the end of the target stack. Since the beam traversed a total of 5 mg/cm^2 of tantalum target material, separated over a distance of 2.4 cm, it can be concluded that small-angle scattering of beam particles in the targets was minimal. Relative to other factors, such as the 2 mm beam diameter, small-angle scattering was not a significant concern.

Heating of the targets by the beam presented a concern, because the target array would have to dissipate ≈ 5 W in vacuum at 10 pnA. All of the parts in thermal contact with the target mount were constructed of aluminum and ceramic to eliminate problems with plastic parts breaking down at high temperatures.

116
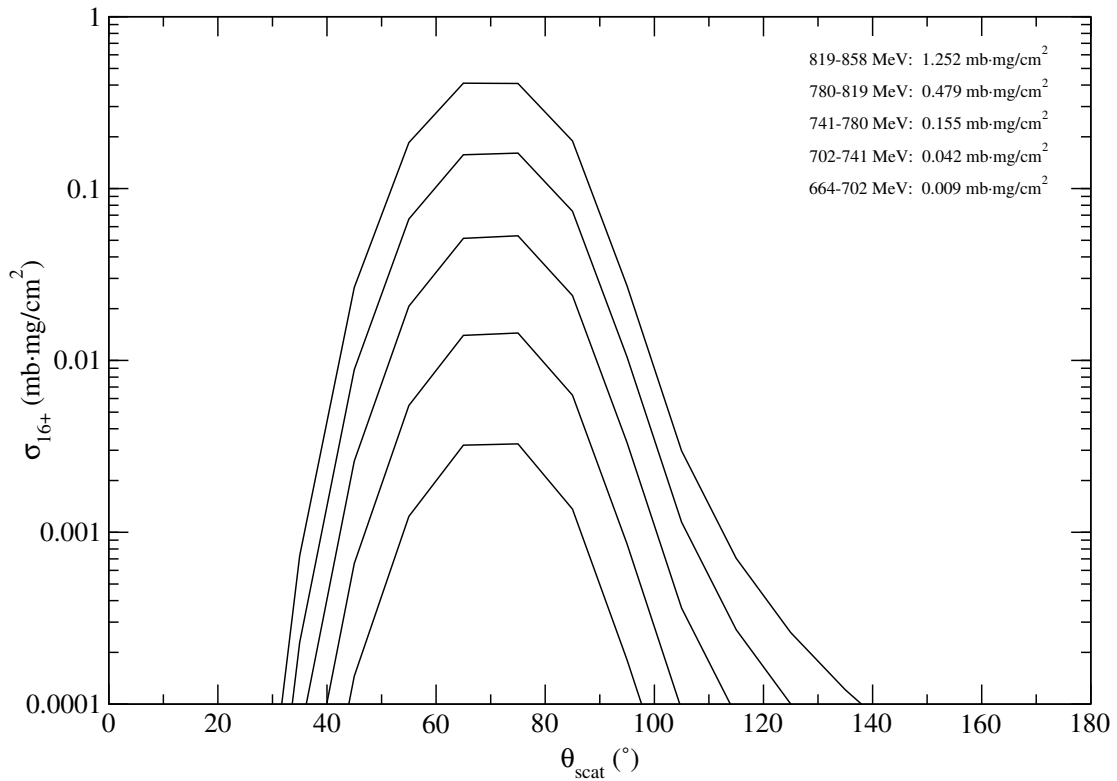
Figure 5-3: 16^+ isomer activation cross sections calculated for $10°$ bins in the ^{178}Hf scattering angle. 780 MeV is the safe energy for Coulomb excitation. Total cross sections (upper right corner) and energy ranges correspond to individual 1 mg/cm^2 targets in a stack and an initial beam energy of 858 MeV.

5.1.2 Activation Apparatus

Silicon Counter   Figure 5-5 shows the arrangement of the activation apparatus installed in ATSCAT, the 36" scattering chamber at ATLAS. The silicon detector (60 μm sensitive thickness) was mounted at $45°$ to count forward scattered beam and target nuclei in order to measure the total beam dose and normalize the cross sections. The silicon detector was covered with a 0.254 cm (100 mil) diameter aperture and mounted 43.2 cm (17.0 inches) from the scattering foil (Figure 5-6) to reduce the count rate to about 30 Hz, and fitted with a 57 mm long cylindrical Delrin blinder to ensure that particles scattering at the end of the collimator would

117
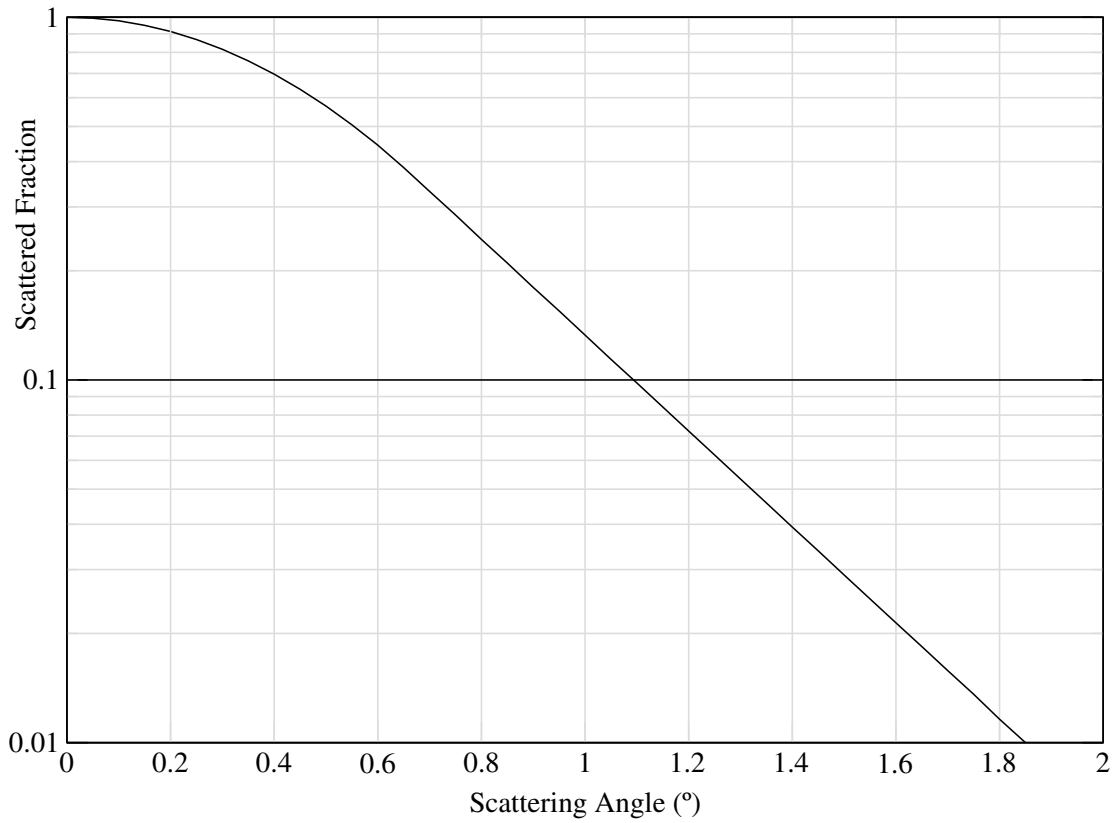
Figure 5-4: The fraction of beam particles scattered as a function of scattering angle, calculated by SMSCAT for scattering by electrons.

be out of the line of sight. The aperture subtended 2.7×10^{-5} sr and $0.34°$ in θ_{scat}. The bias voltage was set at 75 V, resulting in a leakage current of about 0.1 μA.

The scattered Hf and recoiling Ta nuclei of approximately equal mass had equal energies within the precision of the silicon detector of $E_{\text{scat}} \doteq E_{\text{rec}} \approx 300$ MeV after scattering in the sixth Ta foil at an angle of 45°. Consequently, the silicon spectra show one peak representing the total count of Hf and Ta nuclei (Figure 5-7).

Ge Detector A germanium detector, positioned approximately 208 cm (82 inches) from the Faraday cup beam stop, was used to monitor the prompt on-
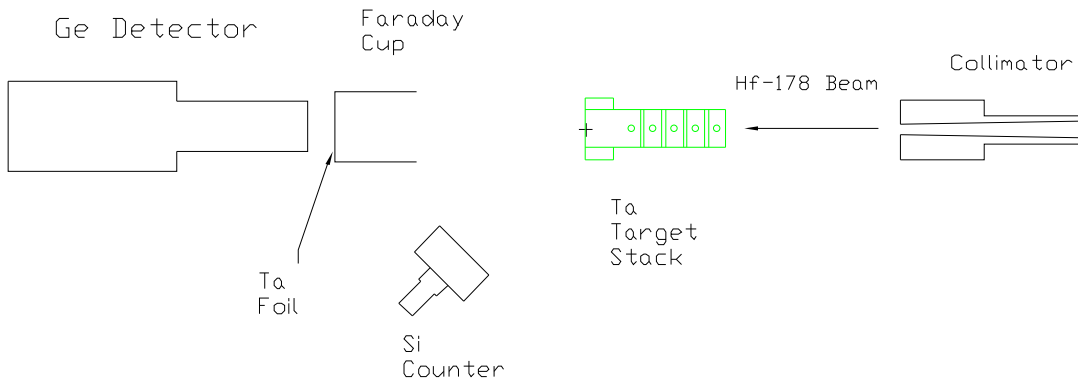
Figure 5-5: A schematic representation of the arrangement of the target stack, Faraday cup, and online monitoring apparatus.

line γ-rays emitted by Hf nuclei stopped in the Faraday cup. In addition to ensuring that the correct species was tuned in the Linac, the Ge detector was used to infer the target ablation as a function of time (section 6.3) and correct for the decreasing target thickness throughout the run. The γ-rays incident on the Ge detector traversed a 0.13 mm (5 mil) thick Ta beam stop and a ≈ 6 mm thick SiO_2 glass window, which resulted in attenuation of the γ-ray intensity by about 11% and 9% [4], respectively, for the 325 keV and 426 keV transitions used to monitor the target thickness, so the corrections for the relative intensities were small.

A sample spectrum from the Ge detector (Figure 5-8) shows transitions up to spin 12^+ in the GSB of ^{178}Hf, ensuring that the correct species was tuned in ATLAS. ^{181}Ta lines from the natural tantalum Faraday cup and several lines belonging to outside contaminants, such as ^{40}K and ^{228}Th in the vicinity of the

119
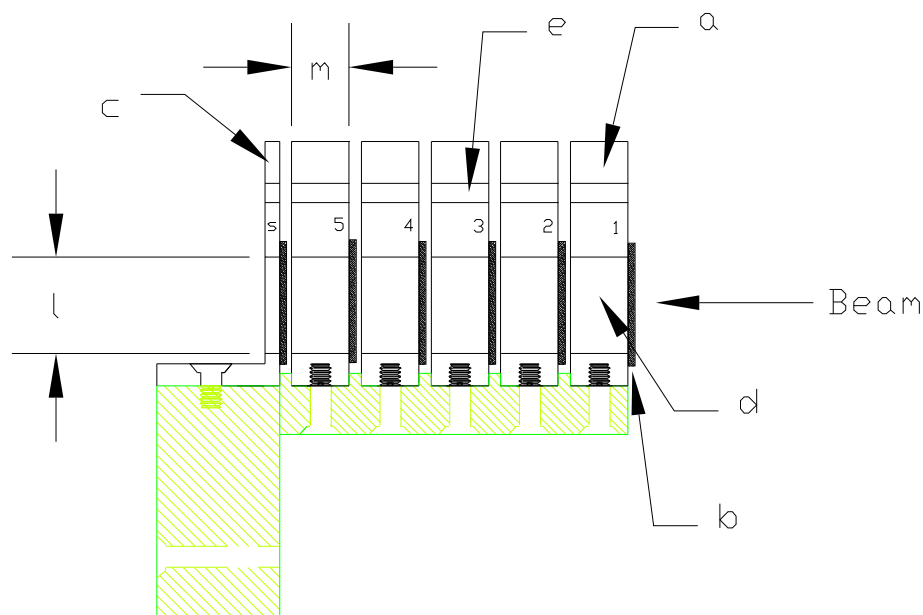
Figure 5-6: The target stack (1–5) and scattering foil (s) on their frame (hatched). Five $m = 0.59$ cm thick aluminum mounts (a) hold five 1 mg/cm^2 Ta targets (b), while a sixth scattering foil (s) is mounted on (c). Holes (d) of diameter $l = 1.0$ cm allow passage of the beam and are lined with 42 mg/cm^2 thick tantalum to catch scattered nuclei. Holes (e) allow visual alignment of the mounts on the frame.

experiment also appear in the spectrum. Some of the higher-spin peaks in the ^{178}Hf spectrum show a small ($\approx 10\%$) Doppler shifted component on the high energy side only, since the stopping nuclei were traveling toward the Ge detector.

Primary Beam Current Monitor A 25 cm long, 3 cm diameter tantalum Faraday cup (the "downstream cup" shown in Figure 5-5) was installed with its 1.3 mm (5 mil) tantalum beam stop approximately 43 cm (17 inches) from the scattering foil. The cup was held by ceramic mounts designed to both insulate the cup from the chamber ground and to withstand the heating by the ≈ 6 W beam. The target stack was biased at 4 kV to prevent a scattered electron current from hitting the cup, and a coaxial feed-through was used to monitor the beam current in the cup.
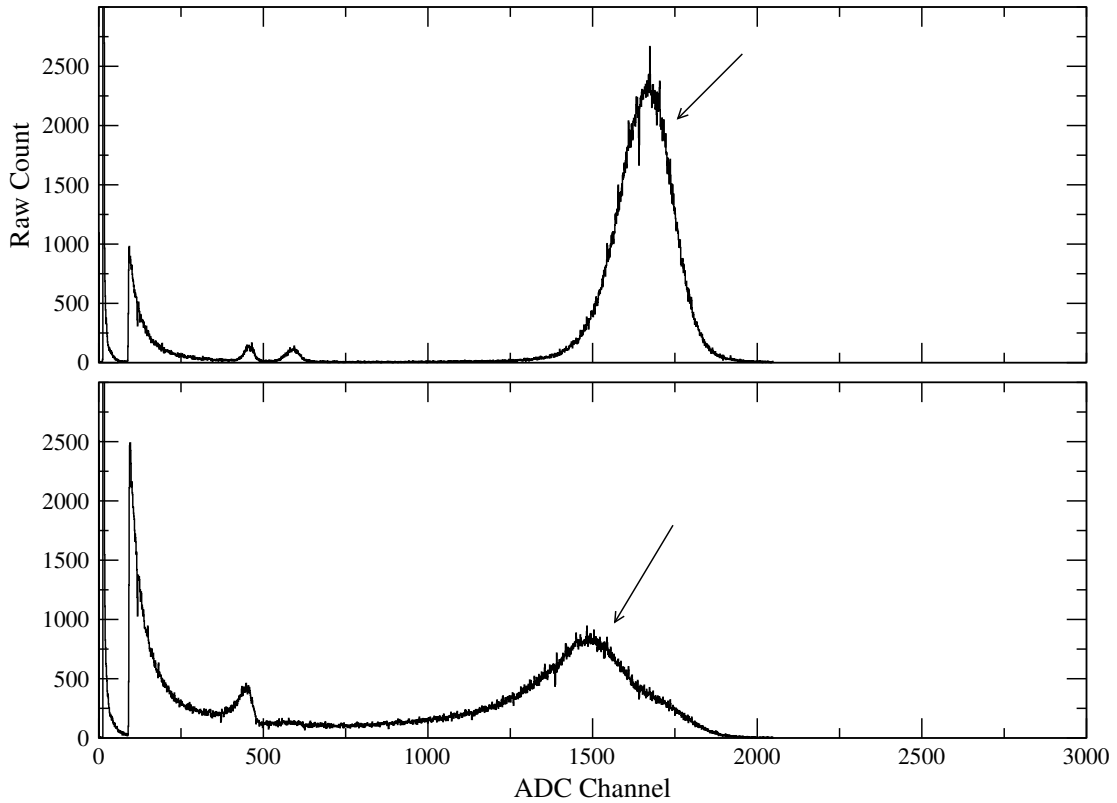
Figure 5-7: Sample silicon energy spectra at the beginning of the run (top) and after approximately half of the total dose (bottom). The Hf and Ta peaks are completely overlapped (arrows).

The beam current was integrated online using a digital current integrator scaled to 20 nC/count, giving an effective resolution of about one part in 10^5 for each run. The current measurement in the Rochester Faraday cup showed an inexplicable disagreement with the measurement taken in the upstream Faraday cup. While the upstream cup measured 14.6 pnA at $Q = 24^+$, the downstream cup measured 21 pnA at $\bar{Q}_{\text{calc}} = 51^+$. However, the discrepancy was constant throughout the experiment, so the cup current provided an accurate monitor of changes in the beam intensity by using the Si detector for an absolute calibration.

Collimator   A tantalum collimator with a 3mm gold aperture was installed in the ATSCAT chamber with its downstream end 35 cm (14 inches) from target 1
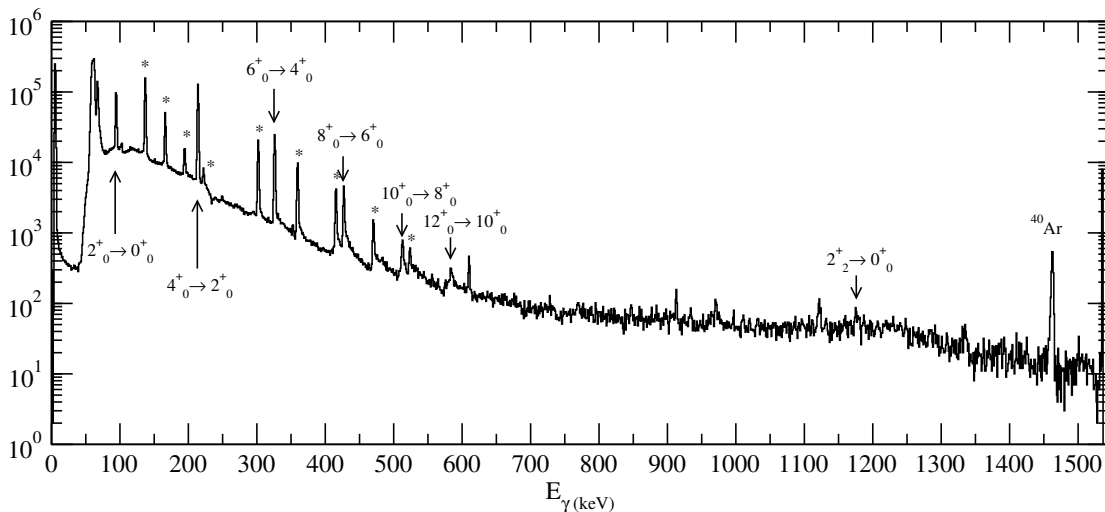
Figure 5-8: A sample online γ-ray spectrum. ^{178}Hf transitions are indicated by $I'_{K'} \to I_K$. ^{181}Ta transitions are indicated by a *. All other peaks are from laboratory background, *e.g.* the ^{40}Ar γ-ray from ^{40}K β-decay.

(Figure 5-5). Tuning and steering of the beam were accomplished by minimizing the beam currents in the collimator and in a 6.3 mm ($\frac{1}{4}$ inch) aluminum aperture placed at the target position during the tuning and steering process. The collimator was mounted in ceramic to avoid heat dissipation problems while the beam was being steered.

5.2   Data Acquisition

A ^{178}Hf^{24+} beam of ≈ 10 pnA at 858 MeV was steered through the center of the target stack position using the 6.3 mm ($\frac{1}{4}$ inch) aperture. During tuning and steering, a thick movable blinder was used to protect the silicon counter from high intensity scattered ions. When the beam was in position, a single test foil was used to ensure that the silicon counter was operating, without applying beam to the targets. (The entire beam dose on the target foils was integrated in order to obtain an absolute normalization.)

The data acquisition electronics were triggered by a logical OR between the

germanium detector hits and the silicon hits. Each event recorded the silicon and germanium energies. The Ge event rate was 7 kHz, reduced to 700 Hz with a X10 scale-down unit, and the silicon rate was $\approx$ 30 Hz. Electronic dead time was not a consideration at these low rates.

The targets were irradiated by approximately 3 days of beam at about 10 pnA, followed by a 15 minute test run on a single foil. The original sharp peak seen in the silicon spectrum (Figure 5-7) degraded significantly during the run. The single foil, which had been exposed to beam for only minutes reproduced the original sharp peak that was seen in the silicon detector at the start of the experiment. The return of the sharp peak indicated that target damage in the form of non-uniformity of the thickness was responsible for the degradation of the silicon peak, rather than radiation damage to the silicon detector itself.

An energy and intensity calibration spectrum was recorded following the shutdown of the Hf beam. A ^{152}Eu source was positioned outside the chamber window in the approximate location of the end of the Faraday cup, the point of origin of the γ-rays measured during the run. Placement of the calibration source outside the scattering chamber necessitated a small correction, described above, in the relative intensities of the online data due to the variation of attenuation with energy as γ-rays traversed the glass and the tantalum beam stop.

5.3   Offline Activity Measurement

5.3.1   Detector Geometry

Two 4-segmented Ge "clover" arrays were arranged with their shield faces nearly in contact, separated by 1 mm (Figure 5-9) and several inches of lead shielding on all four sides. The clover arrays are segmented into four approximately cylindrical crystals, "leaves," which can be read individually, or summed to function as one detector. A target foil and its catcher were positioned between the clovers,

123
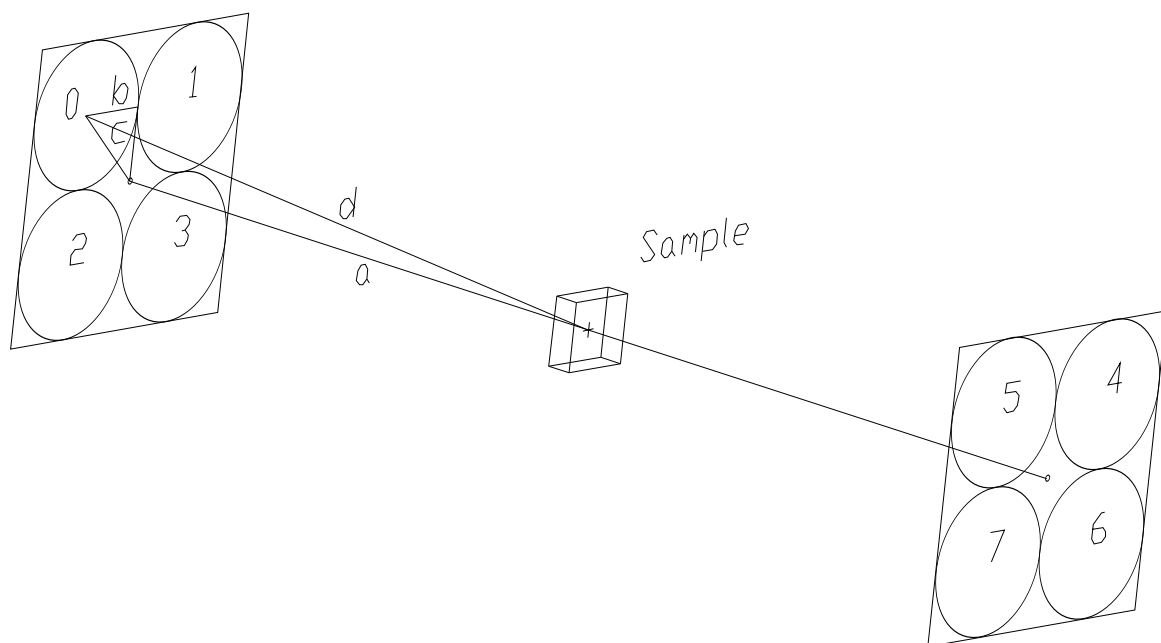
Figure 5-9: A schematic depiction of the geometry of the Yale "clover" detector apparatus, not to scale. Each clover is segmented into four "leaves," which act as independent detectors. $a = 10.5$mm, $b = 22$mm, $c = 31.1$mm, $d = 32.8$mm.

equidistant from all 8 leaves.

5.3.2 Electronics and Trigger

In order to maximize the count rate while reducing the number of sum events (the energy of two or more γ-rays from a single event being measured simultaneously in the same detector), the 8 clover leaves were read individually, triggered by a logical OR of the 8 timing signals. The signal from each leaf was split and sent to a timing filter amplifier to shape the pulse for the trigger (Figure 5-10) and to a spectroscopic amplifier for integration of the pulse energy. The low γ-ray background and lead shields provided a sufficiently low background to count all single γ hits ($n \geq 1$) in the 8 input OR trigger.

124
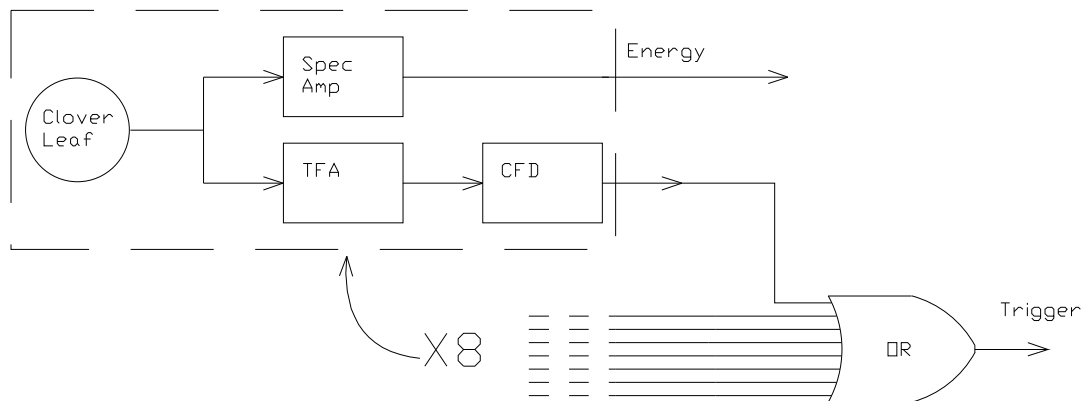
Figure 5-10: Electronics schematic for the readout of the twin clover array. The block in the dashed box is repeated for each of the 8 leaves. A single fan-in unit (OR) generates the trigger signal.

5.3.3 Experimental Run

Relative γ efficiency data were taken using a ^{152}Eu source. Absolute efficiency calculations are described on pages 138 ff. The efficiency data were taken using the trigger described above. The efficiency was measured for the clover pair as a whole, using the average efficiency of the 8 leaves.

Targets 1, 3, 4 and 5 were each counted separately in the clover pair, the only difference among the targets being the count times in Table 5.1. (An electrical fault toward the end of the experiment prevented measurement of target 2.) In every case, the target foil and its catcher foil (unrolled and flattened from its original cylindrical shape) were counted simultaneously. The foil and catcher pairs were positioned overlapping at the center of the detector pair (Figure 5-9) so that they resembled point sources as closely as possible, simplifying the analysis. Both the foil and the catcher were thin enough to cause negligible γ-ray attenuation during the data collection. The total raw count rates from single-γ spectra are summarized in Table 5.1.

125

Target	Counting Time (h)	Single-γ Count Rates (h^{-1})		
		$6_0^+ \to 4_0^+$	$8_0^+ \to 6_0^+$	$10_0^+ \to 8_0^+$
1	16.5	195(12)	173(10)	123(9)
2 *	—	—	—	—
3	17.5	67.4(86)	80.2(61)	73.2(71)
4	105.6	28.5(142)	24.4(19)	17.3(15)
5	237		6.89(164)	10.9(14)

Table 5.1: Count times and raw count rates of GSB transitions (uncorrected for counting efficiency) for each target. Count rates are from γ-ray singles. *Target 2 not counted.

The quiet background and unexpectedly high count rate in the clover detectors showed remarkably prominent ^{178}Hf peaks in the GSB after only 16.5 hours of counting with target 1. Figure 5-11 shows the raw singles ($n \geq 1$) spectrum for target 1. The GSB peaks are well above background, as well as some $K = 8^-$ in-band transitions and the 88 keV decay of the 8^- isomer to the 8_0^+ state.

The peak-to-background ratio of the single γ spectrum was not high enough (4% for target 5) to accurately measure the activation of the lower energy targets. More precise count rates were were obtained from the $n > 1$-fold matrix (2-fold and higher) by gating on a GSB transition and counting the coincident γ-rays in the GSB. Figure 5-12 shows the result of a gate on the $6_0^+ \to 4_0^+$ transition for all five targets. The raw count rates were higher than predicted from the matrix elements of the Hf(Xe,Xe)Hf experiment (already a surprisingly large cross section) by a factor of ≈ 10. The gated spectra of Figure 5-12 give an unambiguous indication that the isomer has been populated by *safe* Coulomb excitation with collision energies as low as 72% of the Coulomb barrier.
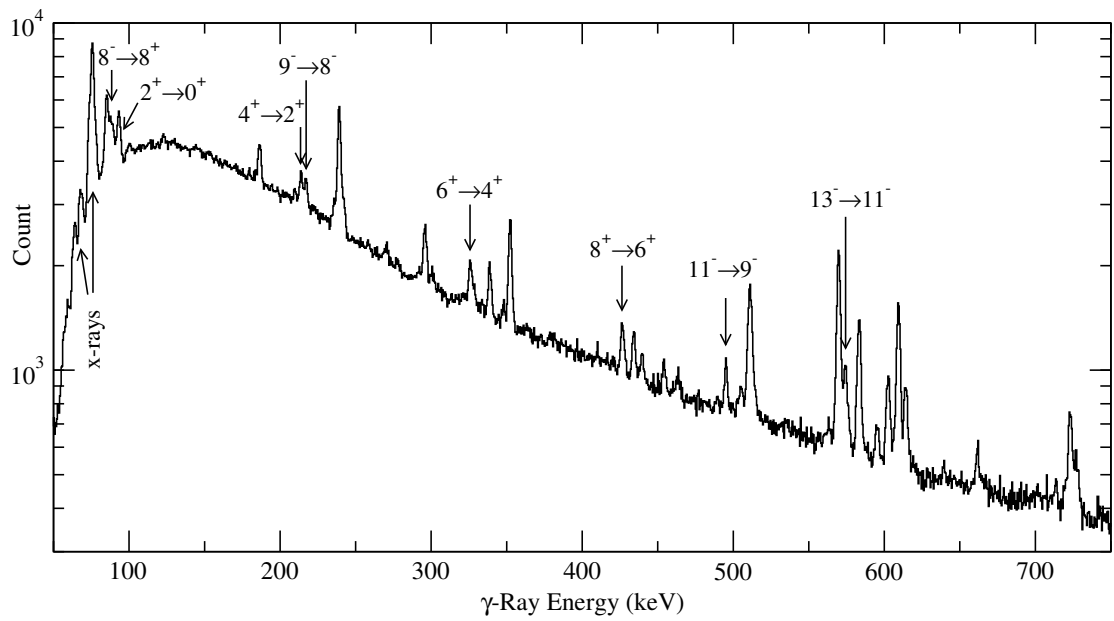
Figure 5-11: A raw γ-ray singles spectrum after 16 hours of data collection on target 1.
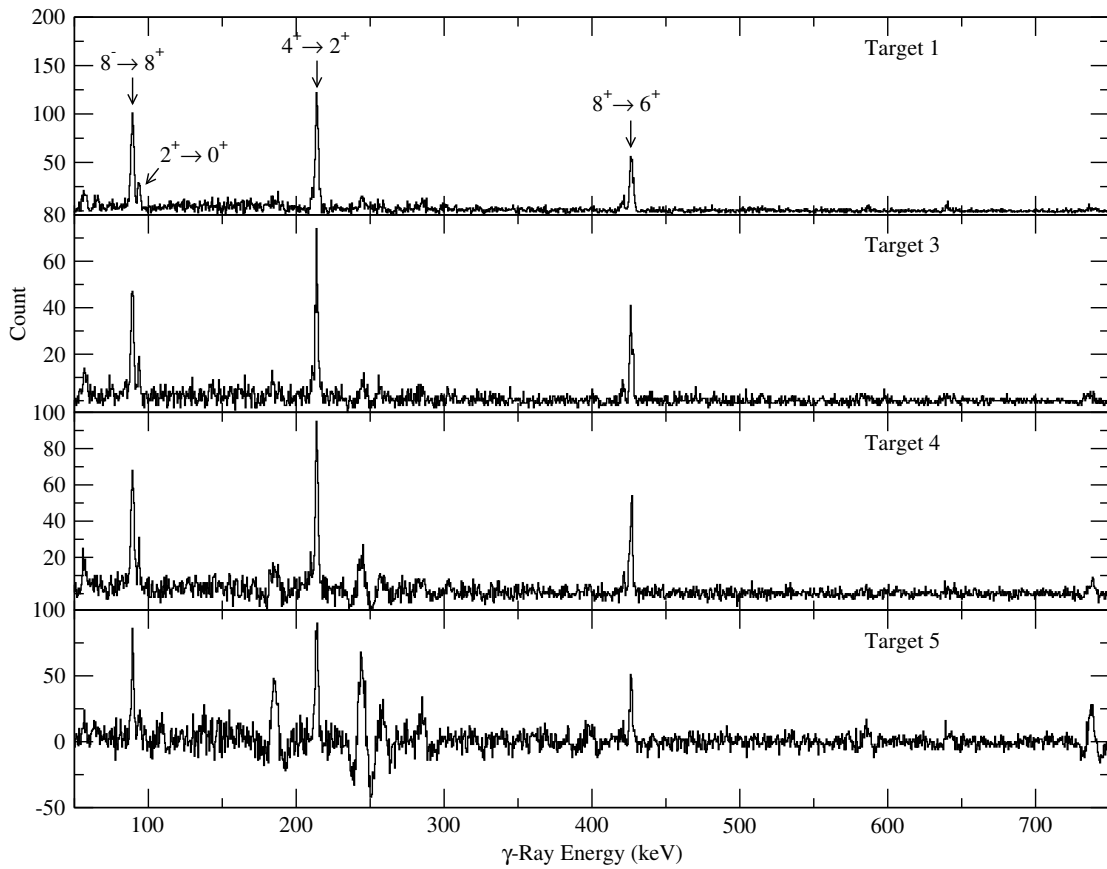
Figure 5-12: Four background-subtracted γ-ray doubles spectra gated on the 325 keV $6_0^+ \to 4_0^+$ GSB transition of ^{178}Hf. The different counting times are given in Table 5.1. Transitions from the 8^- isomer decay cascade are indicated by arrows.

128

Chapter 6

Experiment II Data Reduction

The measurement of matrix elements connecting states in the GSB to those in the $K = 16^+$ isomer band requires that the measured activity in each target be compared to the total dose (integrated ^{178}Hf beam flux) during the experiment. To this end, the present chapter is devoted to calculation of the dose and the subsequent normalization of the activity, while in Chapter 7 several models and sets of matrix elements are evaluated by fitting simultaneously to data from this experiment and the previous Hf^{178}(Xe^{136},Xe^{136})Hf^{178} online Coulomb excitation experiment.

6.1   Dose Measurements

6.1.1   Cross Section For Scattering Into Si Detector

The 0.254 cm diameter aperture on the Si detector subtends 0.17° at a distance of 17 inches from the scattering target, so the Rutherford cross section is nearly constant across the whole detector (Figure 6-1). For an average beam energy of 645 MeV in the sixth target of the stack, the Rutherford cross sections at 45° for the Hf and Ta are $\frac{d\sigma}{d\Omega} = 3.89$ b/sr and 3.83 b/sr, respectively (Figure 6-1). The total differential cross section for the sum of both particles is insensitive to the
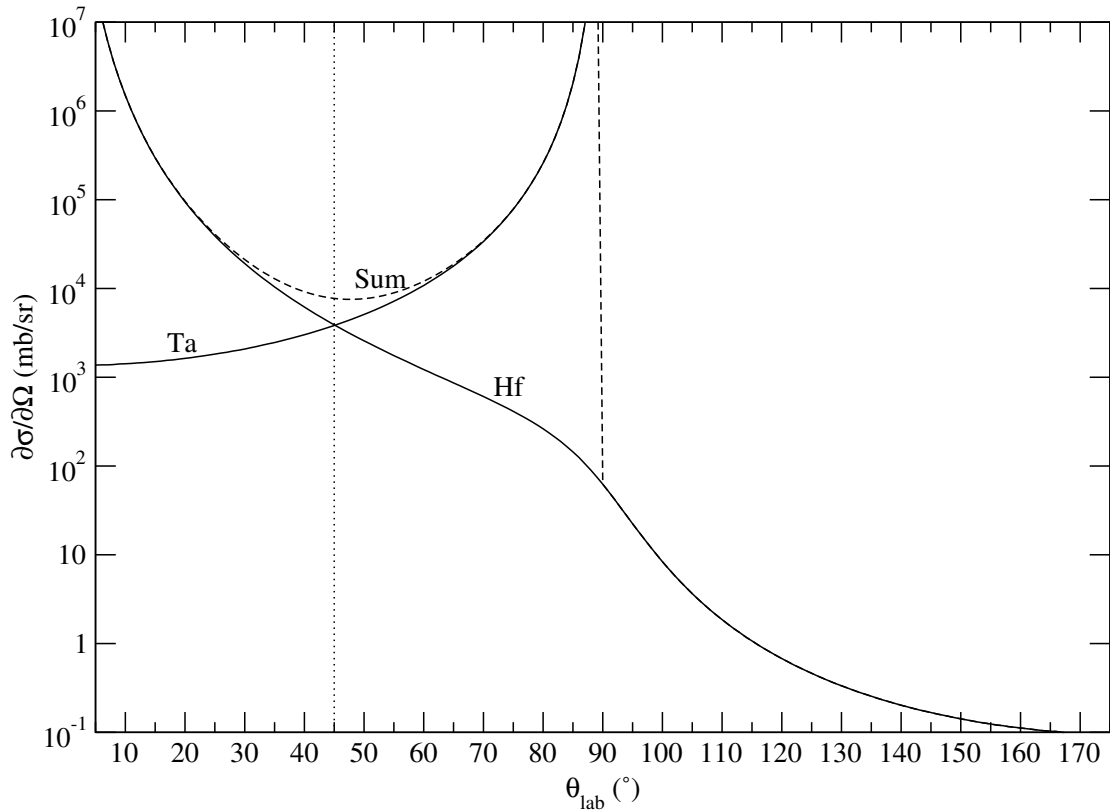
Figure 6-1: Rutherford scattering cross section for ^{178}Hf on natural (181) Ta at 645 MeV, the projectile energy at the middle of the scattering foil. The dashed line shows the sum of the cross sections of the two species. The dotted vertical line at 45° indicates the position of the Si detector, where the slope of the sum is nearly zero.

exact angle and is

$$\frac{d\sigma}{d\Omega} = 7.72 \text{b/sr}. \tag{6.1}$$

6.1.2 Counting Rate in Silicon Detector

The average "areal density" of the scattering target is $\rho_A = 1.0(1)$ mg/cm^2 as calculated from the total measured weight and total surface area. The counting rate in the silicon is

$$R[\frac{\text{ions}}{\text{sec}}] = \frac{d\sigma}{d\Omega} \times \frac{n}{A} \times I \times \Delta\Omega, \tag{6.2}$$

130

where

$$\frac{n}{A} = \frac{\rho_A N_A}{M_A} = 1.0 \frac{\text{mg}}{\text{cm}^2} \times \frac{6.022 \times 10^{23} \text{mol}^{-1}}{180.95 \frac{\text{g}}{\text{mol}}} = 3.328 \times 10^{18} \frac{\text{atoms}}{\text{cm}^2}, \qquad (6.3)$$

$I[\frac{\text{ions}}{\text{sec}}]$ is the beam current, and $\Delta\Omega[\text{sr}]$ is the solid angle subtended by the detector. So, the beam current can be calculated by

$$I = \frac{R}{\frac{d\sigma}{d\Omega} \times \frac{n}{A} \times \Delta\Omega} \qquad (6.4)$$

from a measurement of $R[\text{Hz}]$.

For an aperture of 0.254 cm diameter, 17.0 inches from the sixth scatterer (which was at the center of the chamber), $\Delta\Omega = 2.72 \times 10^{-5}$ sr. Then, the count rate gives the beam current by

$$
\begin{aligned}
I[\frac{\text{particles}}{\text{sec}}] &= \frac{R[\text{Hz}]}{7.72 \times 10^{-24} \frac{\text{cm}^2}{\text{sr}} \times 3.328 \times 10^{18} \text{cm}^{-2} \times 2.72 \times 10^{-5} \text{sr}} \\
&= 1.43 \times 10^9 \cdot R[\text{Hz}] \qquad (6.5)
\end{aligned}
$$

$$I[\text{pnA}] = \frac{1 \text{pnA}}{6.24 \times 10^9 \text{s}^{-1}} \times I[\text{particle} \cdot \text{s}^{-1}] = 0.229 \frac{\text{pnA}}{\text{Hz}} R[\text{Hz}] \qquad (6.6)$$

The total dose on the targets would then be $N \equiv \int I \, dt = 0.229 \text{pnCoul} \cdot C$, where C is the total number of counts on the silicon detector. $N[\text{particles}] = 1.43 X 10^9 C$. $N[\text{particle mCoul}] = 2.29 \times 10^{-7} C$.

6.1.3   Effect of Target Damage on Silicon Detector Accuracy

The silicon detector is believed to be more accurate in the absolute sense than the Faraday cup for integrating the total beam dose. During the run, the upstream Faraday cup gave a beam current of 14.6 pnA, while the downstream (beam-stop) Faraday cup gave a current of 21 pnA, assuming that the charge state of the upstream beam was 24^+, while $\bar{Q} = 47.3$ in the beam-stop Faraday cup. This discrepancy can not be reconciled by beam loss between the Faraday cups'

Run #	Si Peak Position (Channel)	Si FWHM	Si Counts, C (10^4)	Silicon Dose, N (pmCoul)	N_{cup} F. Cup (pmCoul.)	N_{cup}^{corr} Corrected (pmCoul.)
1	1655.5	197	47(2)	0.11(1) †	0.260	0.118(7)
2	1657.8	201	64(3)	0.15(2) †	0.322	0.146(9)
3	1649.1	198	4.3(2)	0.0099(14)†	0.0204	0.0093(5)
4	1655.9	214	45(2)	0.10(1) †	0.210	0.095(6)
5	1641.8	260	101(5)	0.23(3) †	0.542	0.246(15)
6	1577.3	334	93(9)	0.21(3)	0.673	0.30(2)†
7	*Total of over-*		30(3)	0.069(10)	0.206	0.093(5)†
8	*lapped peaks:*		76(8)	0.17(2)	0.478	0.217(13)†
9	"		109(11)	0.25(3)	0.661	0.30(2)†
10	"		18(9)	0.041(21)	0.133	0.060(4)†
11	"		47(23)	0.11(6)	0.319	0.144(9)†
Total:				1.45(9)	3.8	1.7(2)

Table 6.1: Scattered particle counts in the silicon detector. The Hf and Ta ions fall in the same peak. Peak (deposited energy, arbitrary units) position, energy FWHM and dose measurements are given for each run. Deterioration of the targets can be seen in the increase in the FWHM of the peaks in later runs.

positions, so the Si detector data must be used to calculate the dose. However, in later runs, damage to the target foils was becoming significant, and the Si energy peak became extremely broad, so that events were lost in the low-energy tail, resulting in under-counting. To measure the total integrated dose for the entire experiment, then, the Si detector was used to calibrate the Faraday cup from the first five runs (Figure 6-2), and the integrated current from the Faraday cup was used to measure the dose in the remaining runs (Table 6.1). Figure 6-2 shows in the first five runs that the Faraday cup current is proportional to the Si detector
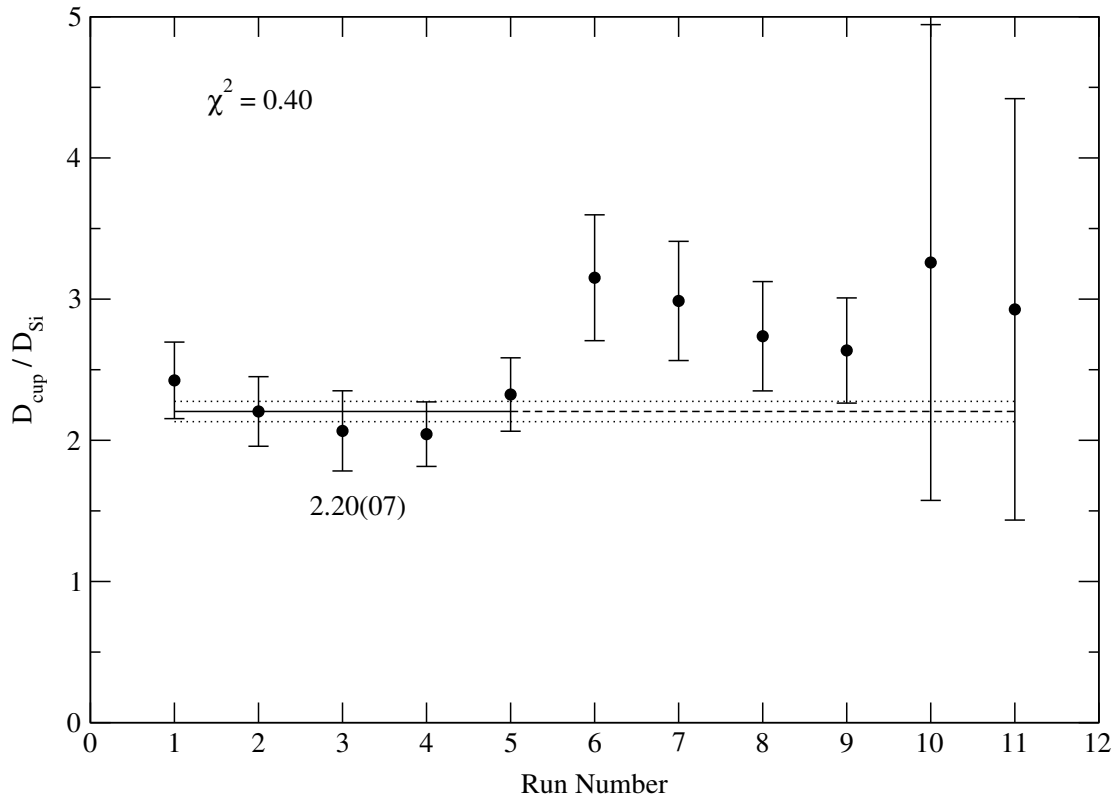
Figure 6-2: Ratio of integrated doses as measured by the Faraday cup and the Si detector. The mean (solid line) and errors (dashed lines) are shown for the first five runs.

rate.

6.1.4 Faraday Cup Data

The absolute doses as measured by the Faraday cup are not trustworthy, but the early measurements from the silicon detector, before much target damage occurred, can be used to normalize the Faraday cup data. The equilibrium average charge state after passing through 6 targets is calculated as $Q_6 = 47.3$. For a single $1\frac{mg}{cm^2}$ target, $Q_1 = 51.4$.

At equilibrium at a beam energy of 858 MeV, $\bar{Q} = 51.4$; at 626 MeV, $\bar{Q} = 47.3$ [95], so there is $< 9\%$ increase in Q_6 over the duration of the run, as long

as there is enough foil to reach charge state equilibrium, which must be the case, since the Si detector collected data throughout the run and the Faraday cup γ-ray yields indicated a total loss of only about 1.5 mg/cm^2 in all five targets and the scattering foil. Equilibrium is known to be achieved over thicknesses of ≈ 100 μg/cm^2 for heavy ions in foils [96, 97]. So, since the total change in $Q_6 < 9\%$, the total effect on the integrated dose must be significantly less, $\sim 1\%$. In fact, the total change in Q_6 resulting from the loss of 2 mg/cm^2 at an incident energy of 858 MeV is only about 1.3.

From the first five runs, the ratio of incident beam-particle counts in the Faraday cup to those in the Si detector is 2.20(7). The target damage would change the projectile energy in the scattering foil and subsequently the Rutherford cross section, so normalized Faraday cup data (normalized with the use of early run Si data) had to be used toward the end of the experiment for an accurate dose measurement.

6.1.5 Calculation of Cross Sections from the Activity and Dose Measurements

The absolute number of nuclei excited to the $K = 16^+$ isomer state by N incident beam particles is

$$
\begin{aligned}
N_{16^+} &= \frac{N N_A}{M_A} \sigma_{16^+} \\
&= \frac{6.24 \times 10^{15}}{\text{pmC}} \frac{\text{b}}{1000\text{mb}} \frac{10^{-24}\text{cm}^2}{\text{b}} \frac{\text{g}}{1000\text{mg}} \\
&\quad \times \frac{N[\text{pmC}] N_A[\text{mol}^{-1}]}{M_A[\frac{\text{g}}{\text{mol}}]} \sigma_{16^+}[\frac{\text{mb mg}}{\text{cm}^2}] \\
N_{16^+}[\text{atoms}] &= 6.24 \times 10^{-15} \frac{N[\text{pmC}] N_A[\text{mol}^{-1}]}{M_A[\frac{\text{g}}{\text{mol}}]} \sigma_{16^+}[\frac{\text{mb mg}}{\text{cm}^2}]
\end{aligned}
\tag{6.7}
$$

(Note that the cross section in the equation above has the dimensions of area·thickness and is integrated over the actual target thickness.)

The expected activity A_{16+} of N_{16+} atoms is $\frac{N_{16+}}{\tau}$ ($t_{1/2} = 31(1)$ y [98]), which can be calculated from N_{16+} above, the measured integrated doses and the calculated values of σ_{16+} from GOSIA.

$$A_{16+}\left[\frac{\text{counts}}{\text{hour}}\right] = 1.591 \times 10^{-20} \frac{N N_A}{M_A} \sigma_{16+} \qquad (6.8)$$

The total dose is $N = 1.7(2)$ pmC, rm so

$$A_{16+}\left[\frac{\text{counts}}{\text{hour}}\right] = 91(9)\, \sigma_{16+}. \qquad (6.9)$$

for all five targets.

6.2 Target Damage Assessment

6.2.1 Description

The intense beam current of ≈ 10 pnA gradually deteriorated all five targets and the scattering foil. The ablation of the targets during the experiment made the energy loss in each target a function of time, rather than a constant. To compensate for the thinning of the targets, the Rutherford cross section in the scattering target would have to be re-calculated or re-measured at regular intervals of beam dose, or, as described above, the Faraday cup could be used in the later runs as the sole monitor of the beam current and total integrated dose. In the case of the five foils used to activate the projectiles, the mean projectile energy would have to be measured as a function of time (assuming that all five targets were ablated at approximately equal rates over time).

6.2.2 Corrections To Projectile Energy Intervals

In addition to applying corrections to the total dose in each target for the target ablation, the Coulomb excitation calculations were integrated over energy intervals in each target that were corrected for the thinning of the targets. There

were two competing effects due to the thinning—increase in the initial projectile energy at the surface of each target (except the first target) and reduction of the energy interval of the beam in each target. These effects were taken to be approximately linear in the integrated beam flux.

Initially, the discrepancy between the measured (weight/area) target thickness and that calculated from the online GSB deexcitation γ-ray yields obtained as the beam stopped in the Faraday cup amount to about 10% of the total thickness, which may be attributed to nonuniformity of the target foils, wrinkles in the surface and so on. The GSB yields shown in figure 6-3 give a measurement of the thickness of the entire stack of 6 foils throughout the run. The total thickness was established by comparing the measurement and the calculation of the ratio $\frac{Y_{8\rightarrow6}}{Y_{6\rightarrow4}}$ of GSB yields from Coulomb excitation of the ^{178}Hf beam particles stopping in the Faraday cup. Coulomb excitation of the GSB is accurately reproduced by the rigid rotor model, and the GSB yield ratios give a sensitive measure of the incident energy on a thick target (e.g. the Faraday cup), which is equivalent to the exit energy from the stack of six foils and allows an accurate measurement of the thickness from the known stopping power [99].

As the targets were ablated gradually throughout the experiment, the increase in the incident beam energy on the Faraday cup was demonstrated by the steady increase in the quantity $\frac{Y_{8\rightarrow6}}{Y_{6\rightarrow4}}$. Figure 6-4 illustrates two possible assumptions that could be derived from the trend in Figure 6-3. Either the initial thickness measurement could be taken from the weight measurement (assumption A), or the GSB yields could be used from the beginning to the end of the run to measure the target stack thickness (assumption B), using only the relative weight measurements to calculate the thickness of individual foils. The well-understood GSB yield ratios were used (assumption B), while the *relative* thicknesses of the foils were measured by $\rho_A = \frac{\text{mass}}{\text{area}}$, to determine the thickness versus time as in the solid-line fit to the data in Figure 6-3. (The uniformity of rolled targets is typi-
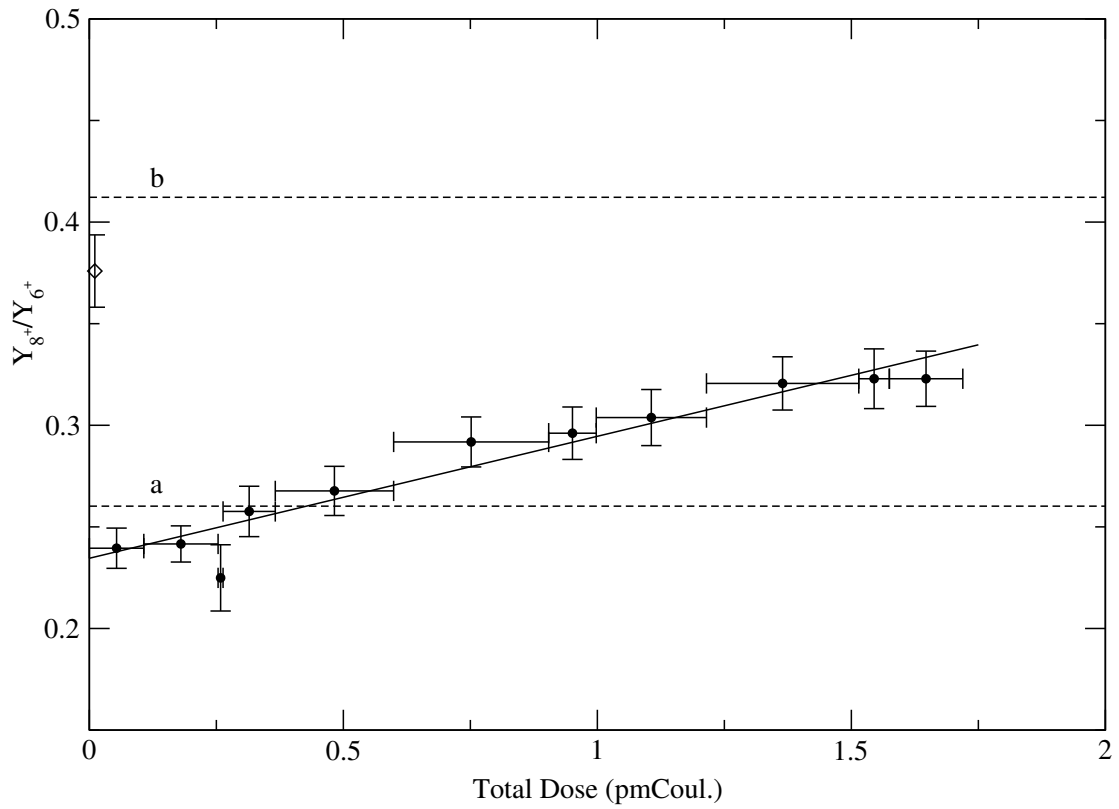
Figure 6-3: Online measurement (during beam activation) of the ratio of the $8^+ \rightarrow 6^+$ yield to the $6^+ \rightarrow 4^+$ yield in the GSB of ^{178}Hf, corrected for Ge efficiency, after stopping in the Faraday cup. Measured points (circles—6-foil stack; diamond—single foil) are corrected for the relative detection efficiency. X-axis intervals represent the dose intervals. (a) calculated for stopping in the Faraday cup after penetration of the measured thickness of all six foils, 5.7(6) mg/cm^2. (b) Calculated for stopping after penetration through the 1.0(1) mg/cm^2 scattering foil.

cally not better than 10%.) Figure 6-5 shows the results of both assumptions in terms of the the energy intervals for integration of the Coulomb excitation fits.
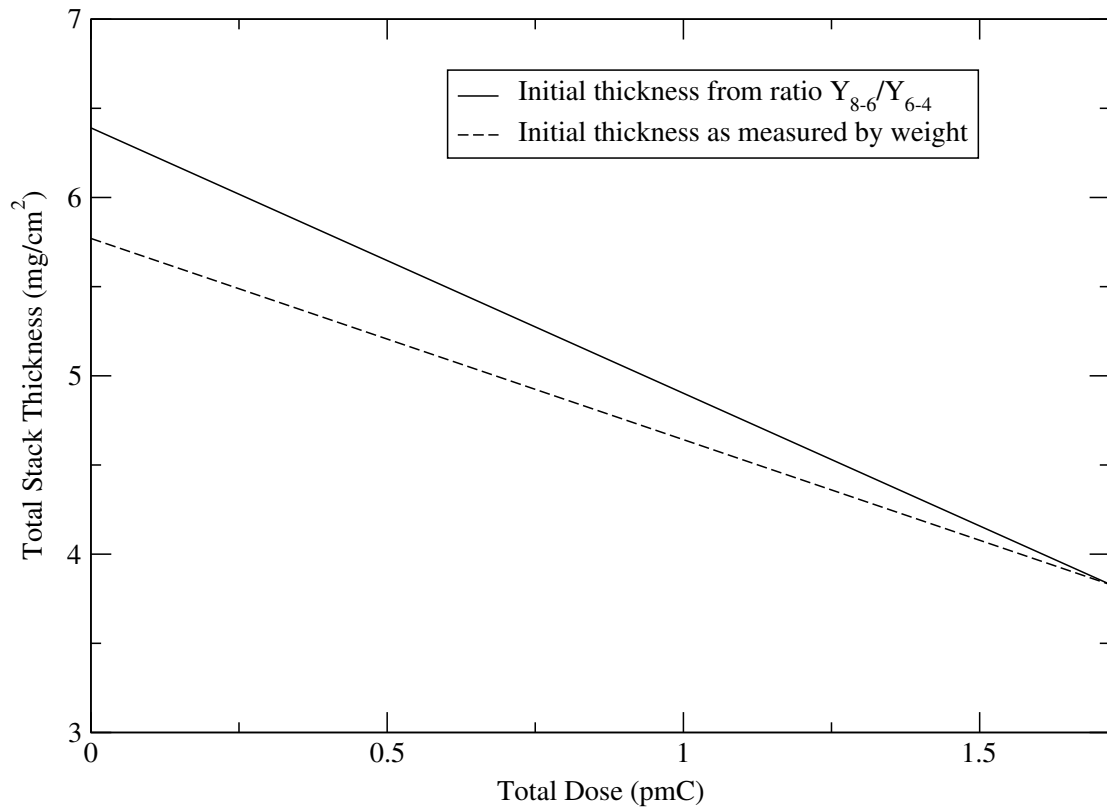
Figure 6-4: The reduction in foil thickness over time. The solid line shows the thickness of the stack assuming that the online GSB yields from the Faraday cup accurately give the initial thickness. The dashed line takes the initial thickness from the weight and surface area measurements.

6.3 Absolute Activity

The isomer activity varies linearly with the raw rates measured in the Ge clover detectors, but there are statistical and geometrical correction factors that must be considered. The absolute efficiency of the individual detectors must be included in the activity measurement, whereas in the Hf(Xe,Xe)Hf experiment relative γ-ray yields required the knowledge of relative efficiency only. The finite size of the Ge detectors and the attenuating effect of the aluminum housing is incorporated in the absolute efficiency, which was calculated numerically. The geometric effects

138
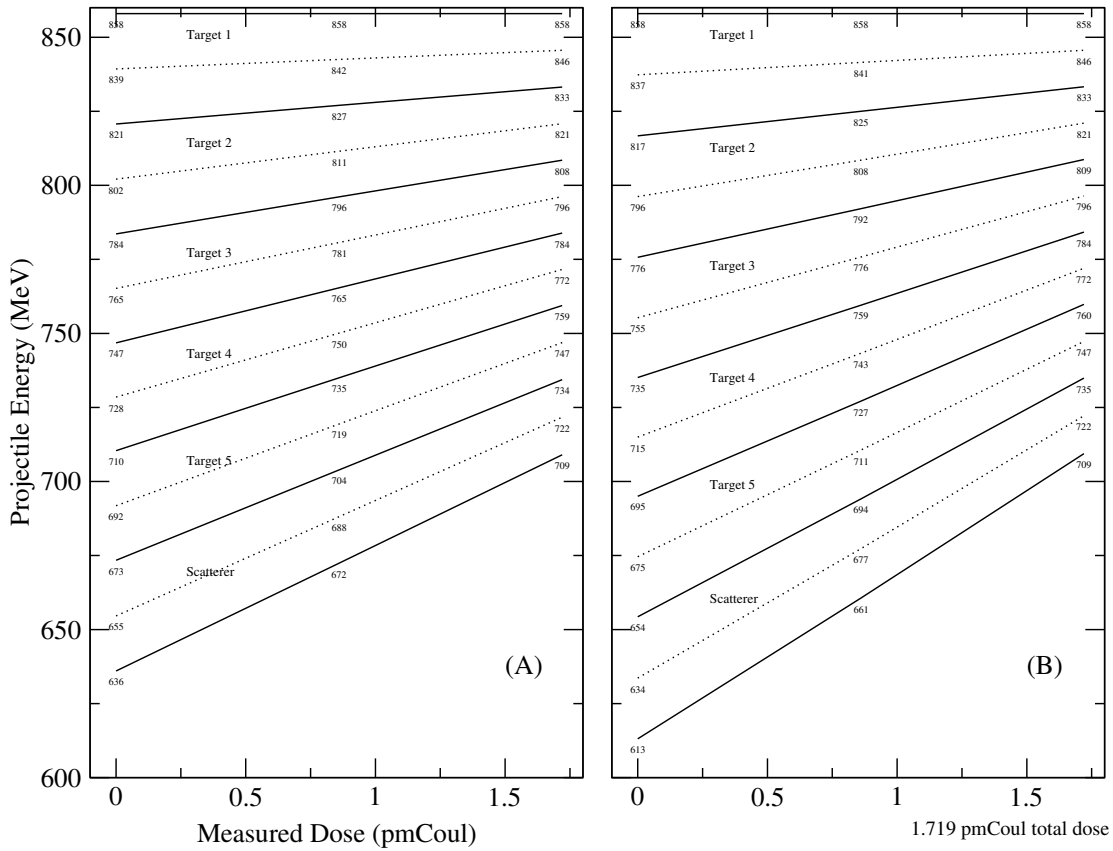
Figure 6-5: The calculated energy intervals versus the measured dose for the Hf projectiles traversing the targets throughout the activation run. Target deterioration is seen as the increase in mean beam energy (dotted lines) at the target mid-point and the narrowing of the energy interval. Solid lines show the incident and exit energies of the projectiles for each target. (A) Initial thickness calculated from the target weight. (B) Thickness taken from the measured ratio $\frac{Y_{8\rightarrow6}}{Y_{6\rightarrow4}}$.

are included in the form of angular correlation functions W, used in computing the probabilities of two particular γ rays being emitted with a particular angular separation θ. The calculations of the angular correlation functions are treated separately for cases of consecutive and non-consecutive γ decays, where nuclear deorientation diminishes the angular correlation effects. Summing (capture of two or more γ rays in the same Ge crystal) and detection probabilities are both treated

using the angular correlation functions, W.

6.3.1 Singles and Doubles Rate

The measured singles rates for the GSB 325 keV $6^+ \to 4^+$ and 426 keV $8^+ \to 6^+$ transitions are linear functions of the absolute isomeric activity A which feeds them in all decay branches, the correction for undetected internal conversion events $\kappa \equiv \frac{1}{1+\alpha}$, the average absolute efficiency (including Compton events) ϵ of the clover segments, the peak-to-total ratio P and the probability that summing (of two γ-rays in one detector) did not obscure the observation of the γ ray. V is the probability that no summing events occurred, that is, that no other photons in the GSB decay cascade entered the detector segment where the photon of interest was detected.

$$S^{426} \;\; = \;\; 8A\kappa^{426}\epsilon^{426}P^{426}V^{426} \tag{6.10}$$

and

$$S^{325} \;\; = \;\; 8A\kappa^{325}\epsilon^{325}P^{325}V^{325}, \tag{6.11}$$

The factor 8 accounts for the 8 individually triggered segments in the two-clover arrangement. The probability V of zero summing can be expressed by the following functions, where $W(\theta, E_{\gamma 1}, E_{\gamma 2})$ is the correlation function giving the probability of emission of two particular photons, $\gamma 1$ and $\gamma 2$, separated in space by an angle θ. Decays are identified by the γ-ray energies for brevity (Figure 4-1). The angle θ_n is the separation between a detector #0 defined by the detection of one γ ray and detector #n, according to the relative positions defined in Figure 6-8. Summing events then have $\theta_0 \equiv 0$ by definition. The no-summing probabilities V for the 325 keV and 426 keV GSB transitions are given by

$$
\begin{aligned}
V^{426} \;\; \equiv \;\; & 1 - W(\theta_0, 426, 325)\kappa^{325}\epsilon^{325} - W(\theta_0, 426, 213)\kappa^{213}\epsilon^{213} \\
& - W(\theta_0, 426, 93)\kappa^{93}\epsilon^{93} - W(\theta_0, 426, 88)\kappa^{88}\epsilon^{88},
\end{aligned} \tag{6.12}
$$

and

$$V^{325} \equiv 1 - W(\theta_0, 325, 426)\kappa^{426}\epsilon^{426} - W(\theta_0, 325, 213)\kappa^{213}\epsilon^{213}$$
$$-W(\theta_0, 325, 93)\kappa^{93}\epsilon^{93} - W(\theta_0, 325, 88)\kappa^{88}\epsilon^{88}. \qquad (6.13)$$

The measured doubles (γ-γ) rates are proportional to the product $\kappa\epsilon P$ for each γ ray, as in the following. (Measurement of the 93 keV and 213 keV decays are difficult because of the long lifetime ($t_{\frac{1}{2}} = 1.5$ ns) of the 93 keV 2^+ level and overlap of other γ-ray peaks near 213 keV. Accurate doubles rates could only be obtained for the 325 keV $6 \rightarrow 4$ and 426 keV $8 \rightarrow 6$ transitions.)

$$D^{426,325} \equiv D = 8A\kappa^{426}\epsilon^{426}P^{426}\kappa^{325}\epsilon^{325}P^{325}\Pi_{\mathrm{ns}}S_W, \qquad (6.14)$$

where Π_{ns} is the probability that no summing occurred in the detectors that counted the 426 and 325 keV γ's, and S_W is the probability that the two photons were emitted in the directions of any two different detectors.

$$S_W = W(\theta_1, 325, 426) + W(\theta_2, 325, 426) + \cdots + W(\theta_7, 325, 426) \qquad (6.15)$$

$$\Pi_{\mathrm{ns}} = [1 - W(\theta_0, 325, 213)\kappa^{213}\epsilon^{213} - W(\theta_0, 325, 93)\kappa^{93}\epsilon^{93}$$
$$-W(\theta_0, 325, 88)\kappa^{88}\epsilon^{88}] \times [1 - W(\theta_0, 426, 213)\kappa^{213}\epsilon^{213}$$
$$-W(\theta_0, 426, 93)\kappa^{93}\epsilon^{93} - W(\theta_0, 426, 88)\kappa^{88}\epsilon^{88}] \qquad (6.16)$$

The peak-to-total ratio P can be calculated from the measured ratio of doubles to single and is given by the equations

$$P^{325} = \frac{1}{\Pi_{\mathrm{ns}}S_W}\frac{V^{426}}{\kappa^{325}\epsilon^{325}}\frac{D}{S^{426}}, \qquad (6.17)$$

and

$$P^{426} = \frac{1}{\Pi_{\mathrm{ns}}S_W}\frac{V^{325}}{\kappa^{426}\epsilon^{426}}\frac{D}{S^{325}}, \qquad (6.18)$$

which will be used below in the calculations of the final count rates.

6.3.2 Angular Correlations Between γ Rays

For the rapid emission of a γ-ray cascade of collective transitions ($t_{\frac{1}{2}} < 1$ ps) by an excited nucleus, the nucleus does not have time to deorient, and angular correlation effects become important considerations in counting experiments. It is necessary to consider the sum effects of all possible cascades where low-granularity detectors are used (as in the present experiment), even when these cascades are not being counted individually.

Pairs of Consecutive E2 Transitions The angular correlation function for a pair of consecutive γ rays which couple even spin states is given by Ferguson [100],

$$
\begin{aligned}
W'(\theta) \ = \ & (4\pi\hat{b})^{-2} \sum_{kL_1L_1'L_2L_2'} (-)^{a-c-L_1-L_1'+k} \bar{Z}_1(L_1bL_1'b; ak)\bar{Z}_1(L_2bL_2'b; ck) \\
& \times \langle b\|L_1\|a\rangle \langle b\|L_1'\|a\rangle^* \langle c\|L_2\|b\rangle \langle c\|L_2'\|b\rangle^* \\
& \times Q_k(1)Q_k(2)P_k(\cos\theta),
\end{aligned}
\tag{6.19}
$$

where the pair of γ rays subtend the angle θ. The odd values of k in the summation are relevant only in cases of polarization and will not be required here. The initial, intermediate and final states (*e.g.* Figure 6-6) are given by a, b and c. L_1, L_2 are the operators representing the γ-ray emission for a particular multipolarity, and L_1', L_2' are operators for a second multipolarity, if they exist. The functions $Q_k(1)$ and $Q_k(2)$ describe the detection efficiency of the measured γ-rays 1 and 2. Q_0 is the familiar first-order efficiency, and the higher order terms represent the angular attenuation. For brevity, the factors $\hat{x}$ are substituted for $\sqrt{2x+1}$ after Ferguson. The $\bar{Z}_1$ terms are defined in terms of Racah coefficients $W(j_1j_2l_2l_1; j_3l_3)$ and Clebsch-Gordan coefficients $\langle j_1m_1j_2m_2 \mid j_3m\rangle$ as

$$
\bar{Z}_1(LbL'b'; qk) \equiv (-)^{k-L+L'-1}\hat{L}\hat{L}'\hat{b}\hat{b}'\langle L1L'^{-1} \mid k0\rangle W(LbL'b'; qk)
\tag{6.20}
$$

after Ferguson [100]. The Racah coefficients can be expressed as 6-j symbols using

$$\left\{ \begin{array}{ccc} j_1 & j_2 & j_3 \\ l_1 & l_2 & l_3 \end{array} \right\} = (-)^{j_1+j_2+l_1+l_2} W(j_1 j_2 l_2 l_1; j_3 l_3) \tag{6.21}$$

after Rotenberg [101].

W can be defined in terms of W' so that it is independent of the matrix elements, giving

$$
\begin{aligned}
W(\theta) &\equiv \frac{(4\pi)^2 W'(\theta)}{Q_0(1)Q_0(2)} \cdot \frac{1}{\langle b \| L_1 \| a \rangle \langle b \| L_1' \| a \rangle^* \langle c \| L_2 \| b \rangle \langle c \| L_2' \| b \rangle^*} \\
&= \frac{1}{\hat{b}^2 Q_0(1)Q_0(2)} \sum_{kL_1 L_1' L_2 L_2'} (-)^{a-c-L_1-L_1'+k} \bar{Z}_1(L_1 b L_1' b; ak) \bar{Z}_1(L_2 b L_2' b; ck) \\
&\quad \times Q_k(1)Q_k(2)P_k(\cos\theta),
\end{aligned} \tag{6.22}
$$

It may then be normalized so that

$$\frac{1}{(4\pi)^2} \int \int W(\theta) d\Omega_{\gamma_1} d\Omega_{\gamma_2} \equiv 1 \tag{6.23}$$

for events without summing in a 4π detector array. In that case, $W(\theta) \approx 1$ indicates that angular effects are small. Sums over L_1, L_1', L_2 and L_2' are irrelevant, because the matrix elements are zero for all but one mode of decay.

$$
\begin{aligned}
W(\theta) &= \frac{1}{\hat{b}^2 Q_0(1)Q_0(2)} [a_0 Q_0(1)Q_0(2) + a_2 Q_2(1)Q_2(2)P_2(\cos\theta) \\
&\quad + a_4 Q_4(1)Q_4(2)P_4(\cos\theta)],
\end{aligned} \tag{6.24}
$$

$(P_0(\cos\theta) \equiv 1)$ where

$$a_k \equiv \bar{Z}_1(L_1 b L_1' b; ak) \bar{Z}_1(L_2 b L_2' b; ck). \tag{6.25}$$

The odd k terms arise only when there is polarization [100], which is not the case for decays from states that are fed by long-lived isomers. For even k and no interfering multipolarities $(L = L')$, $k - L + L' - 1$ takes odd values. In the absence of competing transitions, $L = L'$ and $b = b'$, and $j_1 + j_2 + l_1 + l_2$ is even.

143

Figure 6-6: The consecutive transitions $8^+ \to 6^+$ and $6^+ \to 4^+$ used to measure activity by gated doubles. The spins a, b and c are defined in the figure. $L_1 = L_1' = 2$. $L_2 = L_2' = 2$.

The overall sign is negative, and

$$\bar{Z}_1(LbL'b'; qk) = -\hat{L}\hat{L}'\hat{b}\hat{b}'\langle L1L'^{-}1 \mid k0\rangle \begin{Bmatrix} L & b & q \\ b' & L' & k \end{Bmatrix}. \qquad (6.26)$$

In the cases where $L_1 = L_2 = L_1' = L_2' = ''L''$, i.e. all GSB cascades that do not include the 88 keV E2 isomer decay,

$$
\begin{aligned}
a_k &\equiv \bar{Z}_1(L_1bL_1'b; ak)\bar{Z}_1(L_2bL_2'b; ck) \\
&= \hat{L}^4\hat{b}^4\langle L1L^{-}1 \mid k0\rangle^2 \begin{Bmatrix} L & b & a \\ b & L & k \end{Bmatrix} \begin{Bmatrix} L & b & c \\ b & L & k \end{Bmatrix}.
\end{aligned}
\qquad (6.27)
$$

$$(6.28)$$

144

In the case of the $8^+ \to 6^+ \to 4^+$ cascade (figure 6-6), $L_1 = L_1' = 2$, $L_2 = L_2' = 2$, $a = 8$, $b = 6$, and $c = 4$, giving

$$
\begin{aligned}
\frac{a_0}{\hat{b}^2} &= \bar{Z}_1(2626; 80)\bar{Z}_1(2626; 40)\frac{1}{2b+1} \\
&= 1 \\
\frac{a_0}{\hat{b}^2} &= 0.102 \\
\frac{a_0}{\hat{b}^2} &= 0.009
\end{aligned}
$$

γ^3 **Correlations**   The angular correlation for a $\gamma\gamma\gamma$ cascade with the intermediate γ undetected is given by,

$$
\begin{aligned}
W(\theta) &= \frac{1}{Q_0(1)Q_0(3)}\sum (-)^{L_1 - L_1' + L_2}\bar{Z}_1(L_1 b L_1' b; ak)W(bcbc; L_2 k)\bar{Z}_1(L_3 c L_3' c; dk) \\
&\quad \times Q_k(1)Q_k(3)P_k(\cos\theta), \hspace{4cm} (6.29)
\end{aligned}
$$

again with the normalization $\iint W(\theta)d\Omega_1 d\Omega_2 \equiv 1$. (The 88 keV $8^- \to 8^+$ transition is almost entirely E1, so summation over L_1, L_1', etc. in a cascade of the 88 keV, 426 keV and 325 keV γ's is also irrelevant, as in the previous cases, because the matrix elements are identically zero by the selection rules.) The factor $(-)^{L_1 - L_1' + L_2}$ can be dropped, because all $L_1 = L_1'$, even in the case of the E1 transition, since there is no significant competing branch, and $L_2 = 2$ in every case.

$$
\begin{aligned}
W(\theta) &= \frac{1}{Q_0(1)Q_0(3)}[b_0 Q_0(1)Q_0(3) + b_2 Q_2(1)Q_2(3)P_2(\cos\theta) \\
&\quad + b_4 Q_4(1)Q_4(3)P_4(\cos\theta)], \hspace{3cm} (6.30)
\end{aligned}
$$

where

$$
\begin{aligned}
b_k &\equiv \bar{Z}_1(L_1 b L_1' b; ak)\bar{Z}_1(L_3 c L_3' c; dk)W(bcbc; L_2 k) \\
&= \bar{Z}_1(L_1 b L_1' b; ak)\bar{Z}_1(L_3 c L_3' c; dk)\left\{\begin{array}{ccc} b & c & L_2 \\ c & b & k \end{array}\right\} \\
&= \hat{L}_1^{\,2}\hat{L}_3^{\,2}\hat{b}^2\hat{c}^2\langle L_1 1 L_1^- 1 \mid k0\rangle\langle L_3 1 L_3^- 1 \mid k0\rangle
\end{aligned}
$$

145

10⁻

237

454 9⁻

217

8⁻ 8- Isomer

a 8⁺   88

426

b 6⁺

325

c 4⁺

213

d 2⁺

0⁺ 93
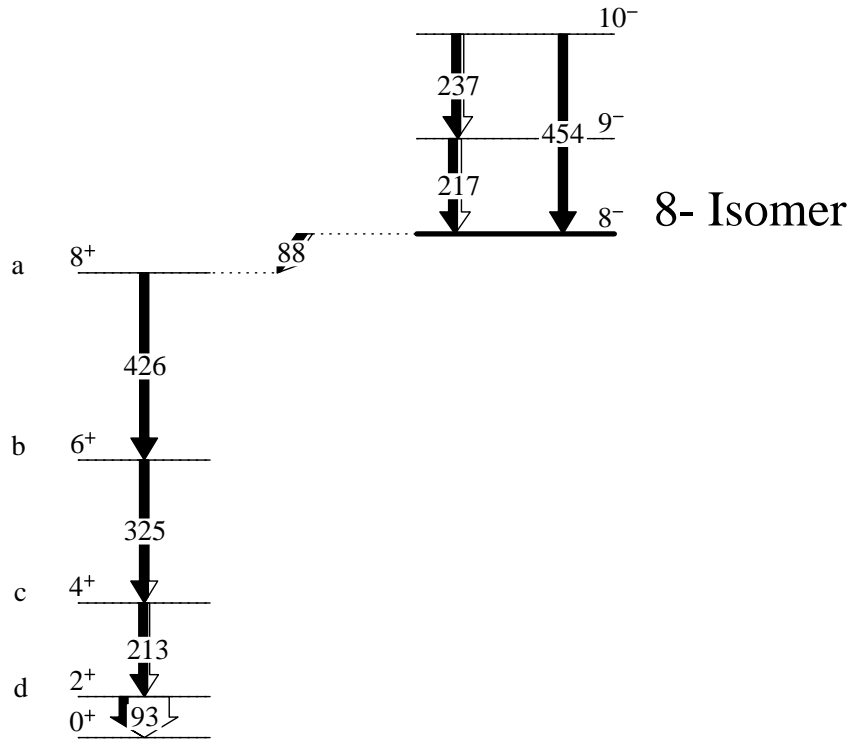
Ground State Band

Figure 6-7: An example of a γ^3 cascade with the intermediate transition unobserved. The spins a, b, c and d are defined in the figure. The first transition is $a \to b$, the second is $b \to c$, and the third is $c \to d$. $L_1 = L_1' = 2$. $L_2 = L_2' = 2$. $L_3 = L_3' = 2$.

$$\times \left\{ \begin{array}{ccc} L_1 & b & a \\ b & L_1 & k \end{array} \right\} \left\{ \begin{array}{ccc} L_3 & c & d \\ c & L_3 & k \end{array} \right\} \left\{ \begin{array}{ccc} b & c & L_2 \\ c & b & k \end{array} \right\} \tag{6.31}$$

Figure 6-7 shows a γ,γ,γ cascade with the second transition undetected.

For the cascade in figure 6-7,

$$b_0 = 1.00000$$

$$b_2 = 0.10204$$

$$b_4 = 0.00907$$

γ^4 **Correlations** There is one correlation factor $W(\theta_0, 426, 93)$ which treats a γ^4 cascade with the *two* intermediate transitions unobserved. The correlation factors for $\gamma - \gamma$ and γ^3 transitions are already close to 1 (Table 6.6), and $W(\theta) \to 1$ as the number of intermediate *unobserved* transitions becomes large. Furthermore, $W(\theta_0, 426, 93)$ occurs with ϵ^{93}, which is a small quantity, so this γ^4 term will taken as ≈ 1.

Calculation of the Q_k Terms The angle subtended by two γ-rays incident on a pair of detectors was computed for each permutation of two detectors in the array. The angles θ_n are defined relative to leaf number 0, arbitrarily chosen in Figure 6-8. These angles and the Legendre polynomials of Table 6.2 were used to compute the angular correlation functions using the geometric symbols of Figure 6-9. Point approximations were used, rather than integrations over the detector surfaces, assuming axially symmetric detectors.

The values of Q_n depend partly on the geometry. To correct for the oblique trajectory of the incident γ rays, in light of the fact that the Q_n's are not meaningful without axial symmetry, the Ge diameter was adjusted in the calculations of Q_n from the actual value of ≈ 5 cm. Without any aluminum shielding to attenuate the γ rays, the geometrical upper limit on the efficiency of a single leaf is $< \frac{4\pi}{8}$, since there is $\lesssim 4\pi$ coverage by the two clovers. Normalizing calculated values of the efficiency in the Ge crystals to the effective surface area for off-axis γ rays, the upper limit of the "effective diameter" of each leaf can be set at 3.05 cm. The distance traversed by a γ ray in the 0.15 mm aluminum shield was $\frac{0.15 \text{mm}}{\cos 71.3°} = 0.47$ mm. The values of Q_n were calculated, including the attenuation in the aluminum shields (Table 6.4).

Calculation of the Angular Correlation Functions The values of $a_k/\hat{b}^2$ and b_k which were calculated for the particular pairs of γ-rays counted (Table 6.5) show that the second order and fourth order terms make $\approx 10\%$ and $\approx 1\%$ contributions,
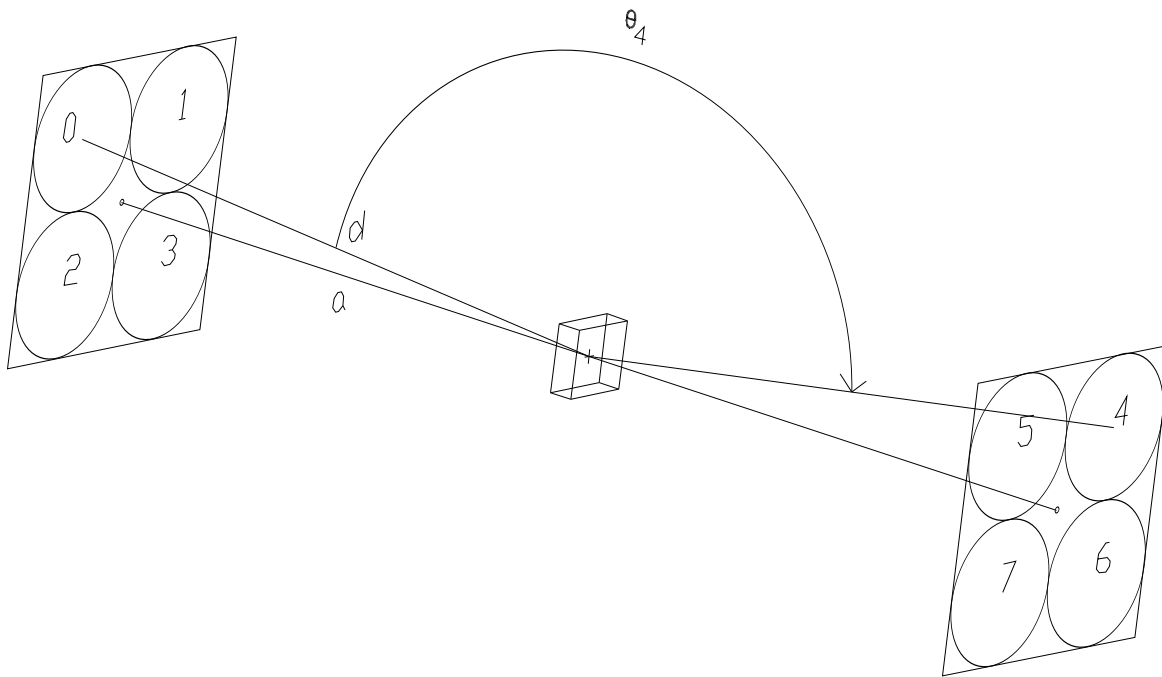
Figure 6-8: The numbering scheme for the clover detectors. An arbitrarily chosen γ-ray defines detector #0, and other γ-rays in the same event are numbered according to this arrangement. Angles θ_n are defined relative to leaf #0, so that $\theta_0 \equiv 0$. $\theta_4(= \theta_7)$ is shown here.

respectively. Higher order terms are not necessary. The correlation functions were calculated from these values and are listed for each permutation of pairs of γ-rays and detectors in Table 6.6. The angular correlation corrections are $< 10\%$ in all cases.
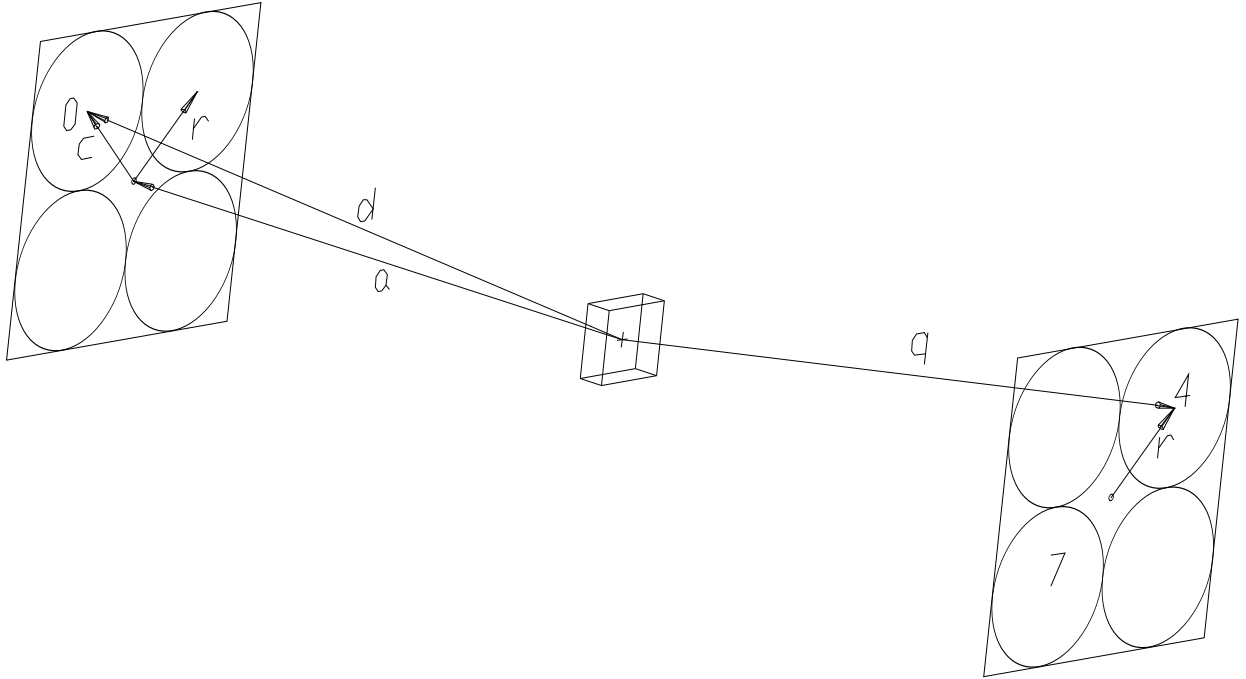
Figure 6-9: Vectors defined to calculate the opening angle between two γ rays. The paths of two photons, $\vec{d}$ and $\vec{q}$, incident on two detectors (taken to be detectors 0 and 4 in the example) are shown, along with the displacement of the center of a clover $\vec{a}$ and the center of a detector $\vec{r}$. ($\theta_4 = \theta_7$ by symmetry.)

Detector, n	θ_n	$\cos(\theta_n)$	$P_2(\cos\theta_n)$	$P_4(\cos\theta_n)$
0	$\equiv 0$	1	1	1
1,2	$2\sin^{-1}(b/d) = 84.2°$	0.101	-0.485	0.337
3	$2\sin^{-1}(c/d) = 143°$	-0.799	0.457	-0.237
4,7	$\cos^{-1}(-a^2/d^2) = 95.9°$	-0.102	-0.484	0.336
5	$\pi - 2\sin^{-1}(c/d) = 37.0°$	0.799	0.457	-0.237
6	$180.0°$	-1.00	1.00	1.00

Table 6.2: Angular separation between each detector and the arbitrarily chosen detector #0. Values of the Legendre polynomials used in the correlation functions.

149
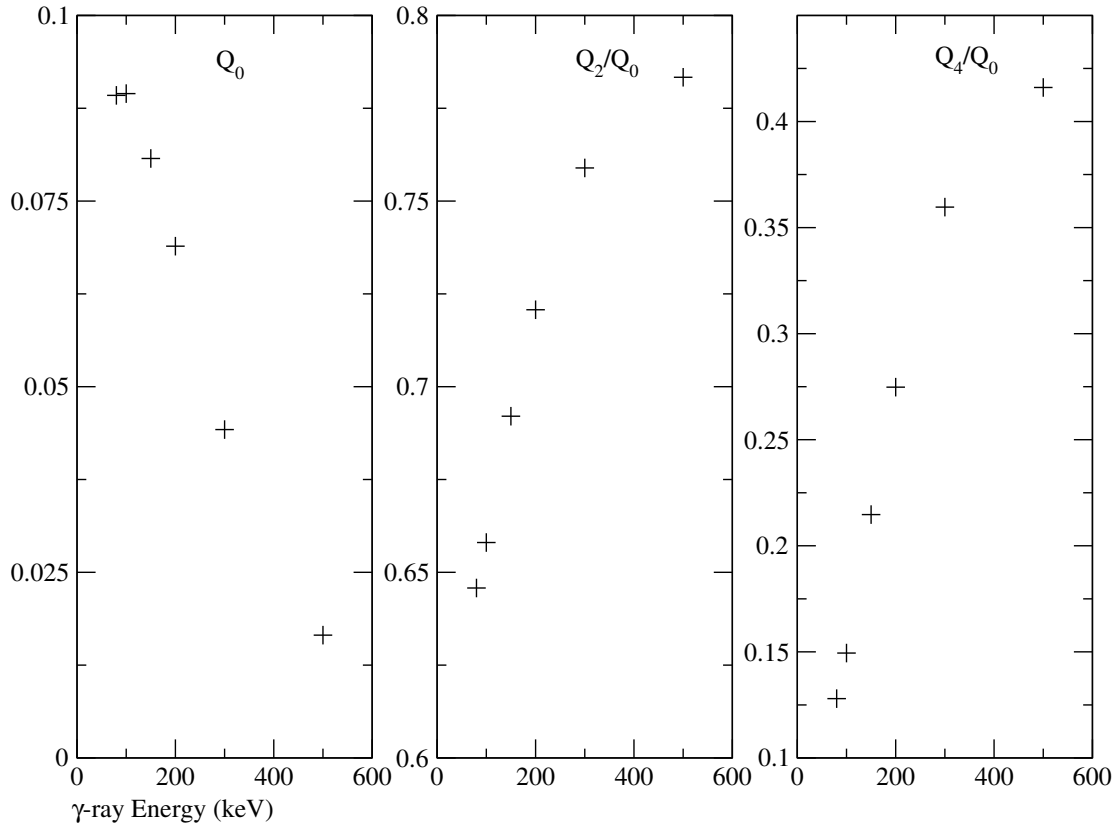
Figure 6-10: Q_0, Q_2 and Q_4 vs. γ energy, all calculated for a 3.05 cm diameter Ge crystal. Intermediate values were interpolated.

E_γ(keV)	α	$\kappa \equiv \frac{1}{1+\alpha}$
93	4.80	0.172
213	0.236	0.809
325	0.0631	0.941
426	0.0296	0.971
88(E1)	0.502	0.666

Table 6.3: Values of the internal conversion coefficients for the five measured decays in the 8^- cascade. Values of α were interpolated from [3].

	E(keV)				
n	88	93	213	325	426
0	0.089336	0.089396	0.064202	0.0418421	0.0256298
2	0.058154	0.058512	0.046593	0.0320956	0.0200830
4	0.012104	0.012753	0.018417	0.0156982	0.0105611

Table 6.4: $Q_n(E)$ values calculated for the five observed γ-rays in the cascade.

Correlated γ's (keV)	$\frac{a_0}{\hat{b}^2}$	$\frac{a_2}{\hat{b}^2}$	$\frac{a_4}{\hat{b}^2}$	$(Q_0(1)Q_0(2))^{-1}$
213, 325	1.000	0.102	0.009	372.
325, 426	1.000	0.102	0.009	932.
88, 426	1.000	0.170	0	437.
(γ^3)	b_0	b_2	b_4	$(Q_0(1)Q_0(3))^{-1}$
213, 426	1.000	0.102	0.009	608.
93, 325	1.000	0.102	0.009	267.
88, 325	1.000	0.167	0	267.

Table 6.5: a_n and b_n values for the angular correlation functions.

6.3.3 Calculation of Activity from Count Rates

The measured activities of the targets are given in Table 6.7 for the two single-γ transitions measured and the $\gamma\gamma$ measurement using the 325 keV and 426 keV transitions. Peak-to-total ratios were calculated from these measurements as follows. The peak-to-total ratio P^E is given by equations 6.17 and 6.18 and the calculated values of $\epsilon^E \equiv Q_0(E)$.

From equation 6.16, the probability of there being no sum-events of the 325

n	θ_n	$E_{\gamma 1}, E_{\gamma 2}$	$P_2(\cos\theta_n)$	$P_4(\cos\theta_n)$	$W'(\theta_n)$	$W(\theta_n)$
0 †	0	213,325 γ^2	1	1	0.0028416	1.05779
0 †	0	213,426 γ^3	1	1	0.0017427	1.05908
0 †	0	325,426 γ^2	1	1	0.0011426	1.06546
0 †	0	426,93 γ^4	1	1	(γ^4)	$\doteq 1$
0 †	0	426,88 γ^2	1	1	0.0024875	1.08641
0 †	0	325,93 γ^3	1	1	0.0039340	1.05173
0 †	0	325,88 γ^3	1	1	0.0040546	1.08469
1,2	84.2	213,325 γ^2	-0.485	0.337	0.0026132	0.97277
1,2	84.2	213,426 γ^3	-0.485	0.337	0.0015998	0.97224
1,2	84.2	325,426 γ^2	-0.485	0.337	0.0010439	0.97342
3	143	213,325 γ^2	0.457	-0.237	0.0027554	1.02571
3	143	213,426 γ^3	0.457	-0.237	0.0016887	1.02626
3	143	325,426 γ^2	0.457	-0.237	0.0011050	1.03039
4,7	84.1	213,325 γ^2	-0.484	0.336	0.0026113	0.97206
4,7	84.1	213,426 γ^3	-0.484	0.336	0.0015999	0.97230
4,7	84.1	325,426 γ^2	-0.484	0.336	0.0010441	0.97361
5	37.0	213,325 γ^2	0.457	-0.237	0.0027554	1.02571
5	37.0	213,426 γ^3	0.457	-0.237	0.0016887	1.02626
5	37.0	325,426 γ^2	0.457	-0.237	0.0011050	1.03039
6	180.0	213,325 γ^2	1.00	1.00	0.0028415	1.05776
6	180.0	213,426 γ^3	1.00	1.00	0.0017427	1.05908
6	180.0	325,426 γ^2	1.00	1.00	0.0011426	1.06546

Table 6.6: Values of the angular correlation function for detector numbers n as in Figure 6-8 calculated for the five observed γ-rays in the cascade. † indicates summing of two γ rays in the same detector. γ^2 indicates a $\gamma - \gamma$ correlation. γ^3 indicates a $\gamma - \gamma - \gamma$ correlation with the middle transition unobserved. γ^4 indicates a 4-γ correlation with the middle *two* transitions unobserved.

E_{beam}	Count	Singles Rate (h^{-1})		Doubles
(% Barrier)	Time(h)	S^{325}	S^{426}	$D(h^{-1})$
88 (targ. 1)	16.5	173(10)	123(9)	19.9(14)
80 (targ. 3)	17.5	80.2(61)	73.2(71)	10.6(10)
76 (targ. 4)	105.6	24.4(19)	17.3(15)	2.46(21)
72 (targ. 5)	237	6.89(164)	10.9(14)	1.04(9)

Table 6.7: The measured "raw" rates for targets 1,3,4 and 5, uncorrected for efficiency.

and 426 keV γ rays is

$$\Pi_{\mathrm{ns}} = 0.748$$

From Table 6.6, the following probabilities can be calculated.

$$S_W = 7.02$$

$$V^{426} = 0.823$$

$$V^{325} = 0.838$$

From equations 6.17 and 6.18, P^{325} and P^{426} are given by

$$P^{325} = \frac{1}{\Pi_{\mathrm{ns}} S_W} \frac{V^{426}}{\kappa^{325} \epsilon^{325}} \frac{D}{S^{426}}$$
$$= 3.98 \frac{D}{S^{426}},$$

and

$$P^{426} = \frac{1}{\Pi_{\mathrm{ns}} S_W} \frac{V^{325}}{\kappa^{426} \epsilon^{426}} \frac{D}{S^{325}}$$
$$= 6.41 \frac{D}{S^{325}},$$

using the conversion coefficients of Table 6.3.

Target, n	P^{325}	P^{426}
1	0.64(6)	0.74(7)
3	0.58(8)	0.85(10)
4	0.57(7)	0.65(7)
5	0.38(6)	0.97(24)

Table 6.8: Summary of measured peak-to-total ratios, P.

Table 6.8 shows a summary of the measurements of P for the four targets. Since P is a measurement of Compton scattered events, it is independent of background and count rates. P is a figure of merit for the detectors alone and must be equal for all 5 targets. Only the values with the best statistics were used, the two values obtained from target 1, $P_{\text{tgt1}}^{426} = 0.74(7)$ and $P_{\text{tgt1}}^{325} = 0.64(6)$ were used to calculate the final activity.

Activity from Singles Rates Using the values of P calculated above and the measured activities, the activity A of each target can be calculated from the measured singles rate S^{426} or S^{325}, equation 6.10 or 6.11. (The two are not independent measurements, because of the method employed above to obtain the efficiencies.)

$$
\begin{aligned}
A^{426} &= \frac{1}{8\kappa^{426}\epsilon^{426}V^{426}} \cdot \frac{S^{426}}{P_{\text{tgt1}}^{426}} \\
&= 8.3(7)\ S^{426}
\end{aligned}
\tag{6.32}
$$

$$
\begin{aligned}
A^{325} &= \frac{1}{8\kappa^{325}\epsilon^{325}V^{325}} \cdot \frac{S^{325}}{P_{\text{tgt1}}^{325}} \\
&= 5.9(6)\ S^{325}
\end{aligned}
\tag{6.33}
$$

Activity from the Doubles Rate Equation 6.14 gives the activity from the doubles rate of 325 keV and 426 keV γ rays.

$$
\begin{aligned}
A_D &= \frac{1}{8\kappa^{426}\epsilon^{426}\kappa^{325}\epsilon^{325}\Pi_{\mathrm{ns}}S_W} \cdot \frac{D}{P_{\mathrm{tgt1}}^{426}P_{\mathrm{tgt1}}^{325}} \qquad (6.34) \\
A_D &= 51(7) \cdot D
\end{aligned}
$$

Summary of Activity Calculations The Activities S^{426}, S^{325} and D are not independent quantities for the first target as they were calculated above. Internal measurements of ϵP using data from target 1, rather than independently measured values, entangled the activities derived from the S^{426}, S^{325} and D values. The measurements of the targets' activities are summarized in Table 6.9. Figure 6-11 shows the activities calculated above. The activity of each target is still above the value expected from calculations based on the $^{178}\mathrm{Hf}(^{136}\mathrm{Xe},^{136}\mathrm{Xe})^{178m2}\mathrm{Hf}$ Coulex experiment.

The cross sections shown in Table 6.9 are calculated for the average target thickness during the ablation of the target material. This introduces another $\approx 20\%$ error in σ_{16+}, calculated from the change in the calculated cross section as the integration limits in projectile energy change throughout the experiment (Figure 6-5).

The activity measurement from gated double-γ data is considered more accurate than the single-γ measurement, because the background is lower and cleaner when gating on the γ-γ matrix. In particular, target number 5, activated at $\approx 72\%$ of the Coulomb barrier shows a 55% difference in the two activity measurements from singles, while the relative errors in the activity from doubles are comparable to the errors in the activity from singles, 17% compared to 12% in the worst case, the slightly larger errors resulting from the necessity of more efficiency corrections in the doubles rates.

Target, n	$A^{325}(h^{-1})$	$A^{426}(h^{-1})$	$D(h^{-1})$	σ_{16+} (mb)
1	1020(120)	1020(120)	1020(160)	11(3)
3	600(80)	470(60)	540(90)	6(2)
4	140(20)	140(20)	130(20)	1.4(4)
5	90(14)	40(11)	53(9)	0.6(2)

Table 6.9: Summary of measured activities of the 4 measured targets. Note that A^{426}, A^{325} and D are not independent measurements in the case of target 1. The cross sections σ_{16+} are calculated from the values D.
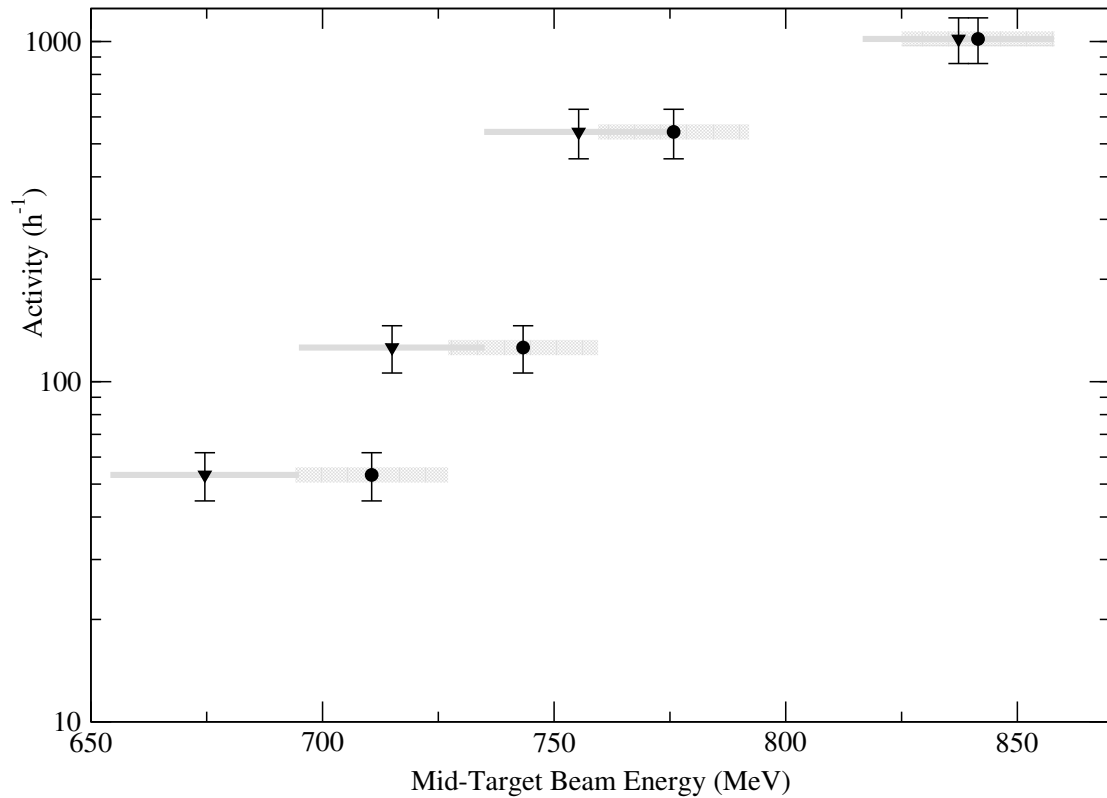
Figure 6-11: Activities versus projectile energy. The triangles show the activity plotted versus the projectile energy calculated from the measured target thickness, assumed to be constant throughout the experiment. The circles show the activity plotted against the time-averaged energy intervals based on the continuous online measurements of target deterioration. The thickness was taken entirely from online γ-ray yields.

Chapter 7

Matrix Elements for the $K^\pi = 16^+$ Band

The 16^+ isomer activity data of Chapter 6 and the prompt 19^+_{16} yields of the first experiment were combined in an effort to find a single set of matrix elements which would reproduce the data of both experiments. Unsuccessful attempts were made using the SDM model and a second spin-dependent model to reduce the number of fit parameters because only 8 data points were available. These methods are described in the section "Model-Based Fits." Ultimately, the GSB$\rightarrow K^\pi = 16^+$ matrix elements were adjusted individually to reproduce the data, observing the physical constraints on the feeding intensity from the GSB, the reasonable upper limits on $B(E2)$ values, etc. This is described in the section "Direct Fit of Matrix Elements." The final section evaluates the effect that feeding from the 14^- isomer into the 16^+ isomer state would have on the results.

7.1 One-Parameter Model-Based Fits

As explained below, it was not possible to simultaneously reproduce the measured activity of the implanted hafnium in the second experiment and the mea-

sured 19^+ level yield of the hafnium target in the first experiment using variations on the SDM model. Two attempts to fit the data using at most two parameters are described below.

7.1.1   SDM Model

The spin-dependent mixing model successfully employed earlier in this work could not be made to reproduce the observed isomer activity without introducing unrealistically large matrix elements at the top of the GSB. As the only adjustable parameter in this model $\langle K = 16 \mid E2 \mid K = 0 \rangle$ was increased, the $B(E2)$ values became unrealistically large, while the calculated isomer activity was still too low by a factor of $\approx$3—6, as seen in Figure 7-1. Using the SDM model, values of hundreds of W.u. at the top of the GSB would be required in order to reproduce the observed isomer activation.

The approximately exponential increase of the reduced matrix elements in the SDM model with increasing spin produces unrealistically large matrix elements connecting the levels of the GSB and the $K = 16$ bands around spin $20\hbar$ (Figure 7-2), and modest matrix elements near the $K = 16$ band head, suggesting an adjustment to the SDM model. A model that will accurately predict the observed isomer populations with realistic $B(E2)$ values must have larger matrix elements at low spin and significantly smaller matrix elements at high spin, compared to the SDM model.

7.1.2   "Linear" Model

A plausible modification to the SDM model is to use a linear variation of the intrinsic matrix element with increasing spin I_f in the $K = 16$ band, where the coupling between the bands takes the same form in the Clebsch-Gordan coefficients as in the SDM model [43] (coupling $K_f - \lambda$ to K_f, where $\mathcal{M}\lambda$ is the transition
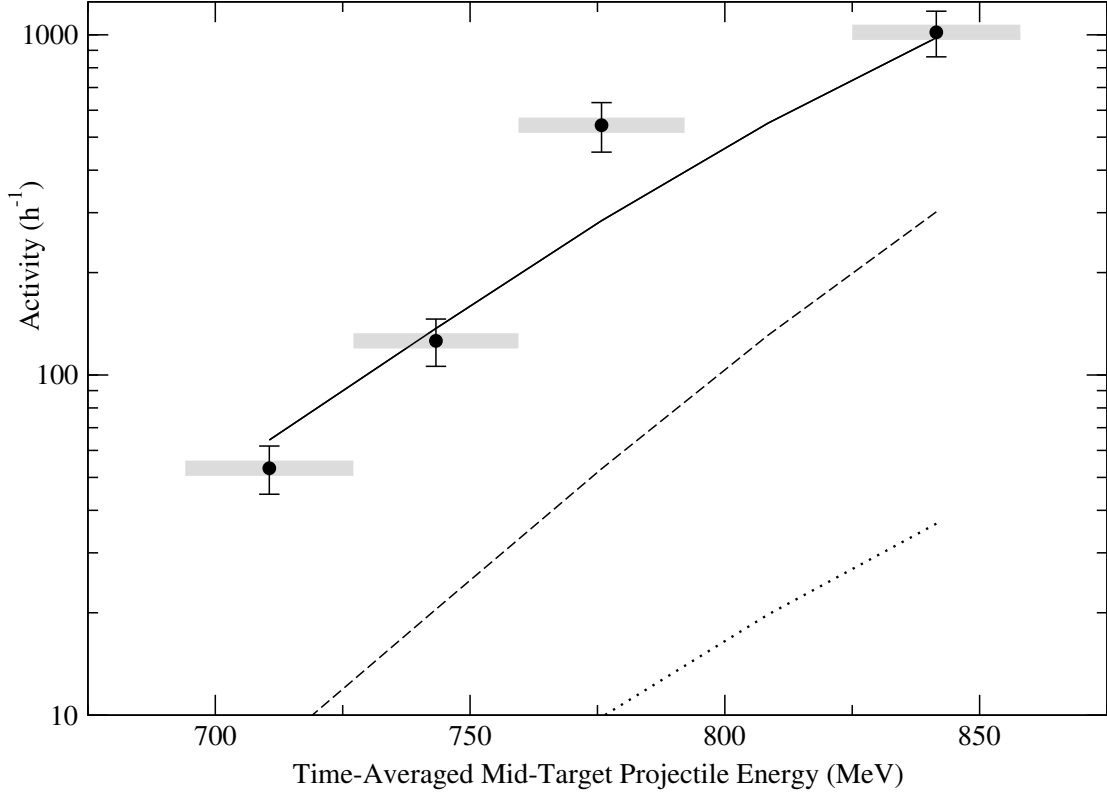
Figure 7-1: Experimental and calculated activity. The result of the direct fit of individual matrix elements (solid line) gave $\chi^2 = 3.5$. The activity calculated using the SDM model (dashed line) with an intrinsic matrix element $\langle K = 16 \mid E2 \mid K = 0 \rangle = 1.09 \times 10^{-18}$ eb, 20% larger than in the fit to the Hf(Xe,Xe)Hf Coulomb excitation experiment, would not reproduce the measurements. The linear model fit (dotted line) normalized to the SDM model fit at $\langle 19^+_K = 16 \| E2 \| 18^+_{\text{GSB}} \rangle = 0.381$ eb was least effective.

multipolarity), but the factor $\sqrt{\frac{(I_1 - K_1)!(I_1 + K_1 + n)!}{(I_1 - K_1 - n)!(I_1 + K_1)!}}$ is replaced by a factor of the form $\alpha + \beta I_f$. In this case, the reduced matrix elements are

$$
\langle I_f, K = 16 \| E2 \| I_i, K = 0 \rangle = \sqrt{2I_i + 1} \langle I_i K_f - \lambda \, \lambda\lambda \mid I_f K_f \rangle (1 + \delta_{K_1,0}[\sqrt{2} - 1])
$$

$$
\times (\alpha + \beta I_f) \langle K_f \mid E2 \mid K_i \rangle. \tag{7.1}
$$

Figure 7-2 shows the matrix elements obtained by adjusting parameters α and β so that the largest matrix element coupling to $I_f = 19$ takes the same value

160
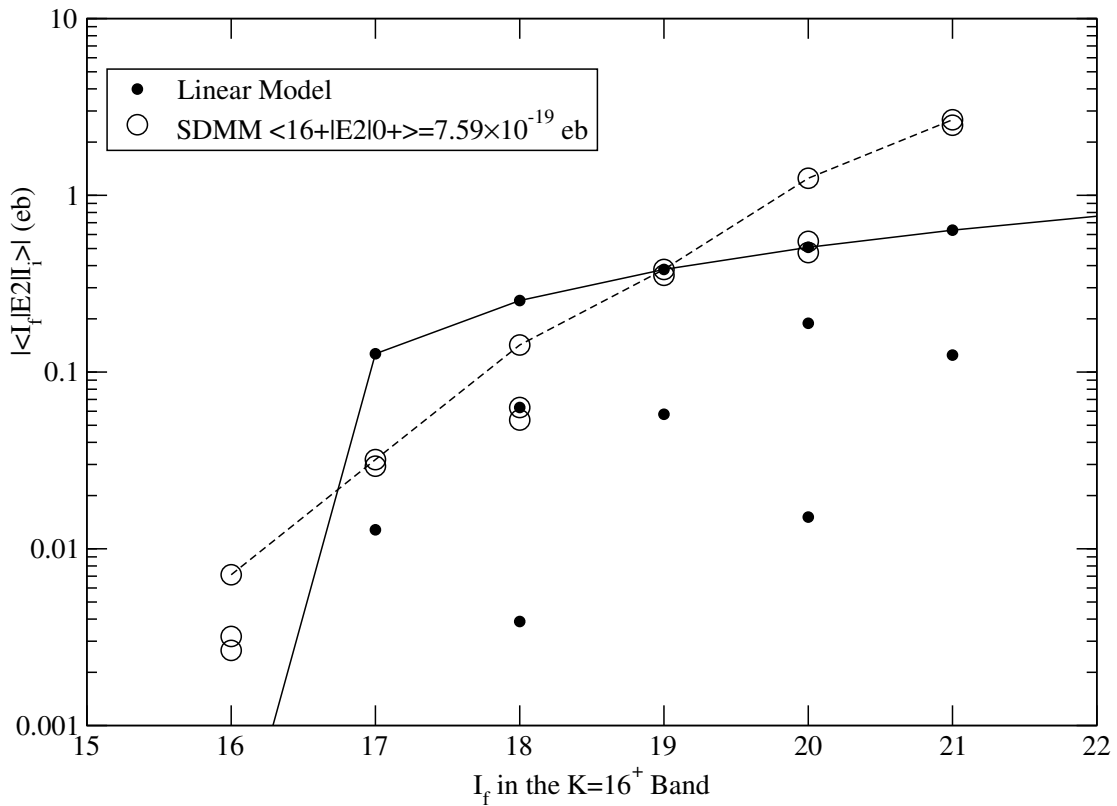
Figure 7-2: Matrix elements of the SDM and linear models normalized at the 19^+ level in the $K = 16$ band.

as in the SDM model fit in the Hf(Xe,Xe)Hf experiment. This normalization is based upon the assumption that the matrix elements connecting to the 19^+ level are most important in reproducing the $19^+ \rightarrow 18^+$ yield observed in the first experiment.

The linear model predicts yields nearly an order of magnitude lower than the SDM model for the highest energy target, with the two models normalized at spin 19^+ (Figure 7-2). As in the previous fit with the SDM model, increase in the population with increasing $B(E2)$ strength is less than linear, so unrealistically large matrix elements at the upper levels would result from increasing the intrinsic matrix element to reproduce the activity.

The coupling to the highest levels is known from the previous experiment to be relatively ineffective, and the largest matrix elements at spins 17^+ through 19^+ are equal to or exceed those of the SDM model, suggesting that the relative strengths of matrix elements with a common I_f are too varied in the present linear model. Had there not been such a large drop in the predicted yield in changing from the SDM model to this linear model, it might have seemed appropriate to retain the present model and adjust α and β in Equation 7.1, but the present coupling scheme is clearly ineffective.

7.2 Direct Fit of Matrix Elements

It was found during the manual adjustment of the matrix elements that the majority ($\gtrsim 75\%$–80%) of the isomer activation comes directly from connections between the GSB and the 17^+ and 16^+ isomer band levels (*e.g.* Figure 7-3), as long as K-mixing between the GSB and the isomer band increases with increasing spin and that reasonable upper limits are imposed on the $B(E2)$ strengths (*e.g.* 10% of the $B(E2)$ strength of the transitions within the GSB). This means that the activity calculated for the Ta(Hf,Hf)Ta experiment and the $19^+ \rightarrow 18^+$ yield calculated for the Hf(Xe,Xe)Hf experiment can be adjusted almost independently, an obvious constraint being that a smooth, monotonic trend in the magnitudes of the matrix elements is maintained.

A second constraint on the fit is that the matrix elements do not introduce γ-decay feeding strengths greater than the upper limits set by non-observation of feeding transitions in the Hf(Xe,Xe)Hf experiment. The feeding limits are $\approx 10^{-4}$ relative to the $8^+_{\text{GSB}} \rightarrow 6^+_{\text{GSB}}$ yield and are represented graphically in Figure 7-4.

The complete set of matrix elements from this fit (Table 9.14) along with upper and lower limits and diagonal errors are shown in Figure 7-4. There was not sufficient sensitivity to determine the set of matrix elements with correlated
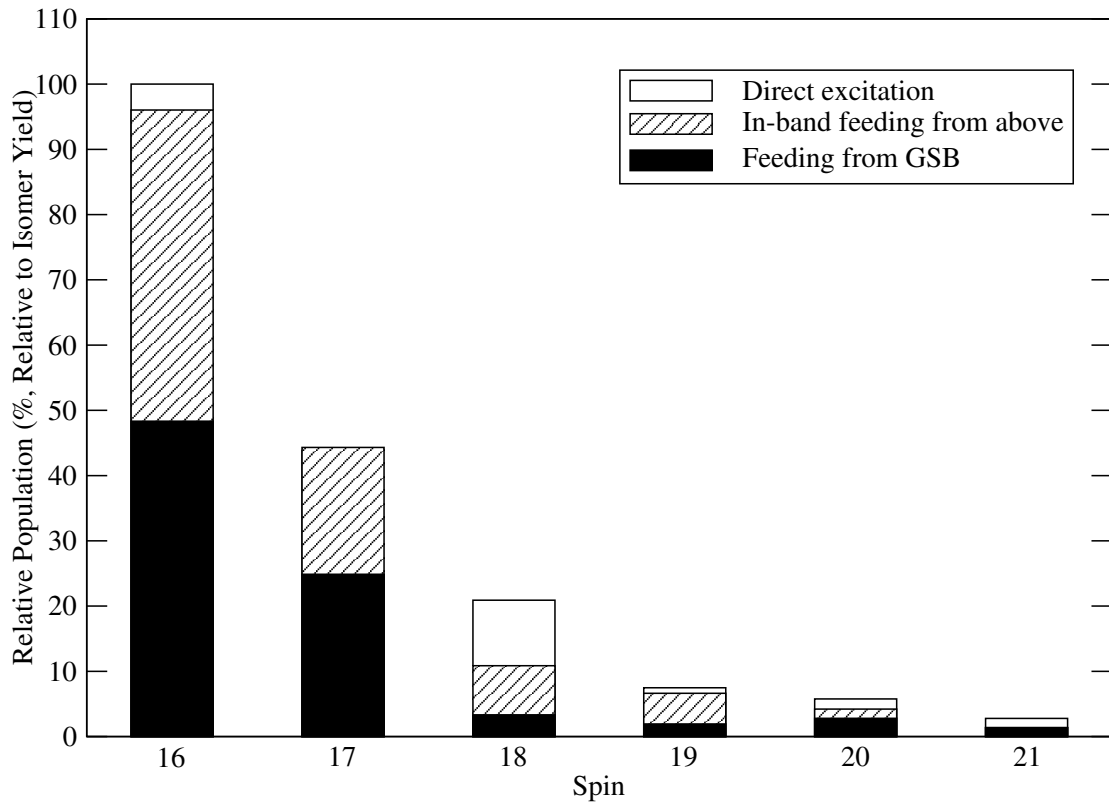
Figure 7-3: Population modes of the 16^+ isomer band based on the fit of matrix elements. The fractions of the population of each level attributed to direct Coulomb excitation and γ-decay feeding are shown for Hf(Xe,Xe)Hf scattering over $52°-78°$. The final set of matrix elements described in the text were used to calculate the three contributions.

errors, but a coherent set of matrix elements with upper limits, some lower limits and diagonal (uncorrelated) errors was found that meets the physical constraints described above. The relationships between the effects of some particular matrix elements used to steer the fit are detailed below.

Figure 7-1 shows the agreement between the calculated and measured isomer activity from the Ta(Hf,Hf)Ta experiment with $\chi^2 = 3.5$. The slope and magnitude are reproduced, the largest χ^2 contribution coming from the third target. (Recall that the energy range was incorporated in χ^2 by including an additional
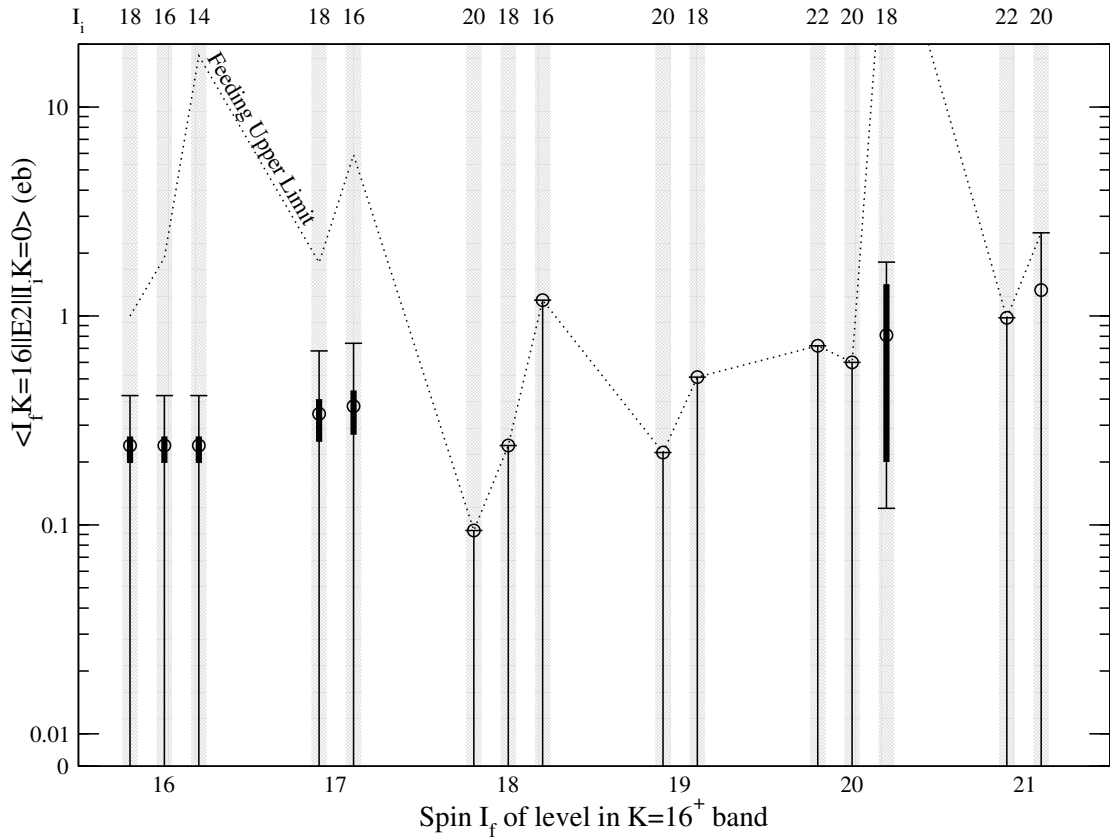
Figure 7-4: Final set of matrix elements (magnitudes only) connecting the GSB to the 16^+ isomer band. Matrix elements (circles) are shown with diagonal error estimates (black bars) and upper and lower limits ($\top$ and $\perp$) where they could be determined. The dotted line represents the upper limits on the matrix elements calculated from measured the upper limits on feeding.

20% error in the activity, as described in chapter 6). The agreement with the measured $19^+ \rightarrow 18^+$ γ-ray yield $\chi^2 = 1.9$ of the Hf(Xe,Xe)Hf experiment is shown in Figure 7-5. This set of matrix elements simultaneously reproduced both the measured activity and the $19^+ \rightarrow 18^+$ yield. The adjustments to the matrix elements are described in the next two sections.

For the phases of the matrix elements, the arbitrary choice was made to use the signs of the Clebsch-Gordan coefficients $\langle I_{\mathrm{GSB}} 16 - \lambda \lambda \lambda \mid I_{K=16} 16 \rangle$, borrowed
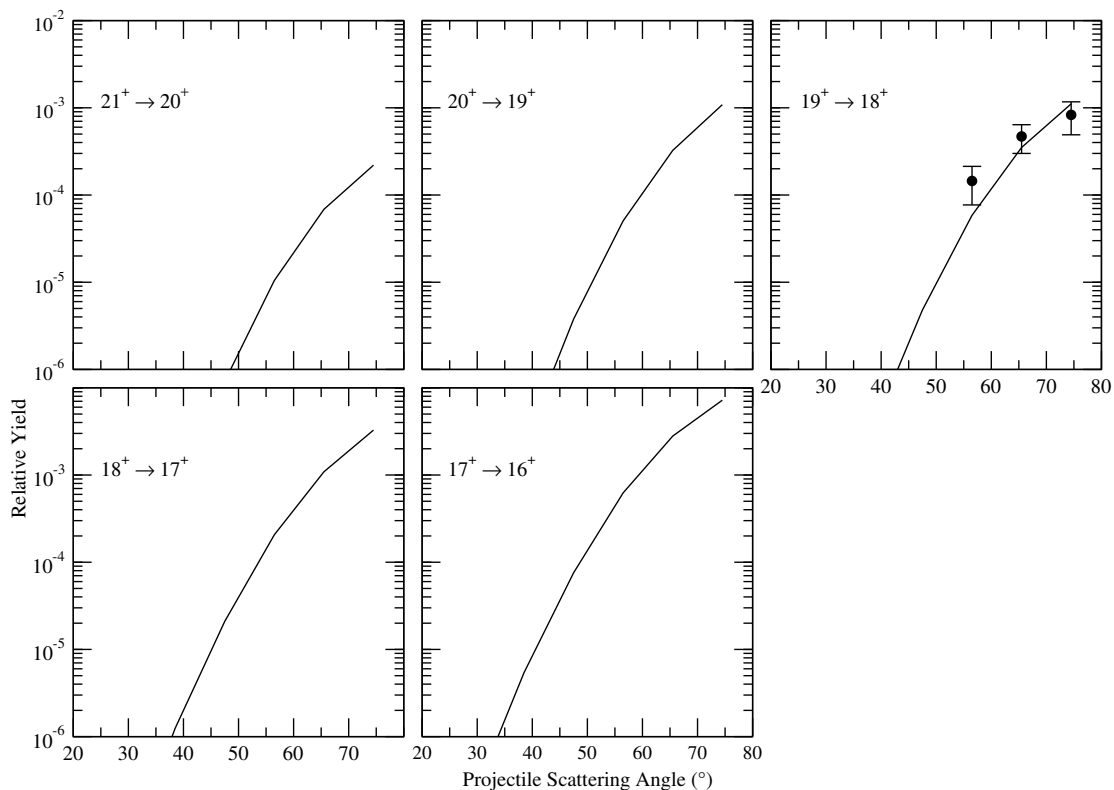
Figure 7-5: Experimental and calculated in-band γ-ray yields for the matrix elements described in the text of this section. $\chi^2 = 1.9$

from the SDM model, but the goodness of the fit was found to be insensitive to the relative phases, because feeding was more important than direct population in the isomer activation and the 19^+ level yield. The $18^+_{K=16}$ level yield may be more sensitive to interference, but was not measurable in either experiment.

7.2.1 Fit Considerations from the Activity Measurements

The relative strengths of the three matrix elements $\langle 16^+_{K=16} \| E2 \| 14^+_{\text{GSB}} \rangle$, $\langle 16^+_{K=16} \| E2 \| 16^+_{\text{GSB}} \rangle$ and $\langle 16^+_{K=16} \| E2 \| 18^+_{\text{GSB}} \rangle$ have the greatest influence on the slope of the activity vs. bombarding energy (A vs. E) calculation. As the beam energy in the target increases and the upper GSB levels are populated more

strongly, the higher-spin matrix elements become more effective. The best agreement with the A vs. E slope was obtained by setting $\langle 16^+_{K=16}\|E2\|14^+_{\text{GSB}}\rangle = \langle 16^+_{K=16}\|E2\|16^+_{\text{GSB}}\rangle = \langle 16^+_{K=16}\|E2\|18^+_{\text{GSB}}\rangle$. Systematic arguments suggest similar, but slightly larger matrix elements for the $17^+_{K=16}$ level: Balancing a general increasing trend in K-mixing with the constraints imposed by the upper limits on GSB$\rightarrow K = 16^+$ feeding, the matrix elements connecting to the $18^+_{K=16}$ state must take on a local variation of decreasing magnitude with increasing GSB spin, because the upper limits on feeding are lower at the 18^+ level. The overall magnitudes of the $17^+_{K=16}$ matrix elements were roughly interpolated between the $16^+_{K=16}$ and $18^+_{K=16}$ matrix elements, imposing a trend of increasing K-mixing with increasing spin.

7.2.2   Fit Considerations from the 19^+ Yield

The matrix elements for the $16^+_{K=16}$, $17^+_{K=16}$ and $18^+_{K=16}$ levels shown in Figure 7-4 were found to be ineffective in populating the $19^+_{K=16}$ level, whose yield was measured in the Hf(Xe,Xe)Hf experiment, so the measured $19^+ \rightarrow 18^+$ yield could be fit independently by adjusting the matrix elements connecting the GSB to the $19^+_{K=16}$, $20^+_{K=16}$ and $21^+_{K=16}$ levels. As in the case of the $18^+_{K=16}$ level, the higher levels' matrix elements were more tightly constrained by the measured upper limit on γ-ray feeding from the GSB. In the upper levels, the feeding limit was typically about 10^{-4}, which set upper bounds on the higher-spin levels' matrix elements as seen in Figure 7-4. The pattern of increasing K-mixing followed in the 16^+—18^+ levels was continued in a general sense in the higher levels, but feeding upper limits imposed some staggering in the matrix elements.

Since most of the 19^+ population comes from the $\langle 19^+_{K=16}\|E2\|18^+_{\text{GSB}}\rangle$ and $\langle 20^+_{K=16}\|E2\|18^+_{\text{GSB}}\rangle$ matrix elements, ranges for the other 5 matrix elements populating the 19^+ level could not be determined, except for the determination of upper limits based on feeding. The absolute upper limit of $\langle 20^+_{K=16}\|E2\|18^+_{\text{GSB}}\rangle$ was esti-

mated by setting $\langle 19^+_{K=16}\|E2\|18^+_{\mathrm{GSB}}\rangle$ to zero and increasing $\langle 20^+_{K=16}\|E2\|18^+_{\mathrm{GSB}}\rangle$ until $\chi^2 = \chi^2_{\min} + 1$. Correlations with the other five matrix elements were insignificant.

Correlated error calculations between the matrix elements $\langle 19^+_{K=16}\|E2\|18^+_{\mathrm{GSB}}\rangle$ and $\langle 20^+_{K=16}\|E2\|18^+_{\mathrm{GSB}}\rangle$ could not define any lower limit or further restrict the upper limit for $\langle 19^+_{K=16}\|E2\|18^+_{\mathrm{GSB}}\rangle$, because the $\langle 20^+_{K=16}\|E2\|18^+_{\mathrm{GSB}}\rangle$ matrix element has a higher upper limit and can independently reproduce the measured $19^+ \rightarrow 18^+$ yield with $\chi^2 < \chi^2_{\min}+1$. However, a lower limit on $\langle 20^+_{K=16}\|E2\|18^+_{\mathrm{GSB}}\rangle$ was obtained by increasing all of the 19^+, 20^+ and 21^+ matrix elements to their upper limits and reducing $\langle 20^+_{K=16}\|E2\|18^+_{\mathrm{GSB}}\rangle$ to reach the $\chi^2 = \chi^2_{\min} + 1$ limit. Figure 7-4 shows the upper and lower limits for $\langle 20^+_{K=16}\|E2\|18^+_{\mathrm{GSB}}\rangle$, which are essentially the correlated error with the $\langle 19^+_{K=16}\|E2\|18^+_{\mathrm{GSB}}\rangle$ matrix element.

The diagonal (uncorrelated) errors (Fig. 7-4) were measured in the six matrix elements which provided enough sensitivity for the calculation. The matrix elements for the $16^+_{K=16}$ level were coupled as one parameter and varied until $\chi^2 = \chi^2_{\min} + 1$, giving a range of 0.20—0.26 eb. The matrix elements of the $17^+_{K=16}$ level were coupled in an identical error calculation, giving ranges of 0.27 eb$\leq \langle 17^+_{K=16}\|E2\|16^+_{\mathrm{GSB}}\rangle \leq$ 0.44 eb and 0.25 eb$\leq \langle 17^+_{K=16}\|E2\|18^+_{\mathrm{GSB}}\rangle \leq$0.40 eb.

At its χ^2 minimum, the $\langle 19^+_{K=16}\|E2\|18^+_{\mathrm{GSB}}\rangle$ matrix would exceed the γ-decay feeding upper limit. If the $\langle 20^+_{K=16}\|E2\|18^+_{\mathrm{GSB}}\rangle$ matrix element were increased, $\langle 19^+_{K=16}\|E2\|18^+_{\mathrm{GSB}}\rangle$ could be reduced from the feeding limit and a diagonal error could be calculated, but the strength of the 19^+ level matrix elements would be lower than the systematic trend of increasing K-mixing would suggest.

7.2.3   Upper Limits From Measured Yields

More restrictive upper limits (below the feeding limits) for six matrix elements were obtained based on the measured activities and $19^+ \rightarrow 18^+$ yields. Since each of the connections to the 16^+ level contributes approximately the same fraction

of the total level population, reducing any two to zero would require a factor of ≈ 3 increase in the $B(E2)$ ($\sqrt{3}$ in the matrix element) of the third to maintain the observed yield.

The 17^+ level connections contribute about 25% of the total isomer yield (Fig. 7-3). If the 16^+ level connections were reduced to an ineffective level, the 17^+ matrix elements would have to be increased by a factor of about $\sqrt{\frac{1}{0.25}}$. These considerations lead to the upper limits for the first five matrix elements in Table 9.14 and Figure 7-4.

7.3   The Influence of the 14^- Band

Population of the 16^+ isomer due to feeding from the 14^- isomer could make a significant contribution to the 16^+ activation, if the 14^- isomer is populated to a strength comparable to the direct population of the 16^+ band. The known decay branch to the 16^+ isomer from the 14^- isomer is shown with the known relative intensities in Figure 7-6.

Because of the long half-life of the 14^- isomer, 68 μs, compared to the 1 μs acquisition window, prompt-delayed and delayed-delayed matrix data were not useful for measuring 14^--band yields. In prompt-prompt matrix data there are many possible sources of contamination from impurities in the 89% enriched target which make observation very difficult below the 10^{-2} level relative to the GSB. Triples data were not useful for measuring the 14^- band population either, since only the lowest two $\Delta I = 1$ transitions are known. In a prompt-prompt matrix above the safe angle ($52°$–$78°$), a gate on the $15^- \rightarrow 14^-$ transition yielded a peak possibly belonging to the $16^- \rightarrow 15^-$ transition, but lying in a rich background of coincident peaks. Likewise, the 16^+ isomer band population was measured in the same matrix, although the identities of both peaks were not certain at the 10^{-4} level.
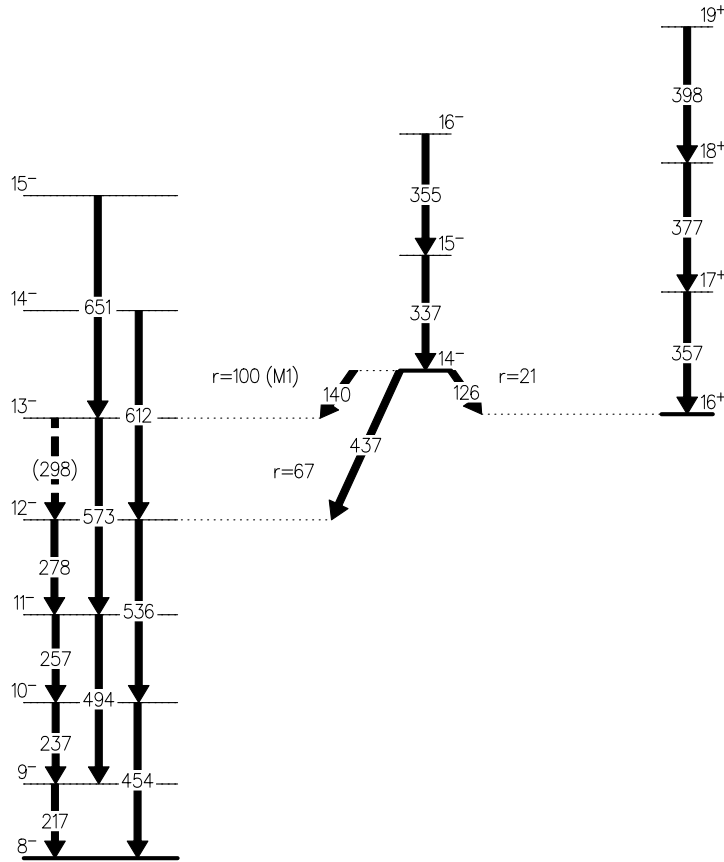
Figure 7-6: Known decay branches of the 14^- 68 μs isomer. Relative γ intensities are shown [10] beside each branch.

After correcting for the relative efficiency of the transition energies and internal conversion, using Mullins' [58] values of $g_K - g_R$ to compute the mixing ratios and using the internal conversion coefficients of Rosel *et al.* [3], the ratio of the populations of the second level in the 16^+ and 14^- isomer bands was found to be $\frac{P_{14-}}{P_{16+}} = 0.47$.

7.3.1 14^- Feeding to the 16^+ Isomer

The EM character of the transition feeding the 16^+ isomer is not known, but three estimates can be made of the contribution to the 16^+ isomer population via the 14^- isomer, one for each possible multipolarity. The fraction of the 16^+

Mλ of $14^- \to 16^+$	α_{126}	$\frac{\Gamma_{126}}{\Gamma_{\text{total}}}$	f
E3	20.9	0.585	$19(5)\%$
M2	16.0	0.523	$17(4)\%$
M4	824.0	0.981	$31(8)\%$

Table 7.1: Estimates of the fraction f of the 16^+ isomer population attributable to feeding from the 14^- isomer. Values of the internal conversion coefficient α were obtained from [4]. Errors in f are primarily from the fits of peaks in the gated projections of the γ-γ matrix.

isomer population that is attributable to the 14^- isomer can be written as

$$
\begin{aligned}
f &\equiv \frac{P_{14^-}}{P_{16^+} + P_{14^-}} \frac{\Gamma_{126\text{keV}}}{\Gamma_{\text{total}}} \\
&= 0.32 \frac{\Gamma_{126\text{keV}}}{\Gamma_{\text{total}}},
\end{aligned}
\tag{7.2}
$$

where $\Gamma_{126\text{keV}}$ and Γ_{total} are the respective decay widths of the $14^- \to 16^+$ transition (including internal conversion) and the 68 μs isomer (all branches, including internal conversion). This ratio is given by

$$
\frac{\Gamma_{126}}{\Gamma_{\text{total}}} = \frac{r_{126}(1 + \alpha_{126})}{r_{140}(1 + \alpha_{140}) + r_{437}(1 + \alpha_{437}) + r_{126}(1 + \alpha_{126})}.
\tag{7.3}
$$

Assuming that the 437 keV transition is E2, which gives the largest feeding estimate to the 16^+ isomer, the following estimates of f can be made for three possible multipolarities of the $14^- \to 16^+$ transition (Table 7.1).

If the 355 keV peak found in coincidence with a gate at 337 keV belongs to the $16^- \to 15^-$ transition in the 14^- isomer band (Figure 7-6) and any multipolarity in Table 7.1 were possible, then feeding from the 14^- isomer could be be responsible for as much as $31(8)\%$ of the 16^+ isomer activity observed. However, the known γ-ray intensities and internal conversion coeffients would indicate reduced transition strengths of $B(E3) = 510$ W.u., $B(M2) = 0.014$ W.u. and

$B(M4) = 1.5 \times 10^{11}$ W.u. The absurdly high values for E3 and M4 leave M2 as the only possibility. Assuming that the 14^- and 16^+ isomers would be populated in approximately the same relative proportions in this and the previous experiment, the two lowest-energy targets' activities would then be overpredicted, but still within 2σ. A $\approx 10\%$ decrease in the matrix elements would make up for the feeding contribution from the 14^- band, but the final set of matrix elements do not include this adjustment.

7.4   Conclusion

The SDM model could not simultaneously reproduce the data of the first and second experiments, even with unrealistically large matrix elements, nor could matrix elements which increased linearly with spin. The $\langle I_{16+} \| E2 \| I_{\text{GSB}} \rangle$ matrix elements (Table 9.14) were adjusted individually to reproduce the measured yields of both experiments while adhering to the measured upper limits on γ-decay feeding from the GSB. The population of the isomer band head was found to proceed primarily $\approx 75\%$ by γ-decay feeding to the 16^+ and 17^+ levels. The final set of matrix elements was nearly constant with increasing spin, showing that the relevant admixtures in the GSB reach a saturation point at high spin, which will be discussed in Chapter 10.

Chapter 8

Levels and Bands

A level scheme (Figure 8-1) was built from the γ-decays of ^{136}Xe and ^{178}Hf excitation observed in the ^{178}Hf(^{136}Xe,^{136}Xe)^{178}Hf experiment. In most cases, level placement was determined using three-fold γ-ray data, as explained in Chapter 3. A new band, possibly an extension of the known β-band in ^{178}Hf, as well as extensions of many bands in several hafnium isotopes, are presented. Structural features are deduced from the level energies and moments of inertia, leading to conclusions regarding the origin of K-mixing and the population of high-K isomers in both experiments.

8.1   The GSB and the γ-band

The 20^+_{GSB} level in ^{178}Hf found by Mullins *et al.* [58] was confirmed, but a 22^+ level could not be found. The γ-band at 1175 keV, previously known up to the 6^+ level, was extended to the 14^+ level with tentative 15^+ and 16^+ levels (Figure 8-1). The γ-band's even and odd signatures have nearly equal moments of inertia and do not diverge up to spin $16\hbar$, in contrast with the strong signature splitting and diverging moments seen in ^{180}Hf [18] (Figures 8-2 and 8-3). This indicates a major change in band interactions with the γ-band in ^{180}Hf upon the addition of

two $i_{13/2}$ neutrons.

The relationship between the level energies and the spin I (Figures 8-2 and 8-4) shows that for $I > 8$ the GSB and γ-band level energies follow a shallower curve than is typical for a rotor, suggesting that they both interact with one or more other bands, such as the lowest 2 quasiparticle aligned band. A more sensitive indicator of band interactions and mixing is a change in the slope of the moment of inertia, such as the increase at spin $\approx 8\hbar$ in both the GSB and the γ-band (Figure 8-5) This suggests the possible onset of K-mixing, in striking agreement with the conclusions drawn from the matrix elements determined in both experiments. In contrast, a much slower, more uniform increase was seen in the moments of inertia of the isomer bands.

8.2 A Possible β-vibrational Band

In the ^{178}Hf(^{136}Xe, ^{136}Xe)^{178}Hf experiment, four intermediate levels in an unidentified band, "A" in Figure 8-1, were observed feeding into the GSB, suggesting a small K value. A fifth level was tentatively placed at the top of the band, but the intraband transitions were weak, making it impossible to follow the cascade to the band head. The spacing of the observed levels, as well as the decay pattern (Figure 8-1) into the GSB, show that the observed intraband transitions of band A must have $\Delta I = 2$. The γ-ray intensity ratios of the interband transitions favor the lower energy decay from each level, while the intraband transitions are weak enough that their relative intensities could not be measured.

The relative yields, normalized to the $8^+_{\mathrm{GSB}} \rightarrow 6^+_{\mathrm{GSB}}$ transition for a scattering angle range of $52° \leq \theta_{\mathrm{scat}} \leq 78°$ were measured using the γ-ray triples matrix (Figure 8-6). Yields could not be measured for the intraband transitions because the branching ratios needed to correct for gating were not measurable, but lower limits were found. From the decay pattern and the level spacing, possible spin-

Figure 8-1: Master level scheme showing all of the levels observed in the ^{178}Hf(^{136}Xe,^{136}Xe)^{178}Hf experiment. New levels and isomer states are shown as bold lines.

174
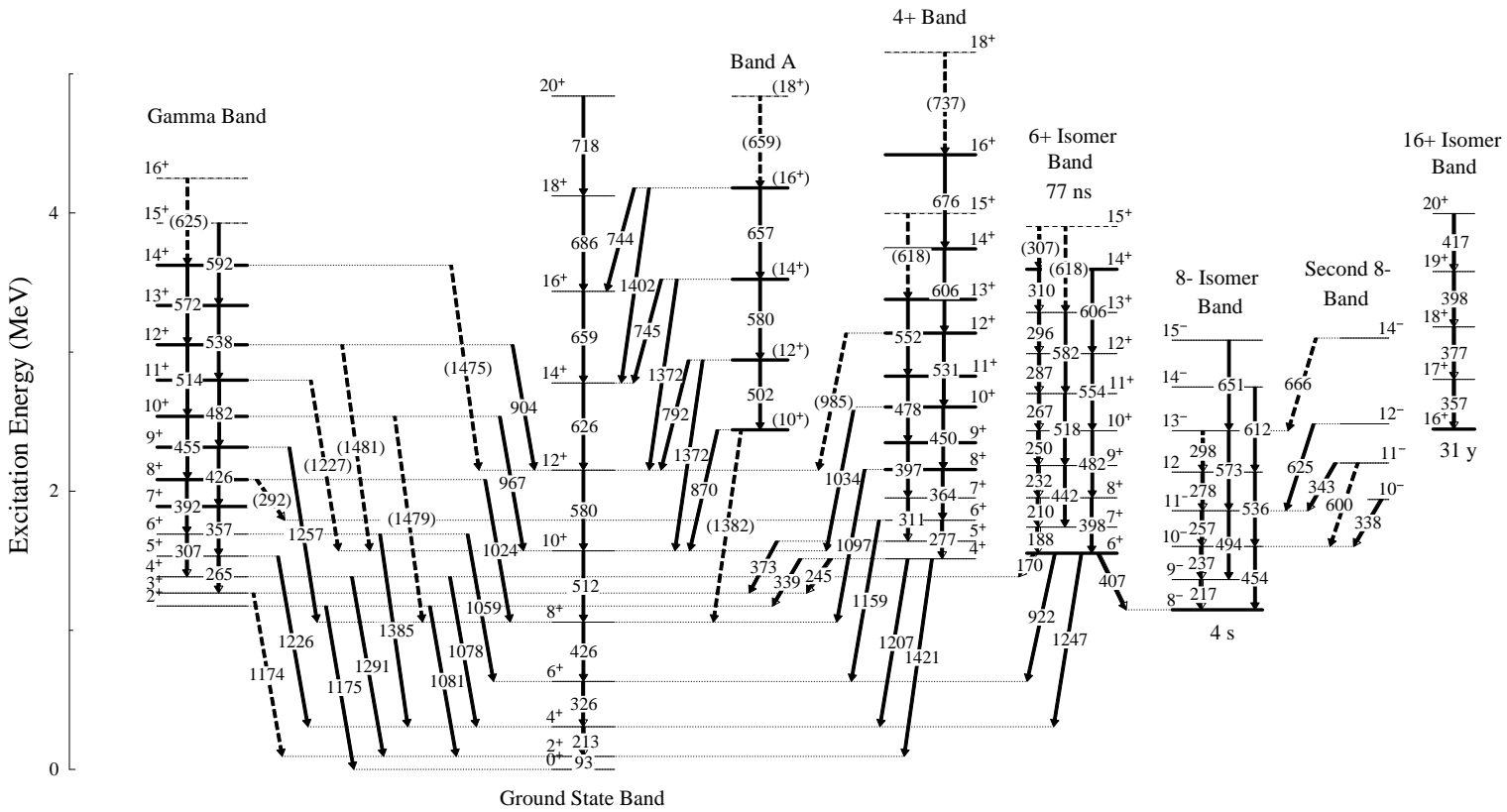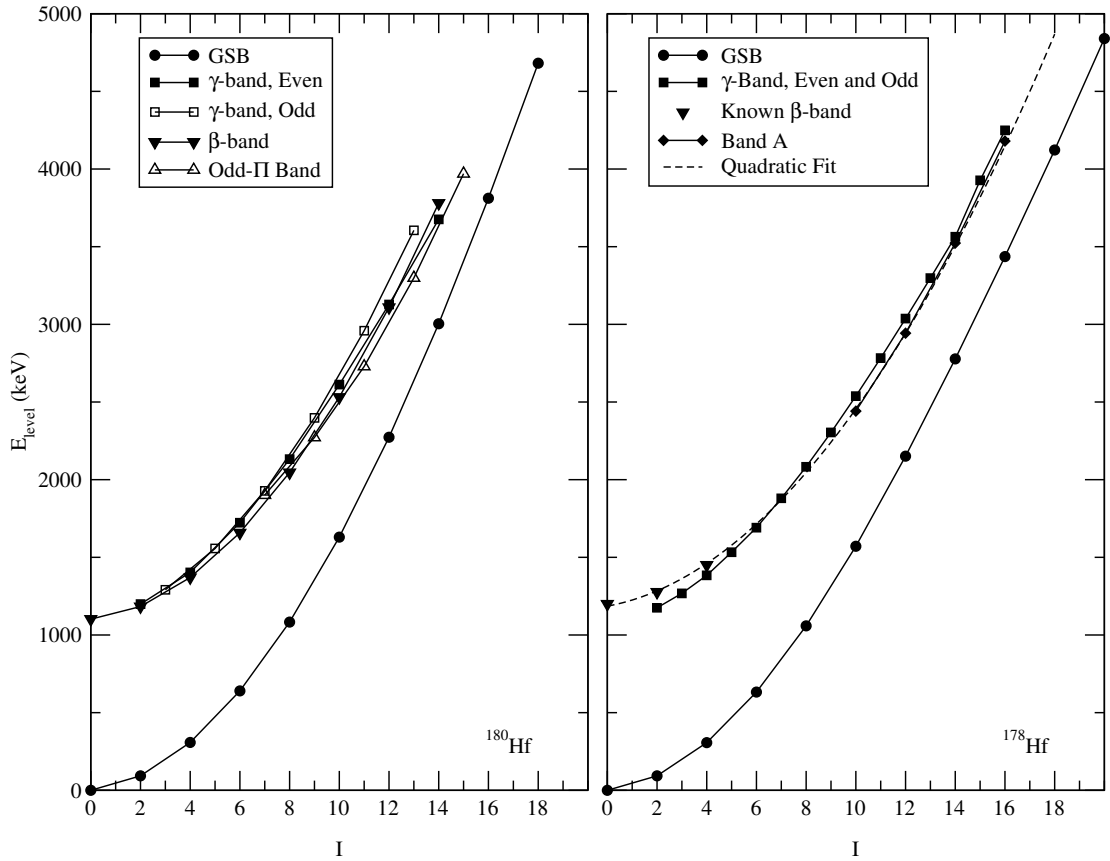
Figure 8-2: Level energy vs. spin. Comparison of ^{178}Hf levels (right) with known bands in ^{180}Hf [18] (left). The dashed line is a quadratic fit to the combined levels of the known β-band and band A.

parity assignments for the lowest observed level are 10^+, 9^- and 8^+. Odd parity is assumed for spin 9, because only one signature of the band is seen, more likely the natural parity states.

The only relative γ-ray intensities that could be measured in the data gave $\frac{\Gamma_{745}}{\Gamma_{1372}} = 0.2(1)$ and a $B(E2)$ ratio of $\frac{B(E2;745\text{keV})}{B(E2;1372\text{keV})} = 0.010(5)$. Assuming that $K = 0$ or 2 for band A, the Alaga rule coupling predicts $B(E2) = 1.4$ or 0.060, respectively, significantly larger than the measured values. This brings into question the spin assignments, but if the tentatively assigned spins in band A were reduced by $1\hbar$ or $2\hbar$, this would imply that the $\Delta I > 0$ branches were stronger than the $\Delta I \leq 0$ branches. The unlikelihood of the $\Delta I > 0$ decays having a
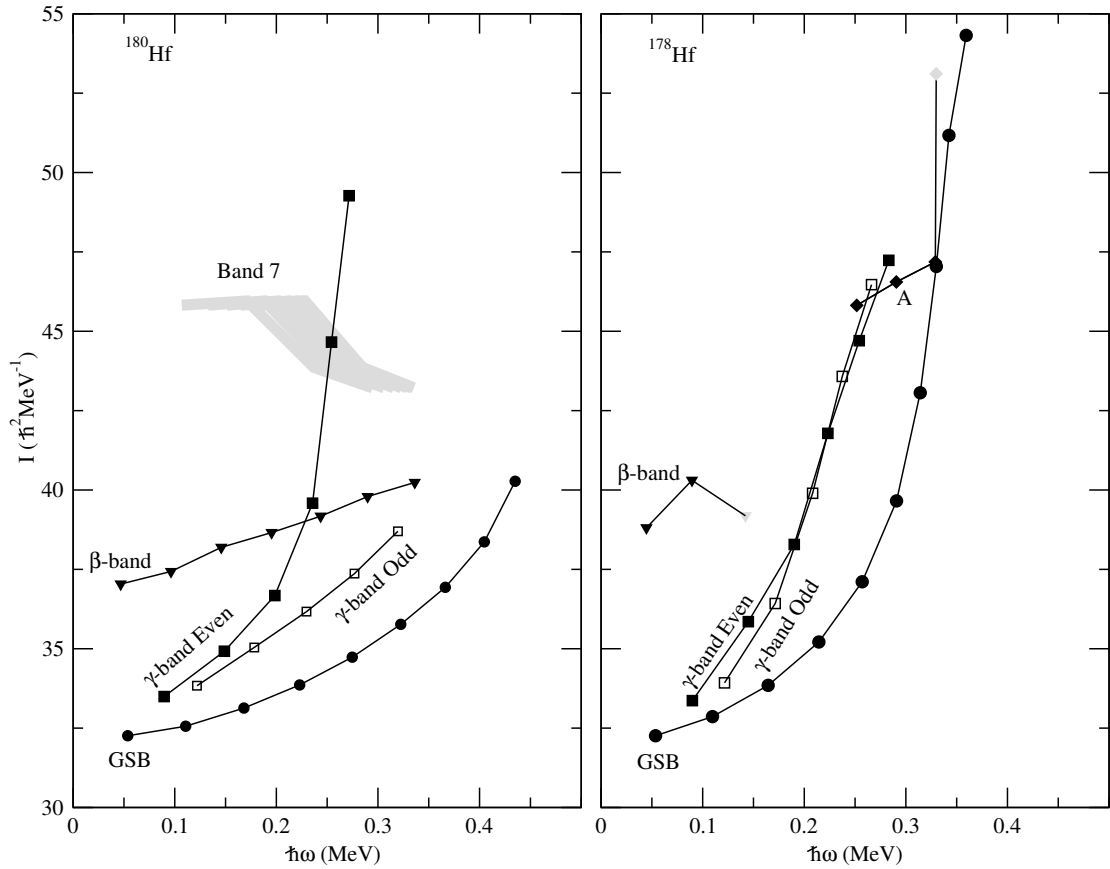
Figure 8-3: Moments of inertia of several bands in ^{180}Hf (left) [18] and ^{178}Hf (right) for even (solid) and odd (hollow) spin levels. Tentative levels are shown in grey. The lowest frequency point in each curve corresponds to $I = K + 2$, except for band A, which begins with $I = 12$. "Band 7" of [18] is shown as a grey region covering all possible K values.

greater intensity suggests that the tentative spin assignments are correct, and the disagreement between the expected and calculated $B(E2)$ ratios (for pure E2 transitions) together with the strength of the lower energy branches implies that there is considerable M1 enhancement in the $\Delta I = 0$ decays.

The known levels and bands in ^{178}Hf (*e.g.* [2, 9, 10, 58, 78]) were exhaustively searched for the complete set of lower levels for the band, using both energy and moment of inertia data and testing all possible values of K and spin-parity. From the level energies alone, several identifications of the band appear plausible.
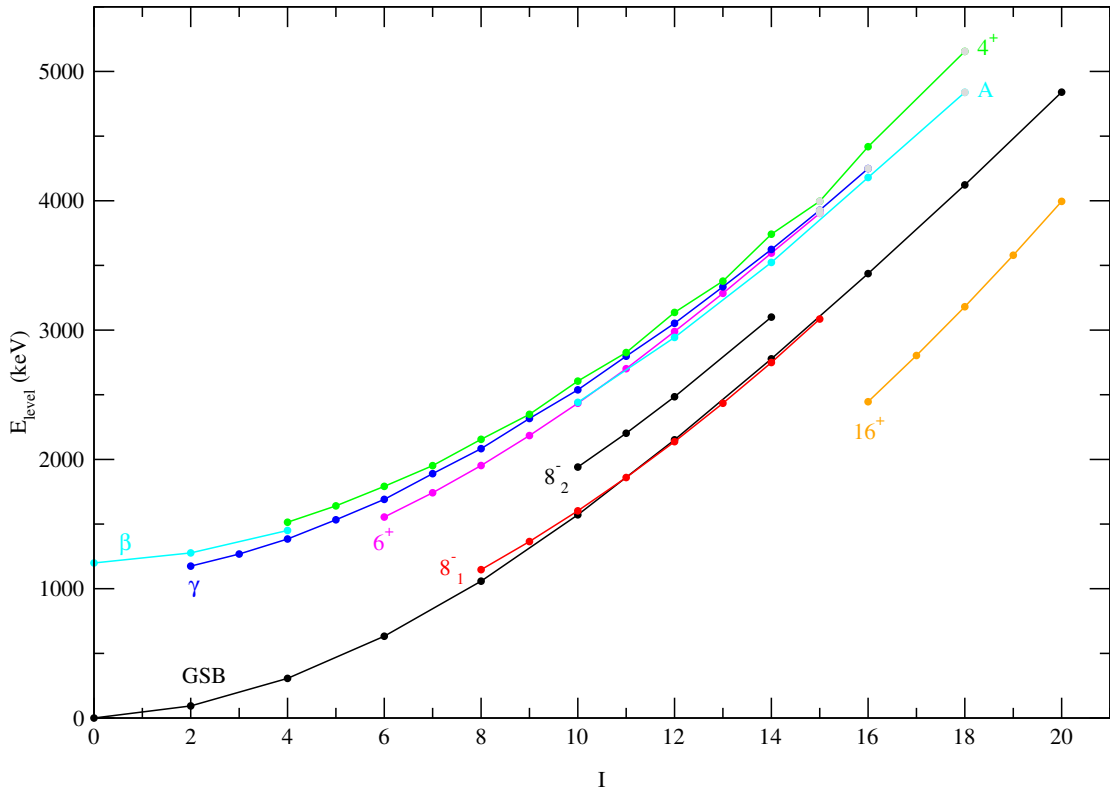
Figure 8-4: Energy as a function of spin I for all bands observed and for the known β-band. 8_1^- indicates the isomer band. Tentative levels are shown in grey. The lowest spin point in each curve corresponds to $I = K$, except for the 8_2^- band at 1479 keV, which was observed for $I \geq 10$.

Comparing the level energies to those found by Ngijoi-Yogo [18] in the Coulomb excitation of ^{180}Hf (Figure 8-2), it appears that band A could be either the analog of "Band 7" in ^{180}Hf, or the continuation of the known β-band [102, 103, 78, 104] found by Nielsen, *et al.* The similarity of the moments of inertia favors the β-band identification (Figure 8-3).

Since the moment of inertia for a particular level is very sensitive to the level spacing, an accurate interpolation of the missing levels' moments would give a precise indication of the expected intermediate γ-ray energies if band A is a continuation of the β-band. Figure 8-7 shows a parabolic fit to the moments of the 2^+ and 4^+ levels of the β-band and the 12^+–16^+ levels of band A, as well as linear
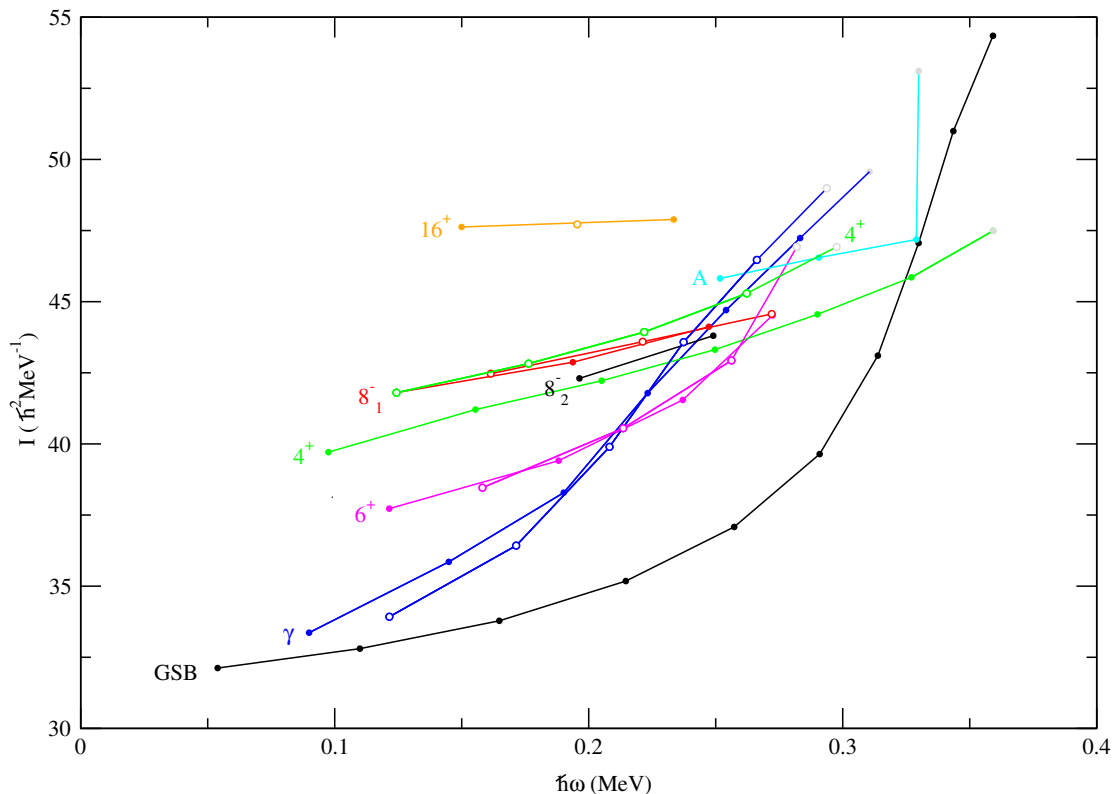
Figure 8-5: Moments of inertia of the observed bands in ^{178}Hf, for even (solid) and odd (hollow) spin levels. Bands are labeled by K^π, 8_1^- indicating the isomer band. Tentative levels are shown in grey. The lowest frequency point in each curve corresponds to $I = K + 2$, except for the 8_2^- band at 1479 keV, which begins with $I = 12$, and band A.

extrapolations from the β- and A bands. The parabolic interpolation gave intermediate γ-ray energies of 261, 345 and 425 keV for the missing transitions, while the linear extrapolations gave 263.5 and 422 keV for the first and third missing transitions. But neither set of transitions gives the correct sum energy for the missing transitions, and neither set of γ-rays was found in the data, presumably because the interband decay branches are stronger. No other coincidental sets of γ-rays were found which gave the correct sum energy.

The tentative placement [2] of the 6^+ level of the β-band in previous work was based on a multiply placed transition, which some authors have suggested feeds the 4_β^+ level [10]. If the 6^+ level energy were correct, and band A is the β-band,

Relative Yield

$2 \cdot 10^{-2}$

10^{-2}

10^{-3}

10^{-4}

10 12 14 16 18

I_i
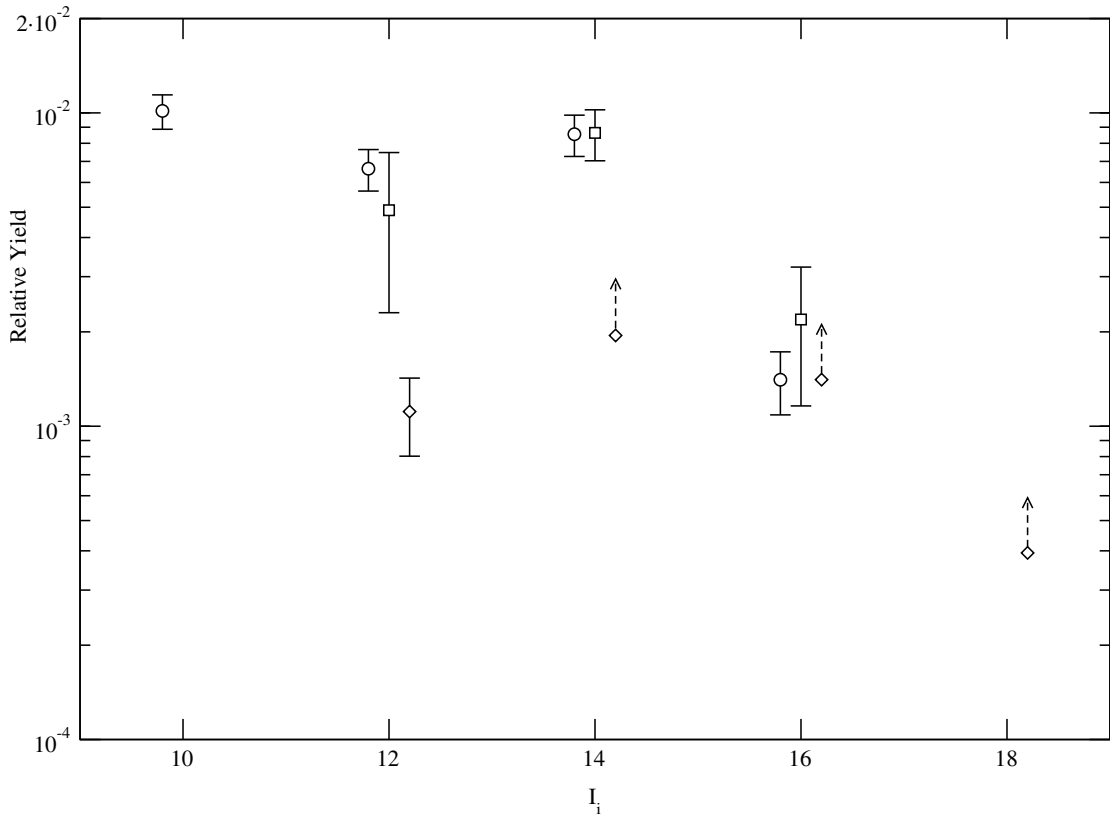
Figure 8-6: Yield vs. spin for decays from band A, normalized to the $8^+_{\mathrm{GSB}} \to 6^+_{\mathrm{GSB}}$ transition for $52° \leq \theta_{\mathrm{scat}} \leq 78°$. Yields are shown for $\Delta I = 0$ (circles) and $\Delta I = -2$ (squares) transitions to the GSB and for intraband $\Delta I = -2$ transitions (diamonds).

then the moment of inertia of the band must oscillate by $\approx \pm 5 \hbar^2 / \mathrm{MeV}$ between the 6^+ and 10^+ levels, in order to satisfy the correct γ-ray sum energy–an unlikely hypothesis, considering the measured moments of Figure 8-7.

The $\Delta I = 0$ transitions are favored in band A, in qualitative agreement with the measured mixing ratios of the β-band, for example in the decay of the β-band 2^+ state at 1276 keV to the 2^+_{GSB} state, by an 1183 keV decay ($\delta^2_{E2/M1} = 0.17(10)$) E2 [103]. Since the β-band is a collective vibration, it should be Coulomb excited in ^{178}Hf to similar strength as in the ^{180}Hf Coulomb excitation work [18]. While band A appears to be the continuation of the β-band, by its population strength, level energies and moments of inertia, the cascade can not be followed to the

179
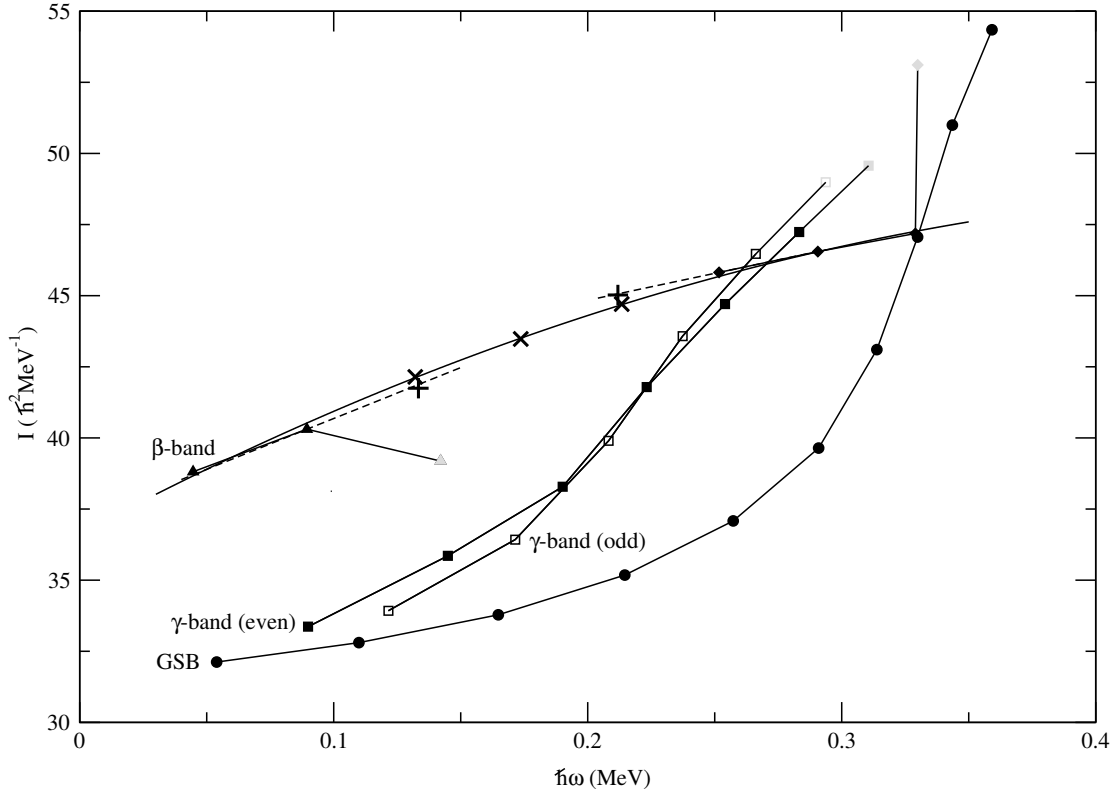
Figure 8-7: Measured moments of inertia for levels in the β-band and band A, connected by a quadratic fit to the firm levels, suggesting interpolated moments of the 6^+, 8^+ and 10^+ states (x's). Linear fits to two levels each in the β- and A bands suggest extrapolated moments of the 6^+ and 10^+ levels (+'s).

band head, because it is populated predominantly at high spin levels which decay out-of-band.

If the present identifications of the β-bands in ^{178,180}Hf are correct, then relative yields of the suspected β-bands in both experiments should be similar and less than relative yields of the γ-bands. At the 10^+ levels, the total relative yield $r_{178\text{Hf}} \equiv \frac{Y_{\text{bandA}}}{Y_{\gamma-\text{band}}}$ is 0.7(2). The relative yield of the 10^+_β state in the Coulomb excitation of ^{180}Hf is $r_{180\text{Hf},^{136}\text{Xe}} = 0.33(3)$, calculated from the data of [18] and corrected for the greater population of the 10^+_γ level relative to the GSB. The relative yields differ by a factor of 2.1(6).

If band A is the upper β-band, then reasonable constraints on the energy

sum and a smoothly varying moment of inertia suggest that the 6_β^+ level currently assigned at 1731 keV [2] will be found closer to 1700 keV. The energy sum requirement also implies an increase in the β-band's moment of inertia at spin $\gtrsim 6\hbar$.

8.3 The 4^+ Band at 1514 keV

The tentative 7^+ level [83] in the previously known 4^+ band at 1514 keV was confirmed, and the band was extended from spin 7^+ to spin 16^+ with tentative 15^+ and 18^+ levels. The moments of inertia (Figure 8-5) of the odd and even 4^+ band signatures show a constant separation and do not diverge up to spin $18\hbar$. The 4^+ bands are not known beyond two or three levels in the neighboring hafnium nuclei for comparison.

8.4 The 6^+ Isomer Band at 1554 keV

A 14^+ level was added to the 6^+ isomer band, along with a tentative 15^+ level. The moment of inertia shows an up-bend above spin $12\hbar$, which is not seen in the other isomer bands. This may indicate an onset of K-mixing near the highest levels populated in the 6^+ band, above the levels most important in the Hf(Xe,Xe)Hf Coulomb excitation.

8.5 The 8^- Bands at 1174 keV and 1479 keV

The 8_1^- (isomer) and 8_2^- (1479 keV) bands were observed up to spin 15^-, but new levels were not found. The moment of inertia does not exhibit any sudden increase with spin, which might accompany a sudden onset of band mixing.

8.6 The 14^- Band at 2573 keV

The $K^\pi = 14^-$ intraband γ-decays were not visible in the data sets, but an upper limit was set at 50% of the 16^+ band population for the 16^- level, based on a possible but uncertain peak in the gated doubles spectra. The short time window for γ-ray collection did not permit observation of the 14^- ($t_{1/2} = 68$ μs) isomer decays.

8.7 The 16^+ Band at 2446 keV

The $K^\pi = 16^+$ levels up to 20^+ were seen in the prompt triple-γ data. The intraband γ-decay yields were measured for the $19^+ \to 18^+$ transition, but the yield of the $20^+ \to 19^+$ transition was too low to measure as a function of scattering angle. The moment of inertia increases slowly with spin up to spin 20^+, showing no sign of band mixing that might lead to K-mixing at levels low enough to be relevant to the present analysis (Chapters 4 and 7).

8.8 Other Isotopes

The 18^+_{GSB} level of ^{180}Hf at 4.683 MeV was found (Figure 8-8), in agreement with the work of Ngijoi-Yogo [18]. The GS bands of ^{177,179}Hf were extended to the $39/2^-$ and $39/2^+$ levels, respectively. Trace contaminants (Table 3.1) of ^{176}Hf in the 89% ^{178}Hf target made the GSB visible up to the 18^+ state.

8.9 Levels and γ-ray Transitions

The levels and γ-ray energies for ^{178}Hf assigned and confirmed in this work are cataloged in Tables 8.1 and 8.2. Levels are only given for bands which have been extended in this work.
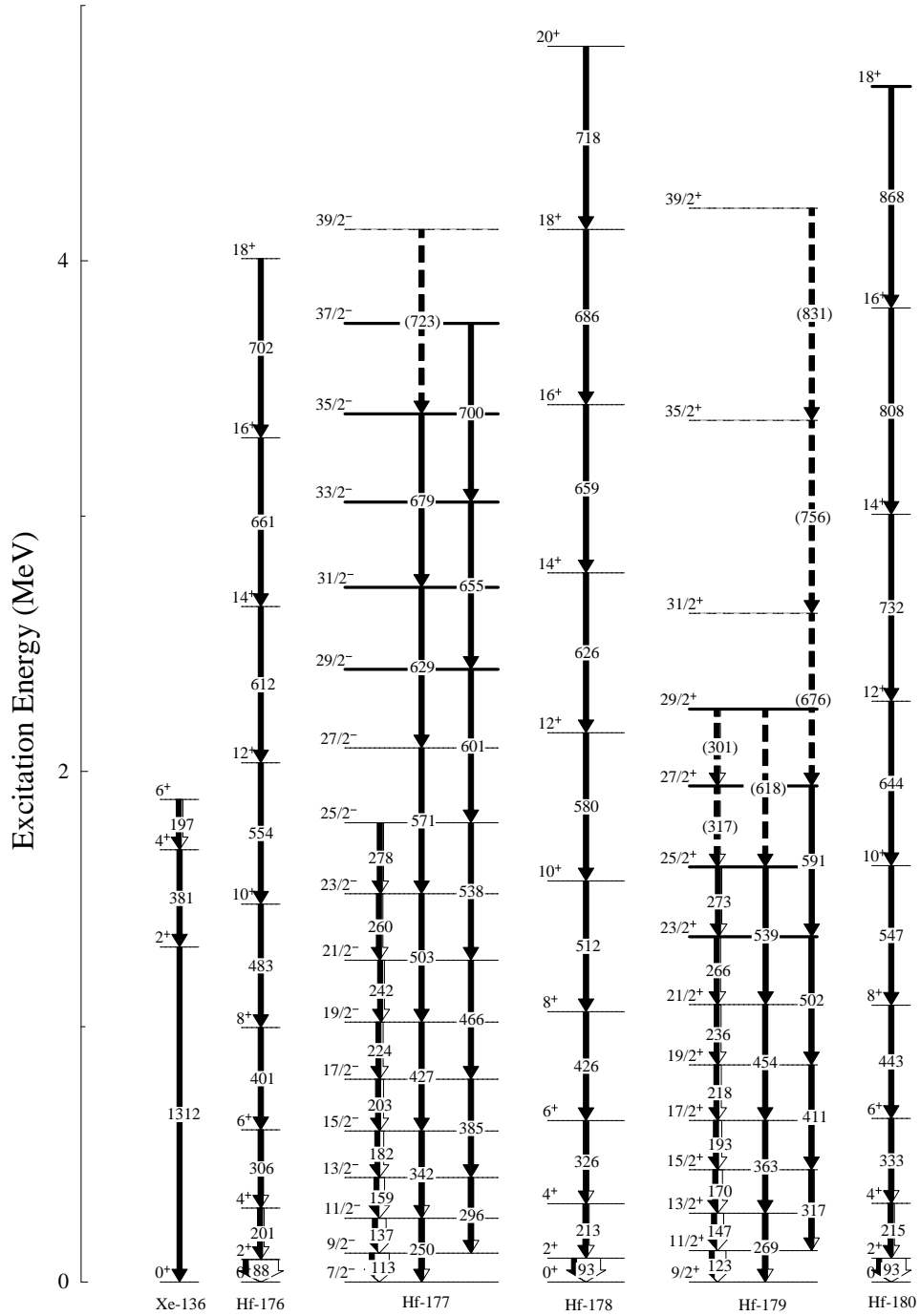
Figure 8-8: Isotopes observed in the γ-ray data, showing the ground state bands of the Hf isotopes in the target foil and the ^{136}Xe $\pi(g\frac{7}{2})^2$ multiplet which was excited in the beam particles. New levels are shown as bold lines.

E_{level} (keV)	I^π	Band
1554	6^+	$K^\pi = 6^+$
1742	7^+	$K^\pi = 6^+$
1952	8^+	$K^\pi = 6^+$
2184	9^+	$K^\pi = 6^+$
2434	10^+	$K^\pi = 6^+$
2701	11^+	$K^\pi = 6^+$
2989	12^+	$K^\pi = 6^+$
3284	13^+	$K^\pi = 6^+$
*3595	14^+	$K^\pi = 6^+$
*3902	15^+	$K^\pi = 6^+$
1175	2^+	$K^\pi = 2^+$
1268	3^+	$K^\pi = 2^+$
1384	4^+	$K^\pi = 2^+$
1533	5^+	$K^\pi = 2^+$
1691	6^+	$K^\pi = 2^+$
*1890	7^+	$K^\pi = 2^+$
*2083	8^+	$K^\pi = 2^+$
*2316	9^+	$K^\pi = 2^+$
*2538	10^+	$K^\pi = 2^+$
*2798	11^+	$K^\pi = 2^+$
*3052	12^+	$K^\pi = 2^+$
*3335	13^+	$K^\pi = 2^+$
*3624	14^+	$K^\pi = 2^+$
*3927	15^+	$K^\pi = 2^+$

Table 8.1: Levels of the ^{178}Hf bands extended in the ^{178}Hf(^{136}Hf,^{136}Hf)^{178}Hf experiment. Uncertainties in the level energies are ≈ 1 keV. *New level.

E_{level} (keV)	I^π	Band
*4249	16^+	$K^\pi = 2^+$
1514	4^+	$K^\pi = 4^+$
1640	5^+	$K^\pi = 4^+$
1791	6^+	$K^\pi = 4^+$
1951	7^+	$K^\pi = 4^+$
*2156	8^+	$K^\pi = 4^+$
*2348	9^+	$K^\pi = 4^+$
*2605	10^+	$K^\pi = 4^+$
*2826	11^+	$K^\pi = 4^+$
*3136	12^+	$K^\pi = 4^+$
*3378	13^+	$K^\pi = 4^+$
*3742	14^+	$K^\pi = 4^+$
*3996	15^+	$K^\pi = 4^+$
*4418	16^+	$K^\pi = 4^+$
*5155	18^+	$K^\pi = 4^+$
*2441	(10^+)	A
*2943	(12^+)	A
*3523	(14^+)	A
*4180	(16^+)	A
*4839	(18^+)	A

Table 8.1, continued.

E_i (keV)	Band$_i$	$\rightarrow$	Band$_f$	I_i^π	$\rightarrow$	I_f^π	E_γ(keV)
93	GSB	$\rightarrow$	GSB	2^+	$\rightarrow$	0^+	93
1554	$K^\pi = 6^+$	$\rightarrow$	γ-band	6^+	$\rightarrow$	4^+	170
1742	$K^\pi = 6^+$	$\rightarrow$	$K^\pi = 6^+$	7^+	$\rightarrow$	6^+	189
1952	$K^\pi = 6^+$	$\rightarrow$	$K^\pi = 6^+$	8^+	$\rightarrow$	7^+	210
307	GSB	$\rightarrow$	GSB	4^+	$\rightarrow$	2^+	213
1364	$K^\pi = 8_1^-$	$\rightarrow$	$K^\pi = 8_1^-$	9^-	$\rightarrow$	8^-	217
2184	$K^\pi = 6^+$	$\rightarrow$	$K^\pi = 6^+$	9^+	$\rightarrow$	8^+	232
1602	$K^\pi = 8_1^-$	$\rightarrow$	$K^\pi = 8_1^-$	10^-	$\rightarrow$	9^-	238
1514	$K^\pi = 4^+$	$\rightarrow$	γ-band	4^+	$\rightarrow$	3^+	246
2434	$K^\pi = 6^+$	$\rightarrow$	$K^\pi = 6^+$	10^+	$\rightarrow$	9^+	250
1859	$K^\pi = 8_1^-$	$\rightarrow$	$K^\pi = 8_1^-$	11^-	$\rightarrow$	10^-	258
1533	γ-band	$\rightarrow$	γ-band	5^+	$\rightarrow$	3^+	265
2701	$K^\pi = 6^+$	$\rightarrow$	$K^\pi = 6^+$	11^+	$\rightarrow$	10^+	267
1791	$K^\pi = 4^+$	$\rightarrow$	$K^\pi = 4^+$	6^+	$\rightarrow$	4^+	277
2137	$K^\pi = 8_1^-$	$\rightarrow$	$K^\pi = 8_1^-$	12^-	$\rightarrow$	11^-	277
2989	$K^\pi = 6^+$	$\rightarrow$	$K^\pi = 6^+$	12^+	$\rightarrow$	11^+	287
2083	γ-band	$\rightarrow$	$K^\pi = 4^+$	8^+	$\rightarrow$	6^+	292
3284	$K^\pi = 6^+$	$\rightarrow$	$K^\pi = 6^+$	13^+	$\rightarrow$	12^+	296
2435	$K^\pi = 8_1^-$	$\rightarrow$	$K^\pi = 8_1^-$	13^-	$\rightarrow$	12^-	298
1691	γ-band	$\rightarrow$	γ-band	6^+	$\rightarrow$	4^+	307
3902	$K^\pi = 6^+$	$\rightarrow$	$K^\pi = 6^+$	15^+	$\rightarrow$	14^+	307
3595	$K^\pi = 6^+$	$\rightarrow$	$K^\pi = 6^+$	14^+	$\rightarrow$	13^+	310
1951	$K^\pi = 4^+$	$\rightarrow$	$K^\pi = 4^+$	7^+	$\rightarrow$	5^+	311
632	GSB	$\rightarrow$	GSB	6^+	$\rightarrow$	4^+	326

Table 8.2: Energies of the observed γ-rays. Uncertainties are ≈ 1 keV.

E_i (keV)	Band$_i$	$\rightarrow$	Band$_f$	I_i^π	$\rightarrow$	I_f^π	E_γ (keV)
1940	$K^\pi = 8_2^-$	$\rightarrow$	$K^\pi = 8_1^-$	10^-	$\rightarrow$	10^-	338
1514	$K^\pi = 4^+$	$\rightarrow$	γ-band	4^+	$\rightarrow$	2^+	339
2202	$K^\pi = 8_2^-$	$\rightarrow$	$K^\pi = 8_1^-$	11^-	$\rightarrow$	11^-	343
1890	γ-band	$\rightarrow$	γ-band	7^+	$\rightarrow$	5^+	357
2803	$K^\pi = 16^+$	$\rightarrow$	$K^\pi = 16^+$	17^+	$\rightarrow$	16^+	357
2156	$K^\pi = 4^+$	$\rightarrow$	$K^\pi = 4^+$	8^+	$\rightarrow$	6^+	364
1640	$K^\pi = 4^+$	$\rightarrow$	γ-band	5^+	$\rightarrow$	3^+	373
3181	$K^\pi = 16^+$	$\rightarrow$	$K^\pi = 16^+$	18^+	$\rightarrow$	17^+	378
2083	γ-band	$\rightarrow$	γ-band	8^+	$\rightarrow$	6^+	392
2348	$K^\pi = 4^+$	$\rightarrow$	$K^\pi = 4^+$	9^+	$\rightarrow$	7^+	397
1952	$K^\pi = 6^+$	$\rightarrow$	$K^\pi = 6^+$	8^+	$\rightarrow$	6^+	398
3579	$K^\pi = 16^+$	$\rightarrow$	$K^\pi = 16^+$	19^+	$\rightarrow$	18^+	398
1554	$K^\pi = 6^+$	$\rightarrow$	$K^\pi = 8_1^-$	6^+	$\rightarrow$	8^-	407
3995	$K^\pi = 16^+$	$\rightarrow$	$K^\pi = 16^+$	20^+	$\rightarrow$	19^+	417
2316	γ-band	$\rightarrow$	γ-band	9^+	$\rightarrow$	7^+	426
1059	GSB	$\rightarrow$	GSB	8^+	$\rightarrow$	6^+	426
2184	$K^\pi = 6^+$	$\rightarrow$	$K^\pi = 6^+$	9^+	$\rightarrow$	7^+	442
2605	$K^\pi = 4^+$	$\rightarrow$	$K^\pi = 4^+$	10^+	$\rightarrow$	8^+	450
1602	$K^\pi = 8_1^-$	$\rightarrow$	$K^\pi = 8_1^-$	10^-	$\rightarrow$	8^-	455
2538	γ-band	$\rightarrow$	γ-band	10^+	$\rightarrow$	8^+	455
2826	$K^\pi = 4^+$	$\rightarrow$	$K^\pi = 4^+$	11^+	$\rightarrow$	9^+	478
2798	γ-band	$\rightarrow$	γ-band	11^+	$\rightarrow$	9^+	482
2434	$K^\pi = 6^+$	$\rightarrow$	$K^\pi = 6^+$	10^+	$\rightarrow$	8^+	482
1859	$K^\pi = 8_1^-$	$\rightarrow$	$K^\pi = 8_1^-$	11^-	$\rightarrow$	9^-	495

Table 8.2, continued.

E_i (keV)	Band_i	$\rightarrow$	Band_f	I_i^π	$\rightarrow$	I_f^π	E_γ(keV)
2943	A	$\rightarrow$	A	(12^+)	$\rightarrow$	(10^+)	502
1571	GSB	$\rightarrow$	GSB	10^+	$\rightarrow$	8^+	512
3052	γ-band	$\rightarrow$	γ-band	12^+	$\rightarrow$	10^+	515
2701	$K^\pi = 6^+$	$\rightarrow$	$K^\pi = 6^+$	11^+	$\rightarrow$	9^+	518
3136	$K^\pi = 4^+$	$\rightarrow$	$K^\pi = 4^+$	12^+	$\rightarrow$	10^+	531
2137	$K^\pi = 8_1^-$	$\rightarrow$	$K^\pi = 8_1^-$	12^-	$\rightarrow$	10^-	536
3335	γ-band	$\rightarrow$	γ-band	13^+	$\rightarrow$	11^+	538
3378	$K^\pi = 4^+$	$\rightarrow$	$K^\pi = 4^+$	13^+	$\rightarrow$	11^+	552
2989	$K^\pi = 6^+$	$\rightarrow$	$K^\pi = 6^+$	12^+	$\rightarrow$	10^+	555
3624	γ-band	$\rightarrow$	γ-band	14^+	$\rightarrow$	12^+	572
2435	$K^\pi = 8_1^-$	$\rightarrow$	$K^\pi = 8_1^-$	13^-	$\rightarrow$	11^-	573
3523	A	$\rightarrow$	A	(14^+)	$\rightarrow$	(12^+)	580
2151	GSB	$\rightarrow$	GSB	12^+	$\rightarrow$	10^+	580
3284	$K^\pi = 6^+$	$\rightarrow$	$K^\pi = 6^+$	13^+	$\rightarrow$	11^+	582
3927	γ-band	$\rightarrow$	γ-band	15^+	$\rightarrow$	13^+	592
2202	$K^\pi = 8_2^-$	$\rightarrow$	$K^\pi = 8_1^-$	11^-	$\rightarrow$	10^-	600
3742	$K^\pi = 4^+$	$\rightarrow$	$K^\pi = 4^+$	14^+	$\rightarrow$	12^+	606
3595	$K^\pi = 6^+$	$\rightarrow$	$K^\pi = 6^+$	14^+	$\rightarrow$	12^+	607
2749	$K^\pi = 8_1^-$	$\rightarrow$	$K^\pi = 8_1^-$	14^-	$\rightarrow$	12^-	612
3996	$K^\pi = 4^+$	$\rightarrow$	$K^\pi = 4^+$	15^+	$\rightarrow$	13^+	618
3902	$K^\pi = 6^+$	$\rightarrow$	$K^\pi = 6^+$	15^+	$\rightarrow$	13^+	618
2484	$K^\pi = 8_2^-$	$\rightarrow$	$K^\pi = 8_1^-$	12^-	$\rightarrow$	11^-	625
4249	γ-band	$\rightarrow$	γ-band	16^+	$\rightarrow$	14^+	625
2778	GSB	$\rightarrow$	GSB	14^+	$\rightarrow$	12^+	626

Table 8.2, continued.

E_i (keV)	Band$_i$	$\rightarrow$	Band$_f$	I_i^π	$\rightarrow$	I_f^π	E_γ(keV)
3085	$K^\pi = 8_1^-$	$\rightarrow$	$K^\pi = 8_1^-$	15^-	$\rightarrow$	13^-	651
4180	A	$\rightarrow$	A	(16^+)	$\rightarrow$	(14^+)	657
3436	GSB	$\rightarrow$	GSB	16^+	$\rightarrow$	14^+	659
4839	A	$\rightarrow$	A	(18^+)	$\rightarrow$	(16^+)	659
3101	$K^\pi = 8_2^-$	$\rightarrow$	$K^\pi = 8_1^-$	14^-	$\rightarrow$	13^-	666
4418	$K^\pi = 4^+$	$\rightarrow$	$K^\pi = 4^+$	16^+	$\rightarrow$	14^+	676
4123	GSB	$\rightarrow$	GSB	18^+	$\rightarrow$	16^+	686
4840	GSB	$\rightarrow$	GSB	20^+	$\rightarrow$	18^+	718
5155	$K^\pi = 4^+$	$\rightarrow$	$K^\pi = 4^+$	18^+	$\rightarrow$	16^+	737
4180	A	$\rightarrow$	GSB	(16^+)	$\rightarrow$	16^+	744
3523	A	$\rightarrow$	GSB	(14^+)	$\rightarrow$	14^+	745
2943	A	$\rightarrow$	GSB	(12^+)	$\rightarrow$	12^+	792
2441	A	$\rightarrow$	GSB	(10^+)	$\rightarrow$	10^+	870
3052	γ-band	$\rightarrow$	GSB	12^+	$\rightarrow$	12^+	904
1554	$K^\pi = 6^+$	$\rightarrow$	GSB	6^+	$\rightarrow$	6^+	922
2538	γ-band	$\rightarrow$	GSB	10^+	$\rightarrow$	10^+	967
3136	$K^\pi = 4^+$	$\rightarrow$	GSB	12^+	$\rightarrow$	12^+	985
2083	γ-band	$\rightarrow$	GSB	8^+	$\rightarrow$	8^+	1024
2605	$K^\pi = 4^+$	$\rightarrow$	GSB	10^+	$\rightarrow$	10^+	1034
1691	γ-band	$\rightarrow$	GSB	6^+	$\rightarrow$	6^+	1059
1384	γ-band	$\rightarrow$	GSB	4^+	$\rightarrow$	4^+	1078
1175	γ-band	$\rightarrow$	GSB	2^+	$\rightarrow$	2^+	1081
2156	$K^\pi = 4^+$	$\rightarrow$	GSB	8^+	$\rightarrow$	8^+	1097
1791	$K^\pi = 4^+$	$\rightarrow$	GSB	6^+	$\rightarrow$	6^+	1159

Table 8.2, continued.

E_i (keV)	Band$_i$	$\rightarrow$	Band$_f$	I_i^π	$\rightarrow$	I_f^π	E_γ(keV)
1268	γ-band	$\rightarrow$	GSB	3^+	$\rightarrow$	2^+	1174
1175	γ-band	$\rightarrow$	GSB	2^+	$\rightarrow$	0^+	1175
1514	$K^\pi = 4^+$	$\rightarrow$	GSB	4^+	$\rightarrow$	4^+	1207
1533	γ-band	$\rightarrow$	GSB	5^+	$\rightarrow$	4^+	1227
2798	γ-band	$\rightarrow$	GSB	11^+	$\rightarrow$	10^+	1227
1554	$K^\pi = 6^+$	$\rightarrow$	GSB	6^+	$\rightarrow$	4^+	1247
2316	γ-band	$\rightarrow$	GSB	9^+	$\rightarrow$	8^+	1257
1384	γ-band	$\rightarrow$	GSB	4^+	$\rightarrow$	2^+	1291
3523	A	$\rightarrow$	GSB	(14^+)	$\rightarrow$	12^+	1372
2943	A	$\rightarrow$	GSB	(12^+)	$\rightarrow$	10^+	1372
2441	A	$\rightarrow$	GSB	(10^+)	$\rightarrow$	8^+	1382
1691	γ-band	$\rightarrow$	GSB	6^+	$\rightarrow$	4^+	1385
4180	A	$\rightarrow$	GSB	(16^+)	$\rightarrow$	14^+	1402
1514	$K^\pi = 4^+$	$\rightarrow$	GSB	4^+	$\rightarrow$	2^+	1421
3624	γ-band	$\rightarrow$	GSB	14^+	$\rightarrow$	12^+	1476
2538	γ-band	$\rightarrow$	GSB	10^+	$\rightarrow$	8^+	1479
3052	γ-band	$\rightarrow$	GSB	12^+	$\rightarrow$	10^+	1481

Table 8.2, continued.

Chapter 9

Electromagnetic Properties

The principle parameters relevant to intraband and interband electromagnetic transition probabilities are presented for the $K^\pi = 0^+, 2^+, 4^+, 6^+, 8^-, 14^-$ and 16^+ bands studied, along with a summary of the deduced population paths of the isomer bands and the magnitudes of hindrance values. For the 6^+ and 8^- bands, measurements of the mixing of two-quasiparticle configurations are discussed. Tables of the interband intrinsic and reduced matrix elements and a comparison of isomer cross sections are given at the end of the chapter.

9.1 The GSB

The quadrupole moment of the GSB was measured, giving $\sqrt{\frac{5}{16\pi}}eQ_0 = 2.164(10)$ eb, constant within 1.5% between levels up to spin 18^+, despite the strong up-bend observed in the moment of inertia. The present value is in agreement with the results of previous lifetime measurements, $\sqrt{\frac{5}{16\pi}}eQ_0 = 2.17(3)$ eb [1], and indicates a quadrupole deformation parameter of $\delta_{\mathrm{osc}} \approx 0.26$ [43, 44].

9.2 The γ Band at 1175 keV

The quadrupole moment of the γ-band was measured, assuming a rigid rotor, giving $\sqrt{\frac{5}{16\pi}}eQ_0 = 2.21(8)$ eb, in agreement with the GSB value. A linear dependence of the interband intrinsic matrix element $\langle \gamma \mid E2 \mid \text{GSB} \rangle$ on $\Delta \vec{I}^2$ (the Mikhailov term which describes coupling between the rotational and vibrational motions) was included, adjusted to simultaneously fit several previous measurements of $B(E2; I_\gamma \rightarrow I_{\text{GSB}})$. The overall effect of the rotational-vibrational coupling is a $\approx 10\%$ increase in the $B(E2)$ strength between the bottom and the 16^+ state of the γ-band, compared to pure Alaga-rule systematics.

The γ-band was populated as much as 10% (at low spin) relative to the GSB $8^+ \rightarrow 6^+$ transition. The intrinsic matrix element $\langle \gamma \mid E2 \mid \text{GSB} \rangle = 0.252(11)$ eb was measured to first order in ΔI^2, adjusted as a single parameter in the fit. $B(E2; \text{GSB} \rightarrow \gamma)$ values resulting from the fit were as large as 4 W.u. (Table 9.5). This measurement of the $\langle \gamma \mid E2 \mid \text{GSB} \rangle$ matrix element is comparable to values from other nuclei in the $A \approx 180$ mass region [105].

Estimates of the M1 strengths based on previous work were included in the calculations, but measurements of the M1 strengths using the present data were not possible. The population of the γ-band was found to be insensitive to both the intraband and interband M1 intrinsic matrix elements, within the experimental error.

9.3 The 4^+ Band at 1514 keV

As in the $K^\pi = 0^+, 2^+$ bands, a rigid rotor was assumed in fitting the quadrupole moment of the 4^+ band. The correlated error calculation yielded a value of $Q_0 = 2.07(10)$ eb, the same as for GSB and the γ-band.

The 4^+ band has been tentatively identified as the two-phonon γ-vibrational band [106, 107], based largely on the similarity in the dynamic moments of inertia

of the $K^\pi = 2^+$ and $K^\pi = 4^+$ bands. For an isolated harmonic vibrator system, the ratio of the level energies $\frac{E_{2-\text{phonon}}}{E_{1-\text{phonon}}} \approx 2$ is expected. In the present case, the energy ratio is 1.29, suggesting that some anharmonic behavior also might be expected in the transition probabilities between 0-, 1- and 2-phonon states.

Previous $B(E2)$ measurements do not provide sufficient data to calculate the Mikhailov term for the $2^+ \xrightarrow{E2} 4^+$ band transitions, so the intrinsic matrix element connecting the 2^+ and 4^+ bands was fit without the coupling term. The Alaga rule fit gave $\langle K = 4^+ \mid E2 \mid \gamma \rangle = 0.45(2)$ eb and a ratio of intrinsic matrix elements of $\frac{\langle K=4^+|E2|K=2^+\rangle}{\langle K=2^+|E2|K=0^+\rangle} = 1.77(11)$, compared to the expectation of $\sqrt{2}$ for pure harmonic vibrators [105]. The energy of the 2^+ band head is in line with the expectation of ≈ 1 MeV for a harmonic oscillator, and the intrinsic matrix element $\langle K = 2^+ \mid E2 \mid K = 0^+ \rangle = 0.252(11)$ is similar to the values measured in ^{156}Gd, ^{160}Dy and ^{168}Er [105], whereas $\langle K = 4^+ \mid E2 \mid K = 2^+ \rangle = 0.45(2)$ eb is closer to values for heavier osmium nuclei [105]. If the 4^+ state is indeed a two-phonon γ-vibration, then there is significant anharmonicity at the first excited vibrational state, indicated by both the energy ratio and the ratio of intrinsic moments.

Previous attempts to measure the lifetime of the 4_4^+ state have succeeded in finding a lower limit of 0.94 ps [78], and the intensity ratios of its K-forbidden (and K-allowed) γ-decays have been measured, along with a single E2/M1 mixing ratio [2]. The present Xe beam experiment has provided an *upper* limit on the 4_4^+ lifetime of ≈ 4 ns from the width ΔE of the Doppler-corrected 1207 keV $4_4^+ \rightarrow 4_0^+$ E_γ peak and particle time of flight considerations (not to be confused with a Doppler lineshape measurement), as follows. The resolution of the Doppler-shift corrected energy peak measured by the CHICO-Gammasphere combination is given by

$$\frac{\Delta E}{E} \approx \beta \sin(\theta_{\text{p},\gamma}) \Delta \theta_{\text{p},\gamma}, \tag{9.1}$$

where $\theta_{\text{p},\gamma}$ is the true angle between the particle and the γ-ray it emits, in the laboratory frame [17]. The opening angle $\theta_{\text{p},\gamma}$ as measured by the CHICO-

Gammasphere combination is equal to the true laboratory-frame angle only if the γ-ray is emitted while the nucleus is near the center of the detector system. For states with lifetimes > 1 ns and final scattering speeds of $\beta \geq 0.05$, the measured angle $\theta_{\mathrm{p},\gamma}^{\mathrm{lab}}$ deviates far enough from the true laboratory angle that the change in $\frac{\Delta E}{E}$ is measurable. In the limit as the lifetime $\tau \to 0$, the resolution is $\frac{\Delta E}{E} \approx 0.5\%$. The measured FWHM of the 1207 keV peak, $\frac{\Delta E}{E} = 0.8\%$, leads to an upper limit on the lifetime of the 4^+ state of ≈ 4 ns using equation 9.1 and the scattering kinematics. (The slope of the activity as a function of time for the delayed $4_4^+ \to 4_{\mathrm{GSB}}^+$ γ-rays fed by the 6^+ isomer level gives $\tau_{6_6^+} = 107(7)$ ns and a statistical upper limit of $\tau_{4_4^+} < 20$ ns.) The limits 0.94 ps $< \tau_{4_4^+} < 4$ ns suggest approximate bounds for the $\nu = 2$ K-forbidden matrix elements connecting the GSB and 4^+ bands, corresponding to reduced hindrance values of approximately $1 < f_\nu < 90$.

With strong Mikhailov rotational-vibrational coupling parameters included from previous measurements of I_γ [2], the results of the fit of the K-forbidden $\langle 4^+ \mid E2 \mid \mathrm{GSB} \rangle$ and $\langle 4^+ \mid M1 \mid \mathrm{GSB} \rangle$ intrinsic moments gave $\langle K = 4^+ \mid E2 \mid \mathrm{GSB} \rangle = 9.1(5) \times 10^{-4} - 1.47(8) \times 10^{-5} \{ \vec{I}_4^2 - \vec{I}_0^2 \}$ eb in the SDM model (Equation 2.24). This is equivalent to reduced hindrance values of $f_\nu = 9.6$ to 23 for the E2 branches of the 4^+ band head—within the estimated limits, but well below the value of 100 frequently suggested for K-forbidden transitions [47] and suggesting an admixture of one or more $2 \leq K \leq 6$ components at low spin in the GSB. The 4_4^+ lifetime calculated from the fit was 90 ps, again within the upper and lower bounds. The results of the fit gave a calculated E2 fraction of 85(14)% for the $4_4^+ \to 4_0^+$ γ-decay, satisfying both the present γ-ray yield data and the previous measurement of 82(10)% E2 [2]. The GSB to $K = 4^+$ coupling of the SDM model gives f_ν values ranging from 9.0 to 4.9 for the stretched E2 $K = 4 \to \mathrm{GSB}$ transitions from the $I_{4+} = 6^+$ to 18^+ states.

An earlier analysis of the present fit results [57] concluded that the 4^+ band

was populated predominantly by a two-step process from the GSB, through the γ-band. A more systematic analysis of the effect of each intrinsic matrix element indicates that strong interference effects make the GSB$\rightarrow 4^+$ and GSB$\rightarrow \gamma$-band$\rightarrow$ 4^+ paths approximately equal in importance. Both choices of the relative phase of the $\langle 4^+ \mid E2 \mid \text{GSB} \rangle$ and $\langle 4^+ \mid E2 \mid \gamma \rangle$ matrix elements are destructive due to the phases of the Clebsch-Gordan coefficients in the SDM and Alaga systematics. The less destructive sign choice results in a smaller value of $\langle 4^+ \mid E2 \mid 2^+ \rangle$ at the χ^2 minimum, a corresponding $\approx 30\%$ reduction in the $B(E2; K = 2 \rightarrow K = 4)$ strength and an intrinsic moment ratio of $\langle 4^+ \mid E2 \mid 2^+ \rangle / \langle 2^+ \mid E2 \mid 0^+ \rangle = 1.44(9)$, no longer in excess of the harmonic limit. However, this choice of phase is less accurate in its overall reproduction of the behavior of the γ-yields as a function of scattering angle (Figures 4-15 and 4-16). In addition, this choice of phase gives a $\approx 15\%$ greater, though not physically unreasonable, $\langle 4^+ \mid E2 \mid \text{GSB} \rangle$ matrix element at the χ^2 minimum.

The more destructive relative phase of the $\langle 4^+ \mid E2 \mid \gamma \rangle$ matrix element with respect to $\langle 4^+ \mid E2 \mid \text{GSB} \rangle$ gives the best overall agreement with the intraband and interband yield data. This choice of phases gives an increase in some calculated yields, but reproduces the complicated yield vs. θ_{scat} slope features remarkably well (Figures 4-15 and 4-16). Removing the GSB$\rightarrow 4^+$ E2 and M1 coupling *increased* the intraband yields by a factor of ≈ 4, indicating that the interference is considerable.

Regardless of the relative phase, the irregular systematics of the angular momentum coupling in the SDM model produces highly ($\approx 75\%$) destructive interference at the χ^2 minimum for either choice of phase. The Alaga rule (for K-allowed transitions) and the SDM model (for K-forbidden transitions) simultaneously reproduced the many features of the 4^+ band yield data, using reasonable reduced transition probabilities ($\stackrel{<}{\scriptstyle\sim} 10$ W.u.), even at high spin levels. The population of the 4^+ band appears to depend about equally on the $\gamma \rightarrow 4^+$ and GSB$\rightarrow 4^+$

paths. The complete sets of intrinsic and reduced matrix elements coupled to the 4^+ band are listed in Tables 9.4, 9.6, 9.7 and 9.13.

9.4 The 6^+ Isomer Band at 1554 keV

9.4.1 Quasiparticle Structure

The gyromagnetic ratios g, g_K, and g_R are determined by the single-particle structure, and so measurements of the gyromagnetic ratios provide evidence for or against a proposed particle structure. The magnetic moment μ for a single particle orbit is given by [108]

$$\mu_{\text{sp}} = j\left(g_l \pm (g_s - g_l)\frac{1}{2l+1}\right), \tag{9.2}$$

where $j = l \pm \frac{1}{2}$, and g_s and g_l are the g-factors for the particle spin and orbital angular momentum, respectively. For an angular momentum state comprised of rotational and single-particle components, the gyromagnetic ratio is given by [108]

$$g(I) = g_R + (g_K - g_R)\frac{K^2}{I(I+1)}, \tag{9.3}$$

where g_K and g_R are characteristic of the single-particle and rotational motions, respectively. (The two factors g_K and g_R are independent to a first approximation, but are not completely decoupled [6].)

If the gyromagnetic moments $\mu_1 = g_1 I$ and $\mu_2 = g_2 I$ are known for a two-particle state (or, in the present cases, a two-quasiparticle state of an even-even nucleus), the net moment can be calculated according to the additivity relation [109]

$$g(I) = \frac{1}{2}(g_1 - g_2) + \frac{j_1(j_1+1) - j_2(j_2+1)}{2I(I+1)}(g_1 - g_2) \tag{9.4}$$

for two particles p_1 and p_2 with angular momenta j_1 and j_2 in a state of total angular momentum I.

The value of g_K is determined by the single-particle structure of a particular state and can often be determined from measurements in neighboring isotopes

196

and isotones as appropriate, since the neutron and proton orbitals are approximately independent. To a first approximation $g_R \approx \frac{Z}{A}$ is generally assumed to be independent of the single-particle structure, although this is not always a good approximation. Prior *et al.* [110] (cited in [111]) showed using cranking calculations that g_R should be expected to depend upon the single-particle structure.

The $\Gamma_{\Delta I=2}/\Gamma_{\Delta I=1}$ in-band intensity ratios measured in the Xe beam experiment were used to determine the value of $g_K - g_R$, using equations 2.10 and 2.11. The mean value for the 8_6^+–13_6^+ states (Figure 9-1) was $g_K - g_R = 0.56(2)$. (A possible $15_6^+ \rightarrow 14_6^+/14_6^+ \rightarrow 13_6^+$ doublet may have raised the point at $I = 14^+$.) The value $g_R = 0.48(2)$ was obtained, using Equation 9.3 and a previous measurement of $g = 0.959(8)$ [112] for the 6^+ state. This leads to a value of $\bar{g}_K = 1.04(3)$ for the 6^+ band, in agreement with Mullins' measurement of $1.06(7)$ [58], calculated using the same g measurement.

Khoo has proposed a $69\%[404\frac{7}{2}]\pi, [402\frac{5}{2}]\pi$ and $31\%[514\frac{7}{2}]\nu, [512\frac{5}{2}]\nu$ structure [76]. The expected values of $g_K^{\nu^2}$ and $g_K^{\pi^2}$ are 0.222 and 0.768, respectively, using Equation 9.4 and measured values of the single-particle contributions from even-odd neighbors [113, 114, 115]. The 31% ν^2 component seems unlikely, because the present value of $\bar{g}_K$ is not in agreement with a ν^2 admixture, and the $[512\frac{5}{2}]$ orbital appears to be occupied by an $h_{9/2}$ neutron in the Nilsson model. It could be argued that there may be other proton admixtures, (*e.g.* the next $[642\frac{5}{2}]$ orbital in the $f_{7/2}$ subshell) that could contribute to a large value of g_K, but this $f_{7/2}$ orbital, combined with the $g_{7/2}$ proton would be expected to give $\bar{g}_K = 0.84$. No other two-proton Nilsson state appears to have the correct parity, K value and band head energy for the 6^+ state. The present measurement agrees with Mullins' conclusion that the 6^+ band is purely or predominantly π^2 in character.
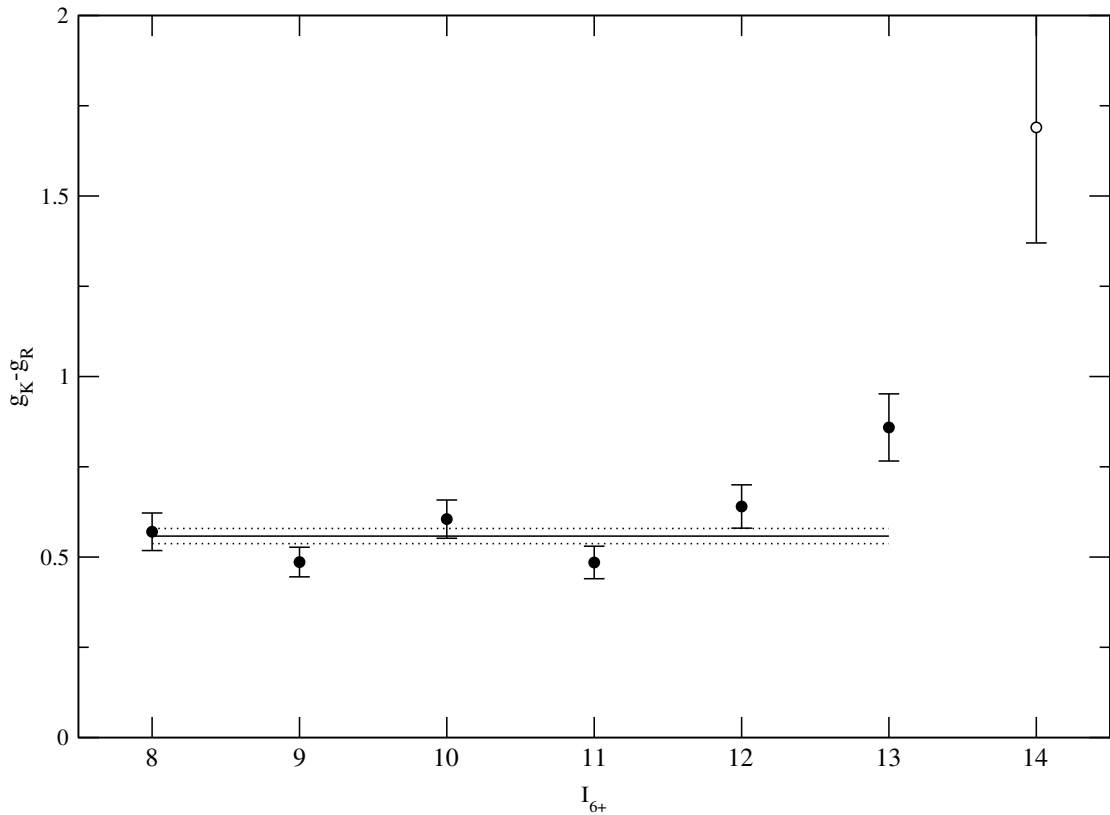
Figure 9-1: The $g_K - g_R$ measurements for the $K = 6^+$ isomer band. The deviant point at spin 14^+ is most likely the result of a doublet between the $15^+ \to 14^+$ and $14^+ \to 13^+$ γ-decays. The solid and dotted lines represent the mean and error, respectively.

9.4.2 Matrix Elements and $B(M\lambda)$

The very precise measurements of $B(\mathcal{M}\lambda)$ values of the 6^+ isomer decay branches (Chapter 3), combined with the Alaga rule (for K-allowed transitions) and the SDM model (for K-forbidden transitions) yielded a strikingly accurate reproduction of the 6^+ isomer band yields with no adjustable parameters (Chapter 4). Within the confines of the Alaga and SDM systematics, the intrinsic matrix elements coupling the $K^\pi = 0^+, 2^+, 4^+$, and 6^+ bands were derived from the measured $B(\mathcal{M}\lambda)$ values (Tables 9.8, 9.9 and 9.10).

The reduced hindrance values for E2 transitions between the 6^+ band and

Branch	ν	f_ν	Branch	f_ν
$6_6^+ \xrightarrow{E2} 6_{\mathrm{GSB}}^+$	4	10.4(2)	$14_6^+ \xrightarrow{E2} 12_{\mathrm{GSB}}^+$	1.2
$6_6^+ \xrightarrow{E2} 4_{\mathrm{GSB}}^+$	4	17.1(3)	$14_6^+ \xrightarrow{E2} 12_{\mathrm{GSB}}^+$	3.5
$6_6^+ \xrightarrow{E2} 4_{K=2}^+$	2	2.7(6)	$14_6^+ \xrightarrow{E2} 12_{K=2}^+$	1.0

Table 9.1: Measured values of the reduced hindrance of the K-forbidden 6^+ isomer decays (f_ν) and decays from the 14_6^+ state.

the GS and γ-band can be calculated in a model-independent way from the measured 6^+ isomer decay branching ratios, giving $2.7 \le f_\nu \le 17$. The reduction in hindrance of the SDM model with increasing spin is seen in Table 9.1.

9.4.3 Population Paths and Relative Phases

The correct choice of relative phases of $\langle 6^+ \mid E2 \mid \gamma \rangle$ and $\langle 6^+ \mid E2 \mid 4^+ \rangle$ (Chapter 4) is more apparent than the analogous problem in the 4^+ band. Since the $\langle 6^+ \mid E2 \mid \mathrm{GSB} \rangle$ matrix element is much less effective than the other two, the problem can be treated as a two-path interference problem. With the magnitudes of the intrinsic moments determined by the isomer branching ratios (using the SDM model for the γ-band coupling), the only effective choice of phases is that of constructive interference between $\langle 6^+ \mid E2 \mid \gamma \rangle$ and $\langle 6^+ \mid E2 \mid 4^+ \rangle$ (Figures 4-26 and 4-27). At large θ_{scat} angles, the $\langle 6^+ \mid E2 \mid \mathrm{GSB} \rangle$ term becomes more important. The over-prediction of the yields for large $\theta_{\mathrm{scat}} > \theta_{\mathrm{scat}}^{\mathrm{safe}}$ leads to one of two conclusions: (1) The SDM model over-predicts $B(E2)$ strengths at high spin, or (2) Coulomb-nuclear interference is becoming important above the $\theta_{\mathrm{scat}} = 53°$ safe angle. The decreased success of the SDM model for higher-K bands indicates the former.

For the final set of matrix elements (Tables 9.8, 9.9 and 9.10) the Coulomb excitation calculations show that the $I \rightarrow I+2$ excitations are most effective in
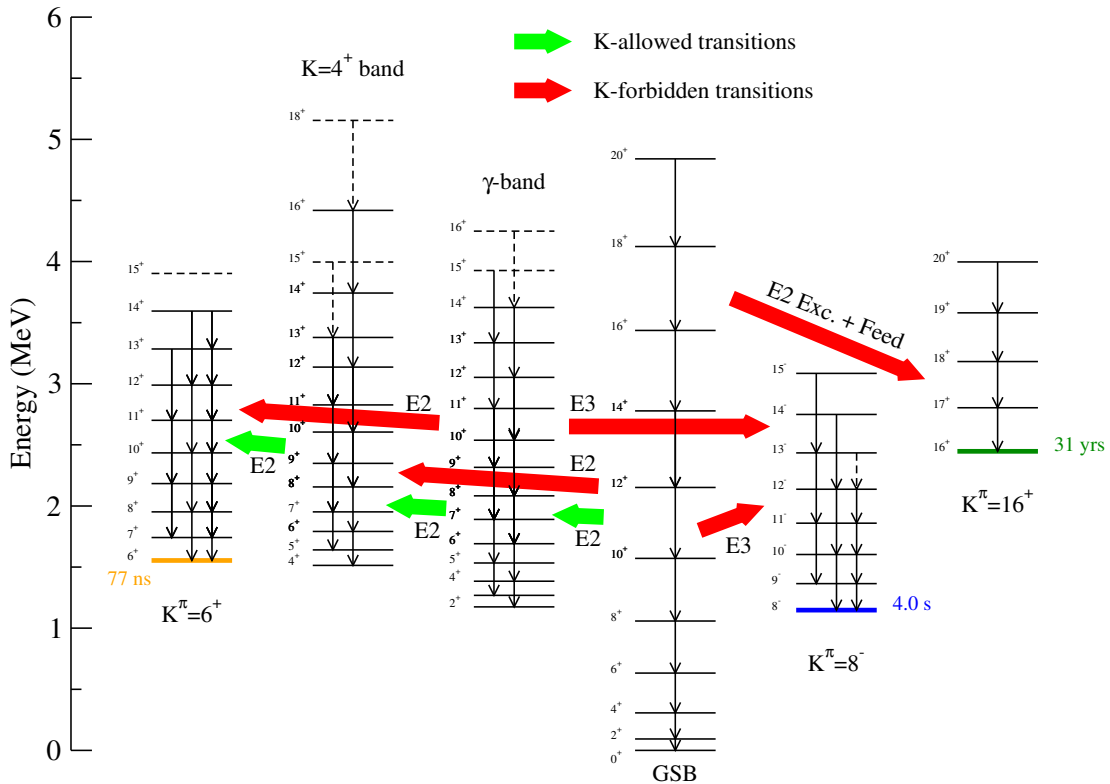
Figure 9-2: A schematic representation of the population paths to the three isomer bands. The red and green arrows represent band→band transitions.

populating the 6^+ band and that the excitation generally follows the path of the fewest possible steps. The three paths to excitation of the 6^+ band are illustrated in Figure 9-2.

9.5 The 8^- Isomer Band at 1147 keV

9.5.1 The Quadrupole Moment

The intrinsic quadrupole moment of the 8^- band could not be determined from the intraband γ-ray yields, because the calculated yields are much more sensitive to the interband E3 matrix elements. Authors [58, 86, 6] have used the value $eQ_0 = 6.95$ eb ($\sqrt{\frac{5}{16\pi}}eQ_0 = 2.19$ eb), apparently originating from an early measurement

of the $B(E2; 2_0^+ \rightarrow 0_0^+)$ strength [6], but direct measurements of the quadrupole moment of the 8^- isomer band have not been made. Measurements for the 16^+ isomer state of $Q_0 = 7.2(1)$ b [116] and $Q_0 = 8.2(11)$ b [117] suggest that the 8^- bands would have very similar quadrupole moments to both the 16^+ band and the GSB, since the 16^+ isomer is believed to be the product of the two-quasiparticle wave functions of the two 8^- bands.

9.5.2 Mixing Between the Two 8^- Bands

The present analysis of the 8^- isomer band population has shown that the coupling (and therefore the mixing) between the two 8^- bands is important in reproducing either band's yields. Many measurements have been made in attempts to measure the mixing amplitudes between the 8_1^- and 8_2^- bands with varied results. Most results indicate that the 8_1^- (isomer) band is predominantly a ν^2 band and that mixing is strong, with interaction potentials of $\gtrsim 100$ keV and a large energy shift between equal-spin levels of the two bands.

The present and past measurements of the mixing of the 8^- bands can be understood in terms of simple two-state mixing [60]. The mixed-state (or "perturbed") wave functions ψ_A and ψ_B can be written in terms of the unmixed (pure) basis states ϕ_a and ϕ_b,

$$\psi_A = \alpha \phi_a + \beta \phi_b \tag{9.5}$$

and

$$\psi_B = -\beta \phi_a + \alpha \phi_b, \tag{9.6}$$

where $\alpha^2 + \beta^2 = 1$. The interaction potential V between the unperturbed states is defined as

$$V = \langle \phi_a \mid \hat{V} \mid \phi_b \rangle. \tag{9.7}$$

In terms of the measurable separation energy ΔE_f between the mixed states and

the mixing fraction β^2,

$$V = \frac{\Delta E_f}{\sqrt{\frac{x^2}{1+x} + 4}}, \tag{9.8}$$

where $x \equiv \frac{1}{\beta^2} - 2$ [60]. The observed gyromagnetic ratios $\bar{g}_K$ of the mixed states are given by

$$
\begin{aligned}
\bar{g}_K^A &= (1 - \beta^2)g_K^a + \beta^2 g_K^b \text{ and} \\
\bar{g}_K^B &= \beta^2 g_K^a + (1 - \beta^2)g_K^b.
\end{aligned}
\tag{9.9}
$$

Then, for the 8_1^-, 8_2^- system, composed as $\psi_{8_1^-} = \alpha\phi^{\nu^2} + \beta\phi^{\pi^2}$, the observed gyromagnetic ratio $\bar{g}_K = (1 - \beta^2)g_K^{\nu^2} + \beta^2 g_K^{\pi^2}$ can be used to measure β^2. For any two-state mixing system an interaction energy of $V \approx \frac{\Delta E_f}{2}$ (166 keV for the 8_1^- and 8_2^- system) indicates that two nearly degenerate basis states are almost completely mixed. (As $V \to \frac{\Delta E_f}{2}$, $\beta^2 \to 0.5$.) Regardless of the variation in the mixing fraction, β^2 values of the order of those measured for the 8^- bands (≈ 0.25–0.5) indicate strong mixing of the two bands and suggest that the $\langle 8_1^- \mid E2 \mid 8_2^- \rangle$ matrix elements may have to be considered in fitting the E3 matrix elements which populate the 8^- bands, as in the present analysis (Chapter 4).

Helmer and Reich proposed that the 8_1^- isomer band is a mixed two quasiproton ($\pi\frac{9}{2}^-[514]\pi\frac{7}{2}^+[404]$) and two quasineutron ($\nu\frac{7}{2}^-[514]\nu\frac{9}{2}^+[624]$) configuration, approximately one third π^2 from their measured γ-ray intensities [118]. This proposed $\pi\frac{9}{2}\pi\frac{7}{2}$, $\nu\frac{7}{2}\nu\frac{9}{2}$ configuration is not inconsistent with any succeeding measurements of the gyromagnetic moments, and the Nilsson potentials indicate this as the most probable configuration, leaving the mixing fractions to measurement.

The proton contributions to $\bar{g}_K$ are dominant, and with the common assumption that $g_R \approx 0.3$, a maximum 70% ν^2 component is predicted in the limit $g_K - g_R \to 0$, using the values $g_K = 1.031(11)$ for the $\pi\frac{9}{2}^-\pi\frac{7}{2}^+$ state and $g_K = -0.013(3)$ for the $\nu\frac{7}{2}^-\nu\frac{9}{2}^+$ state [6]. (Taking an unweighted average from a collection of experimental g_R values [111] for the suspected quasiparticle states in the 8^- states gives $g_R \approx 0.3$, a value sometimes used in the literature.) Natu-

rally, measurements of relative intensities which would give $(g_K - g_R)^2 < 0$ after subtraction of the E2 component give no meaningful result, so that for estimates of $g_R \approx 0.3$, the lower bound on measurements of the π^2 fraction is 30%, not far from many published measurements. However, the mixing matrix element V varies slowly with β^2 for strongly mixed levels and can be measured to good precision within the simple two-state mixing model. (For the two mixed 8_8^- states separated by $\Delta E = 332$ keV, $0.25 \leq \beta^2 \leq 0.35 \Rightarrow 144 \leq V \leq 158$.)

The intraband intensity ratios could not be obtained from the present data set for most states in the 8_1^- band. Ambiguous γ-ray energy peaks, which could not be resolved from the lines of odd-A contaminants and low yields of the upper levels prevented direct measurements of the branching ratios in most cases, but two intraband branching ratios were measured for the 11^- and 10^- levels. Assuming the same quadrupole moment as in the GSB, the branching ratios yield $\mid g_K - g_R \mid =$ 0.12(7) for the 11^- state. (The branching ratio of the 10^- state does not give a real solution for $g_K - g_R$, and Equations 9.9 imply that the $10^- \rightarrow 9^-$ decay is $\approx 100\%$ E2, but the measured γ-ray intensity ratio was $I_\gamma^{\Delta I=2}/I_\gamma^{\Delta I=1} = 2.2(3)$, compared to previous measurements of 1.67(10) [9] and 1.8(5) [5].)

Using $g_R = 0.48(2)$ from the present 6^+ band measurements and de Boer's calculated g_K values for the neutron and proton configurations, the result from the present measurement of the 11^- state is a 58(7)% π^2 component, more than twice the result of Tlustý *et al.* [86], suggesting that the π^2 component is dominant in the 8_1^- band. The present measurement of $\beta_{11^-}^2$ is about twice previous measurements, but V differs by at most 15% from previous measurements (Figure 9-4). (The error includes *only* the error in the branching ratio, not in the estimate of g_R.) For $g_R \approx 0.3$, the π^2 component becomes 41(6)% of the admixture in the 8_1^- band, and from de Boer's data, a 30(2)% π^2 component can be calculated for the 11^- level (Table 9.2.)

Other quantitative measurements of the mixing fractions of the two Nilsson

configurations have given the following results. De Boer *et al.* [6] have calculated the mixing fractions $37.3(20)\%$ π^2 in the 8^- level from two β-decay experiments and $36.0(16)\%$ π^2 in the 10^- and 9^- levels from E2/M1 mixing ratio (δ) measurements. Postma *et al.* have measured the magnitude and sign of δ and found a $42(10)\%$ π^2 component in the 9^- level [7] and calculated from the branching ratio measurements of Venema *et al.* [8] an average $31(3)\%$ π^2 component in the 10^-–13^- levels (Table 9.2), in contrast with the result of the present experiment.

Tlustý *et al.* [86] have measured $\delta_{E2/M1}$ for the 9^-–13^- states using γ-ray angular correlation data and calculated a five-point fit to the function

$$(g_K - g_R) = A(I)A(I-1)(g_K - g_R)_{\nu^2} + B(I)B(I-1)(g_K - g_R)_{\pi^2} \qquad (9.10)$$

using de Boer's calculated values of $(g_K - g_R)_{\nu^2}$ and $(g_K - g_R)_{\pi^2}$ and supposing that A and B are linear in $\vec{I}^2$. This allowed an extrapolation to the 8^- state and does not have the lower-limit problem of equation 9.9.

Table 9.2 gives π^2 admixture fractions (β^2) and their corresponding interaction potentials V from the previous measurements. The conclusion common to all previous measurements is that the two bands do appear to be strongly mixed, the lower 8^- (isomer) band apparently containing the majority of the ν^2 configuration. It is curious that in lighter isotopes (*e.g.*^{172}Hf [112], ^{174}Hf [119], ^{176}Hf [120]) the configuration of the lower of the two 8^- band heads (the only one observed in ^{172}Hf) has been identified as a nearly pure π^2 state, whereas all previous measurements for ^{178m}Hf indicate a strongly mixed system, with a dominant ν^2 admixture. But the energies of the 8^- isomers in the lighter isotopes are 400–850 keV higher than ^{178m}Hf, suggesting that the mixing of states in ^{178}Hf, and therefore the repulsion $\Delta E_f - \mid E_A - E_B \mid$, may be different, consistent with anomalous strong mixing in ^{178m}Hf.

Khoo suggests that with weak ($V \approx 40$ keV) mixing at the band head, the mixing is almost complete at the 12^- levels in ^{176}Hf, whereas Tlustý's measurement for ^{178}Hf suggests smaller mixing with increasing spin, in agreement with

204

the calculations described by Smith *et al.* [5].

It is interesting to note that any spin-dependence of V (increasing *or* decreasing) may enhance the interband transition strength between two admixed bands. For example, for a state of spin I in one of two mixed bands of K_A and K_B (Figure 9-3), the ratio $r = \frac{B(E2;K_A,I\to K_B,I-2)}{B(E2;K_A,I\to K_A,I-2)}$ of the stretched interband to intraband E2 transition probability is given by

$$r^{1/2} = \beta_I\sqrt{1 - \beta_{I-2}^2} \cdot \frac{\langle I K_B 2 0 \mid I-2\, K_B\rangle}{\langle I K_A 2 0 \mid I-2\, K_A\rangle}\frac{Q_0^B}{Q_0^A} - \beta_{I-2}\sqrt{1 - \beta_I^2}, \quad (9.11)$$

where β_I^2 and β_{I-2}^2 are the respective mixing fractions in the I and $I - 2$ states (Equations 9.5 and 9.6), and A and B refer to the two mixed bands.

Of course, as the mixing potential tends toward zero, so does the interband transition probability, but to first order (assuming that the matrix elements between the unperturbed states are small), for similar Q_0 moments and equal K values of two bands, the interband transitions will be enhanced by either an increasing or decreasing spin-dependence of β^2.

9.5.3 Population Paths

The strong mixing measured between the two 8^- bands makes the problems of reproducing their measured γ-decay yields inseparable. Feeding from the 8_2^- band to the 8_1^- band was found to be important in predicting the relative populations of the odd and even 8_1^- states. The SDM systematics of Equation 2.24, which worked well for lower-K bands, failed for $K = 8$, giving an explosive increase in the $B(E3)$ strength with spin. The Alaga rule, attenuated gradually for $I \to 8$ to force agreement with the large hindrance of the isomer decays ($f_\nu = 79(1)$

I	$g_K - g_R$ (or δ)	β^2	V (keV)	$\dfrac{V}{E_{8_2}(I)-E_{8_1}(I)}$
8–13		≈ 0.4	[118] ≈ 167	≈ 0.49
8		[a]0.373(20)	[6] 160(2)	0.484(5)
8		[b]0.36(2)	[86] 159(2)	0.480(6)
8		[c]0.36	[5] [c]159	0.479
9–10	0.096(9),0.103(17)	[d]0.360(16)	[6] 160(2)–162(2)	0.480(5)
9	$(0.64 \leq \delta \leq 1.88)$	[e]0.42(10)	[7] 165(5)	0.494(16)
9	0.097(12)	[b]0.33(2)	[86] 157(2)	0.470(7)
9		[c]0.31	[5][c]154	0.461
10–13		[f]0.31(3)	[7, 8]156(4)–163(4)	0.462(12)
10	0.099(18)	[b]0.30(2)	[86] 155(3)	0.458(9)
10		[g]0.370(25)	[9] 163(2)	0.483(7)
10		[h]0.34(2)	[5] 160(2)	0.474(7)
10		[c]0.26	[5] [c]149	0.441
11	0.036(13)	[b]0.26(2)	[86] 150(4)	0.439(11)
11		[c]0.22	[5] [c]143	0.417
11	0.12(7)	[i]0.58(7)	169(4)	0.494(11)
12	0.00(12)	[b]0.22(2)	[86] 145(5)	0.414(14)
12		[h]0.38(2)	[5] 169(2)	0.485(5)
12		[c]0.19	[5] [c]137	0.393

Table 9.2: A survey of measurements of V and β^2 values of the 8_1^- band states. Errors in V were calculated from the errors in the authors' measured quantities. Systematic uncertainties in estimates of g_R and g_K values are not included. [a]From β-decay experiments. [b]From a simultaneous fit of $g_K - g_R$ to a quadratic function of $\vec{I}^2$. The author's largest error estimate was used. [c]V calculated [5], β^2 calculated from V. [d]De Boer used $g_R = 0.262(14)$. [e]From δ, using $g_K - g_R$ from [6]. [f]Calculated in [7] from the data of [8]. [g,h]Calculated from the intraband intensity ratios of [9, 5] using $g_R = 0.3$. [i]Present work.

206
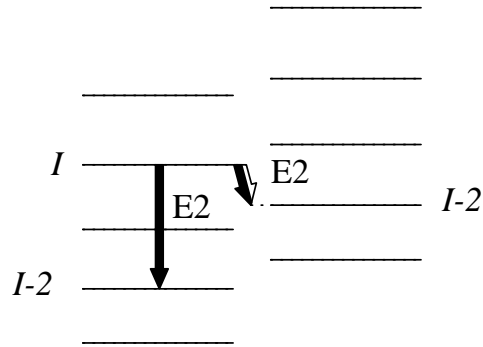
Figure 9-3: Two mixed bands, A (left) and B (right), showing an intraband E2 transition and an interband E2 transition. The γ-ray intensity ratio can be used to measure the band mixing.

I	$g_K - g_R$ (or δ)	β^2	V (keV)	$\frac{V}{E_{8_2}(I) - E_{8_1}(I)}$
13	-0.039(18)	[b]0.18(2)	[86] 136(6)	0.384(17)
13		[h]0.34(2)	[5] 167(2)	0.474(7)
13		[c]0.16	[5][c]131	0.371

Table 9.2, continued.

for the $8_8^- \xrightarrow{E1} 8_{\mathrm{GSB}}^+$ transition, calculated from the known lifetime and the upper limit on the E3 component of the decay [121]), reproduced the measured yields and their behavior with respect to scattering angle. The attenuated Alaga-rule systematics assuming the lowest possible K admixture, $K = 5$, gave a range of $B(E3)$ strengths which was reasonable for ^{178}Hf [89].

Two paths for each 8^- band, $\gamma \to K = 8$ and GSB$\to K = 8$ were required in order to reproduce the measured yields with reasonable $B(E3)$ values. The 8^- isomer cross sections calculated from the final set of E3 matrix elements gave 16(4) mb for the Xe beam experiment at 96% of the barrier from the best-fit intrinsic matrix elements, $\langle 8^- \mid E3 \mid 2^+ \rangle = 0.36\ ^{+0}_{-0.07}$ eb$^{3/2}$ and $\langle 8^- \mid E3 \mid 0^+ \rangle = 0.37\ ^{+0.07}_{-0.01}$ eb$^{3/2}$ (the saturation-values of the intrinsic matrix elements for $I_\gamma > 8$
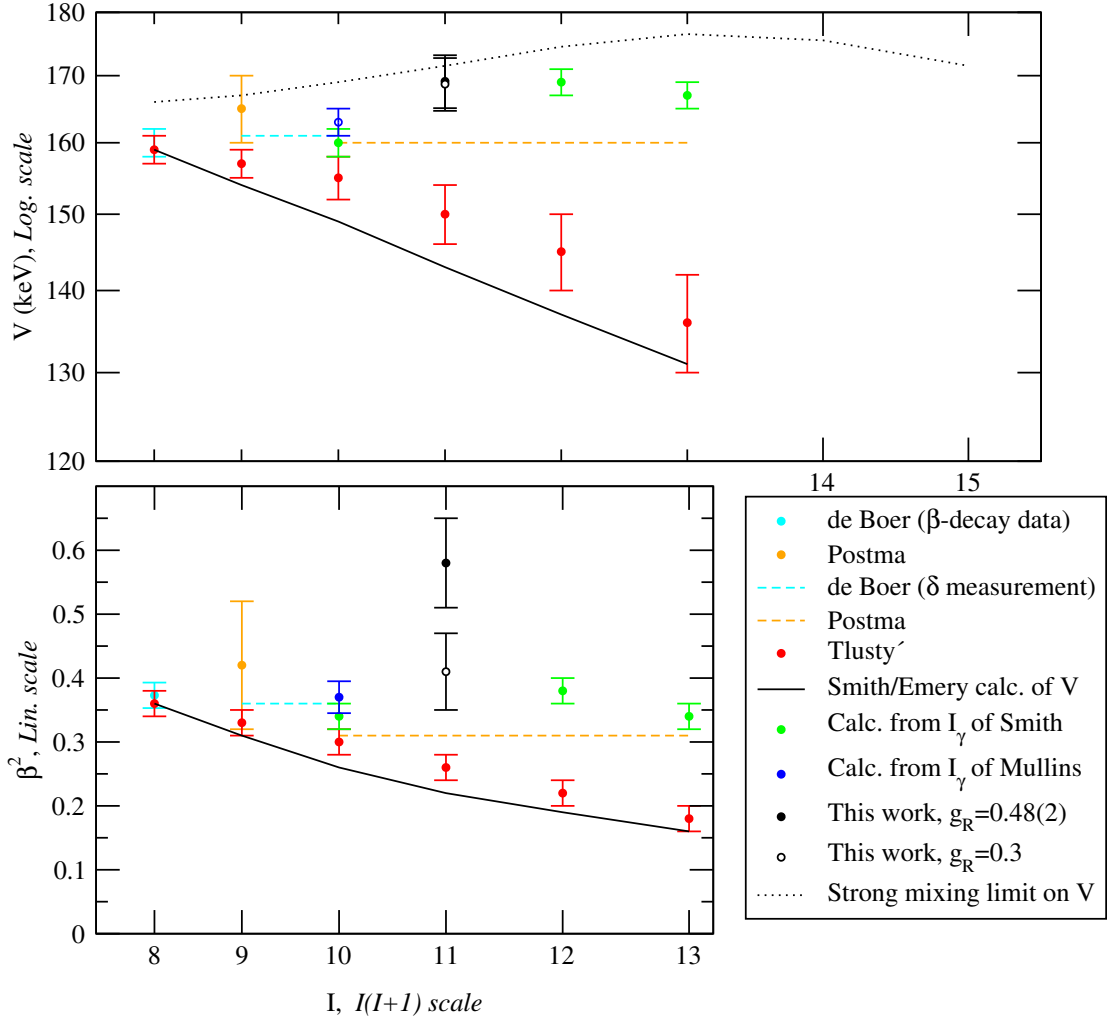
Figure 9-4: Measured and calculated values of β^2 (bottom) and V (top) values, as a function of $I_{8_1^-}$. For strong mixing, large fractional variations in β^2 result in small fractional variations in V.

and $I_{\text{GSB}} > 10$).

The reduced hindrance value for the most effective matrix element, $\langle 12_8^- \| E3 \| 10_{\text{GSB}}^+ \rangle$, populating the 8^- band from the GSB is $f_\nu = 0.6$, in the modified Alaga systematic, in contrast with the large E1 hindrance of the isomer decay. (Hindrance values are similar for the fit of the $\langle 12_8^- \| E3 \| 10_\gamma^+ \rangle$ matrix elements.) The gradual increase in strength imposed on the $B(E3)$ with increasing I_γ or I_{GSB}

resulted in a drop in the reduced hindrance from $f_\nu = 1.7$ to 0.6 for the $I \to I + 3$ excitations from the 6^+ to 12^+ levels. A similar result could be obtained assuming spin-dependent mixing in the 8^- band, but this is a less likely hypothesis. For instance, the large hindrance of the $16_{16}^+ \xrightarrow{E3} 13_8^-$ shows that there are no significant $13 \le K \le 19$ admixtures in the 8_1^- bands.

9.6 The 14^- Isomer Band at 2574 keV

It was not possible to find an unambiguous sign of population of the 14^- isomer band, but an upper limit on the cross section was calculated from the γ-ray doubles data (Chapter 7). A $\langle K = 14 \mid E3 \mid K = 0 \rangle$ matrix element was fit to the upper limit, assuming that the 14^- band is populated directly from the GSB by $\langle I_f, K = 14 \| E3 \| I_i, K = 0 \rangle$ matrix elements, all of approximately magnitude. The upper limit on the isomer cross section was calculated for the Xe beam experiment based on this simple model, giving $\sigma_{14^-} < 2$ mb, considerably smaller than the other isomers populated (Table 9.3). The upper limits of the reduced transition probabilities were equivalent to 3 W.u.$< B(E3) < 5$ W.u. and a $15_{14}^- \xrightarrow{E3} 12_{GSB}^+$ reduced hindrance value of 0.7, compared to $f_\nu = 87$ for the 140 keV M1 branch and $f_\nu = 33$ for the 437 keV E2 branch.

9.7 The 16^+ Isomer Band at 2446 keV

9.7.1 Quadrupole Moment

A direct measurement of the quadrupole moment of the 16^+ band using laser spectroscopy on ^{178m2}Hf nuclei gave $Q_0 = 7.2(1)$ b [116], while Coulomb excitation of a 16^+ isomer-enriched target gave $Q_0 = 8.2(11)$ b [117]. The first measurement is within 5% of the Q_0 moment of the GSB, and the second is within $\approx 1\sigma$ (19% greater), giving no indication that the quadrupole deformation of the 16^+ state

is different from the ground state deformation. The $19^+ \rightarrow 18^+$ yields are not sensitive enough to the quadrupole moment to allow a measurement using the present Xe beam data set.

The measured (model-independent) 16^+ isomer cross sections from the ^{178}Hf beam activation experiment (Tables 6.9 and 9.3) gave excitation probabilities of $30(8) \times 10^{-4}$ and $14(5) \times 10^{-4}$, respectively, at 100% and 80% of the Coulomb barrier, while the cross section for the $25° \leq \theta_{\mathrm{scat}} \leq 78°$ scattering range in the ^{136}Xe beam experiment was $4(2) \times 10^{-4}$ (calculated from deduced matrix elements).

The 16^+ band appears to be populated directly from the GSB. In the Xe beam experiment, calculations based on the fitted matrix elements showed that the principle mode is by γ-decay feeding ($\approx 10\%$ direct excitation). The E2 strength deduced from the combined data of the Xe-beam (Chapter 4) and Ta-target (Chapter 7) experiments is ≤ 7 W.u. (Table 9.14), and the modest 0.26–0.7 W.u. transitions to the 16^+ and 17^+ states are responsible for $\approx 80\%$ of the isomer population in the Xe experiment, as a consequence of the high energies of the feeding transitions.

Even with these small transition probabilities feeding the 16^+ band, the reduced hindrance values f_ν range from 0.87—1.10, a factor of one hundred smaller than the prediction of Rusinov's rule. The Coriolis matrix elements are small near the band head, which indicates that the K-mixing must occur primarily in the GSB. The transitions to the 16^+ band reveal the onset of $14 < K < 18$ components in the $I \geq 14$ levels of the GSB (Chapter 10). The majority of the population of the isomer appears to be due to direct GSB$\rightarrow 16^+$ γ-decay feeding of the 17^+ ($\approx 25\%$ feeding) and 16^+ ($\approx 50\%$ feeding) levels, where Coriolis forces are small or zero, indicating that the K-mixing must be in the upper levels of the GSB with admixtures of $14 \leq K \leq 18$.

9.8 Matrix Elements and Cross Sections

Below are the summarized isomer cross sections (Table 9.3), intrinsic matrix elements (Table 9.4) and reduced matrix elements (Tables 9.5–9.14) for each inter-band coupling measured. It should be noted that the sets of reduced matrix elements are in general model-dependent. That is, except in the case of the 16^+ band, they follow an angular momentum coupling systematic, such as the Alaga rule or the SDM model, noted in each table. Intraband E2 and M1 reduced matrix elements (not tabulated) did not exhibit any measurable deviation from the rigid rotor (electric) and particle-rotor (magnetic) systematics. *Note: The $B(\mathcal{M}\lambda)$ values in the tables are arbitrarily given in the upward direction, from I_i to I_f. For A=178, the relevant Weisskopf estimates are $B(E2 \uparrow)_\mathrm{W} = 0.0297 \ e^2 b^2$, $B(E3 \uparrow)_\mathrm{W} = 0.0132 \ e^2 b^3$, $B(M1 \uparrow)_\mathrm{W} = 5.37 \ \mu_\mathrm{N}^2$ and $B(M2 \uparrow)_\mathrm{W} = 2.61 \ \mu_\mathrm{N}^2 b$.*

$^{178}\text{Hf}(^{136}\text{Xe},^{136}\text{Xe})^{178}\text{Hf}$ (calc.)			
$\frac{E_{\text{beam}}}{E_{\text{barrier}}} = 96\%,\ 25° \leq \theta_{\text{Xe}} \leq 78°$			
Level	Model/Fit	σ_{fit} (mb)	$\sigma_{\text{fit}}/\sigma_{\text{Ruth}}$
2^+_{GSB}	Rotor	[a]9690(90)	0.900(8)
6^+_{isom}	SDM model	[b]6.4(11)	$5.9(10) \times 10^{-4}$
8^-_{isom}	Alaga, total	[a]16(4)	$15(4) \times 10^{-4}$
	" GSB contrib.	6.5	6.0×10^{-4}
	" $\gamma \rightarrow 8^-$ contrib.	10.3	9.6×10^{-4}
14^-_{isom}	Upper limit	[c] < 2	$< 2 \times 10^{-4}$
16^+_{isom}	Direct Fit (Ch. 6)	[d]4(2)	$4(2) \times 10^{-4}$

$\text{Ta}(^{178}\text{Hf},^{178}\text{Hf})\text{Ta}$ (meas.)			
$40° \leq \theta_{\text{Hf}} \leq 180°$			
Level	$\frac{E_{\text{beam}}}{E_{\text{barrier}}}$ (%)	σ_{meas} (mb)	$\sigma_{\text{meas}}/\sigma_{\text{Ruth}}$
16^+_{isom}	88	[e]11(3)	$30(8) \times 10^{-4}$
16^+_{isom}	80	[e]6(2)	$14(5) \times 10^{-4}$
16^+_{isom}	76	[e]1.4(4)	$3.0(8) \times 10^{-4}$
16^+_{isom}	72	[e]0.6(2)	$1.2(4) \times 10^{-4}$

Table 9.3: Summary of calculated (top) and measured (bottom) cross sections for the isomers. (The cross sections for the Xe beam experiment were integrated from the intrinsic matrix elements fitted to the online data.) The total Rutherford cross sections are 11.0 b (top) and 3.7 b (bottom, 88% E_{barrier}). Error estimates: [a]from the correlated error calculations, [b]from the errors in the measured 6^+ branching ratios, [c]upper limit measurement, [d]from the largest diagonal error in the fitted set of matrix elements, [e]measured directly.

The intrinsic matrix elements $\langle K_f \mid \mathcal{M}\lambda \mid K_i \rangle = m_0 + \Delta \vec{I}^2 m_1$				
m	ν	m_0	m_1	Comment
$\langle 2^+ \mid E2 \mid 0^+ \rangle$	0	0.266(12) eb	-0.00347(15) eb	[a]$m = 0.252(11)$
$\langle 4^+ \mid E2 \mid 2^+ \rangle$	0	0.447(19) eb		
$\langle 4^+ \mid E2 \mid 0^+ \rangle$	2	9.1×10^{-4} eb	-1.47×10^{-5} eb	$\pm 6\%$
$\langle 4^+ \mid M1 \mid 0^+ \rangle$	3	6.3×10^{-5} μ_{N}	-9.5×10^{-7} μ_{N}	$\pm 30\%$
$\langle 6^+ \mid E2 \mid 4^+ \rangle$	0	0.094(3) eb		
$\langle 6^+ \mid E2 \mid 2^+ \rangle$	2	0.00116(10) eb		
$\langle 6^+ \mid E2 \mid 0^+ \rangle$	4	1.57×10^{-6} eb	$-2.10 \times^{-8}$ eb	$\pm 3.5\%$
$\langle 6^+ \mid M2 \mid 8^- \rangle$	0	0.102(9) $\mu_{\mathrm{N}}\mathrm{b}^{1/2}$		
$\langle 8^- \mid E3 \mid 2^+ \rangle$	3	$0.36\,^{+0}_{-0.07}$ eb$^{3/2}$		[b]Alaga rule
$\langle 8^- \mid E3 \mid 0^+ \rangle$	5	$0.37\,^{+0.07}_{-0.01}$ eb$^{3/2}$		[b]Alaga rule

Table 9.4: Intrinsic matrix elements $m = \langle K_f \mid \mathcal{M}\lambda \mid K_i \rangle$. The errors do not include error in the slope or offset of the Mikhailov fit. Errors for the 6^+ band intrinsic matrix elements were propagated from measured isomer branching ratios. Correlated errors are given for the other bands. [a]To first order in $\Delta \vec{I}^2$. [b]For $I_{\mathrm{GSB},\gamma} > 9$ only; reduced matrix elements were attenuated for $I < 8$.

I_i	I_f	m (eb)	$B(E2) \times 10^3$ (e²b²)	I_i	I_f	m (eb)	$B(E2) \times 10^3$ (e²b²)
0	2	0.347	120.	10	8	0.483	11.1
2	2	0.449	40.3	10	9	-0.948	42.8
2	3	-0.548	60.1	10	10	1.05	52.4
2	4	0.318	20.2	10	11	-0.683	22.2
4	2	0.119	1.57	10	12	0.212	2.14
4	3	-0.415	19.1	12	10	0.595	14.2
4	4	0.668	49.6	12	11	-1.10	48.8
4	5	-0.612	41.6	12	12	1.15	52.6
4	6	0.302	10.1	12	13	-0.680	18.5
6	4	0.253	4.92	12	14	0.166	1.10
6	5	-0.615	29.1	14	12	0.708	17.3
6	6	0.817	51.3	14	13	-1.26	54.5
6	7	-0.652	32.7	14	14	1.24	52.7
6	8	0.280	6.03	14	15	-0.667	15.3
8	6	0.370	8.05	14	16	0.113	0.440
8	7	-0.787	36.4	16	14	0.824	20.6
8	8	0.941	52.1	16	15	-1.41	60.2
8	9	-0.675	26.8	16	16	1.32	52.8
8	10	0.250	3.68	18	16	0.942	24.0

The table above is headed by the following spanning block:

GSB→ γ-band

K-allowed $\langle \gamma \mid E2 \mid \mathrm{GSB} \rangle = 0.266(12)$

$-3.47(15) \times 10^{-3}\{I_\gamma(I_\gamma + 1) - I_0(I_0 + 1)\}$ (eb)

Table 9.5: Reduced matrix elements $m = \langle I_f, K = 2^+ \| E2 \| I_i, K = 0^+ \rangle$ and $B(E2) = B(E2; \mathrm{GSB} \to \gamma)$ values for the K-allowed E2 transitions. $\langle \gamma \mid E2 \mid \mathrm{GSB} \rangle = 0.252(11)$ eb to first order in ΔI^2.

			γ-band$\rightarrow K = 4^+$ band				
			K-allowed $\langle K = 4^+ \mid E2 \mid \gamma \rangle = 0.45(2)$ eb				
I_i	I_f	m (eb)	$B(E2) \times 10^3$ (e^{2}b^2)	I_i	I_f	m (eb)	$B(E2) \times 10^3$ (e^{2}b^2)
2	4	1.0	200	7	6	-0.42	12.
3	4	-0.75	80.	7	7	0.89	53.
3	5	0.92	120	7	8	-1.1	87.
4	4	0.44	22.	7	9	0.84	47.
4	5	-0.92	93.	8	6	0.15	1.3
4	6	0.87	85.	8	7	-0.51	15.
5	4	-0.20	3.6	8	8	0.99	58.
5	5	0.64	37.	8	9	-1.2	84.
5	6	-1.0	93.	8	10	0.84	41.
5	7	0.85	66.	9	7	0.19	1.8
6	4	0.06	0.28	9	8	-0.59	18.
6	5	-0.32	7.9	9	9	1.1	61.
6	6	0.78	47.	9	10	-1.2	81.
6	7	-1.1	91.	9	11	0.84	37.
6	8	0.84	54.	10	8	0.22	2.3
7	5	0.11	0.73	10	9	-0.66	21.

Table 9.6: Reduced matrix elements $m = \langle I_f, K = 4^+ \| E2 \| I_i, K = 2^+ \rangle$ and $B(E2) = B(E2; \gamma \rightarrow 4^+)$ values for the K-allowed E2 transitions.

I_i	I_f	m (eb)	$B(E2) \times 10^3$ (e^{2}b^2)	I_i	I_f	m (eb)	$B(E2) \times 10^3$ (e^{2}b^2)
10	10	1.2	64.	13	15	0.87	28.
10	11	-1.3	79.	14	12	0.35	4.2
10	12	0.85	34.	14	13	-0.91	28.
11	9	0.26	2.8	14	14	1.4	69.
11	10	-0.73	23.	14	15	-1.4	72.
11	11	1.2	65.	14	16	0.88	27.
11	12	-1.3	77.	15	13	0.38	4.5
11	13	0.86	32.	15	14	-0.96	30.
12	10	0.29	3.3	15	15	1.5	70.
12	11	-0.79	25.	15	16	-1.5	70.
12	12	1.3	67.	15	17	0.89	26.
12	13	-1.4	75.	16	14	0.40	4.9
12	14	0.86	30.	16	15	-1.0	31.
13	11	0.32	3.7	16	16	1.5	70.
13	12	-0.85	27.	16	17	-1.5	69.
13	13	1.4	68.	16	18	0.90	25.
13	14	-1.4	73.				

The table above is headed by:

γ-band$\rightarrow K = 4^+$ band, continued

K-allowed $\langle K = 4^+ \mid E2 \mid \gamma \rangle = 0.45(2)$ eb

GSB$\to K = 4^+$ band
K-forbidden $\langle K = 4^+ \mid E2 \mid \text{GSB} \rangle = 9.1(5) \times 10^{-4}$
$-1.47(8) \times 10^{-5}\{I_4(I_4 + 1) - I_0(I_0 + 1)\}$ (eb)

I_i	I_f	m (eb)	$B(E2) \times 10^3$ (e^{2}b^2)	I_i	I_f	m (eb)	$B(E2) \times 10^3$ (e^{2}b^2)
2	4	0.0110	0.0242	12	10	0.223	1.99
4	4	0.0240	0.0640	12	11	-0.489	9.56
4	5	-0.0420	0.196	12	12	0.574	13.2
4	6	0.0310	0.107	12	13	-0.351	4.93
6	4	0.0100	0.00769	12	14	0.0480	0.0922
6	5	-0.0450	0.156	14	12	0.391	5.27
6	6	0.0920	0.651	14	13	-0.790	21.5
6	7	-0.0990	0.754	14	14	0.847	24.7
6	8	0.0510	0.200	14	15	-0.443	6.77
8	6	0.0440	0.114	14	16	-0.00300	0.00031
8	7	-0.131	1.01	16	14	0.626	11.9
8	8	0.202	2.40	16	15	-1.19	42.9
8	9	-0.172	1.74	16	16	1.18	42.4
8	10	0.065	0.249	16	17	-0.526	8.38
10	8	0.112	0.597	16	18	-0.0950	0.273
10	9	-0.275	3.60	18	16	0.942	24.0
10	10	0.361	6.21	18	17	-1.71	78.6
10	11	-0.258	3.17	18	18	1.59	68.0
10	12	0.0670	0.214	20	18	1.35	44.7

Table 9.7: Reduced matrix elements $m = \langle I_f, K = 4^+ \| E2 \| I_i, K = 0^+ \rangle$ and $B(E2) = B(E2; K = 0^+ \to K = 4^+)$ values for the K-forbidden ($\nu = 2$) E2 transitions in the SDM model.

			$K = 2^+$ band$\rightarrow K = 6^+$ band					
			K-forbidden $\langle K = 6^+ \mid E2 \mid K = 2^+ \rangle = 0.00116(10)$ eb					
I_i	I_f	m (eb)	$B(E2) \times 10^3$ (e^{2}b^2)	I_i	I_f	m (eb)	$B(E2) \times 10^3$ (e^{2}b^2)
4	6	0.0370	0.152	10	10	0.254	3.07
5	6	-0.0430	0.168	10	11	-0.357	6.07
5	7	0.0680	0.420	10	12	0.288	3.95
6	6	0.0330	0.0838	11	9	0.0430	0.0804
6	7	-0.0860	0.569	11	10	-0.161	1.13
6	8	0.102	0.800	11	11	0.340	5.03
7	6	-0.0180	0.0216	11	12	-0.451	8.84
7	7	0.0710	0.336	11	13	0.348	5.27
7	8	-0.139	1.29	12	10	0.0630	0.159
7	9	0.141	1.33	12	11	-0.220	1.94
8	6	0.00600	0.00212	12	12	0.439	7.71
8	7	-0.0410	0.0989	12	13	-0.556	12.4
8	8	0.120	0.847	12	14	0.415	6.89
8	9	-0.201	2.38	13	11	0.0880	0.287
8	10	0.184	1.99	13	12	-0.289	3.09
9	7	0.0150	0.0118	13	13	0.552	11.3
9	8	-0.0720	0.273	13	14	-0.674	16.8
9	9	0.181	1.72	13	15	0.487	8.78
9	10	-0.274	3.95	14	12	0.118	0.480
9	11	0.233	2.86	14	13	-0.369	4.70
10	8	0.0270	0.0347	14	14	0.678	15.9
10	9	-0.112	0.597	14	15	-0.803	22.2

Table 9.8: Reduced matrix elements $m = \langle I_f, K = 6^+ \| E2 \| I_i, K = 2^+ \rangle$ and $B(E2) = B(E2; K = 2^+ \rightarrow K = 6^+)$ values for K-forbidden ($\nu = 2$) transitions in the SDM model.

			$K = 4^+$ band$\rightarrow K = 6^+$ band				
			K-allowed $\langle K = 6^+ \mid E2 \mid K = 4^+ \rangle = 0.094(3)$ eb				
I_i	I_f	m (eb)	$B(E2) \times 10^3$ (e^{2}b^2)	I_i	I_f	m (eb)	$B(E2) \times 10^3$ (e^{2}b^2)
4	6	0.28	8.9	10	8	0.022	0.023
5	6	-0.17	2.5	10	9	-0.090	0.39
5	7	0.26	6.3	10	10	0.21	2.0
6	6	0.081	0.5	10	11	-0.29	3.9
6	7	-0.21	3.5	10	12	0.23	2.6
6	8	0.25	4.9	11	9	0.028	0.034
7	6	-0.031	0.064	11	10	-0.11	0.49
7	7	0.12	1.0	11	11	0.23	2.2
7	8	-0.24	3.8	11	12	-0.30	3.9
7	9	0.24	4.0	11	13	0.23	2.3
8	6	0.0080	0.0038	12	10	0.035	0.049
8	7	-0.052	0.16	12	11	-0.12	0.60
8	8	0.16	1.4	12	12	0.24	2.4
8	9	-0.26	4.0	12	13	-0.31	3.8
8	10	0.24	3.3	12	14	0.23	2.1
9	7	0.015	0.012	13	11	0.042	0.065
9	8	-0.072	0.27	13	12	-0.14	0.69
9	9	0.18	1.7	13	13	0.26	2.5
9	10	-0.28	4.0	13	14	-0.32	3.7
9	11	0.23	2.9	13	15	0.23	1.9

Table 9.9: Reduced matrix elements $m = \langle I_f, K = 6^+ \| E2 \| I_i, K = 4^+ \rangle$ and $B(E2) = B(E2; K = 4^+ \rightarrow K = 6^+)$ values for the K-allowed transitions.

I_i	I_f	m (eb)	$B(E2) \times 10^3$ (e^{2}b^2)	I_i	I_f	m (eb)	$B(E2) \times 10^3$ (e^{2}b^2)
			$K = 4^+$ band$\to K = 6^+$ band, continued				
			K-allowed $\langle K = 6^+ \mid E2 \mid K = 4^+ \rangle = 0.094(3)$ eb				
14	12	0.048	0.079	15	14	-0.16	0.85
14	13	-0.15	0.77	15	15	0.29	2.7
14	14	0.27	2.6	16	14	0.060	0.11
14	15	-0.33	3.6	16	15	-0.17	0.92
15	13	0.054	0.094	17	15	0.065	0.12

table							

GSB $\rightarrow K = 6^+$ band							
K-forbidden $\langle K = 6^+ \mid E2 \mid K = 0^+ \rangle = 1.57(6) \times 10^{-6}$							
$-2.09(7) \times 10^{-8} \{ I_6(I_6 + 1) - I_0(I_0 + 1) \}$ (eb)							
I_i	I_f	m (eb)	$B(E2) \times 10^3$ (e²b²)	I_i	I_f	m (eb)	$B(E2) \times 10^3$ (e²b²)
4	6	0.00090	0.00009	10	12	0.0234	0.0261
6	6	0.00260	0.00052	12	10	0.0304	0.0370
6	7	-0.00550	0.00233	12	11	-0.0864	0.299
6	8	0.00480	0.00177	12	12	0.131	0.683
8	6	0.00120	0.00008	12	13	-0.108	0.469
8	7	-0.00670	0.00264	12	14	0.0347	0.0482
8	8	0.0164	0.0158	14	12	0.0814	0.228
8	9	-0.0208	0.0254	14	13	-0.203	1.43
8	10	0.0124	0.00904	14	14	0.272	2.55
10	8	0.00850	0.00344	14	15	-0.194	1.29
10	9	-0.0296	0.0417	16	14	0.183	1.01
10	10	0.0532	0.135	16	15	-0.417	5.27
10	11	-0.0528	0.133				

Table 9.10: Reduced matrix elements $m = \langle I_f, K = 6^+ \| E2 \| I_i, K = 0^+ \rangle$ and $B(E2) = B(E2; K = 0^+ \rightarrow K = 6^+)$ values for the K-forbidden ($\nu = 4$) transitions in the SDM model. Error in the intrinsic matrix element is calculated from the errors in the branching ratios.

			GSB $\rightarrow K = 8^-$ band				
			K-forbidden $m = \langle K = 8^- \mid E3 \mid K = 0^+ \rangle$				
I_i	I_f	m (eb$^{3/2}$)	$B(E3) \times 10^3$ (e^{2}b^3)	I_i	I_f	m (eb$^{3/2}$)	$B(E3) \times 10^3$ (e^{2}b^3)
\multicolumn{4}{c}{$m = 0.018$ eb$^{3/2}$}	\multicolumn{4}{c}{$m = 0.37$ eb$^{3/2}$}			
6	8	-9×10^{-6}	7×10^{-9}	12	13	1.0	42.
6	9	0.053	0.21	12	14	-1.1	50.
\multicolumn{4}{c}{$m = 0.069$ eb$^{3/2}$}	12	15	0.76	23.		
8	8	-0.0020	0.00023	14	11	0.026	0.024
8	9	0.12	0.80	14	12	-0.13	0.59
8	10	-0.19	2.2	14	13	0.39	5.2
8	11	0.17	1.7	14	14	-0.79	21.
\multicolumn{4}{c}{$m = 0.24$ eb$^{3/2}$}	14	15	1.1	44.		
10	8	-0.017	0.014	14	16	-1.1	45.
10	9	0.097	0.45	14	17	0.72	18.
10	10	-0.30	4.2	16	13	0.043	0.056
10	11	0.58	16.	16	14	-0.19	1.1
10	12	-0.73	25.	16	15	0.49	7.4
10	13	0.54	14.	16	16	-0.92	25.
\multicolumn{4}{c}{$m = 0.37$ eb$^{3/2}$}	16	17	1.2	45.		
12	9	0.012	0.0053	18	15	0.061	0.099
12	10	-0.076	0.23	18	16	-0.24	1.6
12	11	0.27	3.0	18	17	0.59	9.4
12	12	-0.64	16.	20	17	0.078	0.15

Table 9.11: Reduced matrix elements $m = \langle I_f, K = 8^- \| E3 \| I_i, K = 0^+ \rangle$ and $B(E3) = B(E3; K = 0^+ \rightarrow K = 8^-)$ values for the K-forbidden ($\nu = 5$) transitions. $m = \langle K = 8^- \mid E3 \mid K = 0^+ \rangle = 0.37 \, {}^{+0.07}_{-0.01}$ eb$^{3/2}$ for $I_{\mathrm{GSB}} > 10$.

I_i	I_f	m (eb$^{3/2}$)	$B(E3) \times 10^3$ (e^{2}b^3)	I_i	I_f	m (eb$^{3/2}$)	$B(E3) \times 10^3$ (e^{2}b^3)
$m = 0.0073$ eb$^{3/2}$				$m = 0.36$ eb$^{3/2}$			
5	8	0.024	0.054	10	8	-0.025	0.030
$m = 0.046$ eb$^{3/2}$				10	9	0.14	0.98
6	8	-0.096	0.71	10	10	-0.44	9.2
6	9	0.14	1.4	10	11	0.85	35.
$m = 0.16$ eb$^{3/2}$				10	12	-1.1	55.
7	8	0.18	2.1	10	13	0.80	31.
7	9	-0.40	10.	11	8	0.0055	0.0013
7	10	0.42	12.	11	9	-0.049	0.10
$m = 0.22$ eb$^{3/2}$				11	10	0.21	1.9
8	8	-0.12	0.85	11	11	-0.54	13.
8	9	0.37	8.1	11	12	0.94	38.
8	10	-0.61	22.	11	13	-1.1	52.
8	11	0.55	18.	11	14	0.77	26.
$m = 0.36$ eb$^{3/2}$				12	9	0.011	0.0052
9	8	0.079	0.33	12	10	-0.075	0.23
9	9	-0.33	5.6	12	11	0.27	2.9
9	10	0.75	29.	12	12	-0.63	16.
9	11	-1.0	58.	12	13	1.0	41.
9	12	0.84	38.	12	14	-1.1	49.

Table title: γ-band$\to K = 8^-$ band; K-forbidden $m = \langle K = 8^- \mid E3 \mid K = 2^+ \rangle$

Table 9.12: Reduced matrix elements $m = \langle I_f, K = 8^- \| E3 \| I_i, K = 2^+ \rangle$ and $B(E3) = B(E3; K = 2^+ \to K = 8^-)$ values for the K-forbidden ($\nu = 3$) transitions. $m = \langle K = 8^- \mid E3 \mid K = 2^+ \rangle = 0.36\ ^{+0.00}_{-0.06}$ eb$^{3/2}$ for $I_\gamma > 9$.

			γ-band$\rightarrow K = 8^-$ band, continued				
			K-forbidden $m = \langle K = 8^- \mid E3 \mid K = 2^+ \rangle$				
I_i	I_f	m (eb$^{3/2}$)	$B(E3) \times 10^3$ (e^{2}b^3)	I_i	I_f	m (eb$^{3/2}$)	$B(E3) \times 10^3$ (e^{2}b^3)
$m = 0.36$ eb$^{3/2}$				$m = 0.36$ eb$^{3/2}$			
12	15	0.74	22.	15	12	0.034	0.037
13	10	0.018	0.012	15	13	-0.16	0.79
13	11	-0.10	0.39	15	14	0.44	6.1
13	12	0.33	4.0	15	15	-0.84	23.
13	13	-0.71	18.	15	16	1.2	44.
13	14	1.1	42.	15	17	-1.1	42.
13	15	-1.1	46.	16	13	0.042	0.054
13	16	0.72	19.	16	14	-0.18	1.0
14	11	0.026	0.023	16	15	0.49	7.2
14	12	-0.13	0.58	16	16	-0.90	25.
14	13	0.38	5.1	16	17	1.2	44.
14	14	-0.78	21.	17	14	0.051	0.074
14	15	1.1	43.	17	15	-0.21	1.3
14	16	-1.1	44.	17	16	0.53	8.2
14	17	0.71	17.	17	17	-0.96	26.

			GSB $\to K = 4^+$ band				
			K-forbidden $\langle K = 4^+ \mid M1 \mid K = 0^+ \rangle = 6.3(19) \times 10^{-5}$				
			$-9.5(29) \times 10^{-7}\{I_4(I_4+1) - I_0(I_0+1)\}$ (μ_N)				
I_i	I_f	m (μ_N)	$B(M1) \times 10^3$ (μ_N)	I_i	I_f	m (μ_N)	$B(M1) \times 10^3$ (μ_N)
4	4	-0.0080	0.0071	12	11	0.40	6.4
4	5	0.014	0.022	12	12	-0.58	13.
6	5	0.018	0.025	12	13	0.33	4.4
6	6	-0.047	0.17	14	13	0.75	19.
6	7	0.048	0.18	14	14	-0.98	33.
8	7	0.071	0.30	14	15	0.49	8.3
8	8	-0.14	1.1	16	15	1.3	50.
8	9	0.11	0.71	16	16	-1.6	74.
10	9	0.19	1.7	16	17	0.67	14.
10	10	-0.30	4.4	18	17	2.1	120
10	11	0.20	2.0	18	18	-2.4	150

Table 9.13: Reduced matrix elements $m = \langle I_f, K = 4^+ \| M1 \| I_i, K = 0^+ \rangle$ and $B(M1) = B(M1; K = 0^+ \to K = 4^+)$ values for the K-forbidden ($\nu = 3$) transitions in the SDM model.

		$B(E2) \times 10^3$	Matrix element (eb)			
				Lower	Upper	Diagonal Error
I_i	I_f	(e^2b^2)	m	Limit	Limit	Range
14	16	2.0	0.24		0.42	0.20–0.26
16	16	1.7	0.24		0.42	0.20–0.26
16	17	4.1	-0.37		0.74	0.27–0.44
16	18	43.	1.19		1.19	
18	16	1.6	0.24		0.42	0.20–0.26
18	17	3.1	-0.34		0.68	0.25–0.40
18	18	1.6	0.24		0.24	
18	19	7.0	-0.51		0.51	
18	20	18.	-0.81	0.12	1.8	0.20–1.4
20	18	0.21	0.094		0.094	
20	19	1.2	-0.22		0.22	
20	20	8.8	0.60		0.60	
20	21	43.	-1.33		2.5	
22	20	11.	0.72		0.72	
22	21	21.	-0.98		0.98	

The header above the table reads: GSB→ $K = 16^+$ band

Table 9.14: Matrix elements $m = \langle I_f, K = 16^+ \| E2 \| I_i, K = 0^+ \rangle$ and $B(E2; K = 0^+ \to K = 16^+)$ values for the K-forbidden ($\nu = 14$) transitions. Matrix elements were adjusted to reproduce the data from both the Hf(Xe,Xe)Hf and the Ta(Hf,Hf)Ta experiments. Upper and lower bounds are given where they could be determined, along with diagonal errors. The 22^+ GSB level has not been found.

Chapter 10

Nuclear Structure Implications

Collective quadrupole deformations are a ubiquitous feature of non-magic nuclei. Rotational bands exist in many strongly deformed nuclei with intraband E2 matrix elements as large as hundreds of single-particle units. The quadrupole shape determines the level energies of the rotational states, as well as the energies of single-particle or quasiparticle states in the deformed potential. The axial symmetry of pure quadrupole shapes (prolate β deformations) is also responsible for the alignment of the angular momentum vector and the conservation of its axial projection K. If the nucleus has perfect axial symmetry, then K will be conserved and the selection rule for K (Equation 2.8) will be strictly obeyed. However, collective deformations break the axial symmetry when they take the form of γ deformations and vibrations.

Over the past fifty years, observations of K-forbidden transitions in many nuclei, along with the discovery of a multitude of isomeric states, have raised intriguing questions about the goodness of the quantum number K and the relationship between the forbiddenness ν and the hindrance F_ν. The Coulomb excitation of high-K states via highly K-forbidden transitions has aroused particular interest, and eluded explanation for decades. The measurement of the electromagnetic matrix elements coupling low-K bands to high-K bands is a di-

rect measure of the hindrance of K-forbidden transitions and therefore a sensitive indicator of the goodness of K in individual nuclear states. The present results for the $K^\pi = 4^+, 6^+, 8^-, 14^-$ and 16^+ bands explain the Coulomb excitation of ^{178}Hf isomers and provide the first quantitative measure of the loss of K-conservation.

10.1 Experimental Results

The analysis of the 6^+, 8^- and 16^+ isomer band yields which resulted from Coulomb excitation of ^{178}Hf revealed electromagnetic excitation paths which facilitate violation of the K-selection rule. The 6^+ isomer is populated via two- and three-step excitations, both K-allowed and K-forbidden, through the γ- and 4^+ bands. (Here, one "step" refers to a transition from one band to another, rather than an excitation within a band.) The 8^- isomer band is populated directly from the GSB through highly K-forbidden transitions. The 16^+ isomer band data also indicate a one-step highly K-forbidden process, but unlike the 8^- band excitation, γ-decay feeding dominates (Figure 9-2).

While each of the three isomer bands has a unique population path, the common feature of each path is that K-mixing must occur in the low-K bands at moderate spin. This does not exclude the possibility of K-mixing in the high-K bands, but does show that it is less important in the observed Coulomb excitation.

10.1.1 Hindrance Systematics

The systematic decrease in the hindrance of K-forbidden transitions with increasing spin is apparent from the data of Table 10.1. In general, with increasing spin in the low-K bands comes a decrease in the hindrance. (The decrease can not be perfectly monotonic, in part due to the angular momentum coupling.) The uniformly low hindrance of the 14-times forbidden GSB$\to 16^+$ band transitions indicates a nearly complete mixing of K values in the GSB beginning near the

Selected reduced hindrance values					
Bands	I_i	I_f	$\mathcal{M}\lambda$	ν	f_ν
GSB$\rightarrow K^\pi = 4^+$	2	4	E2	2	35.03
	6	8	E2	2	12.19
	12	14	E2	2	17.95
GSB$\rightarrow K^\pi = 6^+$	4	6	E2	4	23.97
	8	10	E2	4	7.57
	12	14	E2	4	4.98
GSB$\rightarrow K^\pi = 8^-$	8	8	E1	7	[a]67(1)
	6	8	M2	6	[a] >128
	6	9	E3	5	2.29
	10	13	E3	5	0.99
	12	15	E3	5	0.89
GSB$\rightarrow K^\pi = 16^+$	14	16	E2	14	1.21
	16	18	E2	14	0.97
	18	20	E2	14	1.04
	20	21	E2	14	0.97

Table 10.1: Values of f_ν for selected K-forbidden transitions in ^{178}Hf. The reduced hindrance is defined as $f_\nu \equiv F_\nu^{1/\nu}$. Reduced transition strengths are taken in the directions indicated by the arrows. Weisskopf estimates are $B(E1 \downarrow)_W = 0.0204\text{e}^2\text{b}$, $B(E2 \downarrow)_W = 0.00595\text{e}^2\text{b}^2$, $B(E3 \downarrow)_W = 0.00188\text{e}^2\text{b}^3$, $B(E5 \downarrow)_W = 0.00022\text{e}^2\text{b}^5$, $B(M1 \downarrow)_W = 1.79\mu_N^2$, $B(M2 \downarrow)_W = 0.522\mu_N^2\text{b}$, $B(M4 \downarrow)_W = 0.0553\mu_N^2\text{b}^3$, and $B(\mathcal{M}\lambda \uparrow)_W = (2\lambda + 1)B(\mathcal{M}\lambda \downarrow)_W$. [a]Calculated from the data of [5]. [b]From [5]. [c]From [10].

14^+_{GSB} level. In contrast, the $16^+_{\text{isom}} \rightarrow K^\pi = 8^-$ decays are highly hindered in the 11^-_8 ($f_\nu = 165(5)$), 12^-_8 ($f_\nu = 72(2)$) and 13^-_8 ($f_\nu = 66(1)$) levels in the 8^- band [5], showing that the onset of significant admixtures of very high-K components in the 8^- band must occur at high spin, if at all.

Selected reduced hindrance values, continued					
Bands	I_i	I_f	$\mathcal{M}\lambda$	ν	f_ν
$K^\pi = 2^+ \to K^\pi = 6^+$	4	6	E2	2	13.98
	6	8	E2	2	6.09
	8	10	E2	2	3.86
	10	12	E2	2	2.74
$K^\pi = 2^+ \to K^\pi = 8^-$	5	8	E3	3	6.25
	7	10	E3	3	1.03
	9	12	E3	3	0.7
	11	14	E3	3	0.8
$K^\pi = 16^+ \to K^\pi = 8^-$	16	11	E5	3	[b]165(5)
(decay)	16	12	M4	4	[b]72(2)
	16	13	E3	5	[b]66(1)
$K^\pi = 14^- \to K^\pi = 8^-$	14	13	M1	5	[c]87
(decay)	14	12	E2	4	[c]33

Table 10.1, continued.

Comment on the Rusinov rule. The measurements of the widths of the 6^+ isomer decay branches (Figure 10-1) with errors of 20% in the worst case shows that the Rusinov rule is not accurate within several orders of magnitude, even for the E2 decays. (It has been suggested that decays of different multipolarities could be expected to have different offsets but still follow a slope of 2 [47].) Figure 10-1 shows the hindrance values of several K-allowed and K-forbidden isomer decay branches in ^{178}Hf. It is obvious from the fits that one single relation will not reproduce the decay widths of all K-forbidden decays, even for a single isotope. The measured decay
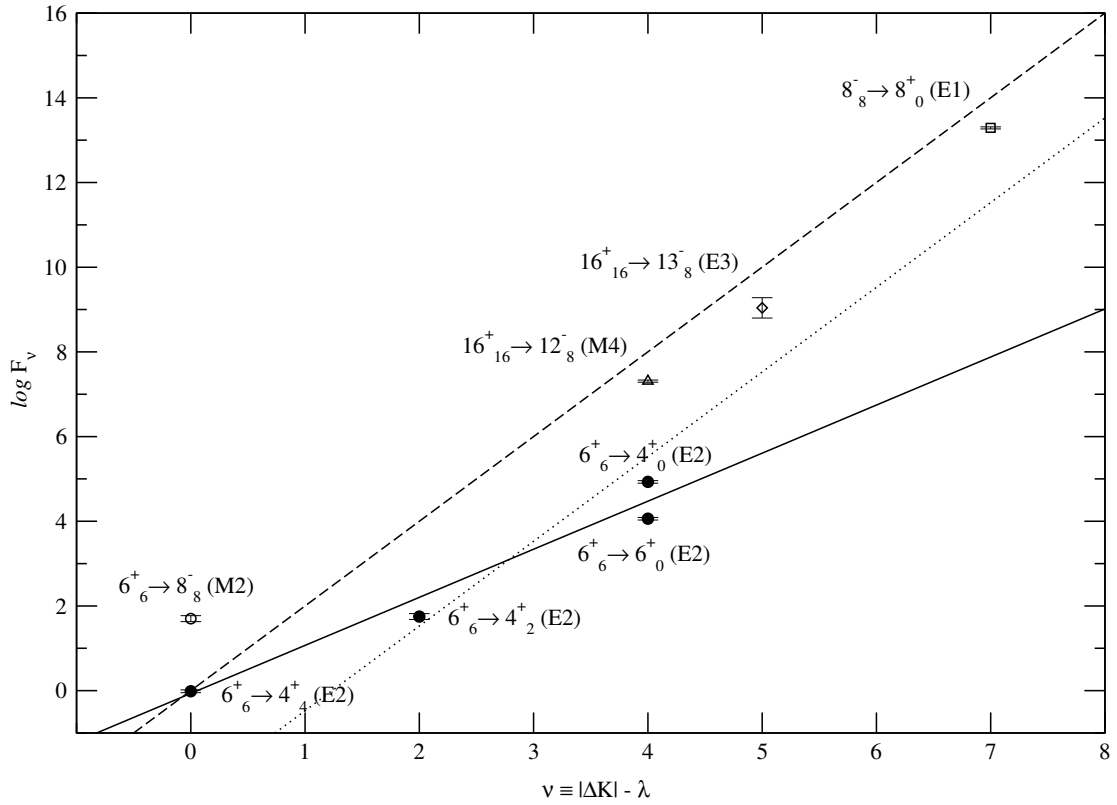
Figure 10-1: Hindrance values F_ν for γ-decay branches of ^{178}Hf isomers. The rule of Rusinov (dash) is shown, along with a fit of the offset (dot) to all 8 points. The two-parameter fit to the hindrance of the 6^+ isomer decay branches only (solid), gave $\log F_\nu = -2.5(9) + 1.1(2)\nu$. Solid points are from the present work. Open symbols are from [10].

widths of the E2 decay branches (Figure 8-1) of the 6^+ isomer were found to obey $\log F_\nu \sim 1.1(2) \cdot \nu$ within about one order of magnitude, but this systematic behavior did not extend even to the other isomer decays in ^{178}Hf, and for $n = 4$, the hindrance values of three known decays span 4 orders of magnitude.

10.1.2 The Measured Strength of K-Mixing

To accurately measure the complete set of matrix elements connecting two bands, the matrix elements generally need to be overdetermined by the data in

order to find a the χ^2 minimum in a multidimensional parameter space. This is especially true at the low ($\sim 10^{-4}$) yield levels measured for many of the isomer band yields. Even the numerous yields measured for 6 scattering angle intervals in the online experiment were insufficient to determine individual matrix elements for the isomer bands. It was necessary to reduce the problem in most cases to a single parameter coupling each pair of bands, with the exception of the 16^+ band, and to rely on the following physical constraints:

1. The calculated lifetimes of the isomers must agree with the known values.

2. The reduced transition probabilities $B(\mathcal{M}\lambda)$ must adhere to physically reasonable limits.

3. There should not be sharp discontinuities in $B(\mathcal{M}\lambda)$ as a function of spin.

Within these limitations, the experimental yields determined the matrix elements using the SDM systematics for the $K < 8$ bands, but the SDM model is not as well-behaved for larger K values. The Alaga rule systematic was adjusted for the $K = 8^-$ band so that the matrix elements $\langle I_f K = 8 \| E3 \| I_i K = 0 \rangle$ and $\langle I_f K = 8 \| E3 \| I_i K = 2 \rangle$ increased smoothly with spin for $I_{\mathrm{GSB}} < 12$ and $I_\gamma < 9$, reproducing the 4.0(2) s half-life of the 8^- isomer. The lifetime of the *yrast* 16^+ isomer did not force any additional constraints, but the individual 16^+ intraband yields, feeding upper limits and measured isomer cross sections were used to set upper and lower limits on each matrix element (Chapters 4 and 6). The resulting $B(\mathcal{M}\lambda)$ values as a function of spin in the GSB and the γ-band (Figures 10-2 and 10-3) lead to the following general conclusions.

The K-mixing (which, it will be shown, appears to originate in the low-K bands) increases to the physical limit for non-collective transitions corresponding to $B(\mathcal{M}\lambda)$ values of about 1 W.u. for $I \gtrsim 12$ in the GSB and the γ-band. In

order to reproduce the measured yields, the reduced transition probability must saturate at ≈ 1 W.u. This saturation point represents the maximum mixing of K in the low-K bands—the breakdown of conservation of the K quantum number.

The strong hindrance of the $K = 16^+ \rightarrow K = 8^-$ and $14^- \rightarrow K = 8^-$ transitions (Table 10.1) suggests that the K is a good quantum number for the high-K bands. (Coriolis alignment effects will be considered for high- and low-K bands in the next section, reinforcing the conclusion that mixing occurs predominantly in the low-K bands.) The population of a band with projection K, assuming that it is reasonably pure, requires admixtures in the low-K bands of $K - \lambda \leq K' \leq K + \lambda$. Hence, the mixing fractions of the $2 \leq K \leq 6$ components are depicted as a function of spin by the $B(E2; K_i \rightarrow K = 4)$ values, the $4 \leq K \leq 8$ components by the $B(E2; K_i \rightarrow K = 6)$ values, etc. In the absence of any contrary information, it may be assumed that the lowest of K-value in each range enters the wave function first. Hence, the EM matrix elements coupling to the high-K bands are sensitive probes of the K-distributions in the low-K bands.

The present work, initially focused on explaining the K-forbidden Coulomb excitation of the $K^\pi = 8^-$ isomer, has reached a conclusion of broader significance: For the first time, the loss of the purity of K with increasing angular momentum in nuclear states has been revealed. The K-mixing is localized in low-K bands, while the high-K bands remain very pure, even at the same spin (I) levels where the low-K bands are completely mixed. The identity of the K-mixed bands will be addressed again in the next section.

10.2   Interpretation

Two effects have been postulated to explain the mixing of high- and low-K states: alignment of the single-particle or quasiparticle angular momenta due to collective rotations, and triaxial deformation effects such as softness to γ defor-
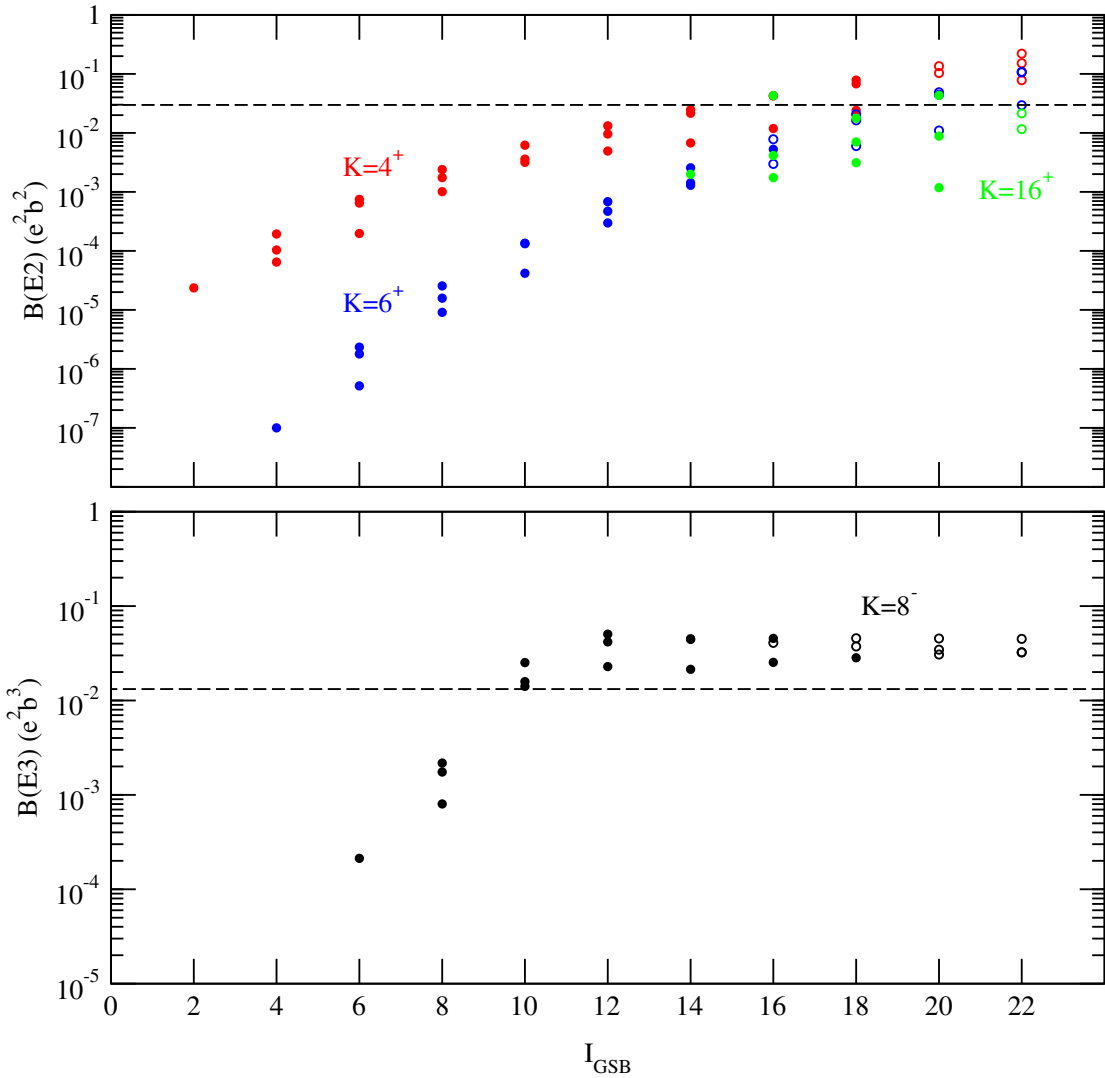
Figure 10-2: Reduced transition probabilities for GSB$\rightarrow K^\pi$ transitions. GSB$\rightarrow$ 16^+ matrix elements were adjusted individually. GSB$\rightarrow 4^+, 6^+$ matrix elements follow the SDM systematics. GSB$\rightarrow 8^-$ matrix elements follow the Alaga rule, attenuated at low spin. Transitions to unknown high-spin levels (open circles), are extrapolated to clarify the spin-dependence of the intrinsic matrix element. A dashed line is shown at one Weisskopf unit, $B(\mathcal{M}\lambda; 0 \rightarrow \lambda)_{\mathrm{W}}$. $B(E2 \uparrow)_{\mathrm{W}} = 0.0297$ e^{2}b^2. $B(E3 \uparrow)_{\mathrm{W}} = 0.0132$ e^{2}b^3.

mation and γ-barrier tunneling.

The measured moments of inertia indicate band interactions typically by an increase in the slope on the moment of inertia plot, or in strong interactions by
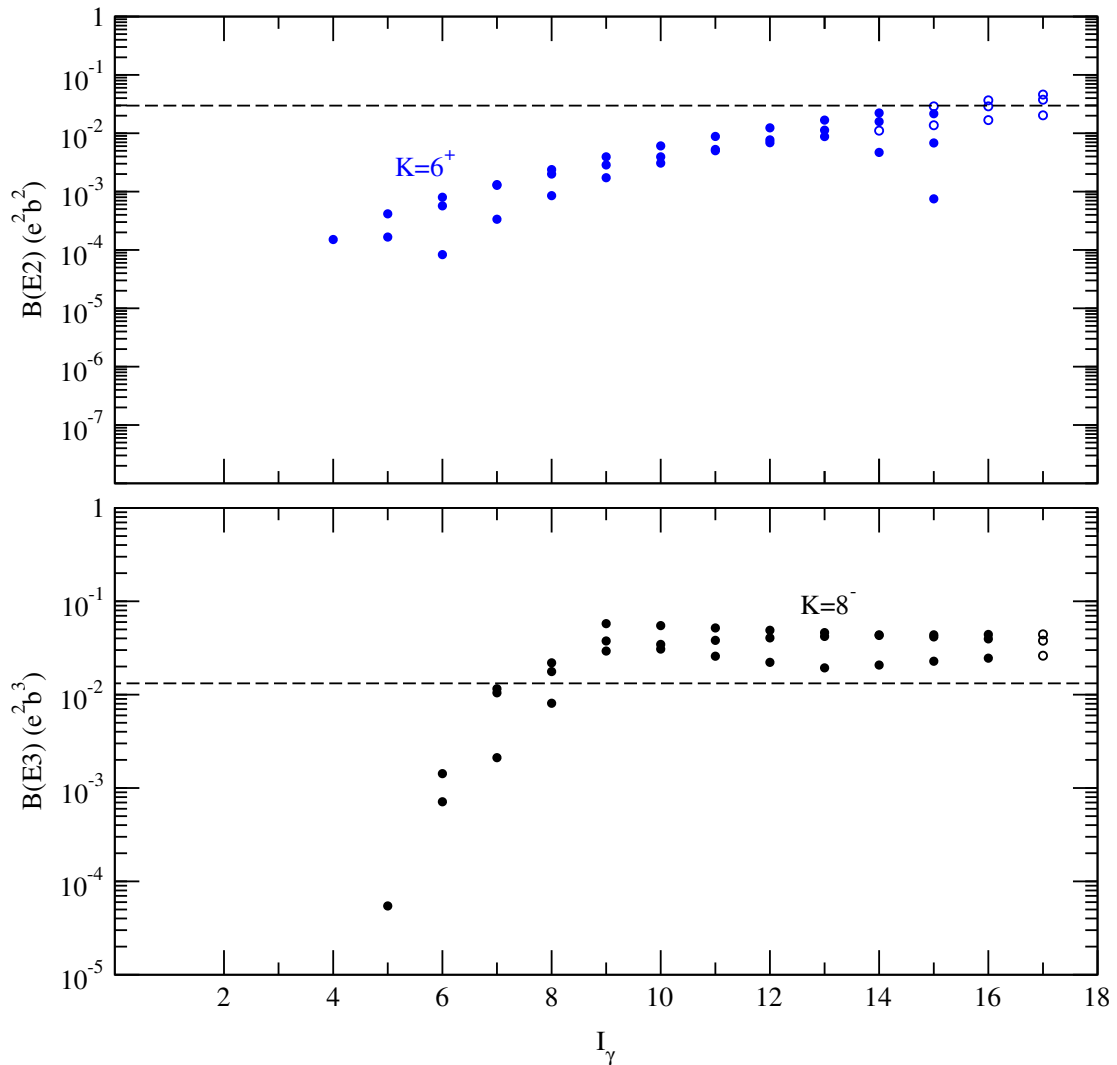
Figure 10-3: Reduced transition probabilities for γ-band$\rightarrow K^\pi$ transitions. γ-band$\rightarrow 6^+$ matrix elements follow the SDM systematics. γ-band$\rightarrow 8^-$ matrix elements follow the Alaga rule, attenuated at low spin. Transitions to unknown high-spin levels (open circles), are extrapolated to clarify the spin-dependence of the intrinsic matrix element. A dashed line is shown at one Weisskopf unit, $B(\mathcal{M}\lambda; 0 \rightarrow \lambda)_\mathrm{W}$. $B(E2 \uparrow)_\mathrm{W} = 0.0297$ e^{2}b^2. $B(E3 \uparrow)_\mathrm{W} = 0.0132$ e^{2}b^3.

a significant backbend. The two-quasiparticle (or multi-quasiparticle) bands have a higher moment of inertia than the GSB due to the decrease in the superfluidity of the core with the breaking of a pair. The rotational alignment of low-K quasiparticle bands often results in mixing with lower-K bands, and the mixing
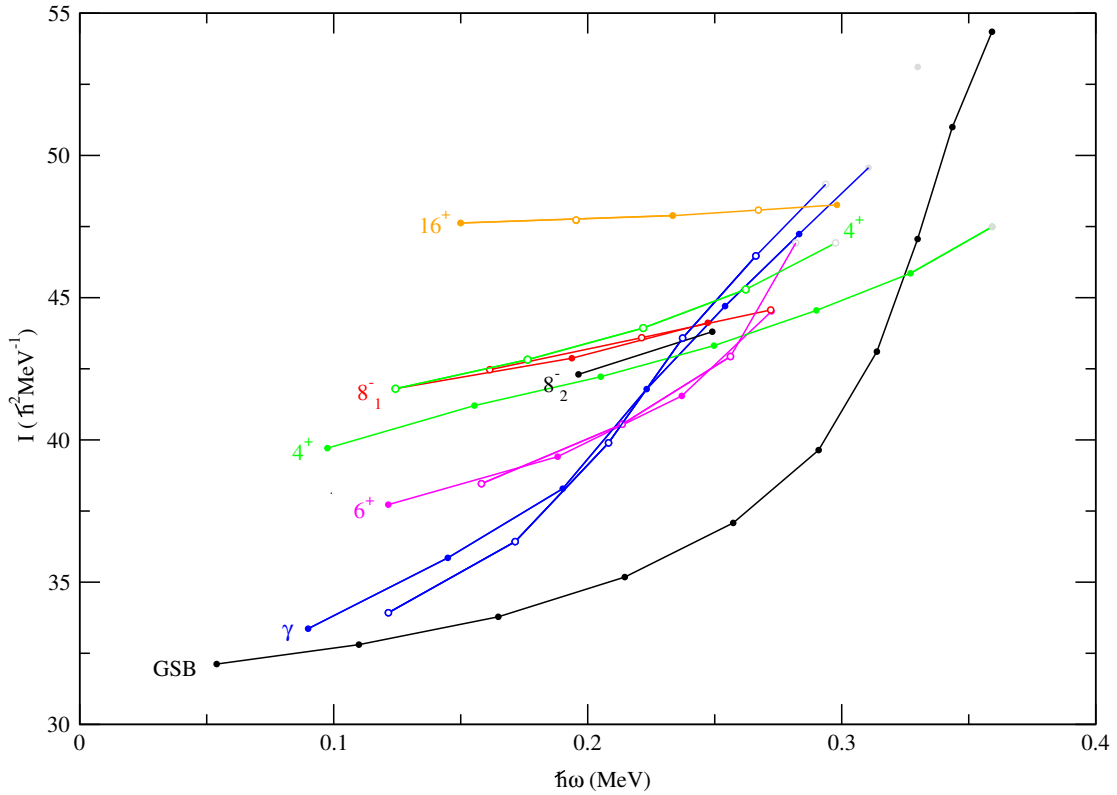
Figure 10-4: A moment of inertia plot with additional 16^+ data from [9].

is seen as an increase in the moment of inertia of the lower-K bands [122]. A comparison of the onset of strong $B(\mathcal{M}\lambda)$ values with the appearance of band mixing (Figures 10-2 and 10-3 compared with Figure 10-4) shows that the low-K bands exhibit interactions at moderate spin, $I \approx 10$, at the same point where the $B(\mathcal{M}\lambda)$ values are forced to saturate to reproduce the experimental yields, which reaffirms the conclusion that mixing in the low-K bands is responsible.

Moreover, the Coriolis matrix elements for a particle of total angular momentum $\vec{j}$ and projection Ω, which vary as $\sqrt{\vec{I}^2 - K(K+1)}\sqrt{\vec{j}^2 - \Omega(\Omega+1)}$, are negligible near the high-K band heads, so the alignment of low-K bands, which would tend to mix with the GSB and the γ-band is expected to happen at much lower spin I than the alignment of high-K bands [14] which are strongly deformation-coupled. This can be seen in the alignment of the two-quasiparticle superband

(s-band) of ^{164}Er [123] which mixes with the γ-band first, at $I \approx 10\hbar$ and with the GSB at $I \approx 14\hbar$. The appearance of interactions (of an unknown band or bands) with the γ-band and with the GSB in ^{178}Hf is similar, (Figure 10-4) indicated by the onset of increasing slope at $I \approx 6\hbar$ and $I \approx 10\hbar$ in the γ- and GS bands, respectively. The moments of inertia of the high-K bands are relatively constant in slope, with the possible exception of the 6^+ band at $I \approx 12\hbar$, suggesting that the high-K bands are not K-mixed to the same degree as the low-K bands. The 16^+ band has a remarkably constant moment of inertia up to $I = 22\hbar$ [9].

10.2.1 γ-Tunneling

The γ-barrier penetration hypothesis has had success in explaining K violations in more γ-soft nuclei such as ^{182}W and ^{181,182,184}Os. However, the same treatment does not reproduce the measured hindrance values in more γ-rigid Hf nuclei [50, 59]. The γ-barrier penetration calculations make an absolute prediction of K-forbidden transition probabilities, whereas the SDM model requires two adjustable parameters, but do not make predictions above the band head, high in the rotational bands where the present work predicts significant transition probabilities. An impure band head is a necessary feature of the γ-tunneling hypothesis, but this is strongly disputed by the measured hindrance values of the isomer decay branches. Predictions by Narimatsu *et al.* [59] of the hindrance of isomer decay branches are in agreement with measured hindrance values for γ-soft nuclei, but differ by several orders of magnitude in the Hf nuclei, ^{178}Hf for instance.

10.2.2 The Spin-Dependence of K-Mixing

The SDM model reproduced the $K \leq 6$ isomer population data with striking accuracy. (The approximation was shown in Chapter 2 to break down for large K.) In the cases of the $K^\pi = 8^-, 16^+$ bands, the sets of matrix elements derived from the data follow qualitatively the form of the SDM model and are consistent

237

with the Coriolis mixing hypothesis.

For the 8^- isomer band the Alaga systematic was employed, with an experimentally derived increase in $B(\mathcal{M}\lambda)$ to saturation which was qualitatively similar to the SDM model. This spin-dependent mixing approach allowed the preservation of the isomer lifetime, an essential quality of any model employed to explain the isomer population. Reasonable in-band γ-ray yields were reproduced using realistic $B(E3)$ strengths. The sets of matrix elements measured in the present work all point to a rapid increase of the $B(\mathcal{M}\lambda)$ strength with spin in the low-K bands, in qualitative agreement with the SDM model and Coriolis alignment, whereas the SDM model does not predict the observed saturation at moderate spin ($\approx 10\hbar$).

10.2.3 The Projected Shell Model

The predictions of the (PSM) are not limited to the high-K band heads or to very small values of R as in the γ-tunneling models. Rather, a softness to γ-deformations is predicted in ^{178}Hf for all states, including low-lying GSB states [124]. This would naturally lead to K mixing in all bands with the loss of axial symmetry for $\gamma > 0$. The PSM in its current state of development gives good agreement with some isomer level energies, but it has not yet been used to calculate electromagnetic transition matrix elements. The predicted γ-softness is not in conflict with the Coriolis mixing model, and future calculations may show that γ-softness makes an additional contribution to the measured strength of K-forbidden transitions to the isomer bands.

10.2.4 The Need for Theoretical Work

Tunneling through the γ-barrier appears to explain many K violations in γ-soft nuclei, but is not universally accurate, even in neighboring nuclei. Coriolis mixing appears to be a sound hypothesis, applicable to the ^{178}Hf isomers where

the γ-barrier penetration hypothesis does not predict the correct hindrance and makes no predictions about the matrix elements above the band head. Higher order corrections to the SDM matrix elements may predict a less explosive trend, more like the matrix elements extracted in this work. The present work has resulted in measurements which are qualitatively similar to the SDM model in the most deviant cases $(8^-, 16^+)$—a rapid increase in mixing with increasing spin, and a pure band head—and agree quantitatively with the SDM model (with two adjustable parameters) in the best case.

None of the three models by themselves—γ-barrier tunneling, SDM and the PSM—have made adequate predictions of the K-forbidden matrix elements or the breakdown of the K-quantum number. However, in this work, the loss of K-conservation and the matrix elements have been probed experimentally. The measured decrease in the hindrance of K-forbidden transitions with increasing spin in the low-K bands has revealed the need for further theoretical work.

10.3   Prospects

These first direct measurements of K-mixing in nuclear structure physics have revealed the locus and behavior of K-mixing with respect to the angular momentum states. Potent Coulomb excitation techniques using high-resolution γ-ray and particle detectors have provided explanations of the population of three isomers in ^{178}Hf, including the long-sought mechanism of the Coulomb excitation of the 8^- isomer. The measured Coulomb excitation cross sections of the 8^- isomer lie between the values measured by Xie it et al. and Hamilton it et al. (Table 4.3). Similar powerful Coulomb excitation technique could be exploited to investigate K-mixing in other nuclei, perhaps expanding the results for ^{178}Hf to a general conclusion for heavy prolate nuclei.

Coulomb excitation of isomer targets could provide enough information, par-

ticularly in the case of the 16^+ isomer, to make precise measurements of matrix elements connecting high-spin states in the isomer bands to lower-K "recipient" bands. The experimental problem of using Coulomb de-excitation to measure the matrix elements can be summarized as follows. A low-K level I populated to a yield of Y_I^{depop} in the Coulomb excitation of the isomer may also be populated directly from the ground state with a contribution Y_I^{direct}. The contribution from the ground state could be significant, if the isomeric enrichment is small, but the ratio of the two contributions $\frac{Y_I^{\mathrm{depop}}}{Y_I^{\mathrm{direct}}}$ will be a function of the bombarding energy E_B, and the beam species, as well as the isomeric enrichment fraction. The de-population yield through a level in the recipient band must have an upper limit with increasing bombarding energy, due to the enrichment fraction and the entry of other reaction channels.

The lower measurement threshold of the yield in low-K recipient bands will require the choice of beam energy and mass to achieve a compromise between high overall yield and a small relative yield of the recipient states directly from the ground state. Alternatively, long-lived isomers which de-excite to lower-K isomer bands with lifetimes of the order of 10 ns (such as the 9^- isomer of ^{180}Ta, which has been depopulated to a 24 ns isomer [125]) would provide an opportunity to measure very low Coulomb depopulation yields by the great selectivity in delayed γ-ray gates. ^{180}Ta targets are available enriched to levels of a few percent, compared to the best ^{178m2}Hf targets which contain $\lesssim 10^{15}$ isomers [34, 35]. Because Coulomb depopulation involves transitions from the isomer band by design, the availability of $\approx 98\%$ enriched ^{242}Am targets should provide an opportunity to make the first measurement of the relevant matrix elements.

The present work has elucidated the loss of K-selection in ^{178}Hf. Because rotational bands are common to all deformed nuclei, the conclusions of the present work may have broad applicability. Coulomb de-excitation experiments are currently being considered for the ^{180}Ta and ^{242}Am isomers by the nuclear structure

group at Rochester to further the understanding of the breakdown of K conservation in the nucleus.

Chapter 11

Prospects for Isomer Depopulation

The desire to induce and control the release of nuclear energy from isomer sources has enticed researchers for over forty years since the conception of the γ-ray laser by Rivlin in 1961. Triggered isomer devices having the potential for coherent $\lesssim 500$ keV γ-ray output at teraWatt power levels and 10^4 MJ/cm^3 storage density with mean lifetimes of years or centuries have been proposed [32, 126]. The failure to find triggering transitions with practical cross sections for known isomers has prevented the realization of Rivlin's concept, but the conjecture on exploiting various techniques (*e.g.* x-ray irradiation and electronic processes such as XENDT and NEET) continues [32, 33]. Although the ^{178}Hf 16$^+$ isomer has commanded the most recent attention in terms of stimulated emission, work continues in other isomers, most notably the successful stimulated depopulation of the 75 keV 9$^-$ isomer in ^{180}Ta ($t_{\frac{1}{2}} > 10^{15}$ y) by ~ 1 MeV γ-ray irradiation [127].

Olariu *et al.* [128] have calculated the laser intensity for selected $85 \leq A \leq 237$ nuclear isomers that would be required to produce sufficient nuclear excitation by interaction of the nucleus with cascading electrons following photo-ionization (the XENDT process) to reduce isomer half-lives by a factor of two. The calcu-

lations for depopulation through a known transition in each nucleus showed that intensities greater than 10^{13} W/cm^2 would be required to stimulate a decay rate of the order of the natural isomer decay rate, a modest goal. Olariu and Olariu followed with a calculation for direct (as opposed to XENDT and NEET) stimulated γ-emission from isomers, including simulated emission of the ^{178m2}Hf 16$^+$ isomer through the 14$^-$ isomer, after which $\approx 50\%$ would decay back to the 16$^+$ state. An incident flux of 126 keV γ-rays with an intensity of 4×10^{14} W/cm^2 was predicted to reduce the isomer half-life by 50% [129].

Following these unfavorable predictions, Collins et $al.$ reported the measurement of a $\approx 4\%$ enhancement of the decay rate of ^{178m2}Hf by x-ray stimulated emission through an unknown intermediate state lying 20—60 keV from the 16$^+$ isomer [130, 131, 132]. Several authors have shown that the reported enhancement, corresponding to an integrated cross section of 3×10^{-23} — 10^{-21} cm^{2}keV, represent $B(\mathcal{M}\lambda)$ values orders of magnitude above physical upper limits [133, 134, 135]. (The integrated cross section may have been overestimated, depending upon the x-ray energy and the intensity and absorption width at that energy [136], but it is not clear that this would resolve the problem.) Attempts to reproduce the stimulated emission results yielded only null results and upper limits on the integrated cross sections [137, 138, 139]. Continued stimulated emission work attempting to exploit the NEET (nuclear excitation by electronic transitions) process led to new measurements of the de-excitation probability of $\sim 10^{-3}$ per l-shell ionization [140], however, this appears to exceed physical limits by 10 orders of magnitude [141].

11.1   Implications of the Present Results

The present results have revealed paths by which Coulomb de-excitation of the ^{178m2}Hf isomer can be achieved, owing to the invariance of the EM matrix elements

under the interchange of the initial and final states. The $16^+ \overset{E2}{\Rightarrow}$ GSB K-forbidden paths would allow Coulomb depopulation of the isomer with a probability of $\leq 1\%$ [142] compared to the in-band excitations, resulting in a cascade of 93 keV—718 keV γ-rays and a net energy gain of 2.4 MeV. The known strength of the K-allowed M2 decay of the 14^- isomer to the 16^+ isomer is irrelevant in Coulomb excitation, but the allowed E3 transitions would have a $\overset{<}{\sim} 1\%$ probability [142] assuming typical E3 matrix elements in ^{178}Hf.

Neither of these paths is expected to be effective for photo de-excitation, since photon absorption is dominated by E1 transitions, but this does not rule out depopulation via a 463 keV E1 transition to the 15^-_{14} state, for example. The $16^+ \overset{E3}{\Rightarrow} 8^-$ transitions are highly forbidden, because K is well-defined in the high-K bands (Chapter 10), making this path ineffectual. While Coulomb de-excitation paths have been discovered, the intermediate states which might mediate the reported stimulated emission by Collins *et al.* were not found.

The stellar nucleosynthesis of ^{180}Ta, the only isotope in nature which exists in an isomer state $(t_{\frac{1}{2}} > 10^{15}$ y), has eluded explanation. Until recently, it was thought that no known process could explain the existence of ^{180}Ta, but the recent stimulated emission results of Walker *et al.* using ≈ 1 MeV γ-ray absorption [127] have promoted the opposite conclusion—that any of the p-, s- and ν-processes are possible explanations [31]. Walker's conclusion is that the de-excitation proceeds through $8 \leq I \leq 10$ levels of a lower-K band. A complete set of matrix elements could be measured by a heavy-ion Coulomb excitation study of an isomer-enriched target. Detailed knowledge of the matrix elements would lead to a comparison of the breakdown of K-conservation in ^{178}Hf and ^{180}Ta and possibly narrow the range of possible nucleosynthesis processes.

11.2 Further Research

Should highly enriched ^{178m2}Hf isomer targets become available, Coulomb de-excitation studies of the isomer would provide an expedient means to search for viable stimulated emission paths through intermediate states. In Coulomb excitation, the bombarding energy does not need to be tuned to match the (virtual) photon absorption energy, whereas photo-excitation studies require the radiation to cover the full range of possible absorption energies, because of the typical widths of short-lived excited states, of the order of 10^{-6} eV.

The observation of stimulated emission of the ^{180}Ta ($K^\pi = 9^-, t_\frac{1}{2} > 10^{15}$ y) isomer following ~ 1 MeV γ-ray absorption [127], and the availability of $\approx$ 1% enriched isomeric target material make it a promising candidate for study. Inasmuch as the present finding, that K conservation breaks down in the low-K bands, extends to other nuclei in the $A \approx 180$ region, it indicates that mixing in the $K^\pi = 5^+$ band should be primarily responsible for the observed de-excitation of the 9^- isomer. Coulomb excitation of ^{180}Ta would provide measurements of the matrix elements coupled to the isomer bands, extending the study of the breakdown of K-conservation to higher-K bands (*e.g.* the $K = 4, 5$ bands) and leading to an understanding of the mechanism of the observed stimulated emission. Similarly, high purity 98% enriched isomeric ^{242}Am target material is available and could be used to get a highly selective measurement of the matrix elements connected to its 5^- ($t_\frac{1}{2} = 141$ y) isomer. Coulomb excitation studies using enriched isomeric targets in high resolution γ-ray and particle detectors provide the means for a complete search for intermediate (triggering) states without the need to confine the search to a particular photon energy range. The Coulomb excitation and analysis techniques of the present work would provide a more complete picture of the K-mixing phenomenon which is also crucial for evaluating the possibility of triggered energy release in other nuclei.

Chapter 12

Conclusion

High-K bands in ^{178}Hf were populated by Coulomb excitation at safe energies below the Coulomb barrier in two experiments, demonstrating violations of the K-selection rule for electromagnetic transitions. An 89% enriched ^{178}Hf target was Coulomb-excited by a $650\,\mathrm{MeV}$ Xe beam, populating the $K^\pi = 2^+$ and 4^+ bands as well as the 6^+, 8^- and 16^+ isomer bands. The 8^- isomer was excited to a strength which indicated excitation probabilities lying between the previous measurements of Hamilton and Xie [29, 30] (Table 4.3). The 6^+ and 16^+ isomers were populated with similar probability to that of the 8^- isomer (Table 9.3). Matrix elements coupling the low- and high-K bands were measured, and led to an understanding of the breakdown of the K-selection rule. In a second experiment, a ^{178}Hf beam was Coulomb excited to the 16^+ isomer state by bombarding a Ta target at energies ranging from 72% to 88% of the Coulomb barrier. The combined data from the two experiments resulted in measurements of the $\langle I_f, K = 16 \| E2 \| I_i, K = 0 \rangle$ matrix elements. Analysis of the Coulomb excitation yields revealed an increasing breakdown of the K-selection rule with increasing spin, through the measurement of matrix elements coupling low- and high-K bands in ^{178}Hf.

This first probe of the K-distribution with respect to spin in nuclei has shown that rotational alignment can explain the rapid breakdown of the goodness of

the K quantum number as the low-K bands are excited to higher rotational frequencies. The rapid increase in the interband matrix elements coincides with the rotational aligment of low-K bands which has a noticeable effect in the moment of inertia above the $I \approx 10$ levels of the γ-band and the GSB. Higher-K components are admixed in the nominally low-K bands with increasing spin, until the reduced transition probabilities saturate for $I \gtrsim 12\hbar$ near ~ 1 W.u. signifying the total breakdown of the K quantum number. For $I > 12$, reduced hindrance values of K-forbidden transitions from low- to high-K bands are as low as $f_\nu \sim 1$, showing that the K-selection rule has little predictive power; highly K-forbidden transitions have similar strength to allowed interband transitions. In contrast, the high-K bands will succumb to rotational alignment only at much higher spin and remain unmixed far above the band heads. This has been verified experimentally (Chapter 10). K remains a good quantum number at much higher spin in the high-K bands, making the interband matrix elements sensitive probes of the K distribution in the low-K bands. Because the effects of collective rotations explain the breakdown of the goodness of K, these conclusions are expected to be applicable to many quadrupole-deformed nuclei.

The breakdown of the goodness of K in the low-K bands has revealed the paths and the matrix elements by which Coulomb depopulation of isomers can proceed at a $\leq 1\%$ level compared to intraband excitations. The attraction of using isomeric states for high density energy storage and for achieving controlled release has led to the search for intermediate states through which x-ray absorption can depopulate high-K isomers. The E1 dominance of excitations by real photons excludes stimulated emission by photon absorption via the particular E2 and E3 matrix elements measured in the present work. However, Coulomb excitation studies have a great potential to reveal intermediate states for photon-stimulated depopulation through the measurement of extensive sets of matrix elements connecting the isomer bands to lower-K bands.

By exploiting the high γ-ray energy resolving power of 4π γ-detector arrays and particle detectors for event-by-event Doppler shift corrections, other studies in nearby $A \approx 180$ nuclei as well as other mass regions would test the universality of the breakdown of K-conservation at high spin. A comparison of the Coulomb excitation of the 8^- isomers in ^{180}Hf and ^{178}Hf, for instance, might untangle single-particle effects from collective rotation effects. The currently available enriched isomeric ^{242}Am and ^{180}Ta targets are expected to provide extensive measurements of matrix elements coupled to the isomer bands, supplementing the current results for $A \approx 180$ and extending the understanding of the breakdown of K-selection to higher mass, as well as revealing practical intermediate states, if they exist, for stimulated emission by photon absorption.

Bibliography

[1] E. Browne. *Nucl. Data Sheets*, 54:199, 1988.

[2] A. M. I. Hague, R. F. Casten, I. Forster, A. Gelberg, R. Rascher, R. Richter, P. von Brentano, G. Barreau, H. G. Borner, S. A. Kerr, K. Schreckenbach, and D. D. Warner. *Nucl. Phys. A*, 455:231, 1986.

[3] F. Rösel, H. M. Fries, K. Alder, and H. C. Pauli. *At. Data Nucl. Data Tables*, 21(4 and 5), 1978.

[4] National Nuclear Data Center online databases. http://www.nndc.bnl.gov.

[5] M. B. Smith, P. M. Walker, G. C. Ball, J. J. Carroll, P. E. Garrett, G. Hackman, R. Propri, F. Sarazin, and H. C. Scraggs. *Phys. Rev. C*, 68:031302R, 2003.

[6] F. W. N. De Boer, P. F. A. Goudsmit, B. J. Meijer, J. C. Kapteyn, J. Konijn, and R. Kamermans. *Nucl. Phys. A*, 263:397, 1976.

[7] H. Postma, B. Kastelein, N. Severijns, D. Vandeplassche, J. Vanhaverbeke, L. Vanneste, E. van Walle, J. Wouters, and J. van Klinken. *Hyp. Inter.*, 52:79, 1989.

[8] W. Z. Venema, R. V. F. Janssens, J. van Klinken, and G. T. Emery. *Nucl. Instrum. Methods*, 201:531, 1982.

[9] S. M. Mullins. Private communication.

[10] R. B. Firestone. *Table of Isotopes*, volume 2. Wiley & Sons, New York, eighth edition, 1996.

[11] C. Flaum. Ph.D. dissertation, University of Rochester, Rochester, NY, 1975.

[12] L. I. Rusinov. *Usp. Fiz. Nauk*, 73:615, 1961.

[13] P. Chowdhury, B. Fabricius, C. Christensen, F. Azgui, S. Bjørnholm, J. Borggreen, A. Holm, J. Pedersen, G. Sletten, M. A. Bentley, D. Howe, A. R. Mokhtar, J. D. Morrison, J. F. Sharpey-Schafer, P. M. Walker, and R. M. Lieder. *Nucl. Phys. A*, 485:136, 1988.

[14] P. Ring and P. Schuck. *The Nuclear Many-Body Problem*. Springer-Verlag, New York, 1980.

[15] M. A. Riley, GAMMASPHERE Users Executive Committee. "GAMMAS-PHERE: The beginning... 1993-1997".

[16] M. W. Simon, D. Cline, C. Y. Wu, R. W. Gray, R. Teng, and C. Long. *Nucl. Instrum. Methods A*, 452:205, 2000.

[17] M. W. Simon. Ph.D. dissertation, University of Rochester, Rochester, NY, 1999.

[18] E. Ngijoi-Yogo. Ph.D. dissertation, University of Massachusetts, Lowell, 2004.

[19] R. D. Evans. *The Atomic Nucleus*. McGraw-Hill Book Co., Inc., New York, 1955.

[20] The Nobel Foundation, editor. *Nobel Lectures, Chemistry 1901-1921*. Elsevier Publishing Co., Amsterdam, 1966.

[21] F. Soddy. *Proc. R. Inst. Gt. Brit.*, 22:117, 1917.

[22] F. Soddy. *J. Chem. Soc.*, 115:1, 1919.

[23] C. F. v. Weizsäcker. *Naturwissenschaften*, 24:813, 1936.

[24] A. Bohr and B. R. Mottelson. *Phys. Rev.*, 90:717, 1953.

[25] F. F. Felber, F. S. Stephens, and F. Asaro. *J. Inorg. Nucl. Chem.*, 7:153, 1958.

[26] P. Walker and G. Dracoulis. *Nature*, 399:35, 1999.

[27] G. Dracoulis. In T. L. Khoo and D. Seweryniak, editors, Proceedings of the Conference on *Nuclei at the Limits*. Am. Inst. Phys., 2005. To be published.

[28] The Nobel Foundation, editor. *Nobel Lectures, Chemistry 1942-1962*. Elsevier Publishing Co., Amsterdam, 1964.

[29] J. H. Hamilton, A. V. Ramayya, R. M. Ronningen, R. O. Sayer, H. Yamada, C. F. Maguire, P. Colombani, D. Ward, R. M. Diamond, F. S. Stephens, I. Y. Lee, P. A. Butler, and D. Habs. *Phys. Lett. B*, 112:327, 1982.

[30] H. Xie, Ch. Ender, J. Gerl, Th. Härtlein, F. Köck, Th. Kröll, P. Reiter, D. Schwalm, P. Thirolf, K. Vetter, A. Wieswesser, and H. J. Wollersheim. *Phys. Rev. C*, 48:2517, 1993.

[31] P. von Neumann-Cosel. *Nucl. Phys. A*, 719:21c, 2003.

[32] J. J. Carroll, S. A. Karamian, L. A. Rivlin, and A. A. Zadernovsky. *Hyp. Inter.*, 135:3, 2001.

[33] J. J. Carroll. *Las. Phys. Lett.*, 1:275, 2004.

[34] J. P. Farrell, V. Dudnikov, J. J. Carroll, and G. Merkel. *Hyp. Inter.*, 143:55, 2002.

[35] S. A. Karamian, J. J. Carroll, J. Adam, and N. A. Demekhina. *Nucl. Phys. A*, 530:463, 2004.

[36] S. Moszkowski. *Phys. Rev.*, 99:803, 1955.

[37] B. R. Mottelson and S. G. Nilsson. *Phys. Rev.*, 99:1615, 1955.

[38] S. G. Nilsson. *Mat. Fys. Medd. Dan. Vid. Selsk.*, 29(16), 1955.

[39] K. Gottfried. *Phys. Rev.*, 103:1017, 1956.

[40] G. Alaga. Ph.D. dissertation, University of Zagreb, 1955.

[41] G. Alaga. *Nucl. Phys.*, 4:625, 1957.

[42] L. R. B. Elton. *Introductory Nuclear Theory*. W. B. Saunders Co., Philadelphia, 1966.

[43] A. Bohr and B. R. Mottelson. *Nuclear Structure*, volume 2. Benjamin, Reading, 1975.

[44] B. Elbek. *Determination of Nuclear Transition Probabilities by Coulomb Excitation*. Munksgaard, Copenhagen, 1963.

[45] G. Alaga, K. Alder, A. Bohr, and B. R. Mottelson. *Dan. Mat. Fys. Medd.*, 29(9), 1955.

[46] J. M. Blatt and V. F. Weisskopf. *Theoretical Nuclear Physics*. Wiley, New York, 1952.

[47] K. E. G. Löbner. *Phys. Lett. B*, 26:369, 1968.

[48] V. M. Mikhailov. *Izv. Akad. Nauk ser. Fiz.*, 30:1334, 1966.

[49] Y. R. Shimizu and T. Nakatsukasa. *Nucl. Phys. A*, 611:22, 1996.

[50] T. R. Saitoh, N. Saitoh-Hashimoto, G. Sletten, R. A. Bark, G. B. Hagemann, and B. Herskind. *Phys. Scripta T*, 88:67, 2000.

[51] P. M. Walker, G. Sletten, N. L. Gjørup, M. A. Bentley, J. Borggreen, B. Fabricius, A. Holm, D. Howe, J. Pedersen, J. W. Roberts, and J. F. Sharpey-Schafer. *Phys. Rev. Lett.*, 65:416, 1990.

[52] P. M. Walker, D. M. Cullen, C. S. Purry, D. E. Appelbe, A. P. Byrne, G. D. Dracoulis, T. Kibédi, F. G. Kondev, I. Y. Lee, A. O. Macchiavelli, A. T. Reed, P. H. Regan, and F. Xu. *Phys. Lett. B*, 408:42, 1997.

[53] T. Bengtsson, R. A. Broglia, E. Vigezzi, F. Barranco, F. Dönau, and Jing ye Zhang. *Phys. Rev. Lett.*, 62:2448, 1989.

[54] D. R. Inglis. *Phys. Rev.*, 96:1059, 1954.

[55] D. R. Inglis. *Phys. Rev.*, 97:701, 1955.

[56] C. Schlegel, P. H. Regan, M. Pfützner, J. Gerl, M. Hellström, Zs. Podolyák, M. Caamaño, P. Mayet, A. Aprahamian, J. Benillure, A. M. Bruce, P. A. Butler, D. Cortina-Gil, D. M. Cullen, J. Döring, T. Enquist, F. Farget, C. Fox, J. Garcés Narro, W. Gelletly, J. Giovinazzo, M. Górska, H. Grawe, R. Grzywacz, A. Kleinböhl, W. Korten, M. Lewitowicz, R. Lucas, H. Mach, M. Minerva, C. O'Leary, F. De Oliveira, C. J. Pearson, M. Rejmund, M. Sawicka, H. Schaffner, K. Schmidt, Ch. Theisen, P. M. Walker, D. D. Warner, C. Wheldon, H. J. Wollersheim, S. Wooding, and F. Xu. *Phys. Scripta T*, 88:72, 2000.

[57] A. B. Hayes, D. Cline, C. Y. Wu, M. W. Simon, R. Teng, J. Gerl, Ch. Schlegel, H. J. Wollersheim, A. O. Macchiavelli, K. Vetter, P. Napiorkowski, and J. Srebrny. *Phys. Rev. Lett.*, 89:242501, 2002.

[58] S. M. Mullins, G. D. Dracoulis, A. P. Byrne, T. R. McGoram, S. Bayer, W. A. Seale, and F. G. Kondev. *Phys. Lett. B*, 393:279, 1997; *Ibid.* 400:401, 1997.

[59] K. Narimatsu, Y. R. Shimizu, and T. Shizuma. *Nucl. Phys. A*, 601:69, 1996.

[60] R. F. Casten. *Nuclear Structure from a Simple Perspective*. Oxford University Press, New York, 1990.

[61] G. R. Satchler. *Introduction to Nuclear Reactions*. Oxford University Press, New York, 1980.

[62] A. E. Kavka. Ph.D. dissertation, Uppsala University, Uppsala, Sweden, 1989.

[63] K. Alder and A. Winther. *Electromagnetic Excitation*. American Elsevier Pub. Co., Inc., New York, 1975.

[64] G. R. Satchler. *Direct Nuclear Reactions*. Oxford University Press, New York, 1983.

[65] K. Alder, A. Bohr, T. Huus, B. Mottelson, and A. Winther. *Rev. Mod. Phys.*, 28:432, 1956.

[66] M. J. Devlin. Ph.D. dissertation, University of Rochester, Rochester, NY, 1995.

[67] R. Bass. *Nuclear Reactions with Heavy Ions*. Springer-Verlag, Berlin, 1980.

[68] D. Cline. *Annu. Rev. Nucl. Part. Sci.*, 36:683, 1986.

[69] D. Cline. *Bull. Am. Phys. Soc.*, 14:726, 1969.

[70] D. Cline, H. S. Gertzman, H. E. Gove, P. M. S. Lesser, and J. J. Schwartz. *Nucl. Phys. A*, 133:445, 1969.

[71] T. Czosnyka, D. Cline, and C. Y. Wu. *Bull. Am. Phys. Soc.*, 28:745, 1983.

[72] T. Czosnyka, D. Cline, and C. Y. Wu. *Coulomb Excitation Data Analysis Code* GOSIA. University of Rochester, Rochester, NY, 1983. Unpublished.

[73] K. Alder and A. Winther. *Coulomb Excitation.* Academic Press, New York, 1966.

[74] D. C. Radford. *Nucl. Instrum. Methods A*, 361:297, 1995.

[75] D. C. Radford. GF2 *Manual.* Oak Ridge National Laboratory, Oak Ridge, TN, 1989. Unpublished.

[76] T. L. Khoo and G. Løvhøiden. *Phys. Lett. B*, 67:271, 1977.

[77] D. Cline and P. M. S. Lesser. *Nucl. Instrum. Methods*, 82:291, 1970.

[78] R. C. de Haan, A. Aprahamian, H. G. Borner, C. Doll, M. Jentschel, A. M. Bruce, and S. R. Lesher. *J. Res. Natl. Inst. Stand. Technol.*, 105:125, 2000.

[79] B. Fogelberg and A. Bäcklin. *Nucl. Phys. A*, 171:353, 1971.

[80] C. Coceva, P. Giacobbe, F. Corvi, and M. Stefanon. *Nucl. Phys. A*, 218:61, 1974.

[81] C. Y. Wu and D. Cline. *Phys. Lett. B*, 382:214, 1996.

[82] S. T. Boneva, E. V. Vasileva, E. P. Grigor'ev, Yu. P. Popov, A. M. Sukhovoi, and V. A. Khitrov. *Izv. Akad. Nauk SSSR ser. Fiz.*, 53:884, 1989; *Bull. Acad. Sci. USSR, Phys. ser.*, 53(5):61, 1989.

[83] E. Browne. *Nucl. Data Sheets*, 72:221, 1994.

[84] N. Pietralla, O. Beck, J. Besserer, P. von Brentano, T. Eckert, R. Fischer, C. Fransen, R.-D. Herzberg, D. Jager, R. V. Jolos, U. Kneissl, B. Krischok,

J. Margraf, H. Maser, A. Nord, H. H. Pitz, M. Rittner, A. Schiller, and A. Zilges. *Nucl. Phys. A*, 618:141, 1997.

[85] C. Baglin. *Nucl. Data Sheets*, 72:617, 1994.

[86] P. Tlustý, D. Vénos, A. Kugler, M. Honusek, and B. Gorski. *Phys. Rev. C*, 48:2082, 1993.

[87] I. Ahmad and P. A. Butler. *Annu. Rev. Nucl. Part. Sci.*, 43:71, 1993.

[88] R. H. Spear. *At. Data Nucl. Data Tables*, 42:55, 1989.

[89] R. M. Ronningen, J. H. Hamilton, A. V. Ramayya, L. Varnell, G. Garcia-Bermudez, J. Lange, W. Lourens, L. L. Riedinger, R. L. Robinson, P. H. Stelson, and J. L. C. Ford, Jr. *Phys. Rev. C*, 15:1671, 1977.

[90] C. Y. Wu, W. von Oertzen, D. Cline, and M. W. Guidry. *Annu. Rev. Nucl. Part. Sci.*, 40:285, 1990.

[91] E. Storm and H. I. Israel. *Nucl. Data Tables*, A7:565, 1970.

[92] National Institute of Standards and Technology XCom online databases. http://physics.nist.gov.

[93] D. Kotlinski. Computer code SMSCAT, 1984. University of Rochester, Rochester, NY.

[94] P. Sigmund and K. B. Winterbon. *Nucl. Instrum. Methods*, 119:541, 1974.

[95] B. Back and G. Voth. Computer code QDIST, September 1993. Argonne National Laboratory, Argonne, IL.

[96] C. D. Moak, H. O. Lutz, L. B. Bridwell, L. C. Northcliffe, and S. Datz. *Phys. Rev. Lett.*, 18:41, 1967.

[97] K. Shima, T. Mikumo, and H. Tawara. *At. Data Nucl. Data Tables*, 34:358, 1986.

[98] R. G. Helmer and C. W. Reich. *Nucl. Phys. A*, 211:1, 1973.

[99] F. Hubert, R. Bimbot, and H. Gauvin. *At. Data Nucl. Data Tables*, 46:1, 1990.

[100] A. J. Ferguson. *Angular Correlation Methods in Gamma-Ray Spectroscopy*. North-Holland Publishing Co., Amsterdam, 1965.

[101] M. Rotenberg, R. Bivins, N. Metropolis, and J. K. Wooten, Jr. *The 3-j and 6-j Symbols*. The Technology Press, Cambridge, MA, 1959.

[102] H. L. Nielsen, K. Wilsky, and J. Zylicz. *Nucl. Phys. A*, 93:385, 1967.

[103] H. L. Nielsen, K. B. Nielsen, and N. Rud. *Phys. Lett. B*, 27:150, 1968.

[104] A. Aprahamian. *Nucl. Phys. A*, 731:291, 2004.

[105] C. Y. Wu and D. Cline. *Phys. Lett. B*, 382:214, 1996.

[106] X. Wu, A. Aprahamian, J. Castro-Ceron, and C. Baktash. *Phys. Lett. B*, 316:235, 1993.

[107] X. Wu, A. Aprahamian, S. M. Fischer, G. Liu W. Reviol, and J. X. Saladin. *Phys. Rev. C*, 49:1837, 1994.

[108] A. Bohr and B. R. Mottelson. *Nuclear Structure*, volume 1. Benjamin, Reading, 1975.

[109] R. D. Lawson. *Theory of the Nuclear Shell Model*. Oxford University Press, New York, 1980.

[110] O. Prior, F. Boehm, and S. G. Nilsson. *Nucl. Phys. A*, 110:257, 1968.

[111] E. Schoeters, R. E. Silverans, L. Vanneste, K. Freitag, and H. Hübel. *Z. Phys. A*, 262:203, 1975.

[112] P. M. Walker, D. Ward, O. Häusser, H. R. Andrews, and T. Faestermann. *Nucl. Phys. A*, 349:1, 1980.

[113] A. O. Macchiavelli and E. Browne. *Nucl. Data Sheets*, 69:903, 1993.

[114] E. Browne. *Nucl. Data Sheets*, 68:747, 1993.

[115] R. B. Firestone. *Nucl. Data Sheets*, 62:101, 1991.

[116] N. Boos, F. Le Blanc, M. Krieg, J. Pinard, G. Huber, M. D. Lunney, D. Le Du, R. Meunier, M. Hussonnois, O. Constantinescu, J. B. Kim, Ch. Briançon, J. E. Crawford, H. T. Duong, Y. P. Gangrski, T. Kühl, B. N. Markov, Yu. Ts. Oganessian, P. Quentin, B. Roussière, and J. Sauvage. *Phys. Rev. Lett.*, 72:2689, 1994.

[117] E. Lubkiewicz, H. J. Wollersheim, R. Kulessa, Ch. Briançon, W. Brüchle, O. Constantinescu, M. Dębowski, E. Ditzel, H. Folger, J. Gerl, F. Hannachi, T. Happ, M. Hussonnois, E. Jäger, S. Karamyan, M. Kaspar, Th. Kröll, Yu. Ts. Oganessian, I. Peter, H. Schaffner, S. Schremmer, R. Schubert, N. Trautmann, K. Vetter, and G. Zauner. *Z. Phys. A*, 355:377, 1996.

[118] R. G. Helmer and C. W. Reich. *Nucl. Phys. A*, 14:649, 1968.

[119] N. L. Gjørup, P. M. Walker, G. Sletten, M. A. Bentley, B. Fabricius, and J. F. Sharpey-Schafer. *Nucl. Phys. A*, 582:369, 1995.

[120] T. L. Khoo, J. C. Waddington, R. A. O'Neil, Z. Preibisz, D. G. Burke, and M. W. Johns. *Phys. Rev. Lett.*, 28:1717, 1972.

[121] J. van Klinken, W. Z. Venema, R. V. F. Janssens, and G. T. Emery. *Nucl. Phys. A*, 339:189, 1980.

[122] M. J. A. de Voigt, J. Dudek, and Z. Szymański. *Rev. Mod. Phys.*, 55:949, 1983.

[123] S. W. Yates, I. Y. Lee, N. R. Johnson, E. Eichler, L. L. Riedinger, M. W. Guidry, A. C. Kahler, D. Cline, R. S. Simon, P. A. Butler, P. Colombani, F. S. Stephens, R. M. Diamond, R. M. Ronningen, R. D. Hichwa, J. H. Hamilton, and E. L. Robinson. *Phys. Rev. C*, 21:2366, 1980.

[124] Y. Sun, X.-R. Zhou, G.-L. Long, E.-G. Zhao, and P. M. Walker. *Phys. Lett. B*, 589:83, 2004.

[125] G. D. Dracoulis, T. Kibédi, A. P. Byrne, R. A. Bark, and A. M. Baxter. *Phys. Rev. C*, 62:37301, 2000.

[126] S. V. Karyagin. *Hyp. Inter.*, 141/142:53, 2002.

[127] P. M. Walker, G. D. Dracoulis, and J. J. Carroll. *Phys. Rev. C*, 64:061302, 2001.

[128] S. Olariu, A. Olariu, and V. Zoran. *Phys. Rev. C*, 56:381, 1997.

[129] S. Olariu and A. Olariu. *Phys. Rev. C*, 58:333, 1998.

[130] C. B. Collins, F. Davanloo, M. C. Iosif, R. Dussart, J. M. Hicks, S. A. Karamian, C. A. Ur, I. I. Popescu, V. I. Kirischuk, J. J. Carroll, H. E. Roberts, P. McDaniel, and C. E. Crist. *Phys. Rev. Lett.*, 82:695, 1999.

[131] C. B. Collins, F. Davanloo, A. C. Rusu, M. C. Iosif, N. C. Zoita, D. T. Camase, J. M. Hicks, S. A. Karamian, C. A. Ur, I. I. Popescu, R. Dussart, J. M. Pouvesle, V. I. Kirischuk, N. V. Strilchuk, P. McDaniel, and C. E. Crist. *Phys. Rev. C*, 61:054305, 2000.

[132] C. B. Collins, F. Davanloo, M. C. Iosif, R. Dussart, J. M. Hicks, S. A. Karamian, C. A. Ur, I. I. Popescu, V. I. Kirischuk, J. M. Pouvesle, P. Mc-Daniel, and C. E. Crist. *Phys. At. Nucl.*, 63:2067, 2000.

[133] S. Olariu and A. Olariu. *Phys. Rev. Lett.*, 84:2541, 2000.

[134] P. von Neumann-Cosel and A. Richter. *Phys. Rev. Lett.*, 84:2543, 2000.

[135] D. P. McNabb, J. D. Anderson, J. A. Becker, and M. S. Weiss. *Phys. Rev. Lett.*, 84:2542, 2000.

[136] C. B. Collins, F. Davanloo, M. C. Iosif, R. Dussart, J. M. Hicks, S. A. Karamian, C. A. Ur, I. I. Popescu, V. I. Kirischuk, H. E. Roberts, P. McDaniel, and C. E. Crist. *Phys. Rev. Lett.*, 84:2545, 2000.

[137] I. Ahmad, J. C. Banar, J. A. Becker, D. S. Gemmell, A. Kraemer, A. Mashayekhi, D. P. McNabb, G. G. Miller, E. F. Moore, L. N. Pangault, R. S. Rundberg, J. P. Schiffer, S. D. Shastri, T. F. Wang, and J. B. Wilhelmy. *Phys. Rev. Lett.*, 87:072503, 2001.

[138] J. J. Carroll, J. Burnett, T. Drummond, J. Lepak, R. Propri, D. Smith, S. A. Karamian, J. Adam, F. Stedile, and F. J. Agee. *Hyp. Inter.*, 143:37, 2002.

[139] H. E. Roberts, M. Helba, J. J. Carroll, J. Burnett, T. Drummond, J. Lepak, R. Propri, and Z. Zhong F. J. Agee. *Hyp. Inter.*, 143:111, 2002.

[140] C. B. Collins, N. C. Zoita, A. C. Rusu, M. C. Iosif, D. T. Camase, F. Davanloo, S. Emura, T. Uruga, R. Dussart, J. M. Pouvesle, C. A. Ur, I. I Popescu, V. I. Kirischuk, N. V. Strilchuk, and F. J. Agee. *Euro. Phys. Lett.*, 57:677, 2002.

[141] E. V. Tkalya. *Phys. Rev. C*, 68:064611, 2003.

[142] D. Cline, A. B. Hayes, and C. Y. Wu. In Proceedings of the 35th Winter Colloquium on *The Physics of Quantum Electronics*. Taylor and Francis, 2005. To be published.